DEPARTAMENTO DE ASTROFISICA

Universidad de La Laguna

Understanding Blazar emission through multifrequency observations

Thesis submitted by
D. Maria Isabel Carnerero Martín
As a requirement for the degree of
Doctor by University of La Laguna

INSTITUTO Đ ASTROFISICA Đ CANARIAS
INAF-OSSERVATORIO ASTROFISICO DI TORINO
July de 2016

Examination date: September, 2016
Thesis supervisor: Dra. Claudia M. Raiteri
Thesis co-supervisor:Dr. Jose A. Acosta Pulido

©Maria Isabel Carnerero Martín 2016
Some of the material included in this document has been already published in *Monthly Notices of the Royal Astronomical Society.*

a mi HÉROE.....mi Padre

The Cosmos is all that is or ever was or ever will be.
Our feeblest contemplations of the Cosmos stir us
-there is a tingling in the spine, a catch in the voice, a faint
sensation, as if a distant memory, or falling from a heigh.
We know we are approaching the greatest of mysteries.

–Carl Sagan–

Science can teach us,
and I think our hearts can teach us,
no longer to look around for imaginary supporters,
no longer to invent allies in the sky,
but rather to look to our own efforts here below
to make the world a fit place to live.

–Bertrand Russell–

Look up at the stars and not down at your feet.
Try to make sense of what you see,
and wonder about what makes the universe exist.
Be curious.

–Stephen Hawking–

Agradecimientos

Estos cuatros años de tesis han sido unos años maravillosos pero a la vez los años más duros de mi vida. Sin embargo gracias a todas esas personsas que he conocido y a las personas que siempre han estado ahí, todo se va superando. Ellas son las verdaderas responsables de que esta tesis haya llegado a su fin. Porque "A la vida hay que darle soluciones, no problemas".

Agradezco al INAF-Osservatorio Astrofísico di Torino y al Instituto de Astrofísica de Canarias por ofrecerme la posibilidad de llevar a cabo este proyecto.

Quiero agredecer a mi directora y mi codirector de tesis. A Claudia gracias por tu apoyo, tu comprensión y tu paciencia. Por estar ahí siempre que te he necesitado, por ayudarme a encontrarme cuando estaba perdida, por despertarme la curiosidad por los Blazars "che sono un casino"y tener siempre unas bonitas palabras y una linda sonrisa. Gracias Jose por confiar en mí y animarme a encaminar esta aventura hacia Italia. Gracias por permitir que me dedicara profesionalmente a lo que siempre soñé, ser astrofísico. Sin tí nada de esto hubiera sido posible, gracias por estar ahí, dando igual el día, la hora... siempre que te necesitaba ahí estabas, gracias por tus ánimos y por hacerme ver que todo se puede. Gracias por todo lo que me habeis enseñado, ha sido un placer aprender y trabajar con vosotros!

A mi familia, en especial a mi Padre. No tendría espacio para escribir todo lo que te tengo que agredecer, para mi fuiste una fuente de admiración. Gracias por ayudarme a conseguir mis sueños, por tus ánimos, tus palabras, tus sonrisas y esa forma de hacer posible lo imposible. Sin ti, nada de esto hubiera sido posible, gracias por enseñarme a valorar la vida y luchar con todas mis fuerzas como tú lo hiciste, porque fuistes un héroe para mí. A mi madre por estar siempre ahí, por tus ánimos, tus palabras, por apoyar cada una de mis decisiones, por haber sido el mejor de los ejemplos de esfuerzo, tenacidad, alegría, y por no dejar que me rindiera. A mi hermano por su paciencia, por hacerme sentir cerca aun estando lejos, por ayudarme en todo momento y por estar siempre ahí. A mi sobrino Borja por ser la luz que ilumina mi vida. Nunca pierdas la curiosidad por las cosas! A mis abuelos, los que están y los que no, por haberme apoyado siempre, desde que inicié mi andadura fuera de casa. A mis tios y primos, por sus consejos, su apoyo y por estar siempre pendientes de mí.

A Ge por aparecer cuando más lo necesitaba, eres de las mejores cosas que me han pasado en la vida. Siempre has estado ahí en los momentos buenos y no tan buenos. No conocemos el futuro, no sabemos que pasará, pero sí tengo claro que quiero caminar a tu lado, que quiero

compartir cada momento que la vida nos ponga en nuestro camino y seguir siendo felices. Cada persona conoce sus propósitos para ser feliz y el mio era conocerte, conquistarte y vivir una vida juntos. Gracias por enseñarme a vivir la vida al 100% y a saber apreciar lo que es realmente importante.

A Carmelina y Donato "El tramposo", gracias por hacerme ver que con lucha y constancia todo se puede, porque sois un ejemplo a seguir. Gracias por vuestra preocupación y porque casi sin conocerme de nada me habeis hecho sentir una más de la familia. A Vito porque aunque veamos la vida de forma diferente sé que siempre estarás ahí y podré contar contigo.

A Ari porque estando en la otra punta del mundo siempre tenías todo el tiempo del mundo para mí. Gracias por estar siempre ahí, por tus buenos consejos, por tus ánimos, paciencia, risas y también lágrimas. Porque para mí ya no eres sólo una amiga eres una hermana. Porque las cosas no se dicen se demuestran, como haces tú. Sigue luchando por tus sueños porque puedes con todo.

A Marina Manganaro, gracias por el entusiasmo que has puesto en la corrección de esta tesis, por tu disponibilidad y por todas las bonitas sugerencias que hicistes.

A la gente del Observatorio que hicieron que esta etapa fuera más divertida y que ayudaron a sobrellevar los momentos más grises, cuando un programa no funcionaba o los datos eran incoherentes... A Leo "El maestro", Seb o Giusseppe? y Antonio "el pollo", por esas pausas de café y esas largas reflexiones. Gracias por crear una atmósfera agradable, por hacer que el día a día fuera algo más que trabajar. Por esas partidas al calcetto; el equipo "blandengue"siempre estará ahí. Y bueno a Manolo Escobar también no Seb?, a él también tenemos mucho que agradecerle. A Massimo Villata por su ayuda prestada y sus sabios consejos. A Catia por convertirse en mi amiga y compañera de viaje durante mis primeros años en Torino. Siempre serás un MURO. A Ummi gracias por tus ánimos, tu apoyo, por tus buenos consejos y por estar siempre pendiente de mí.

A Stefania porque cuando llegué me sentía un poco perdida, pero apareció ella, "la boluda", para ayudarme en todo lo que estaba en sus manos. Gracias por tu ayuda en la instalación de programas, por tus risas, por escucharme y por un sinfín de cosas. Gracias por aparecer!

A todas esas personas que pasaron por mi vida en el "palazzo Erasmus", en especial a Roby y Jasmin mis dos italianas favoritas. Gracias por haberos cruzado en mi vida, por nuestras charlas, risas, por ayudarme a olvidar la ciencia por un ratito. Ahora que cada una volvió a su ciudad, se os echa de menos.

A Luca, Paoletta e la piccola Elisa gracias por esos fines de semana de desconexión en la montaña y por estar siempre animándome en esta etapa final de la tesis. Sois increibles. A Rosa gracias por tu sonrisa, tus palabras de apoyo, por estar siempre pendiente de mí. Es una suerte que te hayas cruzado en mi camino.

A mis amigos de siempre Carmen y Álvaro y a los dos chiquitines de la casa, Nazaret y

David. Os cruzasteis en mi vida de casualidad y pasasteis a formar parte de ella, doy gracias porque eso pasara. Sois ese tipo de personas que da igual donde estés o donde vayas, siempre están ahí, preocupandose por tí, sacándote una sonrisa, haciéndote ver que la vida es bonita y que hay que hacer lo que a uno le haga feliz. Gracias por ser como sois, os quiero mucho. A Antonio, Raul, Mercedes, Rocío, Maite, Rubén, Lucia... gracias por apoyarme siempre, aunque no hablamos tanto como deberíamos sé que estáis ahí.

A toda esa gente de Tenerife que hace que volver allí sea siempre un placer. A Ana y Adur porque sé que siempre puedo contar con ellos. A Santi, Ivan, Paloma, Juanan, Andrea, ... Al grupo de observadores de Blazars que también han contribuido a que esta tesis sea posible, Cristina P., Cristina M., Sergio, Patricia, Pedro, Maria Jesus, Carlos, Alberto, Noel, Irene, Javi, Gustavo, Alejandra, Francesca...GRACIAS!

A Heylene y Karen, porque el trío se separó hace cuatro años pero seguimos siempre juntas incluso en la distancia. Siempre estarán nuestras charlas, risas... y nuestros bailes! :) Acordarme de vosotras es siempre sacar una sonrisa.

Estos cuatro años no hubieran sido lo mismo sin todos vosotros. Sólo os puedo decir

GRACIAS.

Maribel Carnerero Martín

Ringraziamenti

Questi quattro anni di tesi sono stati anni meravigliosi, però a volte, anche gli anni più duri della mia vita. Grazie a tutte le persone nuove che ho conosciuto e a quelle che ci sono sempre state si pu superare tutto. Loro sono i veri responsabili se questo lavoro di tesi è arrivato alla fine. Perchè "Alla vita bisogna darle soluzioni, non problemi".

Ringrazio l'INAF-Osservatorio Astrofisico di Torino e l'Istituto di Astrofisica delle Canarie per avermi dato l'opportunità di portare avanti questo progetto.

Innanzitutto voglio ringraziare la mia direttrice ed il mio co-direttore di tesi. A Claudia, grazie per il tuo supporto, la tua comprensione e la tua pazienza. Per essere stata disponibile tutte le volte che ho avuto bisogno, per avermi aiutata a ritrovarmi quando mi sono persa, per aver saputo svegliare in me la curiosità per i Blazars "che sono un casino"e per avere sempre una buona parola ed un bel sorriso. Grazie Jose, per aver avuto fiducia in me ed avermi incoraggiata ad iniziare questa avventura in Italia. Grazie per aver permesso che mi dedicassi professionalmente a ciò che ho sempre sognato, essere una astrofisica. Senza di te niente di ciò sarebbe stato possibile. Grazie per essere sempre presente a prescindere dal giorno e dall'ora...tutte le volte che ho avuto bisogno eri lì presente. Grazie per il tuo supporto e per farmi vedere che tutto è possibile. Grazie per tutto ciò che mi avete insegnato, è stato un piacere imparare e lavorare con voi!.

Alla mia famiglia, specialmente a mio Padre, perchè non ho qui lo spazio per scrivere tutto ciò per cui devo ringraziarti. Per me sei stato una fonte di ammirazione. Grazie per aiutarmi a conseguire i miei sogni, per il tuo supporto, le tue parole, i tuoi sorrisi e questo modo di rendere possibile anche l'impossibile. Senza di te, niente di tutto questo sarebbe stato possibile. Grazie per avermi insegnato ad apprezzare la vita e a lottare con tutte le mie forze, come hai fatto tu, che sei stato un eroe per me. A mia madre per essere sempre lì, per il suo supporto, per le sue parole, per appoggiare tutte le mie decisioni, per essere stata per me il migliore esempio di sforzo, tenacità, allegria e non permettere che mi arrendessi. A mio fratello per la sua pazienza, per farmi sentire vicina pur essendo lontani, per aiutarmi in tutti i momenti e per essere sempre l. Al mio nipote Borja, per essere la luce che illumina la mia vita. Non perdere mai la curiosità per le cose!. Ai miei nonni, quelli presenti e quelli che non ci sono più, per avermi sempre, appoggiata da quando ho iniziato a vivere fuori di casa. Ai miei zii e cugini, per i loro consigli, il loro supporto e per essere sempre attenti a me.

A Ge, per comparire quando più lo necessitavo, sei una delle cose migliori che siano successe

nella mia vita. Sei stato sempre l nei momenti belli e meno belli. Non conosciamo il futuro, non sappiamo cosa succederà, però ho chiaro che voglio camminare al tuo fianco, condividere ogni momento che la vita metterà sul nostro sentiero e poterti rendere felice. Tutte le persone conoscono i propri propositi per essere felici ed il mio era conoscerti, conquistarti e vivere una vita insieme. Grazie per insegnarmi a vivere la vita al 100% e saper apprezzare ciò che è veramente importante.

A Carmelina e Donato "El tramposo", grazie per farmi vedere che con lotta e costanza si può tutto, siete un esempio da seguire. Grazie per le vostre preoccupazioni e per avermi fatto sentire una in più della famiglia senza quasi conoscermi. A Vito perchè anche se vediamo la vita in modo diverso so che sarai sempre lì e che potrò contare su di te.

Ad Ari perchè pur vivendo all'altra punta del mondo ha avuto sempre tutto il tempo per me. Grazie per essere sempre lì, per i tuoi buoni consigli per il tuo appoggio, la tua pazienza, le tue risate ed anche per le lacrime. Per me non sei solo una amica, sei una sorella. Perchè le cose non si dicono, si dimostrano, come fai tu. Continua a lottare per i tuoi sogni perchè tu puoi tutto.

A Marina Manganaro, grazie per l'entusiasmo nella correzione di questa tesi, per la tua disponibilità e per tutti i bei suggerimenti che mi hai dato.

Alla gente dell'Osservatorio que ha fatto sì che questa tappa fosse più divertente e che mi hanno aiutata a superare i momenti più grigi, quando un programma non funzionava o i dati erano incoerenti. A Leo "el maestro", Seb o Giuseppe? e Antonio "el pollo", per tutte le pause caffè e le lunghe riflessioni. Grazie per creare un'atmosfera piacevole, per fare sì che la quotidianità fosse qualcosa di più che lavorare. Per le partite a calcetto, la squadra "blandengue" sarà sempre lì. E ovviamente anche a Manolo Escobar, no Seb? anche a lui dobbiamo molti ringraziamenti. A Massimo Villata per i suoi aiuti ed i suoi saggi consigli. A Catia per essere diventata la mia amica e compagna di viaggio durante i miei primi anni a Torino, sarai sempre un MURO. A Ummi, grazie per i tuoi incoraggiamenti, il tuo appoggio, per i tuoi buoni consigli e per preoccuparti sempre per me.

A Stefania, perchè quando sono arrivata e mi sentivo un poco persa è comparasa lei, "la boluda", ad aiutarmi in tutto ciò che ha potuto. Grazie per il tuo aiuto nell'installazione dei programmi, per le tue risate, per ascoltarmi e per una serie infinita di cose. Grazie per essere comparsa!

A tutte quelle persone che sono passate nella mia vita nel "palazzo Erasmus", specialmente a Roby e Jasmin, le mie due italiane favorite. Grazie per aver incrociato la mia vita, per le nostre chiacchierate, risate, per aiutarmi a dimenticare la Scienza per un pò. Adesso, che siete ritornate alle vostre città, mi mancate.

A Luca, Paoletta e la piccola Elisa, grazie per i fine settimana di disconnessione in montagna e per stare sempre lì ad incoraggiarmi in questa tappa finale della tesi. Siete incredibili. A Rosa, grazie per i tuoi sorrisi, le tue parole di appoggio, per essere sempre presente. È una fortuna che i nostri cammini si siano incrociati.

Ai miei amici di sempre, a Carmen e Álvaro e ai due piccoletti della casa, Nazaret e David. Le nostre vite si sono incrociate casualmente e siete entrati a far pienamente parte della mia vita. Vi ringrazio perchè questo sia successo. Siete quelle persone che non importa dove stai o dove vai, loro sono sempre lì a preoccuparsi per te, strappandoti un sorriso, facendoti vedere che la vita è bella e che si deve fare ciò che ci rende felici. Grazie per come siete, vi voglio molto bene. Ad Antonio, Raul, Mercedes, Rocío, Maite, Rubén, Lucia...grazie per appoggiarmi sempre, anche se non ci sentiamo spesso come dovremmo so che siete lì.

A tutte quelle persone di Tenerife che fanno in modo che tornare lì sia sempre un piacere...A Ana e Adur, perchè so che posso sempre contare su di loro. A Santi, Ivan, Paloma, Lucia, Juanan, Andrea,... Al gruppo di osservatòri di Blazars che hanno contribuito anche a che questa tesi fosse possibile, Cristina P., Cristina M., Sergio, Patricia, Pedro, Maria Jesus, Carlos, Alberto, Noel, Irene, Javi, Gustavo, Alejandra, Francesca...GRAZIE!

A Heylene e Karen, perchè il trio si è separato da quattro anni ma continuiamo ad essere unite nonostante la distanza. Resteranno sempre le nostre chiacchiere, le risate...ed i nostri balli :). Ricordarmi di voi equivale a sorridere tutte le volte.

Questi quattro anni non sarebbero stati lo stesso senza tutti voi. Solo posso dirvi

GRAZIE.

Maribel Carnerero Martín

Resumen

La idea principal de esta tesis es el estudio multifrecuencia, desde radio frequencias hasta rayos γ, de un tipo de Núcleos Activos de Galaxias (AGNs) llamados "blazars" (BL Lacs y FSRQs). La emisión de estos objetos está generalmente dominada por la radiación no térmica de unos chorros de plasma acelerados a velocidades relativistas (los llamaremos "jet" por su nombre en inglés), por ello son los mejores candidatos para investigar las propiedades de los jets en los AGNs.

Nosotros presentamos un análisis del flujo observado de estos objetos desde radio hasta rayos γ. Los datos de radio, óptico e infrarrojo cercano se han obtenidos gracias a la colaboración internacional WEBT-GASP y al seguimiento espectropolarimetrico del Observatorio de Steward, mientras que los restantes datos los hemos obtenido de bases de datos de observatorios espaciales. En particular, los datos en los rangos de frecuencias a ultravioleta y rayos X se obtuvieron de la misión *Swift* y los datos de rayos γ de la misión *Fermi*.

Con estos datos podemos construir las curvas de luz multifrecuencias, estudiar la variabilidad de estos objetos y ver las correlaciones con el flujo en las diferentes bandas y sus respectivos retardos.

Además con la recopilación de datos multifrecuencia podemos realizar la distribución espectral de energía (SED). Estos resultados nos permiten conocer el mecanismo y estructura de emisión del jet, la localización de la región de emisión. Escogiendo datos simultáneos de las diferentes frecuencias y en diferentes estados de brillo, podemos detectar si existen contribuciones de emisión que no provengan del jet pero sí del núcleo del AGN. Por ejemplo, en algunos blazars observamos estados en los que la emisión proviene posiblemente del disco de acreción y en otros casos ésta es originada en el disco después del reprocesamiento por nubes de gas que se mueven rápidamente alrededor del disco de acreción, también conocida como BLR. La detección del disco de acreción y/o la emisión de la BLR es de gran importancia porque nos ayuda a comprender la relación entre los blazars y los otros tipos de AGNs. Cabe mencionar que en la construcción de la SED es conveniente tener una cobertura espectral lo más completa posible, lo cual es muy difícil en la región ultravioleta por estar fuertemente afectada por la absorción galáctica.

Una vez construidas las curvas de luz y las SEDs, las usaremos para realizar diferentes pruebas con los modelos de jet propuestos para interpretar la emisión de los blazars. Sabemos que

la emisión del blazar a baja energía es debida a la emisión sincrotrón de los electrones relativistas moviendose a lo largo de las líneas del campo magnético, mientras que la radiación a alta energía es producida por el efecto Compton inverso, que es la dispersión de fotones de baja energía por electrones relativistas. Sin embargo, el origen de estos fotones es muy debatido, hay varios procesos que pueden contribuir, por ejemplo la propia emisión sincrotrón de los electrones relativistas, o de otras regiones del núcleo activo como pueden ser el disco de acrecimiento, la región de emisión de lineas anchas, o a mayor distancia el toro molecular.

En los ultimos años se ha realizado un gran esfuerzo en la obtención de datos polarimétricos para poder conocer mejor el comportamiento del campo magnético. En la presente tesis, analizamos un amplio conjunto de datos polarimétricos para diferentes blazars, y así intentar identificar sus propiedades. Encontramos que los objetos tienen comportamientos diferentes. Algunos tienen comportamientos ordenados y otros más caoticos, con lo cual una explicación simple, o muy genérica no parece posible. Es muy probable que la mayor parte del tiempo el campo magnético se vea afectado por el medio turbulento que forma el plasma del jet. Todas estas cuestiones siguen siendo objeto de debate y se espera que proporcionen un amplio campo para investigar durante muchos años.

Abstract

The heart of this thesis is the study of the multifrequency behaviour of a very special family of active galactic nuclei (AGNs) called blazars. The emission of these sources is generally dominated by non-thermal radiation from a plasma jet, making them the best candidates to investigate the properties of jets in AGNs.

We present an analysis of the flux and broad-band spectral variability of these objects from radio to the γ rays. The radio, optical and near-infrared data were mostly obtained thanks to the Whole Earth Blazar Telescope (WEBT) Collaboration and Steward Observatory blazar spectropolarimetric monitoring, while high-energy data come from space observatories. In particular, ultraviolet and X-ray data were taken from *Swift* and γ-ray data from *Fermi*.

We produce multifrequency light curves that allow us to investigate the variability properties of these objects on different time scales, the correlation between flux changes in the different bands and possible time delays. From these results we infer which are the most plausible physical mechanisms for blazar emission and the jet structure, in particular where the emission is located and the jet possible curvature.

From this collection of multifrequency data we can determine the energy spectral distribution (SED). Observing simultaneously at different frequencies and in different brightness states, we can detect whether there are emission contributions that are not coming from the jet, but from the AGN nucleus. In some cases we are able to observe activity states in which emission might flow from the accretion disk, while in other ones it comes from the disk after reprocessing by fast-moving gas clouds around the accretion disk, known as broad line region (BLR). The detection of the accretion disk and/or BLR emission is very important because it helps us to understand the relation between the blazars and the other types of AGNs. This is a challenging topic since very high-quality data are needed, especially at ultraviolet frequencies, i.e. in a spectral region strongly affected by Galactic absorption.

Once we have built light curves and SEDs we use them to test different jet models proposed to describe blazar emission. We know that the blazar emission at low energies is synchrothron radiation produced by relativistic electrons moving in a magnetic field. The radiation at high energies is likely produced by an inverse Compton process, where soft photons are scattered by the same relativistic electrons. However, the origin of these photons is still under discussion. As for the variability mechanisms, particle injection, acceleration and cooling are likely at work,

together with shocks propagating along the jet and orientation effects in curved and dynamic jets.

Recently, a lot of observing effort has been devoted in providing polarimetric data in order to obtain information on the behaviour of the magnetic field. We analyze a wide dataset of polarimetric data on several blazars to identify characteristic properties. We found a variety of behaviours, some of them ordered but the majority of them resulting in a chaotic trend, so that a simple and all-inclusive explanation is not possible. Indeed, it is very likely that turbulence affects the magnetic field most of the time. All the above issues are still matter of debate and are expected to provide a wide research field to explore for many years.

Contents

Agradecimientos **vii**

Ringraziamenti **xi**

Resumen **xv**

Abstract **xvii**

Introduction **1**

1 Active Galactic Nuclei: an overview **3**
1.1 Classification of AGNs . . . 4
1.1.1 Seyfert galaxies . . . 5
1.1.2 Liners . . . 6
1.1.3 Quasars . . . 7
1.1.4 Radio Galaxies . . . 8
1.2 The Unified Model and structure of an AGN . . . 10
1.2.1 The accretion disk . . . 12
1.2.2 The torus . . . 14
1.2.3 The jets . . . 14
1.3 Relativistic effects . . . 15
1.3.1 Relativistic beaming . . . 15
1.3.2 Superluminal motions . . . 16
1.4 Emission processes . . . 17
1.4.1 Synchrotron emission . . . 18
1.4.2 Inverse Compton process . . . 23
1.5 Spectral Energy Distribution (SED) . . . 23

2 Observing Activities and facilities **27**
2.1 The GASP-WEBT Collaboration . . . 27
2.1.1 Optical photometry . . . 28
Data reduction . . . 30
Photometric Calibration . . . 31
2.1.2 Near-Infrared photometry . . . 31

Data reduction . . . 32
Photometric Calibration . . . 37
2.2 The *Swift* Telescope . . . 41
2.2.1 Burst Alert Telescope (BAT) . . . 42
2.2.2 X-ray Telescope(XRT) . . . 43
Data reduction . . . 45
2.2.3 UV/Optical Telescope (UVOT) . . . 47
Data reduction . . . 48
2.3 The *Fermi* γ-ray Space Telescope . . . 48
2.3.1 Large Area Telescope (LAT) . . . 49
Data reduction . . . 50

3 Infrared properties of blazars. 51
3.1 The GASP sources into context . . . 54
3.2 Near-IR flux variability . . . 60
3.3 Near-IR colour variability . . . 63
3.4 Infrared-to-optical spectral energy distribution . . . 63
3.4.1 BL Lac objects . . . 71
3.4.2 Flat spectrum radio quasars . . . 73

4 Multiwavelength behaviour the FSRQ object OJ 248. 81
4.1 Optical and near-IR photometry . . . 83
4.2 Optical polarimetry . . . 85
4.3 Optical spectroscopy . . . 88
4.4 Observations at radio and millimetre wavelengths . . . 91
4.5 *Swift* observations . . . 95
4.5.1 UVOT observations . . . 95
4.5.2 XRT observations . . . 95
4.6 *Fermi* observations . . . 97
4.7 Correction for Galactic and DLA extinction . . . 101
4.8 Cross-correlation between variability at high and low energies . . . 102
4.9 Broad-band SED . . . 104

5 Multiwavelength behaviour of the BL Lac object Mrk 421. 107
5.1 Optical photometry . . . 108
5.2 Near-infrared photometry . . . 110
5.3 Removal of the host galaxy contribution . . . 111
5.4 Colour analysis . . . 113
5.5 Observations by *Swift* . . . 114
5.5.1 UVOT . . . 114
5.5.2 XRT . . . 115
5.6 Multiwavelength light curves of Mrk 421 . . . 119
5.7 Long term optical polarization variability . . . 121
5.8 Spectral variability of optical polarization . . . 126
5.9 Discrete Correlation Function (DCF) . . . 129

5.10 Broad-band spectral variability 132

6 Blazar polarimetry on a sample of blazars 135
6.1 A long-term analysis of the optical polarimetry in a sample of bright γ-ray blazars 136
6.1.1 Polarization behaviour in BL Lac type 137
6.1.2 Polarization behaviour observed in FSRQ types 141
6.2 Multi band polarimetry behaviour 144
6.2.1 Near-infrared polarimetry observations and data reduction 144
6.2.2 Results 145

7 Conclusions. 149

A Other multiwavelength studies. 153
A.1 Variability of the blazar 4C 38.41 (B3 1633+382) from GHz frequencies to GeV energies 153
A.2 The awakening of BL Lacertae: observations by Fermi, Swift and the GASP-WEBT 154
A.3 MAGIC gamma-ray and multi-frequency observations of flat spectrum radio quasar PKS 1510-089 in early 2012 155
A.4 The WEBT campaign on the BL Lac object PG 1553+113 in 2013. An analysis of the enigmatic synchrotron emission 155
A.5 Multiwavelength Study of Quiescent States of Mrk 421 with Unprecedented Hard X-ray Coverage Provided by NuSTAR in 2013 156
A.6 Exceptional outburst of the blazar CTA 102 in 2012: The GASP-WEBT campaign and its extension 157

Bibliography 159

Introduction

Among the huge number of galaxies visible in our Universe, each one of them composed by billions of stars, blazars are extremely fascinating objects to study. First of all they are quasars, incredibly bright active galactic nuclei (AGNs) hosting a supermassive black hole (SMBH) weighting 10^9 times the mass of our Sun: their jets, narrow streams propagating out of the SMBH and travelling almost at the speed of light, are pointed directly to the Earth. Blazars are powerful particle accelerators and studying the nature of their emission at all wavelengths, from radio to high energy γ-rays, is a very exciting work. The synergy created by the different instruments devoted to their observation, each of them with their specific waveband and characteristics, is a great tool to understand such exotic objects. Building a multiwavelength picture of a blazar is like putting together the pieces of a puzzle, and indeed many questions on blazars are still open. How jets are being accelerated? Where the high energy jet emission comes from? How accretion disk and jet are connected? The present work wants to add some pieces at the blazars puzzle, focusing in particular on two very interesting sources: the FSRQ OJ 248 and the BL Lac object Mrk 421, two blazars both studied in a wide multifrequency context.

The manuscript is organized as follows: the first chapter gives a general overview of AGNs and their classification, through the description of their properties and of their peculiar broad-band emission. The second one introduces the main data sources: the Whole Earth Blazar Telescope (WEBT) Collaboration along with its GLAST-AGILE Support Program (GASP), the IAC80, STELLA and TCS telescopes in the Teide Observatory, the *Swift* and *Fermi* satellites, and describes the data reduction processes. The third chapter deals with the infrared properties of blazars, carefully studied in the framework of the GASP-WEBT Collaboration. The fourth and fifth chapters are the core of this thesis, presenting the multifrequency study of the FSRQ object OJ 248 and the BL Lac object Mrk 421, respectively. The last chapter describes a comparison between the flux and polarization behaviour in a selected sample of blazars. A summary of the results from this work and of the possible future developments are presented in the Conclusions.

1

Active Galactic Nuclei: an overview

Active Galactic Nuclei show a strong energetic emission from their nuclear region that is not correlated to the host galaxy morphology and cannot be explained by using the well-known galactic (massive stars, HII regions,..) emission mechanisms.

In the most commonly accepted scenario, the AGNs emission is explained by assuming the existence of a supermassive black hole (SMBH) in the centre of the galaxy. The SMBH is responsible for the conversion of gravitational energy into electromagnetic one, where the fuel of the mechanism is the material close to the black hole (gas, dust, stars). The angular momentum of this material creates an accretion disk. The viscosity of the disk reduces progressively the angular momentum until the material collapses into the black hole.

The observed high luminosity suggests that the mass must be large enough for the balance between gravitation and the force due to the radiation pressure. The temporal variation of the AGNs emitted radiation is in the scale of years, but this can be drastically reduced to the order of days, hours or minutes. This variability in very compact regions also suggests the presence of highly energetic processes, more efficient than the nuclear fusion. AGNs are actually considered as the most powerful stable sources in the Universe. The emission crosses the whole electromagnetic spectrum, with the maximum usually in the UV. The nuclear emission is not spatially resolved, but in the radio band interferometric techniques leading to a spatial resolution of the order of 1/1000 arc seconds are able to show collimated fluxes of materials at relativistic velocities (jets).

The AGN spectra in the rest frame optical range are the result of the superimposition of multiple components: nuclear, stars, gas, dust. In other words, they in general show emission from the star population affected by the AGN, from the gas and dust around the AGN, and from particles accelerated by the AGN. It is possible to separate the AGN emission spectra in different components usually temporally variable:

- Emission from the accretion disc.

- Emission from the jet.
- A component of relatively narrow lines (coming from the narrow line region, NLR), but still larger than the ones of normal galaxies, corresponding to forbidden lines (i.e., NII, OIII, OII). The forbidden lines are generated by transitions from a very stable excited status. Such transitions are admitted only in very low atomic density regions, that at the usual Earth densities would be depopulated by electronic collisions.
- A set of broad lines (coming from the broad line region, BLR) composed by permitted lines, like the H Balmer series, HeI and HeII.
- Some typical lines of star formation process. Usually AGN and star formation coexists in the majority of galaxies so that the identification and the separation of the two processes is not easy.

1.1 Classification of AGNs

The origin of the different type of AGNs seems to be the same and the current approach is to find a unified theory or model explaining the different observational properties.

The classification can help us in the understanding of the AGN phenomenology and nature. The term AGN includes a large variety of astronomical objects, like the Seyfert galaxies, the quasars (both radio-quiet, QSO, and radio-loud, QSR), the radio-galaxies, the blazars and also the so-called low-luminosity AGNs that include the LINERs. Most of these labels are coming from the analysis of the spectra at visible wavelengths.

The development of the radio classification schemes (for the strong radio emitting objects) is parallel to the optical discovery of the AGNs. From the first optical identification of the extragalactic radio sources (Bolton et al., 1949; Baade & Minkowski, 1954) was clear that the emission spectra of these radio galaxies are similar to the one of the Seyfert galaxies (Schmidt, 1963). In the case of the BLRG (Broad line radio galaxies), they are equivalent to the Seyfert 1 while the NLRG (Narrow line radio galaxies) to the Seyfert 2. There are also radio-galaxies with strong radio activity (WLRG) but weak optical emission lines and low ionization (Hine et al., 1979; Laing et al., 1994; Tadhunter et al., 1998) sometimes similar to the LINERs. Very interesting is the case of some AGNs with strong radio emission, classified for the fast optical variability. These objects known as Blazars include the BL Lac objects (with a few emission lines) and the flat-spectrum radio quasars.

Another classification scheme for the strongly radio emitting AGNs is based on their radio structure. In 1974 Fanaroff & Riley start to distinguish between galaxies brightest at the edge (FRII) and galaxies brightest at center (FRI). Usually FRII are stronger radio sources than FRI. Among quasars we separate the SSRLQ (steep spectrum radio loud quasars) from the FSRLQ (flat spectrum radio loud quasars).

The AGNs classification is not easy and is complicated by the use of several classification methods, but, as already said, the objective of the classification is not limited to find the labeling rules, but to find the rules and the laws that can lead to the understanding of the phenomena. For this reason, we introduce an AGNs classification based on their properties: the presence (or not) of forbidden lines in the optical spectrum, the radio intensity and the luminosity. By using this classification it is possible to place the AGNs in a 3-D diagram, as in (Tadhunter, 2008).

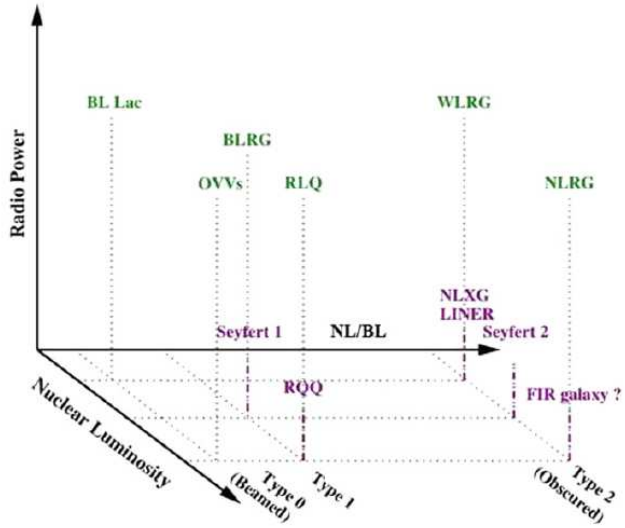

FIGURE 1.1— Tridimensional classification of AGNs (Tadhunter, 2008).

Viceversa, one can make important considerations on AGNs by studying the common properties, instead of the differences, among the different classes. In fact, most AGNs are compact, extremely powerful, characterized by the capability of creating strongly collimated jets. It is not easy to find a mechanism able to explain all these properties that is not the gas accretion around a supermassive black hole (Rees, 1977).

The relevant characteristics of the different AGNs types are summarized here below, starting from the AGNs with low radio emission (Seyfert galaxies and LINERs) and following with strong radio emitting AGNs (quasars, blazars,...).

1.1.1 Seyfert galaxies

The most commonly used classification is the one originally proposed in 1943 by Seyfert. Only two types of Seyfert galaxies are established but is possible to find some intermediate objects (Osterbrock, 1998). These two types are (Khachikian & Weedman, 1974):

- **Seyfert 1:** Characterized by the presence of very bright NLs and BLs, with a continuum with few absorption lines, dominated by a central object. They have a strong emission in

X-rays and a variability in the scale of hours (or days).

- **Seyfert 2:** Characterized by the absence of broad lines (or weak), with the spectrum dominated by narrow lines, a weakest continuum and contribution of stellar emission. The X-ray emission is weaker than in Seyfert 1, because, as revealed by the spectral analysis, some absorption occurs.

These galaxies are not commons (10-20% of the total of galaxies) and usually are located in spiral galaxies. Several of them interact with others (companion).

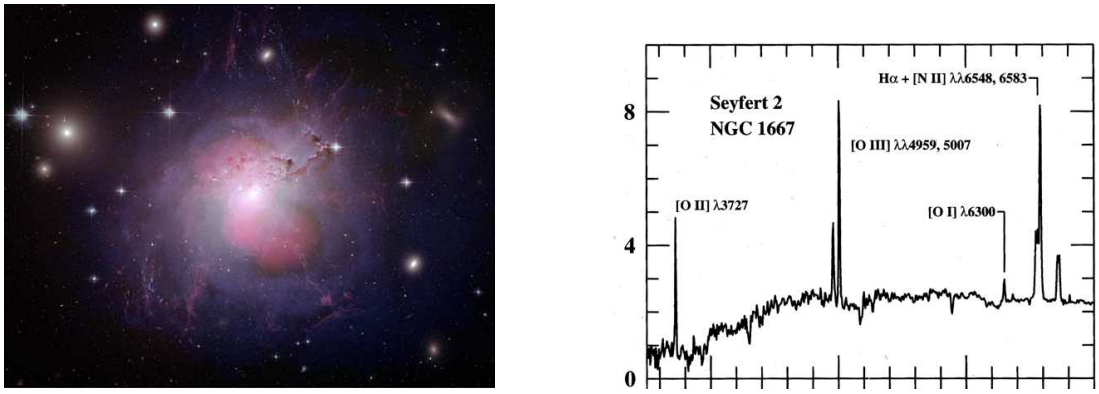

FIGURE 1.2— In panel (a) the image of the Seyfert galaxy NGC 1275 (multi-wavelength composite) and in Panel (b) the spectrum of NGC 1667 (Seyfert 2). (Ho et al., 1993)

1.1.2 Liners

The LINERs (Low Ionization Nuclear Emission-line Regions) present very bright low ionization lines ([OI], [OII], [NII]), which are associated to the presence of excited (or ionized by collision) material. The LINERs seem to be related to AGNs and star formation processes. Almost all the spiral galaxies have nuclear LINER spectra. This spectrum is visible also in some HIII regions (Heckman, 1980).

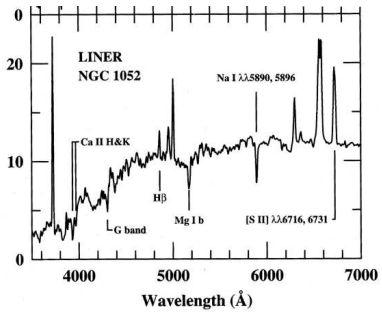

(a) (b)

FIGURE 1.3— In panel (a) an image of NGC 1052 galaxy taken by Sloan Digital Sky Survey (SDSS) and in panel (b) its spectrum (Ho et al., 1993)

Objects with strong emission in Radio.

1.1.3 Quasars

Quasars have been discovered in 1963 and they have a quasi-stellar aspect. Their spectra show a power law continuum and broad emission lines. The spectral lines are similar to the Seyfert 1, with a not so important narrow component and more emission from highly ionized atoms. With respect to the normal galaxies, they emit strongly in the IR and at other wavelengths. About the 10% of the quasars are radio loud and the radio emission is very bright especially in the jets visible sometimes in the optical.

Quasars are visible also at very high redshifts due to their intrinsic brightness.

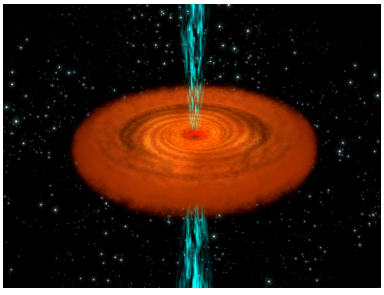

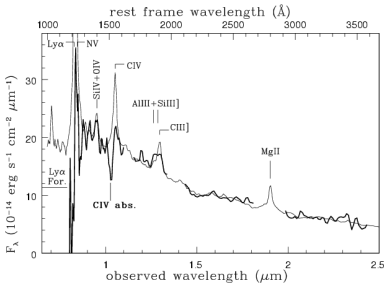

(a) (b)

FIGURE 1.4— Artistic view of a quasar (a) and its spectrum (b) (Francis et al., 1991).

1.1.4 Radio Galaxies

This kind of AGNs were discovered with radio observations. The radio emission is usually focalized in the nucleus, lobe and jets far away from the central core. Sometimes it is possible to observe two jets, and sometimes only one. The jets are composed by material ejected by the central object that penetrates up to 100 kpc into the inter-galactic-medium (IGM) and produce synchrotron radiation stopping. These galaxies also show an important X-ray emission. They usually have an elliptical shape. They are estimated to be 100 times less numerous than the Seyfert galaxies. A common classification of the radio galaxies is the following (Fanaroff & Riley, 1974):

- **FRI:** with a radio brightness decreasing with the distance from the center of the galaxy. Usually they present two curved jets.
- **FRII:** with the peak of the emission at the end of the lobes. Usually they have only one straight jet but sometimes it is possible to see a second, weak, jet.

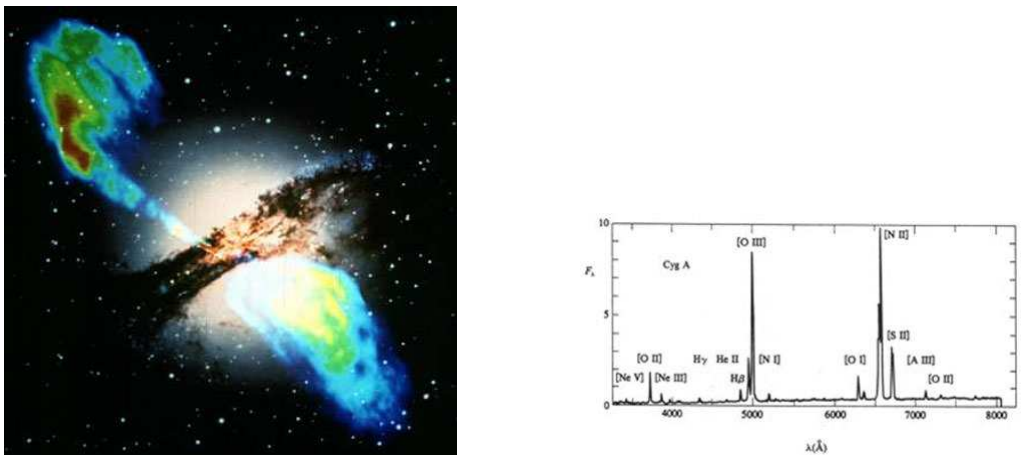

(a) (b)

FIGURE 1.5— Image (a) and spectrum (b) of the radio galaxy Cygnus A.(Osterbrock, 1998)

BLAZARS

Blazars are the most violently variable objects among the AGNs. Their central engine is likely a supermassive black hole of $10^8 - 10^9$ solar masses, fed by infall of matter from a surrounding accretion disc. Two giant plasma jets where matter flows at relativistic speed are escaping perpendicularly to the disc.

The peculiarity of blazars is that one of the two jets is pointing toward us, so that relativistic effects cause amplification of the jet emission and contraction of the variability time scales.

Hence, because of the special geometry, the blazar radiation we observe is mostly produced in the jet, and this makes blazars the best candidates to study the physics and structure of AGN jets and ultimately their relationship with the central engine. The blazar emission extends from the radio to the γ-ray frequencies of the electromagnetic spectrum and shows variability at all wavelength. The observed radio, near-infrared, and optical emissions are also highly polarized and both polarization degree and angle are variable (Miller et al., 1989; Bregman et al., 1990). The origin of the low-energy emission is due to a synchrotron process, while high energies are likely produced by inverse Compton scattering.

After the launch of the high-energy space observatory satellite Compton Gamma Ray Observatory (CGRO) in the 1990s, blazars were discovered to be the protagonists of the extragalactic gamma-ray sky. More recently, with the launch of the AGILE (2007) and the *Fermi* (2008) satellites, the number of detected gamma sources has dramatically increased. Moreover, the daily all-sky monitoring by *Fermi* allows us to approach the high energy processes occurring in blazars from a more detailed perspective.

Blazars include two kinds of objects:

- **BL Lac Objects (BL Lacs):** According to the original classification, they show only very weak lines, if any, in their optical spectrum. As a consequence, many of them have unknown redshift, since this is mostly measured through the analysis of the lines associated to the host galaxy.
- **Flat-spectrum radio quasars (FSRQs):** They are similar to the BL Lac objects with brighter lines, so their redshift can be measured even at high distances. (Peterson et al., 1998).

Both BL Lacs and FSRQs are violently variable objects in many frequency bands, with huge flux variations in short times. Sometimes it is possible to measure an hourly variability or micro-variability, not detected in quasars. Being the subject of our work, blazars will be treated in a more detailed way in a specific section.

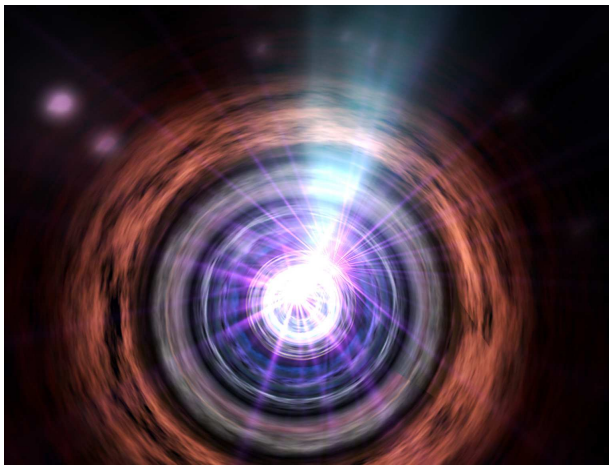

FIGURE 1.6— Artistic view of a blazar. Image courtesy of NASA/Goddard Space Flight Center Conceptual Image Lab.

1.2 The Unified Model and structure of an AGN

The unified model establishes the difference between different types of AGNs as a function of the SMBHs mass, the accretion rate and the orientation of the accretion disk and of the dust torus as seen by the observer perspective (Antonucci, 1993; Urry & Padovani (1995)). For example, a blazar is an AGN observed through the jet with the high variability due to relativistic effects. This model is actually accepted by the most part of community, but still has some problems and probably it is not possible to explain all the different AGNs types with a simple model.

In the following, each of the components of the Unified model are explained in more detail:

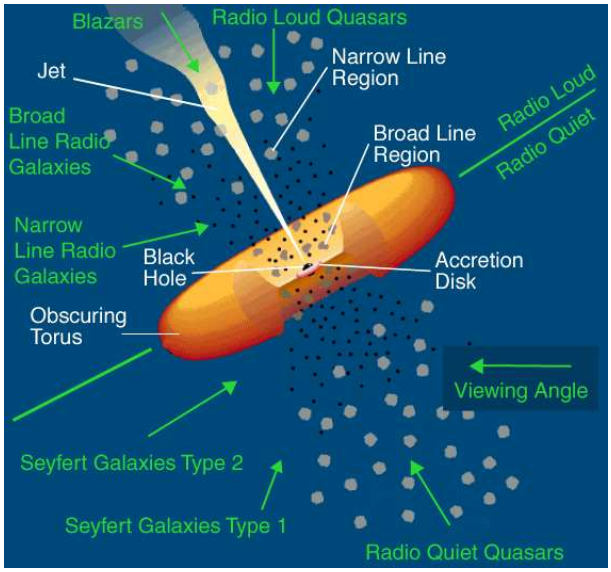

FIGURE 1.7— Unified Model of AGNs (Urry & Padovani, 1995).

Jets: In the radio-loud objects, a pair of twin jets, pointing in opposite directions and perpendicular to the disk plane, appear. These extend from the vicinity of the central SMBH up to large distances from the nucleus (>100 kpc). This component presents relativistic behavior, especially close to the SMBH.

Narrow Line Region (NLR): In this part, ionized matter moving slowly emits narrow lines in the optical spectrum. It is located at $\sim$ 100 pc from the center.

Torus: A dusty region with toroidal shape located at $\sim 1-10$ pc from the center. The presence of the torus is necessary to explain why some types of AGN are obscured, but its structure is still not well known: several models were developed proposing a homogeneous or clumpy distribution with different density and temperature profiles, or even an outflowing wind driven by a magnetic field. The torus emits thermally in IR.

Broad Line Region (BLR): probably made by gaseous clouds, located at $\sim 0.1-1$ pc from the center where the primary continuum emission from the disk is reprocessed photoionizing the gas clouds. The emission lines have a large width, typically a few 10^3 km/s. The principal broadening mechanism is Doppler motion of individual clouds, being the thermal broadening Δv $\sim$10 km/s for a T$\sim 10^4$K gas.

Corona: Located above the disk having a diffuse or clumpy structure depending on the models and a temperature T$\sim 10^9$ K. It is necessary to explain the high energy X$-$ray emission through inverse Compton interaction with the low energy thermal photons emitted by the disk, but the heating mechanism is not known yet.

Accretion disk: The central SMBH accretes matter, distributed into a rotating disk around the SMBH. The temperature of the disk depends on the distance from the SMBH and on the SMBH mass. This could explain the emission in optical/UV (blue bump) as a multicolor blackbody. During the accreting process, a loss of angular momentum, due to viscosity and turbulence, will take place as well. The process depends strongly on the SMBH mas and the accretion rate. The disk emission is limited by the Eddington limit.

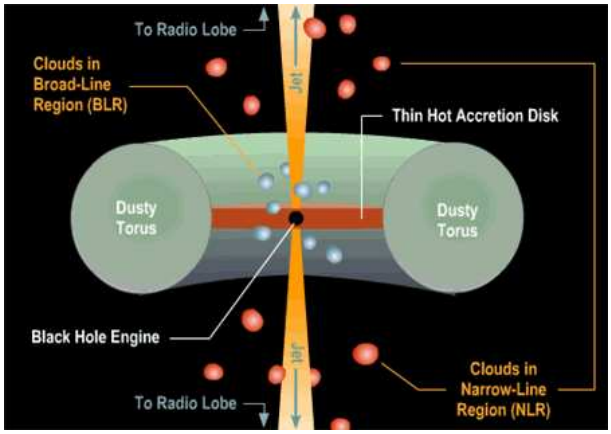

FIGURE 1.8— AGN model. Image credit: Brooks/Cole Thomson Learning.

1.2.1 The accretion disk

As already reported before, the most commonly accepted model explaining the AGNs properties predicts the presence of a super massive black hole (of millions of solar masses) in the centre of the galaxy, surrounded by an accretion disk and a torus of gas and dust. The physical properties of the SMBH, of the disk, together with the disk orientation with respect to the observer, explain the properties of the different AGNs types (Frank et al., 2002).

The formation of the accretion disk would occur when the dust clouds orbiting around the black hole end up reaching a closely circular orbit loosing energy for clouds collisions (viscosity). The rotation direction will be the same for most of the clouds at the starting time of the disk formation. If the disk formation is a merger, the rotation direction should be the one coming from the cannibalized galaxy.

The collisions will also produce a thermal effect, so that the gas of the disk will be very hot, as hot as close to the SMBHs. In addition, the viscosity can be so strong that part of the material can fall into the black hole. Much of the energy radiated by an AGN comes from the accretion disk that can reach temperatures of hundreds of thousands of K.

The material can survive up to a distance of a few Schwarzschild's radii. This radius is twice the one where the gravitational force equals the centrifugal force of a particle traveling at the speed of light in a gravitational field.

The Schwarzschild's radius corresponds to the event horizon, beyond which it is not possible for the electromagnetic radiation to escape. So it is not possible to have information about what happens inside such an unreachable region.

Another important parameter is the Eddington's luminosity, corresponding to the maximum luminosity a body can achieve when there is balance between the force of radiation acting outward and the gravitational force acting inward. The luminosity of the stars are lower than the Eddington limit, but in the case of SMBHs the observed values should be close. The accretion disks are controlled by this parameter, so as the luminosity of the AGN grows, the mass of SMBH should grow up too.

The accretion disk itself may have an internal structure. The models predict roughly this structure:

- an innermost part, which can reach 1000 rs, with very high temperatures and the radiation exceeding the gas pressure (a thick and hot disk). This part is probably responsible for the UV emission of the AGN.
- an outermost region, up to 100000 rs, with a thin disk balanced by the gas pressure. This part of the disk is wider when furthest from the SMBHs. Due to the wide inner part, the hot disk can irradiate the more external disk. The outermost region would break in clouds of individual gases (that can fall to the internal region due to the collisions).

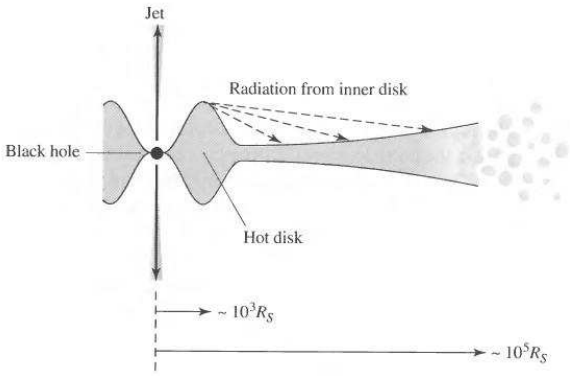

FIGURE 1.9— Structure of an accretion disk (Carroll & Ostlie, 1996).

The hot material of the disk can produce huge magnetic fields. The strong magnetic field, which should be powered also by the SMBHs rotation, can explain the expulsion of charged particles at relativistic speeds. The energy could be enough to accelerate particles that, moving

in a spiral trajectory around the magnetic field lines, will emit synchrotron radiation. This kind of observation is common in AGN.

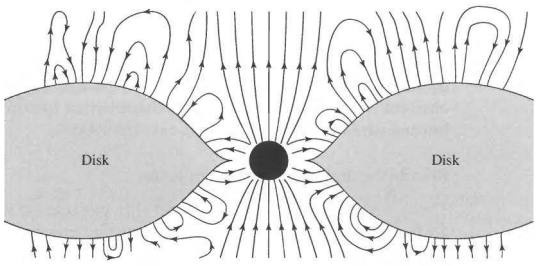

FIGURE 1.10— Relationship between the magnetic field and the accretion disk (Carroll & Ostlie, 1996).

1.2.2 The torus

A high-density torus of gas and dust is expected to produce a relevant extinction of the radiation from the inside. The presence of a torus is required for explaining the observation in the MIR and FIR of the emission of several AGN. The torus dust must be at a temperature of less than about 2000 K (the sublimation temperature of the most resistant grains), it absorbs X and UV radiation and re-emits radiation in the MIR and FIR. If the torus is very large and dense, it can absorb all the radiation and hide the active nucleus. The inner radius of the torus is given by the sublimation radius, the one in which the dust is able to absorb the radiation and to re-emit it without sublimate. The best models of torus seem to be the ones predicting a clumpy torus (Nenkova et al., 2008).

1.2.3 The jets

The presence of a thick disc nearby the SMBH as well as the presence of magnetic fields are studied as possible causes for the existence of jets in the AGNs. These studies suggest that the jets are aligned with the rotation axis of the disc. The thick disk acts as a bottleneck for the material that is ejected at relativistic velocities. The mechanism which produces the jets is still not well defined. The current opinion (Blandford & Payne, 1982) is that the lines of the magnetic field twist around the surrounding inside the inner accretion disk. Then they are blocked in a double helix configuration, which increases the velocity of the particles to values close to the speed of light.

The jet emission is synchrotron radiation, which has a characteristic power-law spectrum. The particles emit synchrotron radiation "loosing" their energy, which means that the jet suffers a deceleration. Typically, these particles should stop completely before 10000 yr, so the existence of very large jets is not possible. However, these "jets" are observed, so a mechanism of acceleration in the "jet" itself might exist. In many AGNs only one jet is observed. This

is normally explained by orientation effects. If the jet is slightly aligned with the line of sight, relativistic effects appear. Because of this, the "jet" which is pointing towards the observer looks brighter than the jet which is pointing opposite to the observer.

In general, the emission of the jet is highly collimated, so it might appear very well defined.

1.3 Relativistic effects

1.3.1 Relativistic beaming

The Doppler factor δ relates intrinsic and observed properties of a source moving at relativistic speed $v = \beta\, c$. It is defined as:

$$\delta = \frac{1}{\Gamma(1 - \beta \cos\theta)} \tag{1.1}$$

where Γ is the bulk Lorentz factor of the jet plasma:

$$\Gamma = (1 - \beta^2)^{-1/2} \tag{1.2}$$

If the source is approaching, time intervals measured from the observer are shorter than in the rest frame:

$$t = \delta^{-1}\, t' \tag{1.3}$$

This implies that the emission is blue-shifted:

$$\nu = \delta\, \nu' \tag{1.4}$$

If the emission is isotropic in the rest frame and if the intrinsic flux density follows a power-law $F'_{\nu'} \propto (\nu')^{-\alpha}$, then:

$$F_\nu(\nu) = \delta^{n+\alpha}\, F'_{\nu'}(\nu) \tag{1.5}$$

where $n = 2$ for a smooth, continuos jet, while $n = 3$ for a discrete source. Broad-band fluxes transform as

$$F = \delta^{n+1}\, F' \tag{1.6}$$

.

An external observer sees the emission highly beamed in the direction of motion in a cone of semi-aperture $1/\Gamma$. If the observer happens to be in this precise direction (for blazars, the jet is pointing toward the observer), the luminosity can reach tremendous values. On the contrary if the source is moving away from the observer, its emission is deboosted. This contrast leads to the observed disparity between the jet and the counter jet of radio-galaxies.

1.3.2 Superluminal motions

Superluminal motion of knots is generally derived from radio images of compact sources with very bright central cores. The projected source separation is typically tens of parsecs, and the proper motions observed over a number of years imply transverse velocities as large as $v_T \approx 10$ c.

When we have a lot of observations of the sources, we can extrapolate the proper motion backward in time, and at the time of zero separation between the components an outburst of the continuum is often found, which is detected over a broad frequency range.

The explanation for these apparent superluminal velocities is ascribable to bulk relativistic motion close to the line of sight (Blandford & McKee, 1977) .

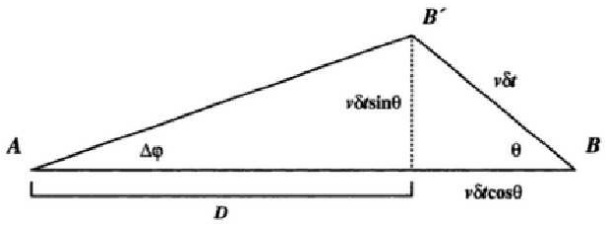

FIGURE 1.11— Geometry assumed to explain apparent superluminal expansion of radio sources.

Let us consider a source travelling from B to B'. A photon emitted at point B at time t_1 is detected by the observer at point A at time t'_1 after the light has crossed the distance AB. At $t_2 = t_1 + v\delta t$ the source has moved from B to B' and a second photon emitted in B' will be observed at t'_2. The distance between A and B is $D + v\delta t \cos\theta$.

The angular separation for the second observations for the two sources is:

$$\Delta\phi = \frac{v\delta t \sin\theta}{D} \tag{1.7}$$

The observer can measures the time between the two observations:

$$t'_1 = t_1 + \frac{D + v\delta t \cos\theta}{c} \tag{1.8}$$

$$t'_2 = t_2 + \frac{D}{c} \tag{1.9}$$

The measured interval between the observations:

$$\Delta t = t'_2 - t'_1 = t_2 - t_1 - \frac{v\delta t \cos\theta}{c} = \delta t(1 - \beta\cos\theta) \tag{1.10}$$

The apparent transverse velocity inferred by the observer is:

$$\beta_T = \frac{v_T}{c} = \frac{v \sin\theta}{c(1 - \beta\cos\theta)} = \frac{\beta \sin\theta}{1 - \beta\cos\theta} \tag{1.11}$$

The transverse velocity β_T is mesured as a function of the angle to the line of sight θ and is maximized when:

$$\frac{\delta\beta_T}{\delta\theta} = \frac{\beta\cos\theta}{1 - \beta\cos\theta} - \frac{(\beta\sin\theta)(\beta\sin\theta)}{(1 - \beta\cos\theta)^2} = 0 \tag{1.12}$$

which yields θ_{max}=$\cos^{-1}\beta$. From this we can write:

$$\beta_T^{max} = \frac{\beta(1 - \beta^2)^{1/2}}{(1 - \beta^2)} = \beta\Gamma \tag{1.13}$$

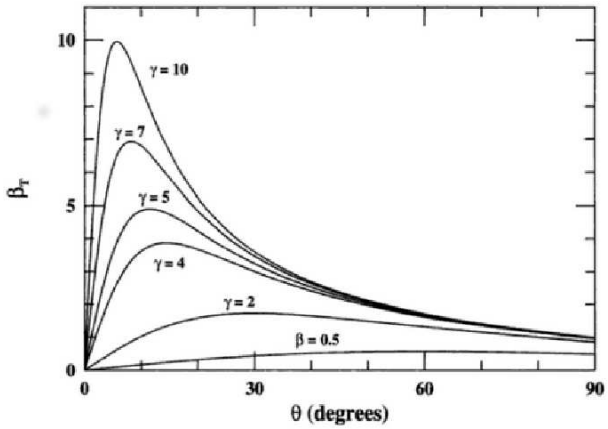

FIGURE 1.12— The apparent transverse velocity of a source moving at an angle θ to the observer's line of sight.

So if $\beta \approx 1 \Rightarrow \beta_T^{max} \approx \Gamma$. For relativistic bulk motions close to the line sight the observer may detected projected transverse velocities apparently in excess of the speed of light.

1.4 Emission processes

In the relativistic AGN jets we observe non-thermal continuum emission produced by synchrotron and inverse Compton processes.

1.4.1 Synchrotron emission

Synchrotron radiation is produced when charged particles are accelerated by a magnetic field in the jets, where the relativistic electrons are accelerated by the Lorentz force:

$$\frac{d}{dt}(\gamma \mathrm{m}\vec{v}) = \frac{q}{c}(\vec{E} + \vec{v}x\vec{B}) = \vec{F} \tag{1.14}$$

where: $\vec{F}$ is the Lorentz force, $\vec{E}$ is the electic field, $\vec{v}$ is the particle velocity and $\vec{B}$ is the magnetic field.

$$\frac{1}{\sqrt{1-(v/c)^2}} \text{ is the Lorentz factor} \tag{1.15}$$

The velocity of the particle is given by its parallel and perpendicular components relative to the magnetic field.

In the parallel case the angle between $\vec{v}\mathrm{x}\vec{B}$ is 0°

$$F_{||} = \gamma \mathrm{m} a_{||} = \frac{q}{c}(E_{||} + v_{||}Bsin(0)) \tag{1.16}$$

In the perpendicular case the angle between $\vec{v}\mathrm{x}\vec{B}$ is 90°, for this the force has the maximum contributions.

$$F_{\perp} = \gamma \mathrm{m} a_{\perp} = \frac{q}{c}(E_{\perp} + v_{\perp}Bsin(90^\circ)) \tag{1.17}$$

Then the aceleration components related to this force are:

$$a_{||} = \frac{q}{\gamma mc}E_{||} \tag{1.18}$$

$$a_{\perp} = \frac{q}{\gamma mc}(E_{\perp} + v_{\perp}B) \tag{1.19}$$

Typically the high conductivity of the fully ionized plasma ensures that there are no large-scale electric fields present in the jet, only local electric fields from charged particles which can produce Bremsstrahlung. For this reason we do not use the electric field in the future calculations.

The resulting motion is helical with a pitch angle θ, combination of a circular motion around the field lines and a uniform motion along the field lines. The particle is under a perpendicular acceleration and therefore it must radiate. In the relativistic case, it is called synchrotron emission. As we are interested in relativistic sources, we will consider only synchrotron emission here.

The radiative power by a single electron is given by the Larmor equation:

$$P(t) = -\frac{dE}{dt} = \frac{2}{3}\frac{e^2}{c^3}a^2(t) \tag{1.20}$$

We know, however, that the emitted power is Lorentz invariant, hence we can simply write:

$$P = \frac{2}{3}\frac{e^2}{c^3}a^2 = \frac{2}{3}\frac{e^2}{c^3}(a_{||}^2 + a\ \perp^2) \tag{1.21}$$

Substituting $a_\perp$ in the Larmor formula:

$$P(\theta) = \frac{2}{3}\frac{e^4}{m^2c^3}\gamma^2\beta^2B^2sen^2(\theta) \tag{1.22}$$

We can see that the power is larger when the magnetic field is larger. Another important aspect is that the power is $\propto m^{-4}$. For this reason it is assumed that the synchrotron radiation observed in the jets is generated primarily by electrons and positrons, because the power that protons can generate is negligible due to their own high mass.

We can write the equation 1.22 introducing the Thomson scattering cross-section, which is given by:

$$\sigma_T = \frac{8\pi}{3}r_0^2 = \frac{8\pi}{3}(\frac{e^2}{m_e^2c^2})^2 = 6.65 \times 10^{-25}cm^2 \tag{1.23}$$

and the magnetic energy density:

$$U_B = \frac{B^2}{8\pi} \tag{1.24}$$

The resulting for power emitted by an ensemble of electrons:

$$P = \frac{4}{3}c\sigma_T\gamma^2\beta^2U_B \tag{1.25}$$

In the synchrotron case, the spectral distribution of the radiation is mainly concentrated around a critical frequency (ν_c), as plotted in Fig. 1.13. The critical frequency is the frequency where $\nu = 0.29\nu_c$. The equation of critical frequency is:

$$\nu_c = \frac{3}{4\pi}\frac{\gamma^2e}{m_ec}Bsin(\theta) \tag{1.26}$$

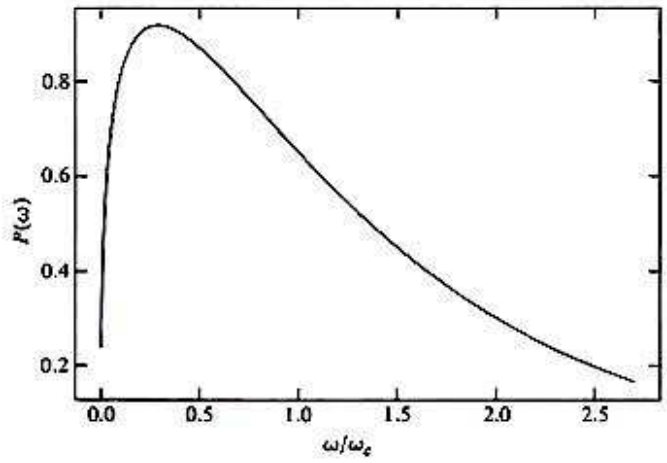

FIGURE 1.13— Single electron spectrum due to synchrotron radiation. Hughes(1991).

For frequencies lower than ν_c the power increases according to a power law with exponent 1/3 and the maximum emission is close to ν_c.

However, we will not observe the spectrum from a single electron, but that due to the superposition of the emission of all implicated electrons. Typically in high energy astrophysics, the particle energy distribution is assumed to be a power law (Rybicki & Lightman, 1979):

$$N(E)dE = KE^{-p}dE, \qquad E_{min} \leq E \leq E_{max} \tag{1.27}$$

where: N(E) is the density of electrons with energies between E and E+dE and p is the exponent which defines the slope of the distribution.

Assuming an isotropic emission, that the distribution of pitch angles is isotropic and that these assumptions hold for low and high values of E, then:

$$\epsilon(\nu, \theta) \propto KB^{(\alpha+1)}\nu^{-\alpha} \tag{1.28}$$

The power-law electron distribution produces a power-law spectrum with a spectral index of radiation α which is related to the slope of the distribution of electrons as α=(p−1)/2.

The counterpart of this process is called synchrotron absorption and the cross section of the process can be mathematically described as:

$$\sigma(\nu, \gamma, \theta) = \frac{16\pi^2 e}{3\sqrt{3}B} \frac{1}{\gamma^5 \sin(\theta)} K_{5/3}\left(\frac{\nu}{\nu_c \sin(\theta)}\right) \tag{1.29}$$

The synchrotron emission from an AGN is typically emitted from radio to X-rays and presents a high degree of polarization.

Polarization

The synchrotron emission is characterized by being highly polarized, depending on the properties of the magnetic field. To characterize the polarized emission one has to analyze the vibration of the electric field emission, that for a monochromatic wave has the form:

$$E_x(t) = E_x(0)\cos(\omega t - \phi_1) \tag{1.30}$$

$$E_y(t) = E_y(0)\cos(\omega t - \phi_2) \tag{1.31}$$

where: $E_x(0)$ and $E_y(0)$ are the magnitudes of the vibration, ϕ_1 and ϕ_2 are their corresponding phases, X and y directions are located in a plane perpendicular to the observer line of sight.

George Stokes in 1852 introduced four parameters for defining the properties of polarized emission. These Stokes parameters are defined as follows:

$$I = \langle E_x^2(0)\rangle + \langle E_y^2(0)\rangle \tag{1.32}$$

$$Q = \langle E_x^2(0)\rangle - \langle E_y^2(0)\rangle \tag{1.33}$$

$$U = 2\langle E_x(0)E_y(0)\cos(\phi_2 - \phi_1)\rangle \tag{1.34}$$

$$V = 2\langle E_x(0)E_y(0)\sin(\phi_2 - \phi_1)\rangle \tag{1.35}$$

where:

I is the total intensity.
Q quantifies a difference in the intensities in x and y, thus providing information on linear polarization.
U quantifies a difference between the two field components diagonal to the x and y coordinates, thus likewise probing linear polarization.
V corresponds to the circularly polarized intensity.

With the Stokes parameters we can define the degrees of linear polarization:

$$\prod = \frac{I_{lpol}}{I} = \frac{\sqrt{Q^2 + U^2}}{I} \tag{1.36}$$

The polarization angle actually is the electric vector position angle (EVPA), since it indicates the direction of the oscillation plane of the electric field. This is always perpendicular to the magnetic field and to the direction of propagation of the electromagnetic wave. However, when we try to infer the direction of the magnetic field in the emitting source from the observed direction of the EVPA we have to consider that we are dealing with different reference frames (the observer and the source frames). We need to consider the relativistic Lorentz transformations, i.e. that the components of the magnetic field perpendicular and parallel to the velocity vector of the plasma transform in different ways (e.g. $\sim$ Blandford Koumlnigl, 1979). This means that the orientation of the magnetic field in the emitting source could be different from the one we measure in our reference frame. Although there is an additional effect that distorts our view of the linear polarization angle, that can be rotated by the Faraday effect, this occurs when the electromagnetic wave propagates through a magnetized and non-relativistic plasma containing a considerable population of free electrons.

The EVPA is defined as:

$$\chi = \frac{1}{2} \arctan(\frac{U}{Q}) \tag{1.37}$$

For a homogenous source without Faraday rotation and considering a power law energy distribution of electrons, the degree of linear polarization for an optically thin region with uniform magnetic field is:

$$\prod = \frac{p+1}{p+\frac{7}{3}} \tag{1.38}$$

For an optically thick source:

$$\prod = \frac{3}{6p+13} \tag{1.39}$$

The degree of polarization is independent of the frequency, but depends on the energy distribution of electrons (characterized by p). For example if we consider p=2, in the case of optically

thin region the maximum theoretical polarizacion degree is 69% and in the case optically thick region is 12%, while for p=3 in the optically thin region we have 75% and in the optically thick region 10% (Pacholczyk, 1970).

It is important to notice that the polarization is strongly correlated to the magnetic field order, so that the variations in the magnetic field orientation in the jet reduce the degree of polarization with respect to the maximum values mentioned above.

1.4.2 Inverse Compton process

The Compton effect is the scattering of a photon by a charged paricle. With a particle initially at rest, it results in a decrease of the photon energy: there is a transfer of energy from the photon to the particle.

This process has been originally described by Compton (1923) who studied the elastic collision of X-ray photons with electrons. He showed that X-rys were scattered through an angle θ and were subject to a change in wavelength called Compton shift given by the relation:

$$\Delta\lambda = \frac{h}{m_e c}(1 - \cos\theta) \tag{1.40}$$

In the inverse Compton process the photon acquires energy at the expenses of the particle. This process occurs when the relativistic electrons of the jet interact with the radiation field. The origin of this radiation field is very debated. One possibility is that the seed photons for the inverse Compton process are the same synchrotron photons emitted from the jet itself, and in this case the mechanism is called Synchrotron Self-Compton (SSC).

Alternatively, the radiation can come from a region external to the jet, for example the accretion disk, the BLR, the torus. In this case the name is External Compton (EC).

In general, both the SSC and EC process can be at work in the jet.

1.5 Spectral Energy Distribution (SED)

The radiation emitted by an AGN is attributed to two physical processes (Abdo et al., 2009).

The first process is responsible for thermal radiation originating from in-falling matter strongly heated in the inner parts of an accretion disk close to the black hole. This radiation is often assumed to be Comptonized by a hot corona yielding power law X-ray emission. This process produces radiation in the optical, UV and X-ray bands. When in the AGN this

process dominates, it can be classified as thermal dominated or disk dominated. QSOs and Seyfert galaxies belong to this class. They do not show significant nuclear radio emission compared to the observed emission in the optical or X-ray band.

The second process is the non-thermal emission from highly energetic particles that have been accelerated in a jet of material ejected from the nucleus at relativistic speed. This mechanism emcompasses the entire electromagnetic spectrum from radio waves to the most energetic γ-rays. Objects where this process is dominant are classified as non-thermal radiation dominated or jet dominated sources and are known as radio loud AGN. Depending on the orientation of their jets with respect to the line of sight, these can be classified into radio galaxies, steep spectrum radio quasars, and blazars (see previous sections).

Since we are interested in blazars, in the following we will present the spectral energy distribution (SED) of this kind of objects, which is usually plotted as $\log \nu f_\nu$ versus $\log \nu$. As previously stated, they show a flat radio spectrum, radio core dominance, as well as strong and rapid variability. These are observational indicators that these objects point their radio jet in a direction that is closely aligned to our line of sight. Their light is strongly amplified by relativistic effects and the time-scales of observed variations are significantly shortened. Depending on their spectral properties, we distinguish between strong-lined FSRQs and (almost) featureless BL Lac objects. While the SEDs of FSRQs show synchrotron peaks in the infrared, the peaks of BL Lacs can spread over a wide range of frequencies, so these sources are further divided into:

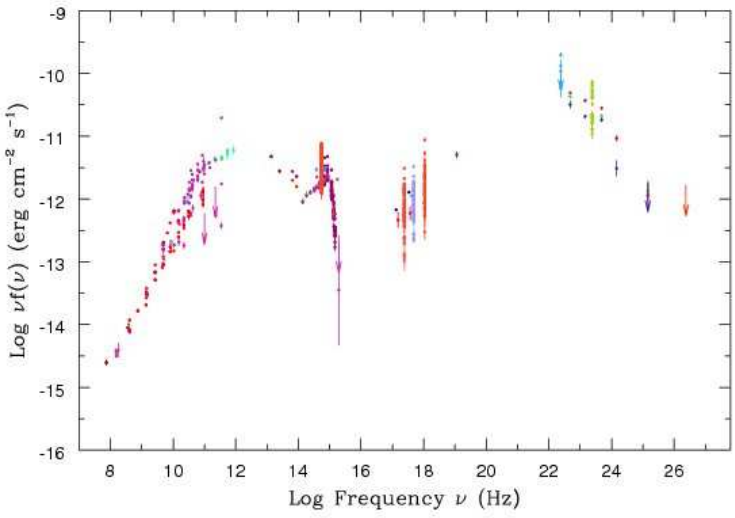

FIGURE 1.14— FSRQ SED of 1633+382.

- **LBL**: They have synchrotron peaks at low energy, in the far IR or IR band with $\nu \lesssim 10^{14} Hz$ and their X-ray emission is flat ($\alpha \approx$ 0.4-0.7) and due to the rising part of the inverse Compton component. The inverse Compton scattering occurs in the Thomson regime.

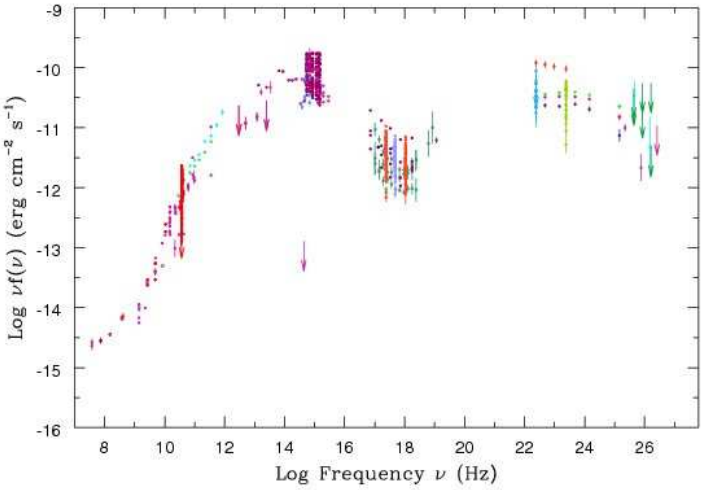

FIGURE 1.15— LBL SED of 0716+71.

- **IBL**: The synchrotron emission peaks at intermediate energies ($10^{14} \lesssim \nu_{peak} \lesssim 10^{15} Hz$). The X-ray band includes the tail of the synchrotron emission and the rise of the inverse Compton component.

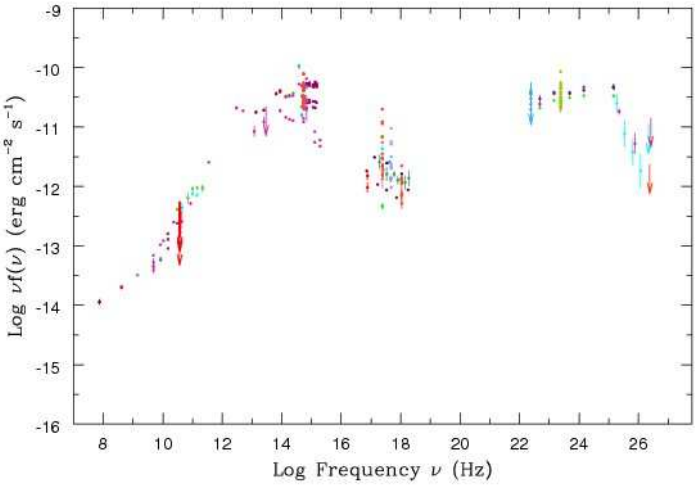

FIGURE 1.16— IBL SED of 0219+428.

- **HBL**: The peak of the synchrotron power reaches UV or higher energies ($\nu_{peak} \gtrsim 10^{15} Hz$). The synchrotron emission dominates the observed flux in the X-ray band and the inverse Compton scattering occurs in the Klein Nishina regime.

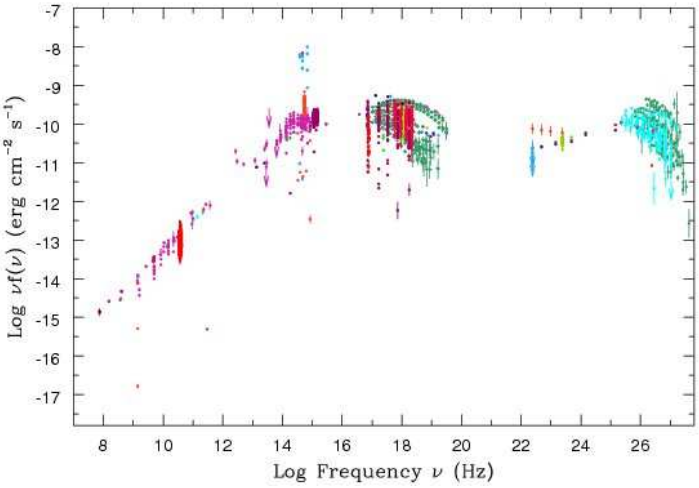

FIGURE 1.17— HBL SED of 1101+384.

2

Observing Activities and facilities

2.1 The GASP-WEBT Collaboration

The Whole Earth Blazar Telescope (WEBT) is a network created by optical astronomers in 1997, in order to monitor blazars in a continuous way, following them from different facilities during the Earth rotation and consequently obtaining a high-temporal-density monitoring of such sources. The geographic distribution of the observatories participating in the WEBT Collaboration is shown in Figure 2.1. There are more than 100 telescopes taking data in the optical band. In 2000, the monitoring activity was extended, and telescopes observing in radio and near-infrared bands joined the collaboration. This upgrade of the initial project has been extremely useful in the understanding of the broad-band continuum emission of blazars, especially in conjunction with observations at higher frequencies (ultraviolet, X and gamma-rays). In 2007 a WEBT project called GASP (GLAST-AGILE Support Program) was launched with the aim of providing long-term and low-energy monitoring of a selected sample of 28 gamma-loud sources (see Table 2.1), for a comparison with the high-energy observations of the *Fermi* (formerly GLAST) and AGILE gamma-ray satellites.

FIGURE 2.1— The WEBT collaboration logo.

The WEBT project includes also a continuous polarimetric monitoring program of blazars in the optical band.

TABLE 2.1— List of the sources monitored by the GASP

IAU Name	Object	RA (J2000)	DEC(J2000)	R	J	K	Redshift
0219+428	3C 66A	02:22:39.6	+43:02:08	14.6	13.1	11.6	0.444
0235+164	AO 0235+16	02:38:38.9	+16:36:59	16.9	16.0	13.9	0.940
0420-014	PKS 0420-01	04:23:15.8	-01:20:33	16.4	14.4	12.6	0.914
0528+134	PKS 0528+134	05:30:56.4	+13:31:55	19.4	16.1	14.0	2.060
0716+714	S5 0716+71	07:21:53.4	+71:20:36	13.2	11.9	10.4	0.300
0735+178	PKS 0735+17	07:38:07.4	+17:42:19	16.1	14.2	12.6	0.424
0827+243	OJ 248	08 30 52.1	+24 11 00	17.1	16.2	15.0	0.939
0829+046	OJ 49	08 31 48.9	+04 29 39	15.9	14.1	12.4	0.174
0836+710	4C 71.07	08 41 24.3	+70 53 42	16.5	...	...	2.172
0851+202	OJ 287	08:54:48.9	+20:06:31	14.5	12.9	11.2	0.306
0954+658	S4 0954+65	09:58:47.2	+65:33:55	16.6	14.1	12.4	0.368
1101+384	Mkn 421	11 04 27.3	+38:12:32	13.2	11.1	10.0	0.030
1156+295	4C 29.45	11:59:31.8	+29:14:44	17.4	15.0	13.0	0.729
1219+285	ON 231	12:21:31.7	+28:13:58	15.0	13.3	11.7	0.102
1226+023	3C 273	12:29:06.7	+02:03:06	12.5	11.7	9.8	0.158
1253-055	3C 279	12:56:11.2	-05:47:21	15.2	13.5	11.5	0.536
1510-089	PKS 1510-08	15:12:50.5	-09:06:00	16.1	14.5	12.6	0.360
1611+343	DA 406	16:13:41.0	+34:12:48	17.1	16.0	14.4	1.401
1633+382	4C 38.41	16:35:15.5	+38:08:04	17.1	14.7	13.0	1.813
1641+399	3C 345	16:42:58.8	+39:48:37	17.4	15.5	13.7	0.593
1652+398	MRK 501	16:53:52.2	+39:45:37	13.3	11.4	10.4	0.034
1739+522	4C 51.37	17:40:37	+52:11:43	17.5	16.2	14.6	1.375
1807+698	4C 69.24	18:06:50.7	+69:49:28	14.3	12.1	10.9	0.051
2155-304	PKS 2155-304	21:58:52.1	-30:13:32.1	12.6	12.1	10.7	0.116
2200+420	BL Lacertae	22:02:43.3	+42:16:40	13.9	11.2	9.5	0.069
2230+114	CTA 102	22:32:36.4	+11:43:51	16.6	15.6	14.4	1.037
2251+158	3C 454.3	22:53:57.7	+16:08:54	16.2	14.9	13.9	0.859
2344+514	1ES 2344+514	23 47 04.8	+51 42 18	14.6	12.7	11.5	0.044

The IAC participates in the WEBT projects providing both optical and near-infrared data. In the following we will present the observing facilities and describe the data reduction and analysis process.

2.1.1 Optical photometry

The optical photometric data are collected by two telescopes located at the Teide Observatory in the Canary island of Tenerife.

Telescope IAC80

The mount of IAC80 is equatorial German with a primary mirror of diameter 82 cm. The instrumentation is installed at the Cassegrain primary focus.
This telescope is well suited for research programs devoted to the variability monitoring of moderately bright sources.

The telescope has two cameras:

CAMELOT (CAmara MEjorada LIgera del Observatorio del Teide): This is the principal instrument of the IAC80 telescope, which consists of a 2048×2048 pixels CCD detector, the pixel size is 13.5 micron, equivalent to 0.33 arcsecond in the sky. The field of view is equivalent to $10.6'$.

TCP (Troms CCD Photometer): This instrument is optimized for fast readout photometry based on CCD technology. The detector is a 1024×1024 pixels CCD camera and the scale of the pixels is 0.537".

FIGURE 2.2— IAC80 telescope.

Observations with IAC80 were initially available through the Spanish Observing Time Allocation Committee (CAT) as a routine program: now it is possible to obtain observing time with IAC80 as part of the Visitor Mode and Service Time Program reserved to IAC researchers.

STELLA

STELLA consists of two fully robotic, 1.2m telescopes at Izaña Observatory sharing the same dome building. The two telescopes combine a wide-field imager, WiFSIP at STELLA-I and a high-resolution spectrograph, SES, at STELLA-II.

Wide Field Stella Imaging Photometer(WIFSIP): is a CCD imager and photometer. It has a usable FOV of 22'×22' at a scale of 0.32"\pixel. The detector is a single 4096×4096 back-illuminated thinned CCD.

FIGURE 2.3— STELLA-I telescope.

The approved proposals have been 114-Stella6-13A, 151-Stella10-13B, 119-Stella7-14A, 86-Stella5-14B and 154-Stella9-15A, for a total amount of $\sim$ 226 hours. Unfortunately, about 50% of the time could not be spent in observations due to technical problems. It is worth to notice that Stella is a robotic telescope built by the AIP-Germany, which was offered to the Spanish community at the beginning of 2013 with a not fully developed facility for external observers. This facility has been progressively improved and now it results in a very user-friendly tool.

Data reduction

Optical observations are taken in the R band with an approximately monthly frequency for all visible sources. Exposure times range from 15 seconds for targets of R magnitude between 8 and 9.5, to 60 s for magnitude R between 13 and 14.5, up to 900 s for those of magnitude R $\geq$ 16.

The data reduction is performed automatically at the end of the night using a pipeline. The images are bias subtracted and flat-field corrected.

Photometric Calibration

Prior to the photometric calibration we correct the astrometric information on the header of our images. The astrometry calibration is usually done using the software *astronomy.net*[1] which transforms the image coordinates in sky coordinates, providing the right information in the World Coordinate System section of the header of the image. Recently, this piece of software has been replaced by a similar but more advanced tool called Parallax, which has been developed by J. J. Sanabria (IAC).

Once the images are astrometrically corrected, then we use Sextractor (Bertin & Arnouts (1996)) to extract the instrumental magnitude for all sources in the field with their celestial coordinates. We adopt the parameter ISO_MAG provided by Sextractor as the best estimator, as it has proved to be a robust one.

The photometric calibration is performed for each image, individually. The Zero Point (ZP) is determined by comparison of the instrumental and calibrated magnitudes of a list of comparison stars which have been previously calibrated (e.g. González-Pérez et al. (2001)). In general, there are 2-3 comparison stars in each field.

$$ZP = mag_{inst.} - mag_{calib.} + 2.5\log(t_{exp}) \tag{2.1}$$

Once the ZP is known we determine the calibrated magnitude of our target from the instrumental magnitude. We have adopted the error estimate provided by Sextractor, which could be slightly underestimated.

2.1.2 Near-Infrared photometry

Carlos Sanchez Telescope (TCS)

The TCS is located at the Izaña Observatory. It was designed by Prof. J Ring from United Kingdom and it started observations in 1972. It was initially thought as an infrared flux collector made of a thin primary mirror. The primary mirror has a diameter of 1.52 m and the focal ratio is 13.8 at its Cassegrain focus. Despite its age, it remains active as one of the few night time telescope focused on infrared photometry.

This telescope has a near infrared camera:

[1] http://astrometry.net

FIGURE 2.4— TCS telescope.

CAmara INfrarroja (CAIN)

CAIN is the principal camera in the TCS, its detector is composed by a mosaic of 256×256 HgCdTe photovoltaic elements (NICMOS 3), sensitive in the 1-2.5 micron range, with four electronic bias and independent reading, each controlling a quadrant. The camera has two optical configurations: the wide mode (W), with a scale of 1"/pixel and 4.2'×4.2' field of view, and the narrow mode (N), with a scale of 0.43"/pixel and 1.8'×1.8' field of view.

The cosmetics of the detector is rather irregular and has a respectable number of hot pixels plus two dead columns in the quadrant joining section. The dead columns are formed by two pixels which are scrambled from the initial columns in the quadrants.

Data reduction

The observations in the infrared band are done with the Carlos Sanchez Telescope (TCS) at J, H and Kshort bands. We observe an average of six nights per month. For these observations we use a dithering pattern of 5 different positions. In each of them, the integration time is one minute (split in individual exposure times of 10, 6 and 6 seconds for the J, H and Kshort bands respectively). For objects with magnitudes 10 to 12 the dither cycle lasts for 5 minutes, for magnitudes 12 to 14 we repeat the cycle twice and for those objects with magnitudes 14 to 16 we repeat 4 cycles. These integration times are illustrative, we need to adjust the exposure

times due to the variability of the objects.

The data reduction is done with the package CAINDR (under IRAF), developed by Rafael Barrena and Jose Acosta. During the data reduction, the main steps are the correction of the sensitivity variation of the pixels and non-uniform illumination of the detector, which corresponds to the flat-field correction. Besides, we substract the background of the sky as well as the contribution due to the telescope and the optical instrumentation. Finally, we combine all the images obtained in the different positions of the dithering pattern.

Next, we explain in more detail the different steps of the data reduction:

CORRECTION FOR THE SCRAMBLED CENTRAL COLUMNS:

The first step to be done is to correct for the scrambled central columns. The two leftmost columns are exchanged with the two rightmost columns, in every quadrant (see Fig. 2.5). This effect is caused by a not perfect synchronization reading pixel scheme.

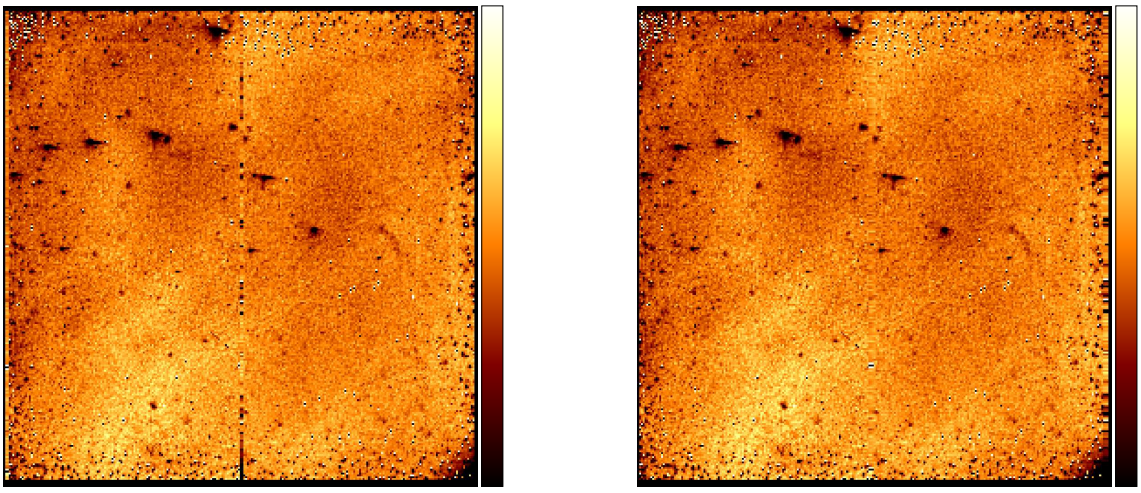

FIGURE 2.5— Figure showing the correction of the scrambled central columns. Left panel shows the image before correction and right panel the image corrected after readjusting the affected columns.

FLATFIELD CORRECTION:

The flatfield images allow us to correct effects of variation in sensitivity between the different pixels of the detector, as well as the vignetting produced by elements of the optical detector and other phenomena, and to identify pixels carrying a signal too low (cold pixels) or too high (hot pixels) with respect to the average.

In the case of J and H filters we only take images of bright flats, however in Kshort filter we take bright and dark flats (with the same exposures times), this is because in the Kshort band the emission of telescope and its surroundings gives a very important contribution to the background emission in addition to the lamp illumination. In this case the flatfield image is generated after the subtraction of the dark exposures.

Once combined images of flatfield of each filter are obtained and normalized (i.e. divided by the median), then the next step is to correct all images of one night for the flatfields. To create the flatfield image, we use *cmkflat* routine of *caindr* package of IRAF.

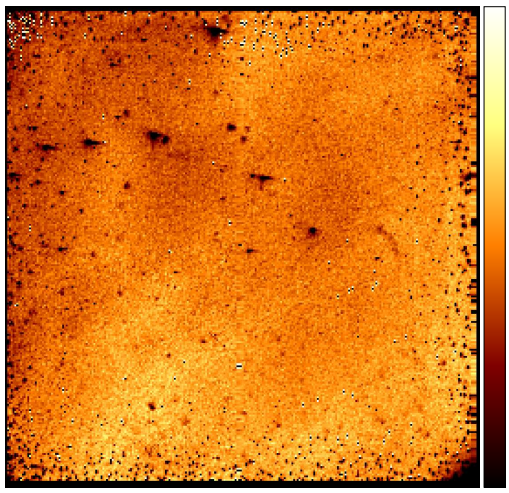

FIGURE 2.6— Flatfield image of Kshort filter.

CORRECTION FOR DEAD AND HOT PIXELS:

Bad pixels are those which present anomalies with respect to the neighbouring pixels, for instance they do not show appreciable signal or on the contrary they always show a very high signal.

We perform this correction by creating a mask from an image taken without illumination (dark). Note that bad pixels increase with exposures times, so, since all images have been taken with 6 and 10 seconds we created two masks, one for each exposures time.

For the correction of bad pixels we use the routine *cbadpix*.

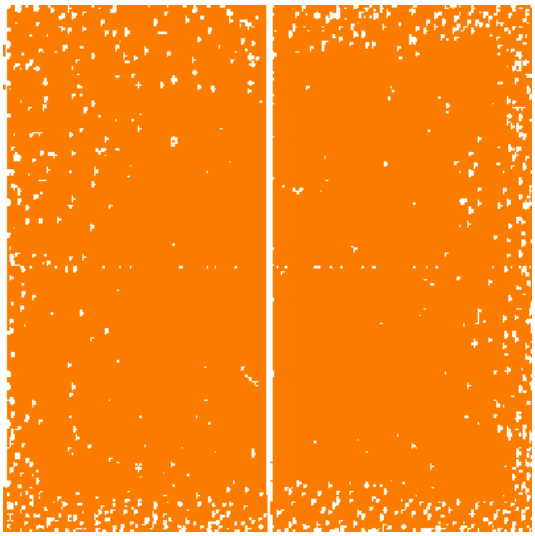

FIGURE 2.7— Mask to correct bad pixels.

SKY SUBTRACTION:

This is one of the most important step during the data reduction of near infrared data since the sky emission commonly exceeds the one from our targets. Furthermore the sky emission presents large variability in scales of few minutes. An estimation of the sky emission must be done on a pixel-by-pixel basis since the variations cannot be simply corrected by the flat-field images. In our case we combine all images taken in one dithering cycle for each filter.

The sky image is generated as the median of each pixel through the cycle. Prior to compute the median, an offset is added to each frame in order to compensate for any global temporal variation of the sky level. In this way the stars are effectively removed and the sky image merely corresponds to the sky background. This image is then subtracted from all frames and the faintest objets appear. Usually a second iteration is performed after the position of the objects is identified in each frame and a mask is created. The process of creating the median image is usually repeated taking into account the object mask.

For the subtraction of the sky we use the routine *subditsky*.

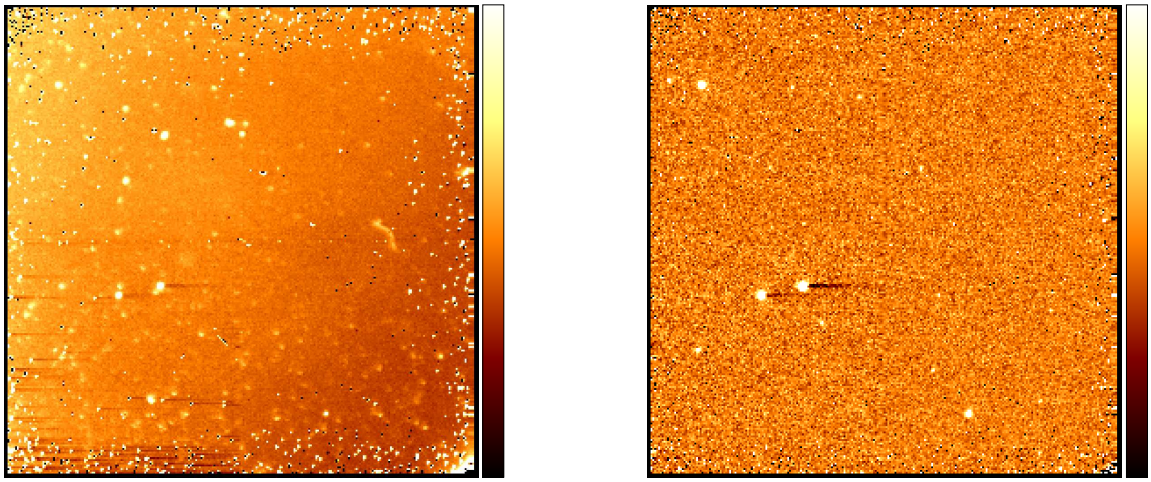

(a) Uncorrected sky image

(b) Corrected sky image

FIGURE 2.8— Sky subtraction.

COMBINATION OF IMAGES:

In this step we combine the images taken at different positions of the dither pattern and create a final image. This technique is commonly called "shift and add". Usually we get an image for every cycle, which consists of 5 dither positions. Sometimes we have detected a certain variation in the photometry which may be intrinsic or due to the variation of the transmission conditions of the atmosphere.

For the combination of images we use the routine *cicomb_cub*. This routine is interactive and is not automatic due to various circumstances affecting the images obtained with CAIN. Sometimes the coordinates in the image headers are not accurate and locating objects in some of the fields is difficult.

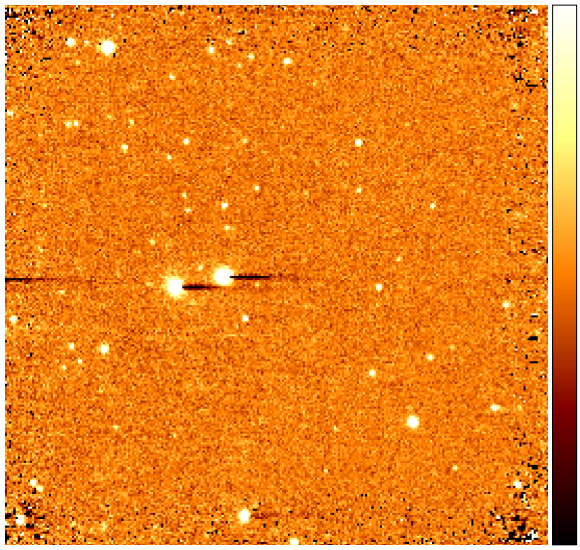

FIGURE 2.9— Combination of different images of the "dither" cycle.

Photometric Calibration

For the photometric calibration at the infrared wavelengths, we use an interactive IDL script (P. Abraham Obs. Konkoly-Hungary): *twomass2tcs*. Below, we describe the calibration process step by step:

In most cases the combination of small field of view (4x4 arcmin^2) and short integration times makes it difficult to find a sufficient number of stars to perform an automatic astrometric calibration. Therefore, an interactive process has to be done on each individual frame. The tool we are using is run by the following command:

twomass2tcs,directory,fitsfile,simbad = "$SIMBADname''$

Where directory, is the data directory, fitsfile the name of the file to analyze and *simbad* = "$SIMBADname''$ is the object name in the simbad catalogue, so the program automatically downloads the object coordinates from the simbad database.

Setting astrometric information:

After the image is displayed, we select a reference object in order to fix the coordinate system. Then all the stars contained in the 2MASS catalogue which are inside the field of view will be marked.

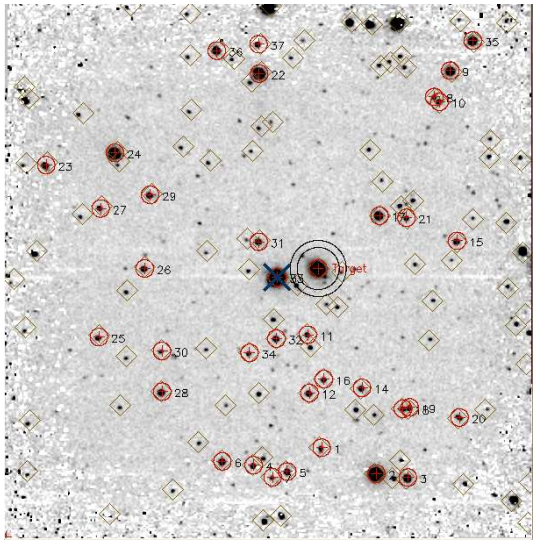

FIGURE 2.10— A typical image after setting astrometric information. The reference target is marked with two concentric rings, the identified 2MASS sources are marked by red circumferences and the blue cross indicates possible saturation.

Selection of optimal aperture:

At this point, the instrumental magnitude of the catalogue stars is plotted versus the calibrated magnitude taken from the 2MASS catalogue (Fig. 2.11). The optimal aperture is selected as the one that mantains a linear relationship between the two quantities.

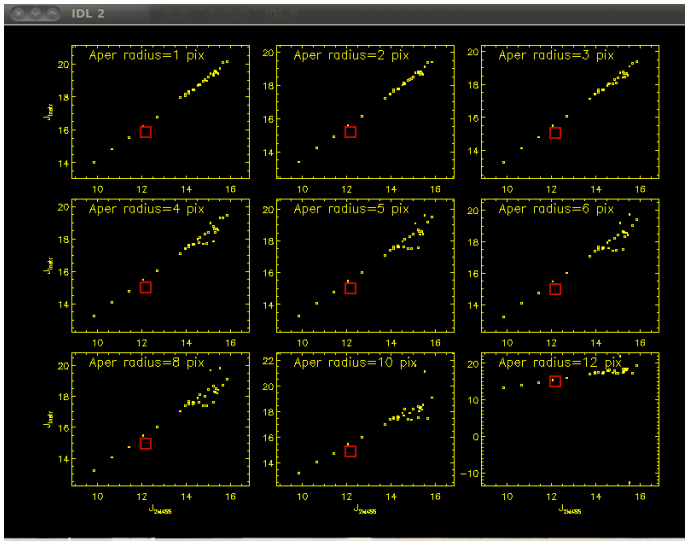

FIGURE 2.11— Instrumental magnitude versus calibrated magnitude. Different panels correspond to different aperture radii. The red circle represents the target.

Determination of photometric zero point:

Fig. 2.12 is a plot of the instrumental and calibrated magnitude differences as a function of the calibrated magnitudes. This graph is useful to eventually discard objects which are too weak, saturated or deviant from the rest, which might indicate variable sources.

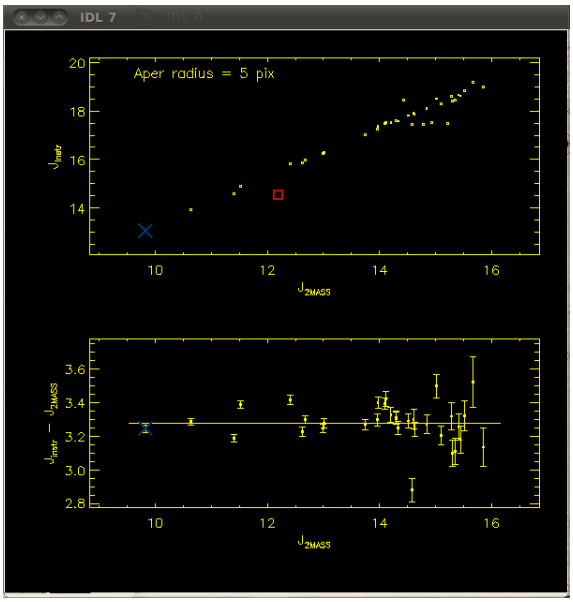

FIGURE 2.12— Selection of reference sources based on the magnitude limits. The red square represents the target to be calibrated.

In addition, a cleaning of reference stars can be done to avoid effects due to the proximity to the field of view boundaries.

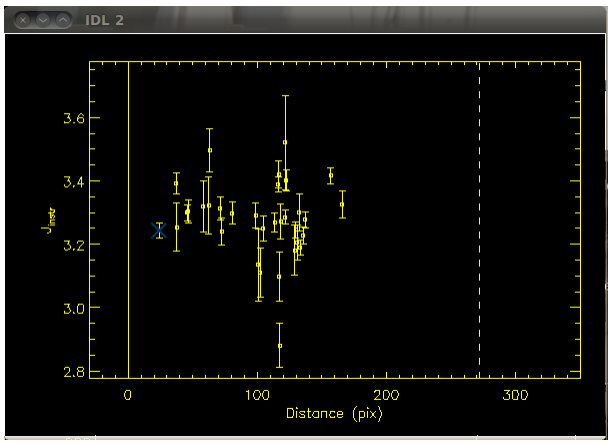

FIGURE 2.13— Election of the limit distance.

A final selection of reference stars can be done by inspecting the aperture growth curves, the deviant sources will be discarded at this point.

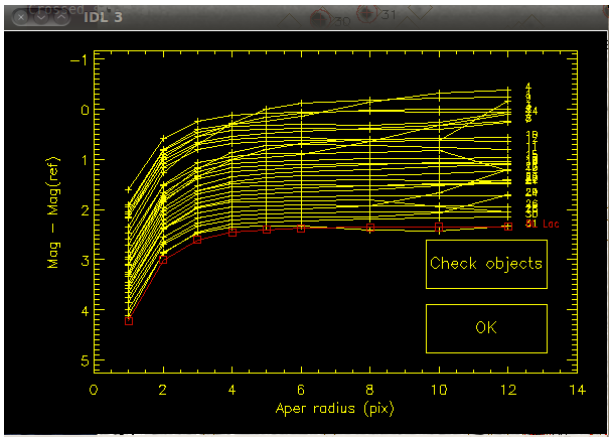

FIGURE 2.14— Aperture growth curves for the different sources to be used as references. The red curve is our target of interest.

Once the reference stars have been selected, after removing the bad ones, the difference between instrumental and calibrated magnitudes is presented in a scattering plot. Here it is decided which value will be used as photometric zero point. Different choices include weighted or unweighted mean values, the median, etc. Most of the times we use the average method and a few times the median one, depending on the number of available reference stars in the field of view. After the selection of the method, the target calibrated magnitude and error are shown automatically.

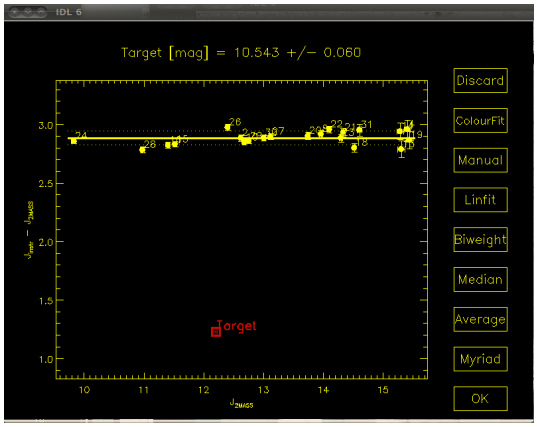

FIGURE 2.15— Setting for calculating the calibrated magnitude.

Data saving:

Finally, all the relevant information such as the calibrated magnitude and its error, the Julian date, the zero point, and information about reference stars is saved in IDL dataset files.

2.2 The *Swift* Telescope

Multiwavelength blazar studies take advantage of public data acquired by satellites for high-energy astronomy like *Swift* and *Fermi*.

Swift is a fast response satellite, launched on 2004 November 20 for the study of the gamma-ray bursts (GRBs). It observes the X-rays, visible and UV radiation. This satellite is largely used for the high energy photometric monitoring of the blazars when not observing the GRBs.

FIGURE 2.16— The *Swift* Telescope.

The *Swift* satellite holds the three instruments described here (see Fig. 2.17):

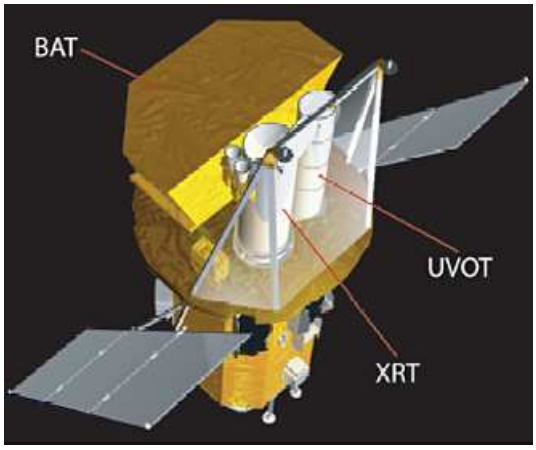

FIGURE 2.17— Instrument on board of the *Swift* satellite.

2.2.1 Burst Alert Telescope (BAT)

BAT is a high-sensitivity, wide field of view instrument. It has been designed for the rapid GRBs detection and their localization within three arcmin. The field of view is 1.4 sr through a codified mask. The sensitivity energy range is between 15 and 150 KeV and up to 500 KeV for the images without the codification. BAT is able to give in few seconds the initial position of the detected GRB and drive the satellite pointing to the GRB origin position.

In order to study bursts in large scales of intensity, duration and temporal structure BAT is designed with high dynamic range and detection capabilities. A codified bidimensional mask and a large area solid state detector allow the instrument to detect the low intensities bursts while the large field of view allows BAT to detect a good ratio of bright bursts. The long time scale GRBs are detected simultaneously at different wavelengths, X-rays, UV and optical due to the BAT codified mask, including the field of view of XRT and UVOT. In Table 2.2 some characteristics of BAT are listed.

BAT operates in two modes, the bursts mode, evaluating the position of the explosions and the identification mode, returning the data of the hard X-rays identification. When operating in the latter one, the instrument collects the data count rates per bins of 5 minutes per 80 energy channels. When an explosion is detected, the instrument changes to photon counting mode, with an intermediate memory where the pre-explosion data are saved.

Up to now several AGNs have been discovered by BAT. In Fig. 2.18 the map of the discovered and studied AGNs is shown.

TABLE 2.2— Instrument characteristics of BAT.

Property	Description
Detecting Area	5200cm^2
Detector Operation	Photon counting
Field of View	1.4 sr (partially-coded)
Detector Size	4mm x 4mm x 2mm
Telescope PSF	17 arcmin
Energy Range	15-150 keV

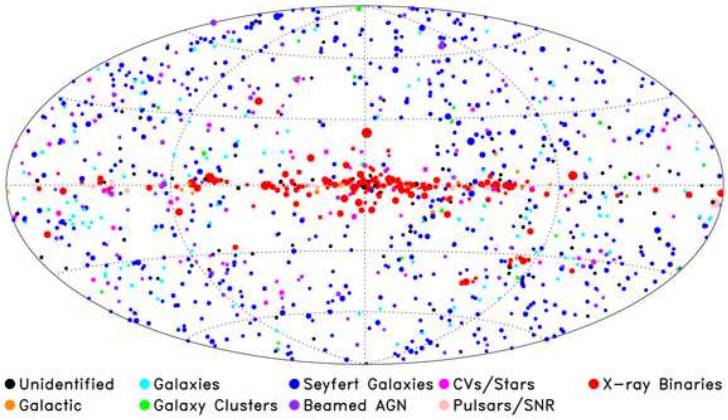

FIGURE 2.18— All-sky map showing classification of the BAT 70 month survey sources.

2.2.2 X-ray Telescope(XRT)

XRT and UVOT are instruments with a narrow field of view, aligned within the BAT field of view. When the BAT instrument detects a burst and localizes it with the accuracy of 4 arcmin, *Swift* points at this location and XRT improves the accuracy of the pointing up to 5 arcsec, usually in less than 10 seconds. The real field of view of XRT is 23.6 squared arcsec.

In the next table, the main characteristics of the XRT detector are summarized.

TABLE 2.3— Instrument characteristics of XRT.

Property	Description
Effective Area	110 cm^2 @ 1.5 keV
Telescope	18 arcsec HPD @ 1.5 KeV
PSF	22 arcsec HPD @ 8.1 KeV
Detector	MAT CCD-22 600 x602 pixels
Detector Operation	Imaging, Timing and Photon-counting
Pixel Scale	2.36 arsec/pixels
Energy Range	0.2-10 keV
Sensitivity	2 x 10^{-14}erg cm^{-2}s^{-1} in 10^4s

XRT has two main operation modes, depending on the source brightness: Windowed Timing (WT) and Photon Counting (PC). The WT mode is used to obtain high temporal resolution (2.2 ms) data, with partial spatial information. The PC mode provides complete spatial information, but with a lower temporal resolution (2.5 seconds).

To eliminate events due to charged particles and to obtain the expected energy resolution, X-ray events from each readout are identified and classified. For the PC mode the distribution of the charge in the 3x3 matrix is classified according to a library of 32 grades (Fig. 2.19). For the PC mode, grades in the range of 0-12 are considered good grades. For the WT mode a 7x1 matrix is used to reconstruct the events and to grade them according to a library of 15 grades. For the WT mode, grades in the range of 0-2 are considered good.

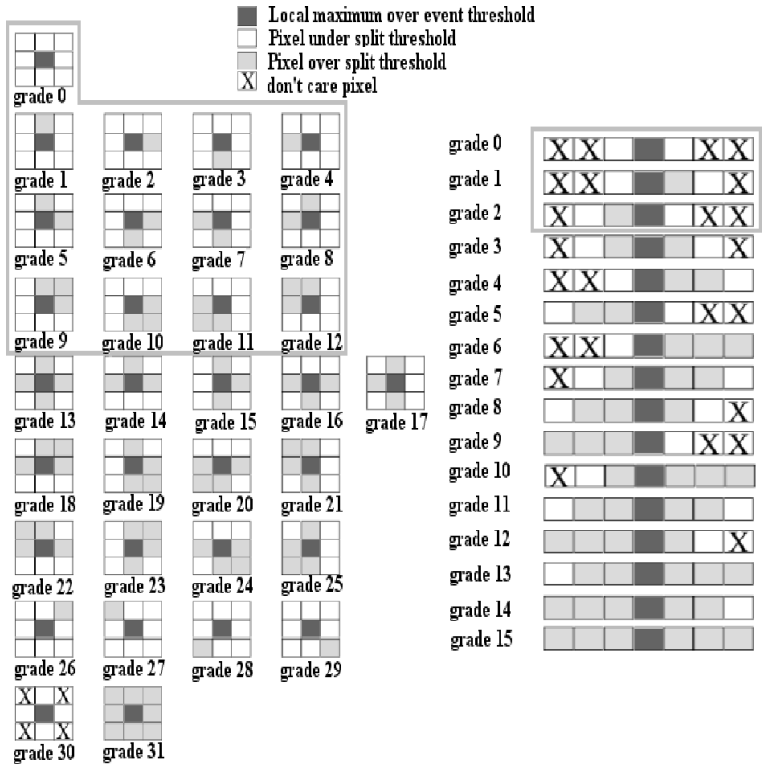

FIGURE 2.19— The definition of the XRT grades for PC (left) and WT (right) modes.

The initial data processing for these different modes are:

Windowed Timing mode:

- Remove partially exposed pixels
- Assign the time to each event
- Reconstruct events and assign grade and Pulse Height Analyser (PHA) value.

- Flag bad columns

Photon Counting mode:

- Flag bad pixels
- Flag thresholded events
- Flag calibration sources
- Calculate and Flag hot and flickering pixels
- Assign grade and PHA values

Data reduction

We analyse the X-ray Telescope data with the HEAsoft package and calibration files contained in the CALDB database at the High Energy Astrophysics Science Archive Research Center (HEASARC). We process the event files acquired in pointing mode. Normally we consider the observations with exposure times longer than 5 min and performed both in photon-counting (PC) and Windowed-timing (WT) mode.

Event files are calibrated and cleaned with standard filtering criteria with the xrtpipeline routine, selecting event grades 0-12 for the PC case and 0-2 for the WT case. Fig. 2.20(a) shows one image in PC mode and Fig. 2.20(b) one in WT mode.

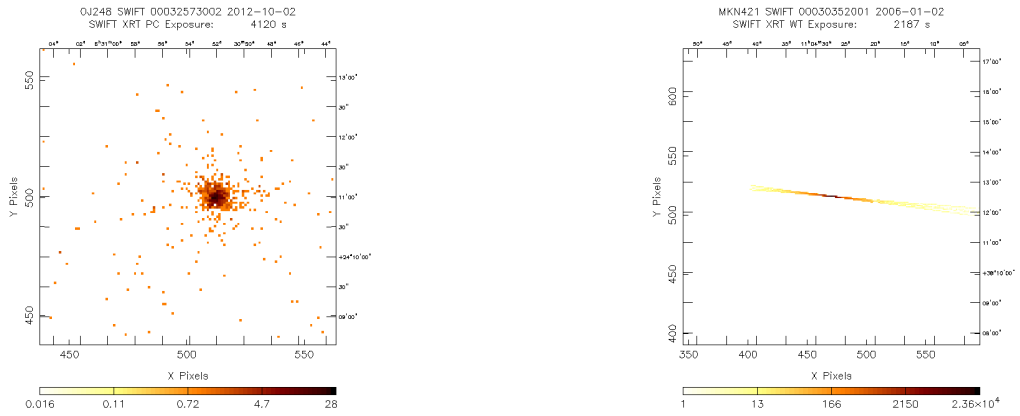

(a) XRT image in pc mode

(b) XRT image in wt mode

FIGURE 2.20— XRT image

Source counts are normally extracted from a circular region with radius of 60-70 arcsec centred on the source, and background counts are derived from a surrounding annular or circular

region. However in the case where the source is very bright background can be neglected.

If the count rate in PC mode is higher than 0.5 cts/s and higher than 100 cts/s in WT mode, we need to correct for pile-up. Pile-up occurs on X-ray CCDs when several photons hit the detector at the same place between two read-outs. In that case they are counted as one (or not at all) and their energies are summed. Pile-up thus affects both flux measurements and spectral characterisation of bright sources. We analyse the pile-up images with the ximage routine and model the wings of the source point spread function (PSF) with the King's function representing the expected PSF of XRT (Moretti et al. (2005)). The extrapolation of the fit to the inner region allows us to define the radius within which pile-up is important. This normally turns out to be 10 arcsec. The source extraction region is then punctured in the centre so that it becomes an annulus with internal radius of 10 arcsec.

We use the xrtmkarf routine to generate ancillary response files (ARF), which account for different extraction regions, vignetting and PSF corrections.

When we have different orbits in the same epoch, we create event files and extract source and background counts separately for each orbit. For each event file we then generate the exposure map with the xrtexpomap task to obtain the ARF for the corresponding source spectrum. Finally we recombine the information from all the orbits of a single observation by summing the source spectra and the background spectra. The ARFs are summed by weighting them according to their orbit contribution to the total counts of the observation.

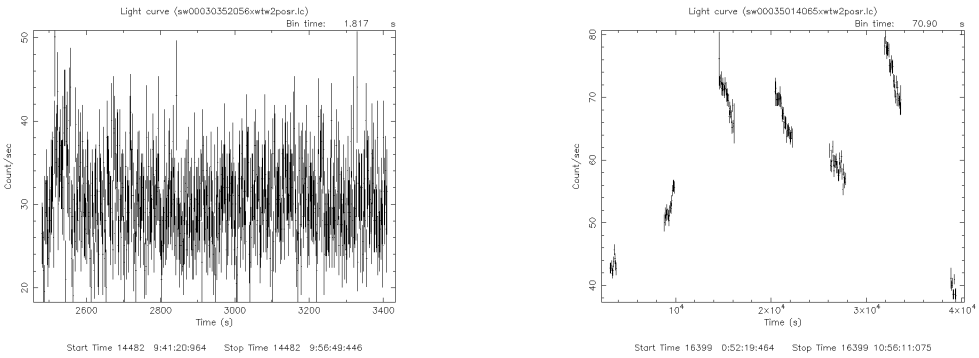

(a) XRT image with one orbit

(b) XRT image with different orbits

FIGURE 2.21— XRT light curves over (a) one orbit or (b) several orbits.

Before the spectral fitting, the 0.3-10 keV source spectra are binned using the *grppha* routine to ensure a minimum of 20 counts per bin. This allows us to use the χ^2 statistics. In the case of a low count number, the binning is not performed and the Cash's statistics is adopted. We fit the spectra with different models, including absorption as well as a model for the intrinsic spectrum. Absorption can either be left free or be fixed to the Galactic column density NH

value in the direction of the source.

The main models used to fit the source spectrum are:

Power law: This is a simple photon power law:

$$A(E) = KE^{-\alpha}$$

where: α is the photon index of the power law (dimensionless) and K is the normalization factor in units of photons $\mathrm{keV}^{-1}\mathrm{cm}^{-2}\mathrm{s}^{-1}$ at 1keV.

Log-parabolic model:

$$A(E) = K(E/E_p)^{-\alpha-\beta\log(E/E_p)}$$

where: α is the slope at the pivot energy, β is the curvature term, E_p is the fixed pivot energy (best near low end of energy range), and K is the normalization factor.

Broken power law:

$$A(E) = KE^{-\Gamma_1}\ ,\ E \leq E_{break}$$

$$A(E) = KE_{break}^{\Gamma_2-\Gamma_1}(\frac{E}{1keV})^{-\Gamma_2}\ ,\ E \geq E_{brea}k$$

where: Γ_1 is the power law photon index for E<E_{break}, E_{break} is the break point for the energy in keV, Γ_2 is the power law photon index for E>E_{break} and K is the normalization factor in units of photons $\mathrm{keV}^{-1}\mathrm{cm}^{-2}\mathrm{s}^{-1}$ at 1keV.

2.2.3 UV/Optical Telescope (UVOT)

The observations are done using different broadband filters and two prisms (one for the optical and one for the UV), mounted in a filter wheel in front of the detector. The UVOT field of view is 17 squared arcmin and the detector is a CCD working in photon counting.

The most relevant characteristics of the UVOT telescope are shown in the following table.

TABLE 2.4— Instrument characteristics of UVOT.

Property	Description
Telescope	Modified Ritchey-Chretien
Focal Ratio	12.7
Detector Operation	Photon counting
Field of View	17 x 17 arcmin
Telescope PSF	2.5 arcsec @ 350 nm
Wavelength Range	170-650 nm
Filters	7
Sensitivity	B=22.3 in white light in 1000s
Pixel Scale	0.502 arcsec
Brightness Limit	v=7.4 mag
Camera Speed	11 ms

Data reduction

We reduce the data with different versions of HEAsoft package and calibration files in the CALDB database at HEASARC. In Figure. 2.22 one example of UVOT image in uvw2 filter is displayed.

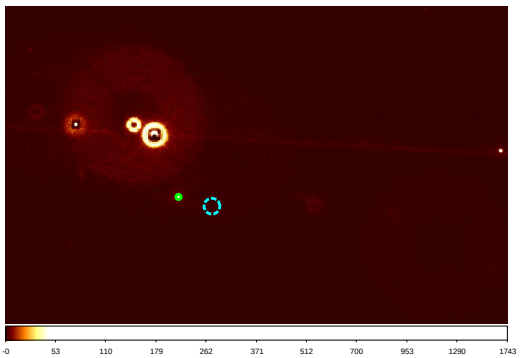

FIGURE 2.22— UVOT image in uvw2 band. The green/cyan circle is the source/background extraction region.

We use the routine uvotimsum for summing the multiple exposures in the same filter at the same epoch. The routine uvotsource is then used for the aperture photometry. Normally we use a circular region with 5 arcsec radius because of the calibration constrains, while the background counts can be estimated in several ways: using a single large circle or considering an annular region center on the source and with a tipycal radius of 10-15 arcsec.

2.3 The *Fermi* γ-ray Space Telescope

Fermi has been launched in a near-Earth orbit on 2008 July 11. The mission lifetime is 5 years with an extension up to 10 yr. The space telescope has been designed for creating a daily map

of the sky.

Fermi is a formidable instrument for the high-energy sky exploration. The Astronomers use its data to study how the jets are expelled and accelerated by the black holes up to relativistic velocities, while physicists and cosmologists interested in subatomic particles with energies much higher than the ones observed at the accelerators can obtain information on the origin and evolution of the Universe.

FIGURE 2.23— *Fermi* Telescope.

Figure 2.24 Map of the sky observed by *Fermi*. Several sources reported are not yet identified.

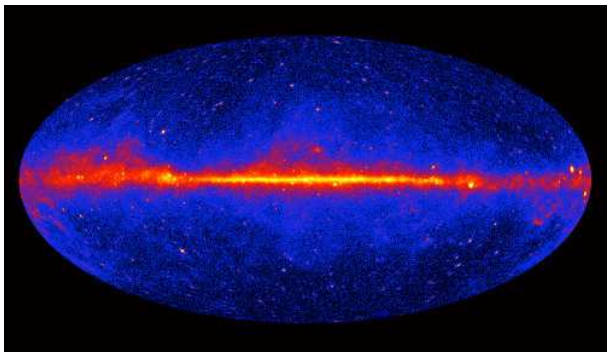

FIGURE 2.24— Sky observed by *Fermi*.

We describe here the primary instrument on board of *Fermi*, the Large Area Telescope (LAT).

2.3.1 Large Area Telescope (LAT)

The energy range of the LAT telescope is between 20 MeV and 300 GeV. These energies are possible only for photons emitted in extreme conditions by relativistic particles. The LAT field

of view covers 20% of the full sky, that is mapped approximatively every 3 hours.

Making use of the observing results from its survey mode, the *Fermi*-LAT collaboration has produced so far three catalogs with the detected gamma-ray sources and the corresponding counterparts at lower energies. The third catalog (3FGL; Acero et al. (2015)) is the most updated and complete one and includes 2192 gamma-ray sources detected at Galactic latitudes larger than 10°. In addition to these catalogs, containing all the γ-ray sources detected by *Fermi*, other catalogs containing only AGNs and related studies have been released. These catalogs are the LAT Bright AGN Sample (LBAS; Abdo et al. (2009)) and the three LAT AGN catalogs (Abdo et al. (2010); Ackermann et al. (2011, 2015)) with the last one, the 3LAC, actually the most updated and complete.

Data reduction

The data of the different sources are downloaded from the LAT online public archive and analysed with standard methods. We normally set a maximum zenith angle of 100 degrees to reduce contamination from the Earth limb γ-rays, which are produced by cosmic rays interacting with the upper atmosphere and a rocking angle of 52 degrees. The adopted software is LAT Science Tools with Instrument Response Function depending on the Science Tools version. For the spectral analysis we used the science tool gtlike. Isotropic and Galactic diffuse emission components are used to model background.

We analyse a region of interest of 10 degrees radius centred at the location of source. We evaluate the significance of the γ-ray signal from the sources by means of test statistic (TS) based on the likelihood ratio test. The TS=2Δ log(likelihood) between models with and without the source is a measure of the probability of having a γ-ray source at the specified location. This compares models whose parameters have been adjusted to maximize the likelihood of the data given the model (Mattox et al. (1996)). The source model used in gtlike includes all the point sources from the second *Fermi*-LAT catalogue (2FGL) and third *Fermi*-LAT catalogue (3FGL) that fall within 20 degrees from the source. We remove from the model the sources having TS < 25 and/or the predicted numer of counts based on the fitted model $N_{pred} < 10$.

For the spectral fitting we adopted different models depending on the sources, as in the X-ray data analysis. These are Power Law, Broken Power Law and Log Parabola.

3

Infrared properties of blazars.

The infrared properties of blazars can be studied from the statistical point of view with the help of sky surveys, like the Wide-field Infrared Survey Explorer (*WISE*) and the Two Micron All Sky Survey (2MASS). However, blazars are known for their strong and unpredictable variability, which can be monitored for a handful of objects only. In this paper we consider the 28 blazars (14 BL Lac objects and 14 flat-spectrum radio quasars, FSRQs) that are regularly monitored by the GLAST-AGILE Support Program (GASP) of the Whole Earth Blazar Telescope (WEBT) since 2007. They show a variety of infrared colours, redshifts, and infrared–optical spectral energy distributions (SEDs), and thus represent an interesting mini-sample of bright blazars that can be investigated in more detail. We present near-IR light curves and colours obtained by the GASP from 2007 to 2013, and discuss the infrared–optical SEDs. These are analysed with the aim of understanding the interplay among different emission components. BL Lac SEDs are accounted for by synchrotron emission plus an important contribution from the host galaxy in the closest objects, and dust signatures in 3C 66A and Mkn 421. FSRQ SEDs require synchrotron emission with the addition of a quasar-like contribution, which includes radiation from a generally bright accretion disc (νL_ν up to $\sim 4 \times 10^{46}\,\mathrm{erg\,s^{-1}}$), broad line region, and a relatively weak dusty torus.

Introduction

BL Lacertae objects (BL Lacs) and flat-spectrum radio quasars (FSRQs) make up the two classes in which the active galactic nuclei (AGNs) known as "blazars" are divided. They share extreme properties, as the noticeable flux variability at all wavelengths, from the radio to the γ-ray energies, and on a variety of timescales, ranging from hours to years. Their radio-to-UV (in some cases also X-ray) emission is mainly non-thermal, polarised synchrotron radiation from a relativistic jet pointing at a small angle to the line of sight, which explains the superluminal motions inferred from the radio images and the extremely high brightness temperature implied by fast radio variability.

According to the classical definition by Stickel et al. (1991) and Stocke et al. (1991), the distinguishing feature of BL Lacs is that their spectra show optical emission lines with a rest-frame equivalent width smaller than 5 Å, if any. This classification is however unsatisfactory, as

objects can change class depending on the level of non-thermal continuum from the jet. Even BL Lacertae itself was found not to behave as a BL Lac in faint states (Vermeulen et al., 1995; Corbett et al., 2000; Capetti, Raiteri & Buttiglione, 2010). New criteria to separate BL Lacs from FSRQs have recently been proposed by Ghisellini et al. (2011) and Giommi et al. (2012), which are based on the luminosity of the broad-line region in Eddington units and the ionization state, respectively.

Differences between the two blazar classes were observed in the wavelength-dependent behaviour of the optical polarisation, when present (see e.g. Smith, 1996). BL Lacs show increasing polarisation toward the blue, likely due to causes intrinsic to the jet emitting region. An opposite behaviour characterises FSRQs, because of the dilution effect toward the blue produced by the unpolarised thermal radiation from the accretion disc (Smith, 1996; Raiteri et al., 2012). Moreover, Very Long Baseline Interferometry (VLBI) observations revealed different polarisation structures, with BL Lacs exhibiting polarisation position angles in the radio knots parallel, while FSRQs perpendicular, to the jet structural axis (e.g. Gabuzda et al., 1992).

From the point of view of parsec-scale jet morphology and kinematics, Karouzos et al. (2012) found that BL Lacs have in general wider and more bent jets than FSRQs, and that transverse motion of inner knots in BL Lacs is more pronounced than the radial one, which would suggest a helical jet structure. Variations of the innermost jet position angle in time are larger in FSRQs than in BL Lacs (Lister et al., 2013).

Besides the classification into FSRQs and BL Lacs, the latter sources are further divided into low-energy peaked (LBL) and high-energy peaked (HBL) BL Lacs, depending on the frequency at which the synchrotron emission component peaks in the spectral energy distribution (SED). The relation between LBLs and HBLs is still a matter of debate (e.g. Laurent-Muehleisen et al., 1999).

Observations by the Wide-field Infrared Survey Explorer (*WISE*) satellite (Wright et al., 2010) led to the development of a new diagnostic tool for AGN. In particular, it was noticed that blazars occupy a well-defined region of the $W1-W2$ versus $W2-W3$ plane[1]: the so-called *WISE* blazar strip (Massaro et al., 2011), which includes a subregion delineating γ-ray emitting blazars (Massaro et al., 2012). This was used by D'Abrusco et al. (2013) and Massaro et al. (2013a) to recognise blazar candidates among the unidentified γ-ray sources detected by the Large Area Telescope (LAT) onboard the *Fermi* satellite.

Using *WISE* data, Plotkin et al. (2012) concluded that there is no evidence of a dusty torus in BL Lacs, which implies structural differences between the two types of blazars, possibly driven by different accretion rate regimes.

Statistical analysis of the blazar properties is facilitated by the presence of an on-line cat-

[1]The *WISE* filters W1, W2, W3, and W4 have isophotal wavelengths of about 3.4, 4.6, 12, and 22 μm, respectively. These $\lambda_{\rm iso}$, together with the magnitude zero-points, are calibrated with respect to Vega (Wright et al., 2010).

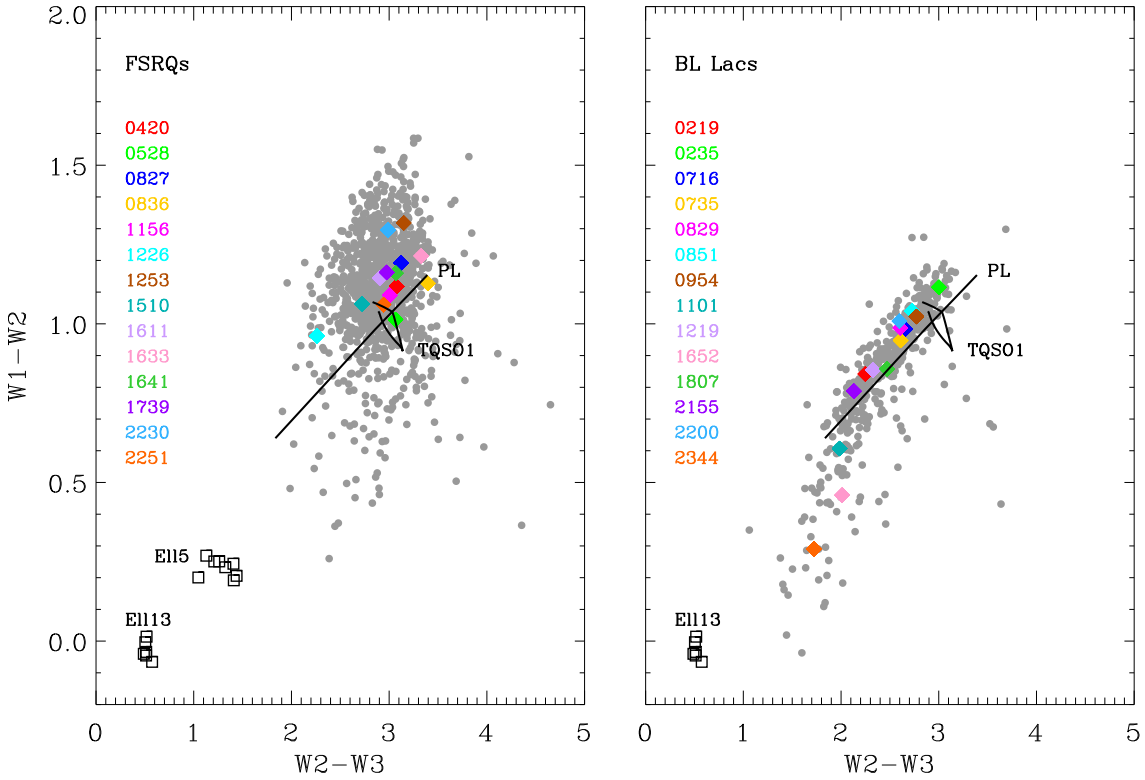

FIGURE 3.1— Colour-colour diagrams built with *WISE* data for FSRQs (left) and BL Lacs (right). Only objects with $S/N > 3$ in all *WISE* bands were considered. The points corresponding to the 28 sources monitored by the GASP-WEBT are highlighted with coloured diamonds. The black squares in the bottom left represent the SWIRE templates of 5 and 13 Gyr old elliptical galaxies at different values of redshift. The locations of Type 1 QSO spectra (TQSO1 SWIRE template) of various redshift, and power-law (PL) spectra with different spectral index are also plotted.

alogue of blazars, the Roma-BZCAT[2] (Massaro et al., 2009), as well as of many catalogues resulting from multifrequency surveys, from both ground and space, as the Sloan Digital Sky Survey[3] (SDSS), the Two Micron All Sky Survey[4] (2MASS), or the *WISE* All-Sky Database[5]. However, generally surveys give information on a single state of each source, while blazars are rapidly and unpredictably variable objects at all frequencies.

On the other hand, the long-term multifrequency behaviour of blazars can be studied in detail only for a handful of sources, and this is usually achieved by large collaborations that share the observing effort. The Whole Earth Blazar Telescope[6] (WEBT) was born in 1997 as an international collaboration of astronomers devoted to blazar studies. The advent of the new-generation satellites for γ-ray astronomy, Astro-rivelatore Gamma ad Immagini Leggero (AGILE) and *Fermi* (formerly GLAST), led the WEBT to organise a long-term monitoring of

[2]BZCAT is available on line at the ASDC website http://www.asdc.asi.it/bzcat.
[3]http://www.sdss.org/
[4]http://www.ipac.caltech.edu/2mass/
[5]http://irsa.ipac.caltech.edu/
[6]http://www.oato.inaf.it/blazars/webt/

TABLE 3.1— The BL Lac objects in the GASP target list.

IAU Name	Other Name	BZCAT Name	z	$E(B-V)$
0219+428	3C 66A	BZBJ0222+4302	0.444	0.0847
0235+164	AO 0235+16	BZBJ0238+1636	0.940	0.0797
0716+714	S5 0716+71	BZBJ0721+7120	0.310	0.0312
0735+178	PKS 0735+17	BZBJ0738+1742	0.450	0.0339
0829+046	OJ 49	BZBJ0831+0429	0.174	0.0329
0851+202	OJ 287	BZBJ0854+2006	0.306	0.0283
0954+658	S4 0954+65	BZBJ0958+6533	0.367	0.1197
1101+384	Mkn 421	BZBJ1104+3812	0.030	0.0153
1219+285	ON 231	BZBJ1221+2813	0.102	0.0233
1652+398	Mkn 501	BZBJ1653+3945	0.033	0.0190
1807+698	3C 371	BZBJ1806+6949	0.046	0.0340
2155−304	PKS 2155−304	BZBJ2158−3013	0.116	0.0219
2200+420	BL Lacertae	BZBJ2202+4216	0.069	0.3280
2344+514	1ES 2344+514	BZBJ2347+5142	0.044	0.2097

28 blazars, 14 BL Lacs and 14 FSRQs, which were selected among the γ-loud, optically brightest and potentially most interesting sources for coordinated low-energy and γ-ray studies. This long-term monitoring project was called the GLAST-AGILE Support Program (GASP) and started its activity in 2007 (see e.g. Villata et al., 2008).

We first put into context the GASP sources by comparing their infrared properties with those of the other classified blazars. Then we present the results of the near-IR monitoring of the GASP sources performed at the Campo Imperatore (Italy) and Teide (Canary Islands, Spain) observatories in 2008–2013. We analyse their flux density variability, colours and SEDs with special attention to the differences between BL Lac objects and FSRQs.

3.1 The GASP sources into context

Tables 3.1 and 3.2 list the GASP sources, divided into the two blazars classes, according to the classical definition adopted in the BZCAT catalogue. For each source we give in Column 1 the IAU name, in Column 2 the name with which the source is most often indicated in the literature, and in Column 3 the BZCAT identification. The source redshift is reported in Column 4. We adopted the redshift values of the BZCAT catalogue, but in the case of 0716+714, for which we set $z = 0.31$ following Nilsson et al. (2008), and of 0735+178, for which we set $z = 0.45$ after Nilsson et al. (2012). Finally, Column 5 gives the Galactic reddening obtained from the Galactic Dust Extinction Service at IRSA[7]. Reddening is particularly important (> 0.1) for the BL Lacs 0954+658, 2200+420, and 2344+514, and for the FSRQs 0420−014, 0528+134, 1510−089, and 2251+158.

As mentioned in the Introduction, the IR survey undertaken by the *WISE* satellite provided

[7]http://irsa.ipac.caltech.edu/applications/DUST/

TABLE 3.2— The FSRQs in the GASP target list.

IAU Name	Other Name	BZCAT Name	z	$E(B-V)$
0420−014	PKS 0420−01	BZQJ0423−0120	0.916	0.1258
0528+134	PKS 0528+134	BZQJ0530+1331	2.070	0.8450
0827+243	OJ 248	BZQJ0830+2410	0.939	0.0333
0836+710	4C 71.07	BZQJ0841+7053	2.218	0.0301
1156+295	4C 29.45	BZQJ1159+2914	0.729	0.0199
1226+023	3C 273	BZQJ1229+0203	0.158	0.0206
1253−055	3C 279	BZQJ1256−0547	0.536	0.0286
1510−089	PKS 1510−08	BZQJ1512−0905	0.360	0.1010
1611+343	DA 406	BZQJ1613+3412	1.397	0.0178
1633+382	4C 38.41	BZQJ1635+3808	1.814	0.0122
1641+399	3C 345	BZQJ1642+3948	0.593	0.0131
1739+522	4C 51.37	BZQJ1740+5211	1.381	0.0355
2230+114	CTA 102	BZQJ2232+1143	1.037	0.0718
2251+158	3C 454.3	BZQJ2253+1608	0.859	0.1078

a new tool to identify blazars. We searched the *WISE* All-Sky Source Catalog for the BZCAT sources. A cone search radius of 3 arcsec was found to be the best choice between having reliable identifications and completeness. Among the 1180 BL Lacs present in the BZCAT catalogue, we obtained 1122 *WISE* counterparts (95%), while we found 1608 identifications for the 1676 BZCAT FSRQS[8] (96%). All of the GASP sources have a *WISE* counterpart.

Figure 3.1 shows the colour-colour *WISE* diagram for the BZCAT blazars, separating FSRQs from BL Lac objects. We assume that Galactic extinction is negligible at *WISE* wavelengths. The points referring to the GASP sources are overplotted in colour. The GASP FSRQs cover the region where most sources cluster and the GASP BL Lacs distribute along almost the whole BL Lac sequence extending toward the elliptical galaxies location. All the GASP sources were detected in γ rays by *Fermi*-LAT (Nolan et al., 2012) and they all lie within the *WISE* Gamma-ray Strip (Massaro et al., 2012, see also D'Abrusco et al. 2012), when considering the refined analysis by D'Abrusco et al. (2013) and Massaro et al. (2013b). In the figure the position of elliptical galaxies is indicated, using the SWIRE template[9] (Polletta et al., 2007) of a 13 Gyr old elliptical galaxy for redshifts between 0 and 0.25, and that of a 5 Gyr galaxy for redshifts from 0.3 to 1. We notice that for a given galaxy age, i.e. a given stellar population, redshift variations result in a small scatter of the points, while changing the model produces a larger shift in the diagram. We also show the trace left by the SWIRE TQSO1 template, i.e. a type 1 QSO with broad emission lines in the optical spectrum and prominent torus, for redshift values in the range $z = 0$–3. Finally, the straight line is obtained from a power-law spectrum $F_\nu \propto \nu^{-\alpha}$ with spectral index $\alpha = 0$–1.5, and represents the typical non-thermal, synchrotron emission from blazar jets. The range of considered α includes both flat ($\alpha < 1$) spectra, as most BL Lac objects show, and steep ($\alpha > 1$) spectra, which characterize most FSRQs (see below). Deviation

[8] Actually, there were 1610 FSRQs *WISE* counterparts, but two sources, BZQJ0607-0834 and BZQJ0917-2131, had double identifications. For these two objects we kept only the closest *WISE* counterpart.

[9] http://www.iasf-milano.inaf.it/∼polletta/templates/ swire_templates.html

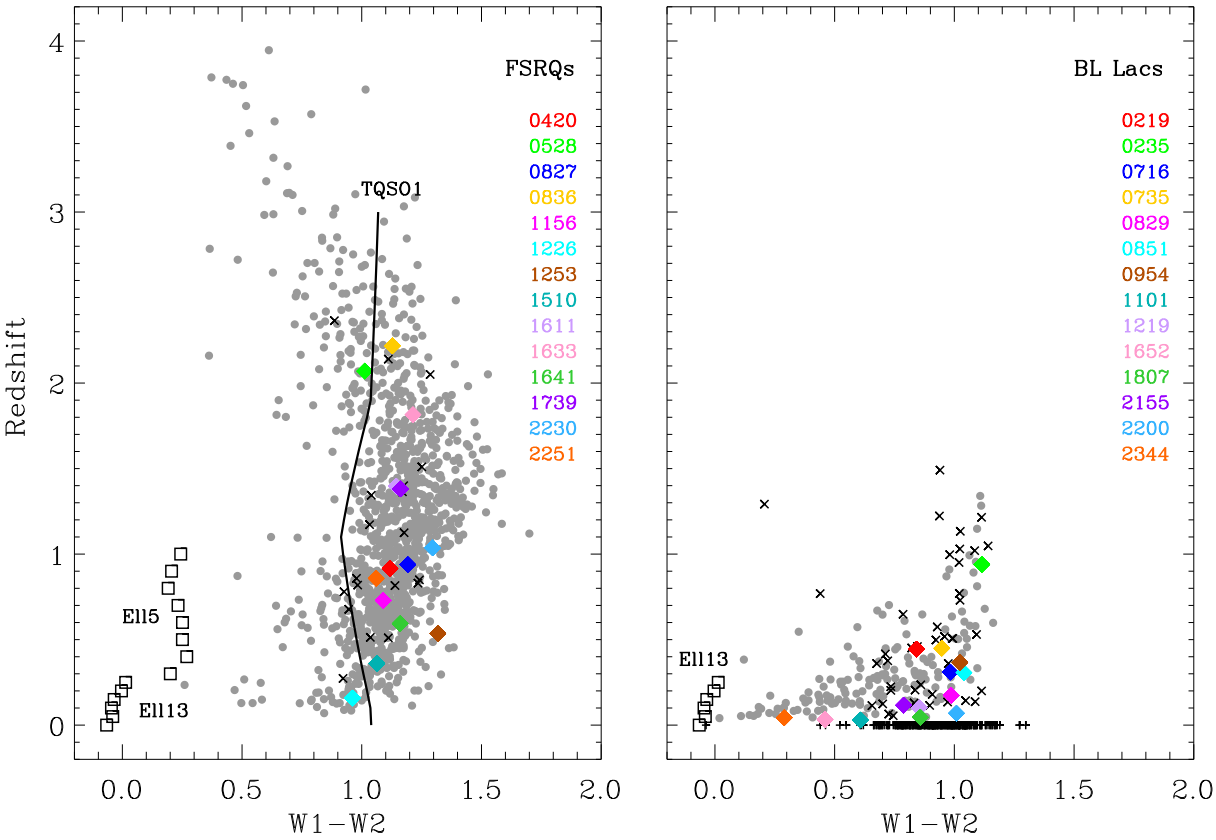

FIGURE 3.2— The redshift versus *WISE* W1-W2 colour for FSRQs (left) and BL Lacs (right). Only objects with $S/N > 3$ in all *WISE* bands were considered. Black crosses indicate sources with uncertain redshift; black plus signs those with undetermined z. The points corresponding to the 28 sources monitored by the GASP-WEBT are highlighted with coloured diamonds. The black squares in the bottom left represent the SWIRE templates of 5 and 13 Gyr old elliptical galaxies at different values of redshift. The location of Type 1 QSO spectra (TQSO1 SWIRE template) of various redshift is also plotted.

from the power-law line means that the source spectrum is not a pure synchrotron spectrum, but that either it is contaminated by other emission contributions (from host galaxy and QSO-like nucleus) or it presents a curvature in the *WISE* bands. This will be studied in depth in Sect. 3.4.

In Fig. 3.2 we plotted the redshift versus the *WISE* W1−W2 colour. We took into account new BL Lac redshift measurements by Landoni et al. (2012), Landoni et al. (2013), Sandrinelli et al. (2013), and Pita et al. (2013). The GASP FSRQs cover fairly well the strip formed by all the FSRQs, apart for the upper part, corresponding to the most distant objects. As for BL Lacs, the GASP source with higher redshift is 0235+164, but there are only few objects that are more distant, most of them with uncertain z. Here again we plotted the position of elliptical galaxies and TQSO1 spectra of different redshifts.

The same search radius of 3 arcsec was adopted to query the 2MASS catalogue for the BZCAT objects. This is the maximum radial offset between the *WISE* sources and associated 2MASS sources in the *WISE* catalogue. The 2MASS catalogue includes sources brighter

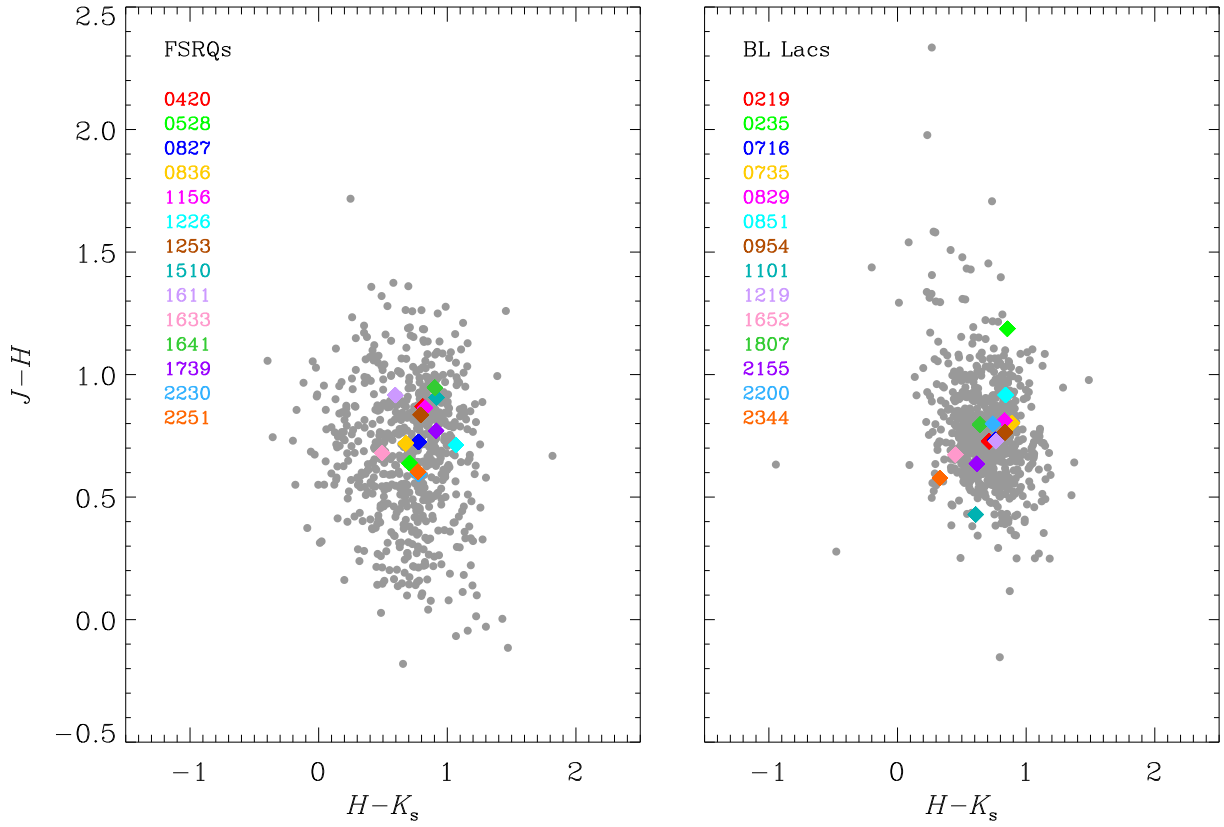

FIGURE 3.3— Colour-colour diagram built with 2MASS data for FSRQs (left) and BL Lac objects (right). The 2MASS magnitudes have been corrected for Galactic reddening according to Schlegel, Finkbeiner & Davis (1998). GASP sources are overplotted with coloured diamonds.

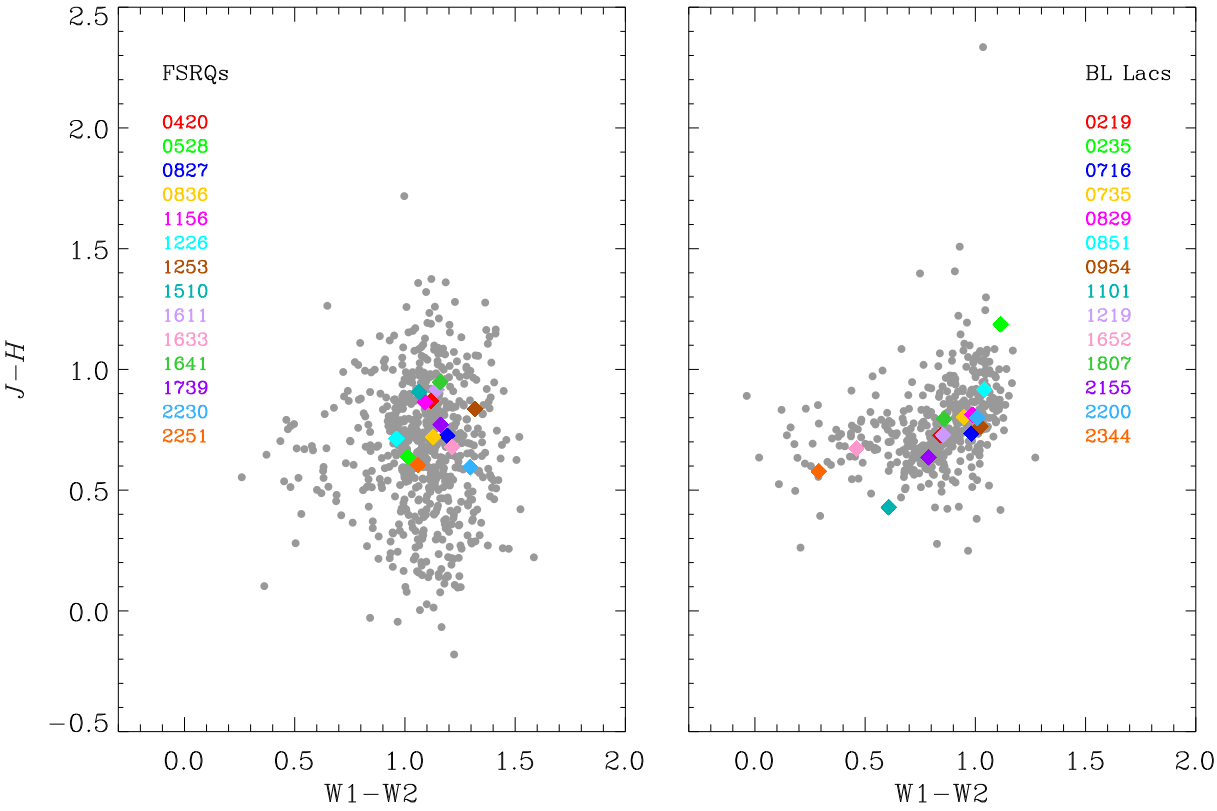

FIGURE 3.4— Colour-colour diagram built with *WISE* and 2MASS data for FSRQs (left) and BL Lac objects (right). The 2MASS magnitudes have been corrected for Galactic reddening according to Schlegel, Finkbeiner & Davis (1998). GASP sources are overplotted with coloured diamonds.

than about 1 mJy in the J, H, and K_s bands, with signal-to-noise ratio (S/N) greater than 10. We found 815 2MASS counterparts in the case of the BL Lac objects (69%), and 686 for the FSRQs (41%). All the GASP sources have a 2MASS counterpart. We corrected for the Galactic extinction according to Schlegel, Finkbeiner & Davis (1998), i.e. using the relative extinction values $A/E(B-V) = 0.902$, 0.576, and 0.367 for the J, H, and K_s bands, respectively, with $E(B-V)$ downloaded from the Galactic Dust Extinction Service at IRSA mentioned above.

Figure 3.3 shows the colour-colour diagram built with 2MASS data for both FSRQs and BL Lac objects. Combining *WISE* and 2MASS information, we obtained the diagram of Fig. 3.4. In both plots the GASP FSRQs are concentrated in the central region of the diagram, while BL Lac objects are more distributed.

It is interesting to compare our results on the 2MASS BL Lac colours with those by Chen, Fu & Gao (2005). These authors started from the Véron-Cetty & Véron (2003) catalogue and found 511 BL Lacs with 2MASS counterparts, including uncertain sources. In the $J-H$ versus $H-K$ plot, the majority of both the Chen, Fu & Gao (2005) and our sources lie in the region where both the colour indices values are in the range 0.2–1.2. However, Fig. 3.3 shows much more objects with $J-H > 1.2$, and a lack of sources in the region with $H-K$ from -0.2 to 0.2 and $J-H$ in the range 0–0.5, where instead there are several objects in the Chen, Fu & Gao (2005) plot. The latter difference in the colour distribution likely reflects the presence of misclassified objects in the Véron-Cetty & Véron (2003) catalogue.

Finally, we searched the BZCAT FSRQs and BL Lacs in the Sloan Digital Sky Survey (SDSS). To be sure that our objects photometry passed all tests to be used for science, we set the `CLEAN` flag to one in the query form. We found 765 BL Lac objects (65% of the sample) and 794 FSRQs (47%) for which clean photometric data in the u, g, r, i, and z bands are available. Among them, only 4 BL Lacs and 8 FSRQs belong to the GASP source list. In Fig. 3.5 we plot the spectral energy distribution (SED) of the BZCAT FSRQs and BL Lacs built with *WISE*, 2MASS, and SDSS data. These latter have been corrected for the Galactic extinction in the same way as for the 2MASS data, i.e. adopting the $A/E(B-V)$ values given by Schlegel, Finkbeiner & Davis (1998) (5.155, 3.793, 2.751, 2.086, and 1.479 from u to z), and $E(B-V)$ as specified above. Transformation of de-reddened magnitudes into fluxes has been done by using the specific zero-mag flux densities. To avoid very uncertain data, we plotted only objects for which *WISE* data have $S/N > 3$ and SDSS magnitudes are less than the survey limits in all bands, which are 22.0, 22.2, 22.2, 21.3, and 20.5 mag in the u, g, r, i, and z bands, respectively. The SEDs corresponding to the GASP sources are highlighted in colour. They show discontinuities between different datasets as a consequence of variability, since the observations by *WISE*, 2MASS, and SDSS were carried out at different epochs, when the sources were evidently in different brightness states. We also display average SEDs. These are within the GASP SEDs or just below them for FSRQs, while they are quite below the SEDs of the GASP BL Lacs, meaning that the GASP choice of BL Lacs is more biased towards the brightest objects than in the case of FSRQs. The average FSRQs SED shows a steep spectrum in the *WISE* bands, while it turns into a flat spectrum in the 2MASS and SDSS bands. The upturn signs the transition from a dominant synchrotron emission contribution to the "big blue bump", which is ascribed to thermal emission from the accretion disc. In contrast, the average BL Lacs SED follows the

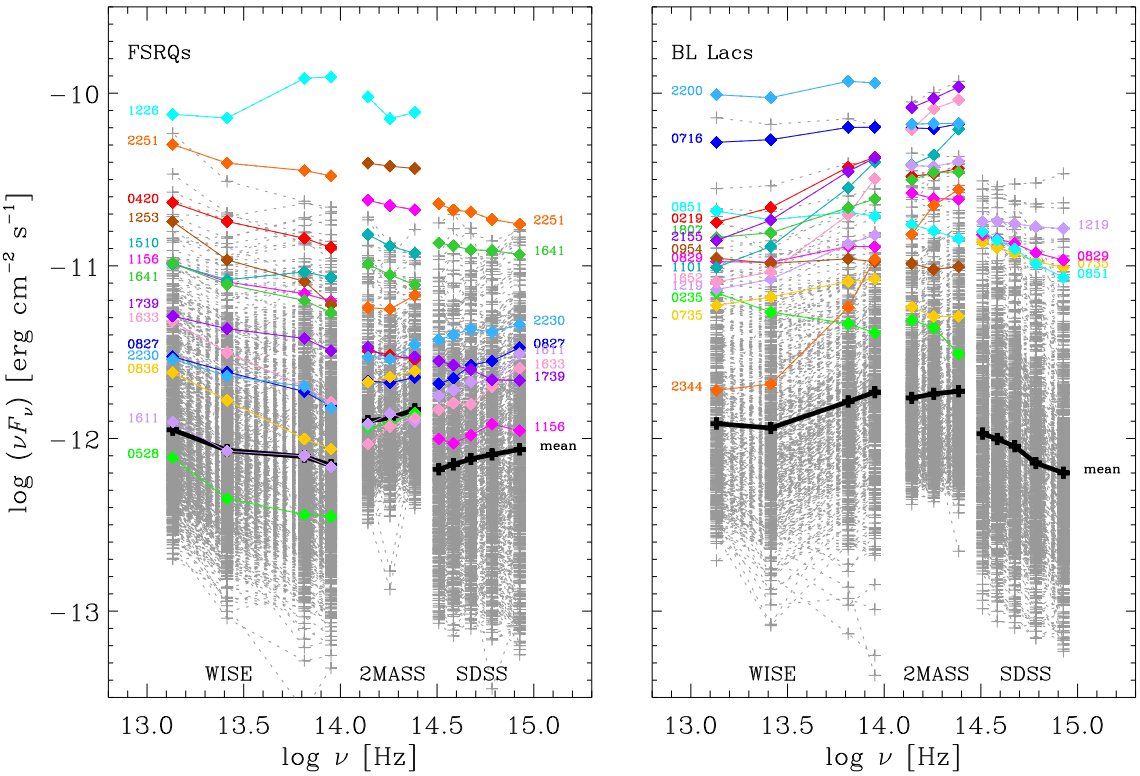

FIGURE 3.5— Spectral energy distributions of the BZCAT FSRQs (left) and BL Lac objects (right) built with infrared and optical data from *WISE*, 2MASS and SDSS. *WISE* and SDSS data are plotted only for objects with $S/N > 3$ and magnitudes brighter than the survey limits, respectively, in all bands. The 2MASS and SDSS data are corrected for the Galactic extinction according to Schlegel, Finkbeiner & Davis (1998). Mean SEDs are highlighted with black plus signs; GASP sources are overplotted with coloured diamonds.

synchrotron hump, with the peak between the 2MASS and SDSS bands.

In conclusion, the GASP sources show a variety of infrared colours, redshifts and infrared–optical SEDs, and thus form an interesting mini-sample of blazars that can be analysed in detail and that is likely representative of the bright objects.

3.2 Near-IR flux variability

Regular monitoring of the GASP sources in the near-IR bands is carried out at the Campo Imperatore (Italy) and Teide (Canary Islands, Spain) observatories.

The observations at Campo Imperatore were obtained by using the 1.1 m AZT-24 telescope and the SWIRCAM camera (D'Alessio et al., 2000). SWIRCAM is based on a Rockwell PICNIC array having 256 × 256 pixels with a size of 40 μm, that corresponds to 1.04″ on the sky. Every final image is composed from five dithered raw images after preliminary processing, that includes sky subtraction, flat-fielding and recentering[10]. Aperture photometry was made using

[10]http://www.oa-roma.inaf.it/preprocess/preprocess.html

TABLE 3.3— Mean fractional variation of the near-IR flux densities, f_i, average de-reddened colour indices $< J-H >$ and $< H-K >$ with their standard deviations (σ) and their mean fractional variations f_{J-H} and f_{H-K} for the BL Lac objects in the GASP target list.

IAU Name	f_J	f_H	f_K	$< J-H >$	$< H-K >$	f_{J-H}	f_{H-K}
0219+428	0.39	0.38	0.37	0.70 (0.04)	0.74 (0.04)	-	-
0235+164	1.50	1.44	1.39	1.07 (0.09)	0.98 (0.07)	0.07	0.05
0716+714	0.49	0.35	0.33	0.83 (0.04)	0.89 (0.04)	-	-
0735+178	0.24	0.27	0.27	0.86 (0.05)	0.83 (0.05)	0.04	0.05
0829+046	0.23	0.22	0.22	0.88 (0.03)	0.85 (0.05)	-	0.04
0851+202	0.39	0.41	0.45	0.89 (0.05)	0.91 (0.05)	0.04	0.01
0954+658	0.45	0.41	0.40	0.90 (0.04)	0.93 (0.05)	-	-
1101+384	0.27	0.26	0.27	0.77 (0.02)	0.25 (0.03)	-	-
1219+285	0.32	0.33	0.31	0.72 (0.03)	0.75 (0.05)	-	0.05
1652+398	0.01	0.01	0.01	0.81 (0.01)	0.40 (0.01)	-	-
1807+698	0.08	0.08	0.07	0.83 (0.01)	0.66 (0.04)	-	-
2155−304	0.20	0.20	0.21	0.61 (0.02)	0.80 (0.01)	-	-
2200+420	0.39	0.38	0.39	0.83 (0.04)	0.79 (0.04)	-	0.01
2344+514	0.09	0.09	0.10	0.75 (0.05)	0.33 (0.03)	0.04	-

properly calibrated field stars[11].

The observations at Teide Observatory (Canary Islands) were obtained with the 1.52 m Carlos Sanchez Telescope (TCS), using the near-infrared camera CAIN. This camera is equipped with a 256 × 256 pixels NICMOS-3 detector and it provides a scale of 1″/pixel with the wide field optics (4.2 × 4.2). Data were acquired in the three filters J, H and $K_{\rm s}$. Observations were performed using a 5-point dither pattern in order to facilitate a proper sky background subtraction. At each point, the exposure time was about 1 min, split in individual exposures of 10 s in the J filter and 6 s in the H and $K_{\rm s}$ filters to avoid saturation by sky brightness. The dither cycle was repeated twice, except for faint sources where the number of cycles was increased.

Image reduction was performed with the `caindr` package developed by Rafael Barrena-Delgado and Jose Acosta-Pulido under the IRAF environment[12]. Data reduction includes flat-fielding, sky subtraction, and the shift and combination of all frames taken in the same dither cycle. Photometric calibration was performed using a IDL routine kindly provided by P. Ábrahám (Obs. Konkoly - Hungary), which uses the 2MASS catalogue (Cutri et al., 2003). The photometric zero point for each combined image was determined by averaging the offset between the instrumental and the 2MASS magnitudes of catalogue sources within the field of view. Whenever deviant targets appear they are excluded before computing the average.

In Figs. 3.6 and 3.7 we show the near-IR light curves of the GASP BL Lacs, while in Figs. 3.8

[11] http://www.astro.spbu.ru/staff/vlar/NIRlist.html
[12] Image Reduction and Analysis Facility – http://iraf.noao.edu/

TABLE 3.4— Mean fractional variation of the near-IR flux densities, f_i, average de-reddened colour indices $< J-H >$ and $< H-K >$ with their standard deviations (σ) and their mean fractional variations f_{J-H} and f_{H-K} for the FSRQs in the GASP target list.

IAU Name	f_J	f_H	f_K	$< J-H >$	$< H-K >$	f_{J-H}	f_{H-K}
0420−014	1.00	1.01	0.89	0.88 (0.08)	0.97 (0.09)	0.07	0.07
0528+134	0.55	0.65	0.64	0.63 (0.16)	0.90 (0.09)	0.23	0.08
0827+243	0.85	0.87	0.93	0.58 (0.12)	0.89 (0.15)	0.19	0.16
0836+710	0.47	0.60	0.65	0.63 (0.13)	0.83 (0.13)	0.20	0.13
1156+295	0.73	0.68	0.69	0.88 (0.08)	0.90 (0.11)	0.08	0.11
1226+023	0.04	0.06	0.05	0.81 (0.04)	1.15 (0.04)	0.03	0.02
1253−055	0.57	0.58	0.59	0.91 (0.09)	0.94 (0.07)	0.09	0.05
1510−089	0.33	0.33	0.31	0.90 (0.06)	1.02 (0.07)	0.04	0.05
1611+343	0.24	0.23	0.32	0.85 (0.08)	0.64 (0.16)	0.08	0.23
1633+382	0.64	0.63	0.58	0.90 (0.11)	0.94 (0.07)	0.12	0.05
1641+399	0.38	0.40	0.40	0.98 (0.05)	0.94 (0.07)	0.03	0.05
1739+522	0.21	0.24	0.26	0.87 (0.09)	0.72 (0.18)	0.09	0.23
2230+114	1.12	1.27	1.25	0.59 (0.17)	0.86 (0.18)	0.28	0.20
2251+158	1.10	1.31	1.32	0.60 (0.30)	0.87 (0.18)	0.49	0.19

and 3.9 those of the GASP FSRQs are displayed. In a few cases (0219+428, 0851+202, 1226+023, and 2344+514) we found offsets due to different source calibration between the Campo Imperatore and Teide data, and corrected for them.

To quantify variability, magnitudes are converted into flux densities as explained in Sect. 3.1 and then the mean fractional variation is calculated. This is defined as:

$$f = \sqrt{\sigma^2 - \delta^2} < F >, \tag{3.1}$$

where $< F >$ is the mean flux, σ^2 the variance of the flux, and δ^2 the mean square uncertainty of the fluxes (e.g. Peterson, 2001). The advantage of this quantity is that it takes into account the effect of errors, which produce apparent variability. Tables 3 and 4 report the mean fractional variation for the GASP BL Lacs and FSRQs, respectively. For a given object, this quantity obviously depends on the considered period and on the amount of data collected. Only one BL Lac (0235+164) and 3 FSRQs (0420−014, 2230+114, and 2251+158) have $f \geq 1$, and 0235+164 is the most variable source. Notice that 0235+164 has sometimes been claimed to belong to the FSRQs (e.g. Raiteri et al., 2007; Ghisellini et al., 2011). The values of the mean fractional variation indicate that FSRQs are typically more variable than BL Lacs. Average f values for the whole BL Lac sample in each of the near-IR bands are around 0.35%, while they are $\sim$ 60% in the case of FSRQs. Moreover, in general BL Lacs are slightly more variable in the J band and FSRQs in the K band. This recalls what happens in the optical domain, where BL Lacs are generally more variable in the blue than in the red, while for FSRQs the opposite is true. The smaller variability of FSRQs toward the blue is a clue in favour of an additional

emission component, i.e. thermal emission from the disc (showing as a "big blue bump" in the SED) and broad line region (BLR, producing a "little blue bump" in the SED). Indeed, the contribution from this "blue" component is expected to extend into the near-IR band, behaving as a base-level under which the flux cannot fall, and affecting the J flux density more than the K one.

3.3 Near-IR colour variability

To analyse the near-infrared spectral variability, we first binned the J, H, and K data of each observatory acquired within 30 minutes and then coupled the binned data with error less than 0.1 mag to build $J-H$ and $H-K$ colour indices. Figures 3.10 and 3.11 show the colour variability of the GASP sources in the $J-H$ versus $H-K$ plot, compared to the 2MASS value (see Fig. 3.3). Correction for Galactic extinction has been performed as explained in Sect. 3.1. In Tables 3 and 4 we report colour indices average values, their standard deviations and mean fractional variations (see Eq. 1). The latter are often imaginary numbers for BL Lac objects, which means that the corresponding colour index variability is dominated by noise. When this is not the case, the value is however low, in the range 1–7%. This is also true for 0235+164, the source with the largest flux variability, which nonetheless is the BL Lac showing the most noticeable spectral changes. In general, larger near-IR spectral variability characterises FSRQs because of the interplay between synchrotron and quasar-like emission components, the latter including contributions from the accretion disc, broad line region, and torus (see Sect. 3.4). Exceptions are 3C 273, PKS 1510−089, and 3C 345. The sources exhibiting the largest colour indices changes are 3C 454.3 and CTA 102.

By looking at Figs. 3.10 and 3.11 one can see that sometimes the 2MASS value is outside the region where most of our points collect. This may partly reflect cross-calibration problems, but may also indicate an even larger variability.

Two sources show clear trends in the colour-colour diagram. The anticorrelation between $J-H$ and $H-K$ in the 3C 273 plot suggests that there is a spectral break in the H band. In contrast, a correlation is visible in the colour-colour plot of 3C 454.3, where the lower-left group of points refer to the source faint state from 2011 onward, while the upper-right group of points come from the bright state before 2011. The colour-colour plot then tell us that the near-IR spectrum is bluer in faint states and redder in bright states. A redder-when-brighter trend has already been noticed when analysing the optical spectrum of this source (e.g. Villata et al., 2006; Raiteri et al., 2008). These spectral behaviours will become clearer in the next section, where spectral energy distributions are presented and interpreted in terms of different emission contributions.

3.4 Infrared-to-optical spectral energy distribution

In this section we present the infrared-to-optical spectral energy distributions of the GASP sources. They are built with the survey data already presented in Sect. 3.1 (*WISE*, 2MASS, SDSS), literature data, and the results of our near-IR monitoring at Campo Imperatore and Teide. Notice that a *WISE* single exposure source database is available, containing multiple observations of the GASP sources. However, the use of this database is discouraged because

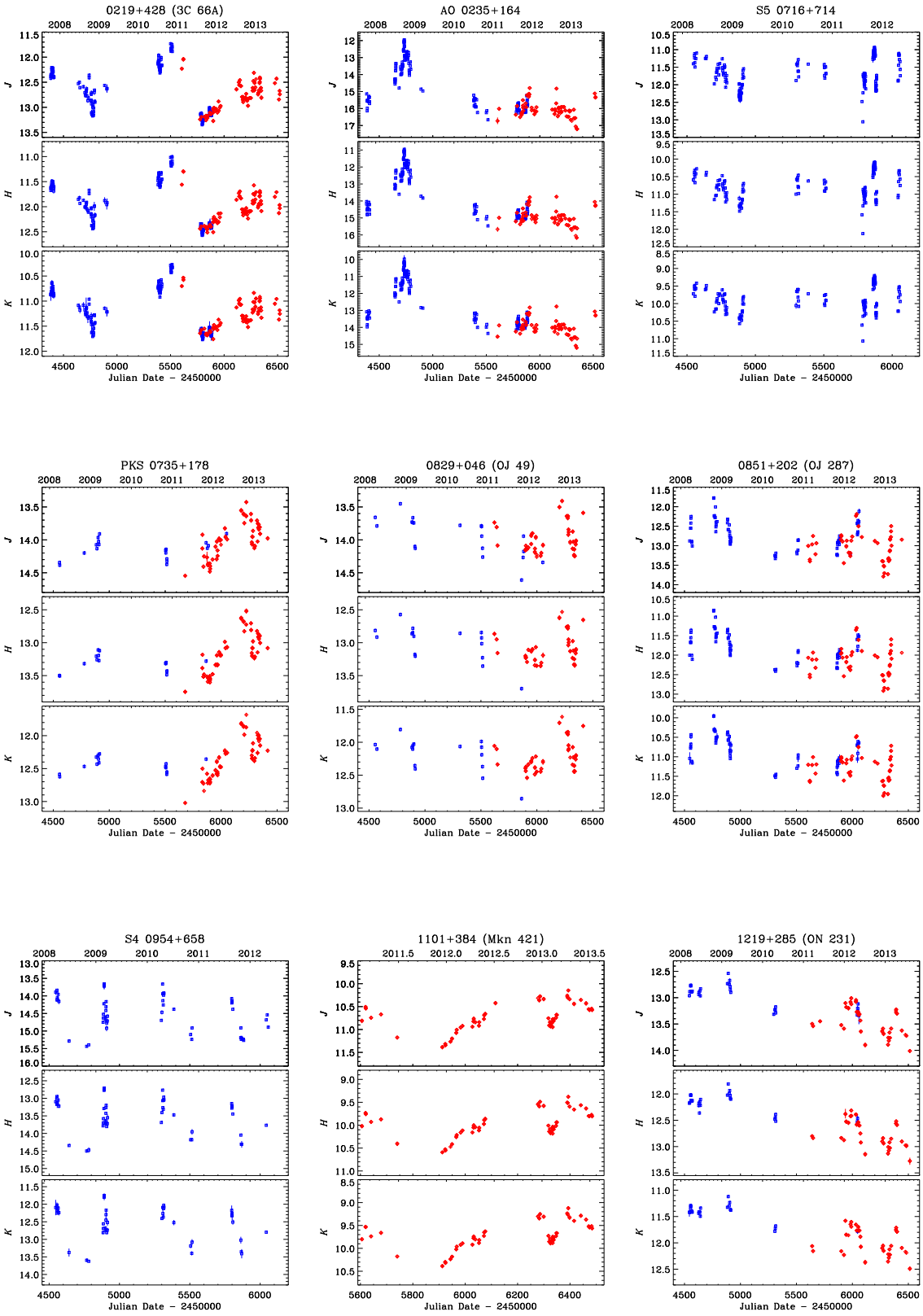

FIGURE 3.6— Near-IR light curves of the GASP-WEBT BL Lac objects. Blue squares indicate data from Campo Imperatore, red diamonds those from Teide.

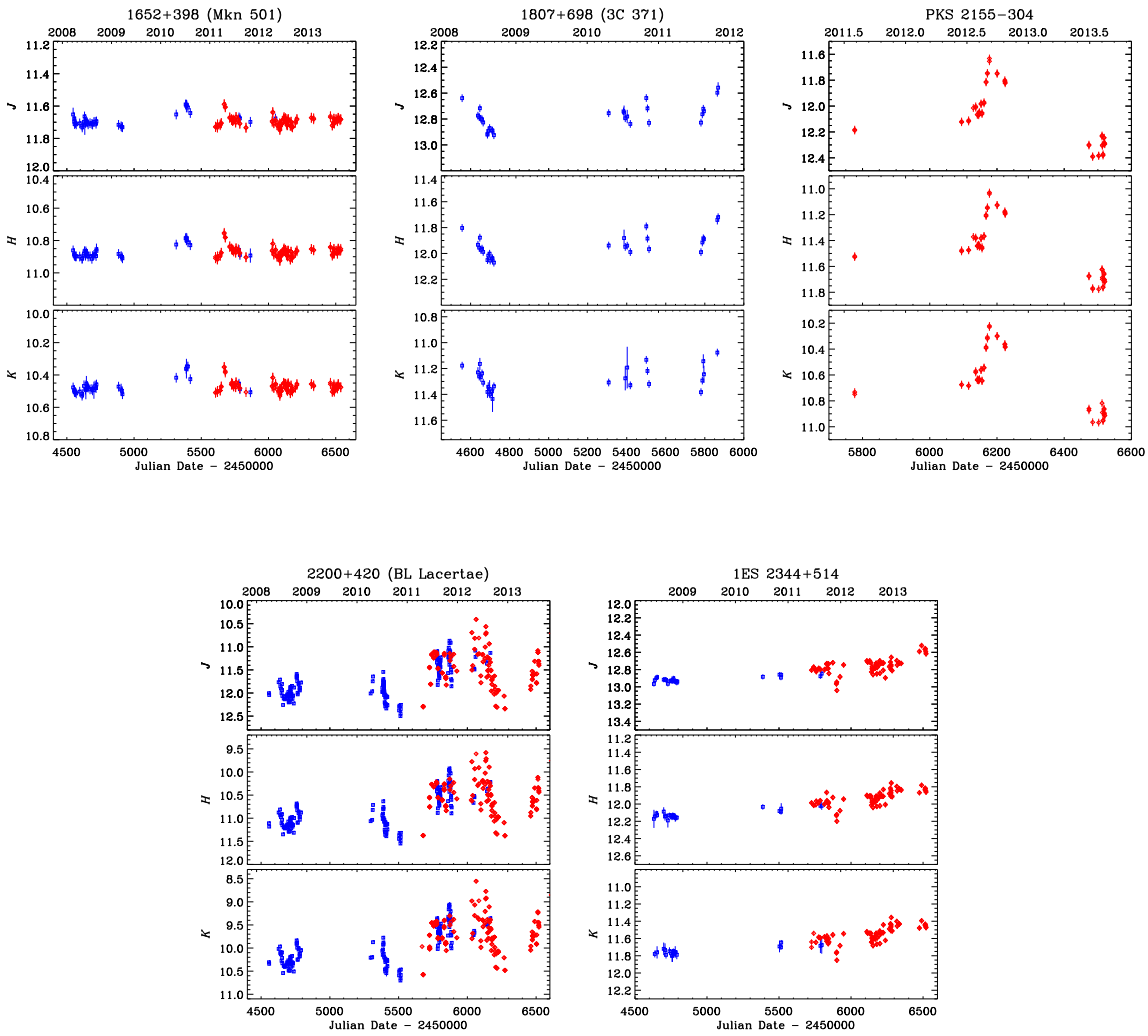

FIGURE 3.7— Near-IR light curves of the GASP-WEBT BL Lac objects. Blue squares indicate data from Campo Imperatore, red diamonds those from Teide.

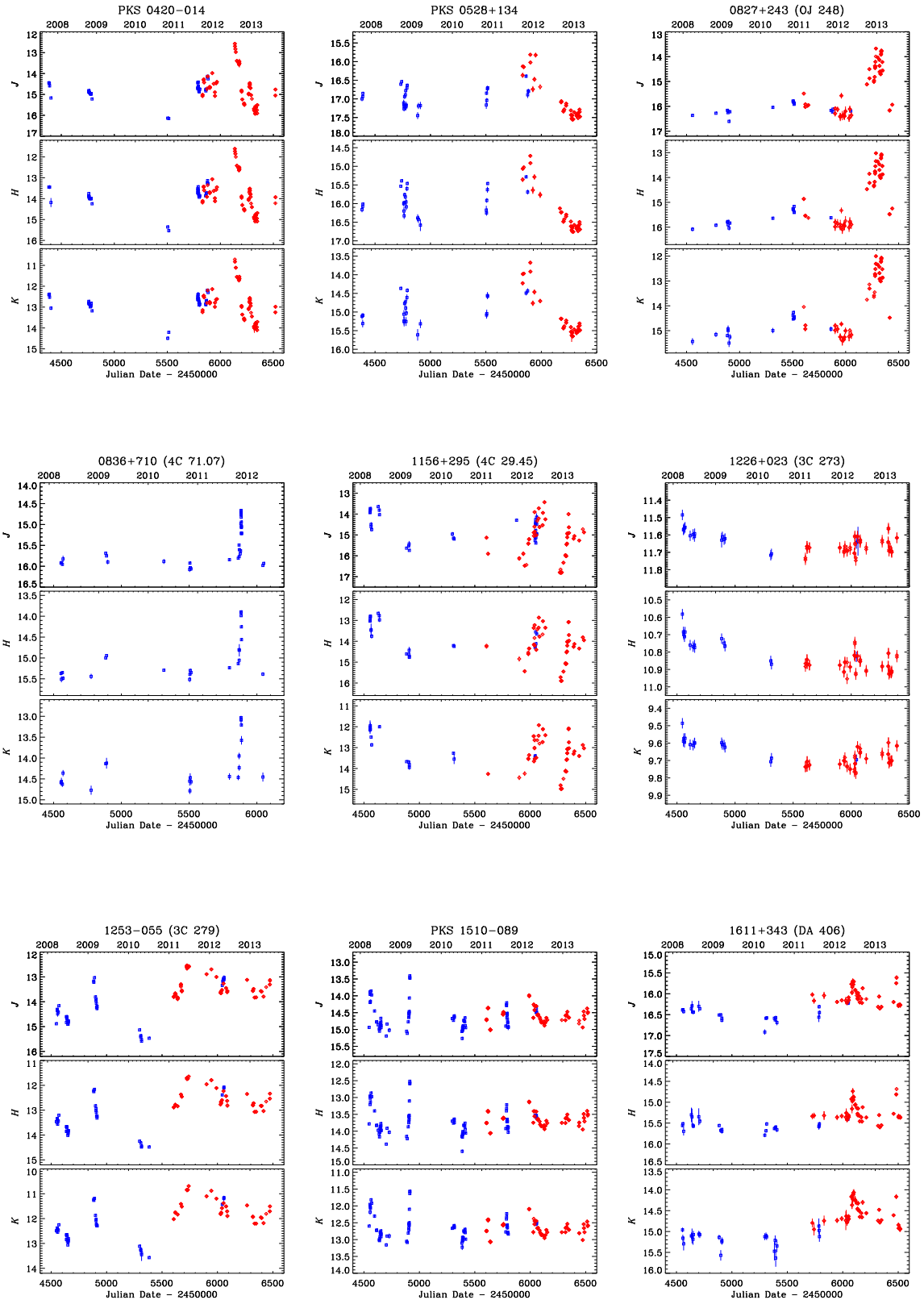

FIGURE 3.8— Near-IR light curves of the GASP-WEBT FSRQs. Blue squares indicate data from Campo Imperatore, red diamonds those from Teide.

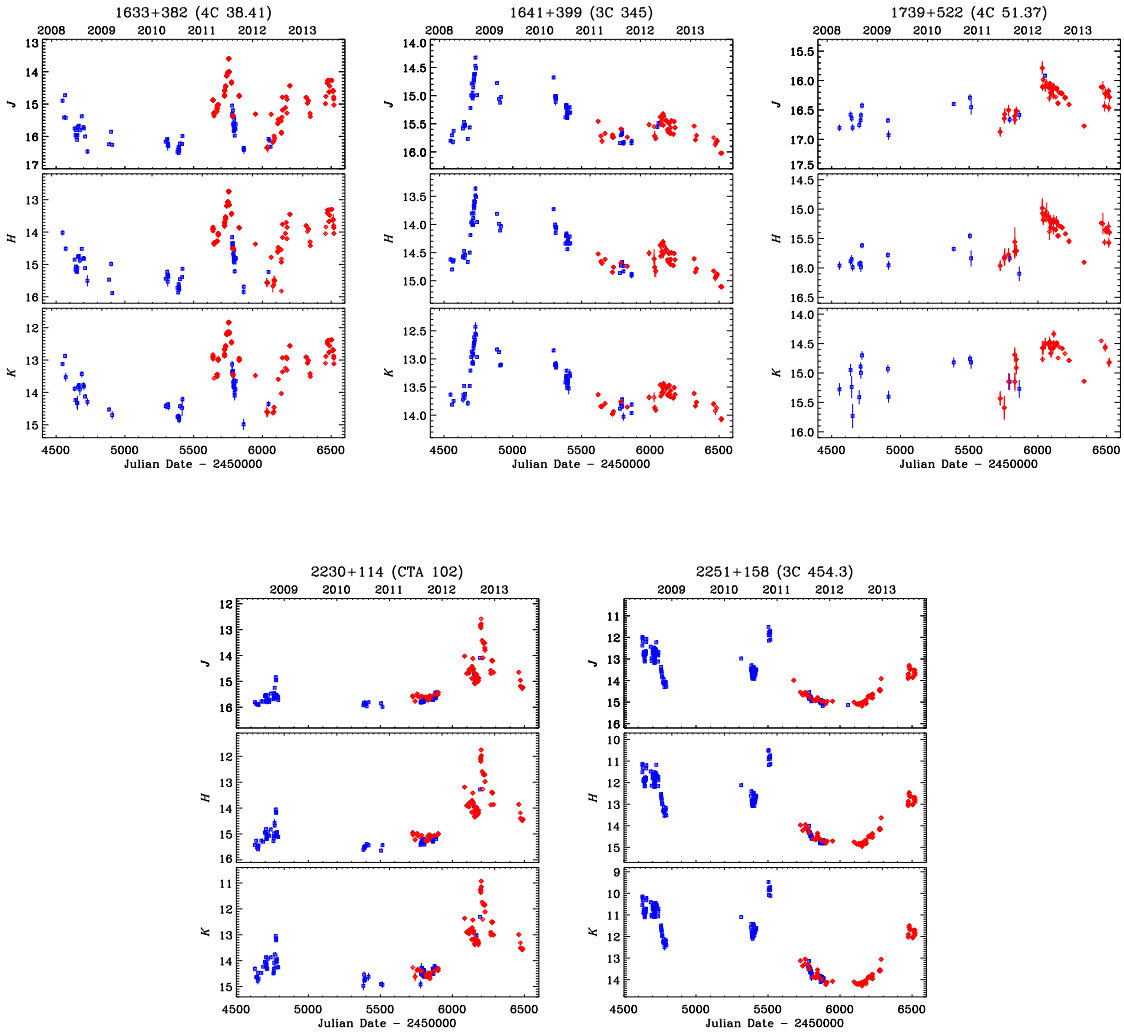

FIGURE 3.9— Near-IR light curves of the GASP-WEBT FSRQs. Blue squares indicate data from Campo Imperatore, red diamonds those from Teide.

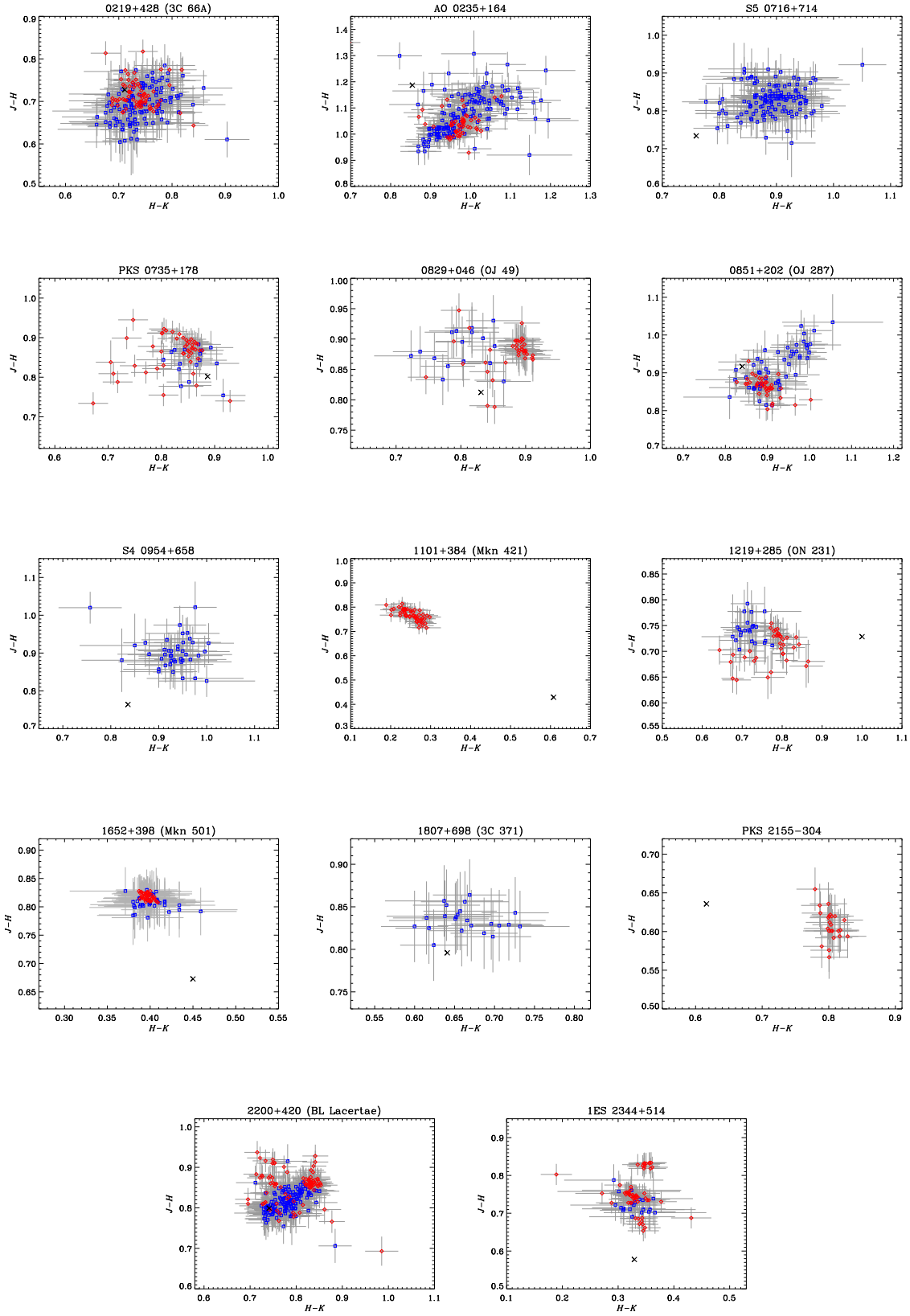

FIGURE 3.10— Near-IR colour-colour plots for the GASP-WEBT BL Lac objects. Data have been corrected for Galactic extinction. Blue squares indicate data from Campo Imperatore, red diamonds those from Teide. The black cross indicates the point obtained from the 2MASS catalogue.

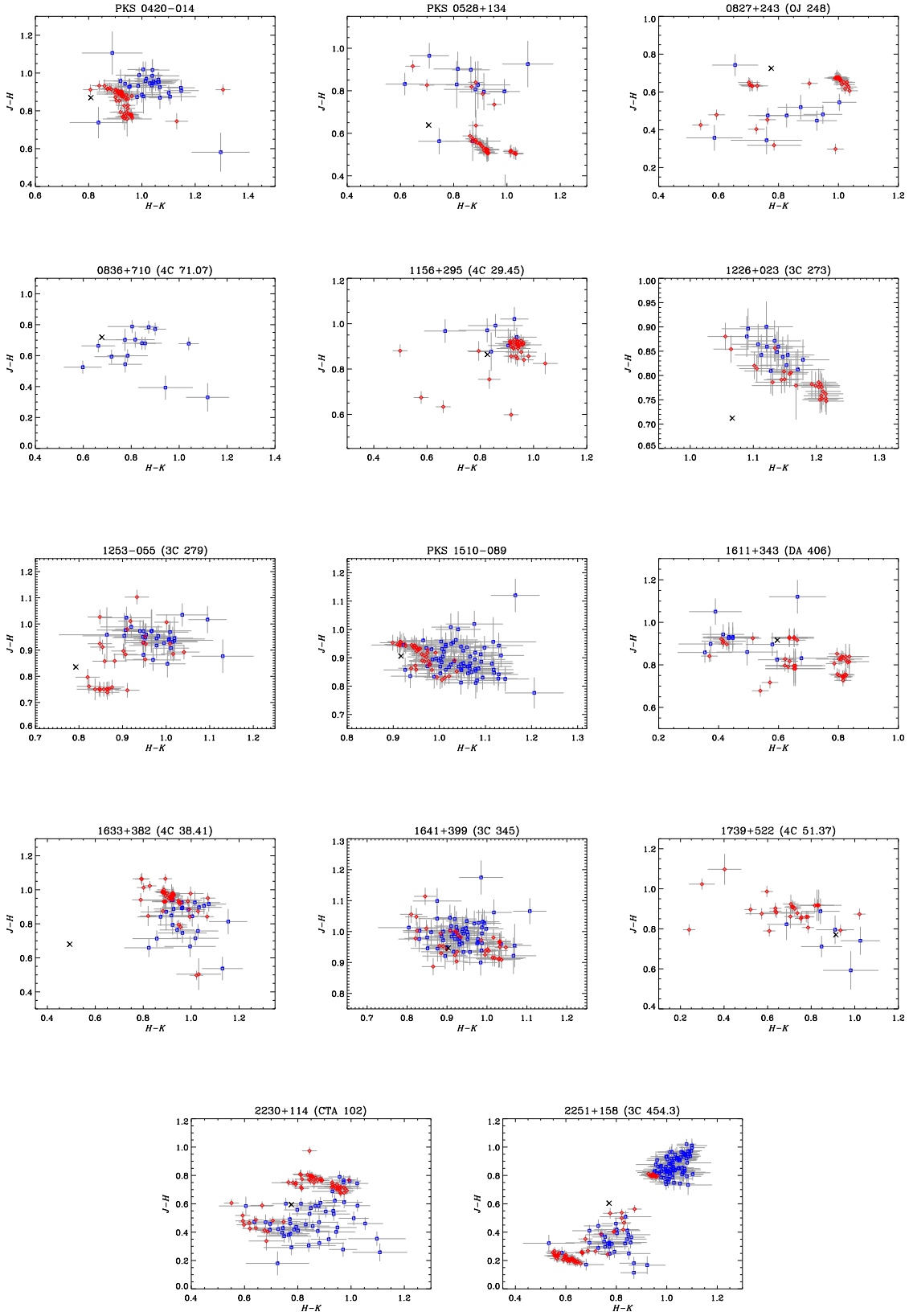

FIGURE 3.11— As in Fig. 3.10 but for the GASP-WEBT FSRQs.

it includes all single exposure images regardless of their quality[13], so we did not consider it. From the literature we extracted data from the Infrared Astronomical Satellite (*IRAS*, Impey & Neugebauer, 1988), the Infrared Space Observatory (*ISO*, Haas et al., 2004), and the *Spitzer* satellite (Malmrose et al., 2011; Ogle et al., 2011). *Herschel* data for 3C 454.3 are from Wehrle et al. (2012). For 3C 273 and 3C 371 we used the optical spectra acquired at the Telescopio Nazionale Galileo (TNG) by Buttiglione et al. (2009), which are available on the NASA/IPAC Extragalactic Database (NED)[14]. In a few cases we reported SEDs from papers involving data from the GASP-WEBT collaboration for a more accurate modelling: D'Ammando et al. (2011) for PKS 1510-089; Raiteri et al. (2012) for 4C 38.41, Raiteri et al. (2011) for 3C 454.3.

Although in general the SEDs do not contain simultaneous data, they can help us understand what are the photons sources intervening in this frequency range. In Figs. 3.12 and 3.13 we show the SEDs together with model fits that take into account the possible emission contributions:

- synchrotron radiation from the jet, which is modelled as a log-parabola following Massaro et al. (2004),

$$\log[\nu F(\nu)] = \log[\nu_{\rm p} F(\nu_{\rm p})] - b\,(\log\nu - \log\nu_{\rm p})^2, \tag{3.2}$$

  where $\nu_{\rm p}$ is the frequency of the synchrotron peak $\nu_{\rm p}F(\nu_{\rm p})$;

- host galaxy emission, for which we consider the SWIRE template of a 13 Gyr old elliptical galaxy;

- QSO-like nuclear contribution from accretion disc, broad line region, and dust torus, all included in the QSO1 SWIRE templates, i.e. templates of QSO with broad emission lines;

- thermal radiation from a black body to simulate dust signatures in the infrared or to enhance the accretion disc flux in FSRQs.

In the plots presented for BL Lac objects in Fig. 3.12, sometimes catalogue data are shifted in νF_ν (the shift is marked by arrows) in order to simulate simultaneous SEDs that can ease the modelling task. Although this is not strictly correct because the spectral shape may change with flux, it is justified by the small spectral variability that we noticed in Sect. 3.3 for BL Lac objects.

Fits to the SEDs of BL Lac objects require a synchrotron emission, plus the contribution of a host galaxy for the nearest objects. This is dominant in the near-IR in the cases of Mkn 501 and 1ES 2344+514, and it is very important for Mkn 421 and 3C 371. For only two BL Lacs (3C 66A and Mkn 421) the far-infrared data from *IRAS* suggest the presence of dust, as already noticed by Impey & Neugebauer (1988).

In general, the FSRQs SEDs need a synchrotron plus a QSO-like emission contribution due to accretion disc, broad line region, and torus. There are three QSO1 templates in the SWIRE database. We first used TQSO1 because it shows a prominent Hα line, which is known to be present in the spectra of our objects. However, its high IR/optical flux ratio (rest frame) appears

[13] http://wise2.ipac.caltech.edu/docs/release/allsky/expsup
[14] http://ned.ipac.caltech.edu

inadequate to model some FSRQs SEDs, so we built a composite QSO1 template, combining the higher-frequency part of TQSO1, i.e. its disc plus BLR emission, with the lower-frequency part of BQSO1, representing a fainter torus emission. Moreover, in some FSRQs a brighter disc is required, which we obtained by adding a black-body component to the QSO1 template. In the following we comment on single source features.

3.4.1 BL Lac objects

0219+428

The model fit indicates that the synchrotron peak falls at optical frequencies. As already noticed by Impey & Neugebauer (1988), there is good evidence for thermal dust emission, which we fitted with a blackbody spectrum with temperature of ~ 41 K.

0235+164

This is the farthest among the GASP-WEBT BL Lac objects and has often revealed an FSRQ-like behaviour (e.g. Raiteri et al., 2007; Ghisellini et al., 2011). As discussed in Sect. 3.3, notwithstanding the strong variability in the near-IR, the spectral slope does not change much. There is no hint of a J-band flux excess due to the contribution of the Hα emission line even in the faintest states. This means that BLR emission is undetected in our observations. Data are compatible with a shift of the synchrotron peak toward higher energies when the flux increases, as shown by the model fits.

0716+714

The near-IR data from the GASP indicate a steep spectrum, which appears steeper in faint states (see also Villata et al., 2008). In contrast, the 2MASS spectrum is flat. *IRAS* data likely belong to a fainter state.

0735+178

By shifting in νF_ν the same log-parabola model, we obtained reasonable fits of two different brightness states traced by SDSS and *WISE* data, respectively.

0829+046

The model fit accounts for a bright state marked by SDSS, 2MASS, and the lowest *IRAS* data points.

0851+202

The lower model fit reproduces the *WISE* and 2MASS SED and its shape also agrees with the SDSS spectrum. The upper model is obtained by shifting vertically the previous one and goes through the scattered *IRAS* data.

0954+658

As in the case of 0716+714, the near-IR data from the GASP show a steep spectrum, in contrast with the 2MASS spectral slope.

1101+384

This is an HBL, whose synchrotron peak lies in the X-ray band, with impressive frequency shifts (Pian et al., 1998). According to Nilsson et al. (2007), the host galaxy has a magnitude $R = 13.18 \pm 0.05$ and contributes up to ~ 10 mJy (for a $10''$ aperture radius and good seeing conditions) to the source photometry. The 2MASS data are from the All-Sky Extended Source Image Server and show a faint state of the source. An infrared excess is visible in the *IRAS* data suggesting thermal emission from dust, as pointed out by Impey & Neugebauer (1988). We then interpreted the SED as a superposition of a jet spectrum, host galaxy contribution, and a black-body dust component with temperature of about 23 K. The model fit presented in Fig. 3.12 goes through the 2MASS and *IRAS* data.

1219+285

The *Spitzer* data, from Malmrose et al. (2011), were acquired in June–July 2007 (plus signs) and January 2008 (crosses); observations with the different instruments (IRS, IRAC, and MIPS) are not simultaneous and this explains the discontinuities of the spectra. The model fit peaks in the z band.

1652+398

This is another HBL, whose near-IR–optical spectrum shows a strong host galaxy signature. The host brightness is $R = 11.92 \pm 0.06$ (Nilsson et al., 2007); its contribution in Fig. 3.12 is ~ 12 mJy, in agreement with the contaminating flux estimate within an aperture radius of 7.5 arcsec.

1807+698

In Fig. 3.12 data from the Infrared Space Observatory (*ISO*) by Haas et al. (2004) and the spectrum from Buttiglione et al. (2009) are also included. The model fit accounts for the *WISE*

and faintest *IRAS* and *ISO* data. It requires an important contribution from the host galaxy.

2155−304

This is the most southern among the GASP sources. The synchrotron peak of the model fit falls in the UV.

2200+420

This is one of the most studied sources by the GASP-WEBT (see e.g. Villata et al., 2002; Raiteri et al., 2013, and references therein). The host galaxy has $R = 15.5 \pm 0.02$ (Scarpa et al., 2000), and affects the source photometry in the near-IR and optical bands, especially in faint states.

2344+514

This is the third HBL in the GASP sample. Its near-IR–optical spectrum is dominated by the host galaxy, whose brightness is $R = 13.90 \pm 0.06$ (Nilsson et al., 2007). In Fig. 3.12 we show a fit to the faint state traced by the 2MASS data. The jet contribution is superposed to a host galaxy contribution corresponding to the contaminating flux entering an aperture radius of 3 arcsec when the FWHM is 3 arcsec.

3.4.2 Flat spectrum radio quasars

0420−014

The near-IR data from the GASP indicate a steep spectrum, with a flux excess in J band during faint states. Indeed, the source redshift implies a contribution from the Hα emission line in this band, as shown by the SWIRE TQSO1 template. The lack of medium or far-infrared data in a low state prevents us to derive information on the torus emission.

0528+134

The near-IR spectra traced by both 2MASS and GASP data in faint states reveal a concave shape, suggesting the transition from a spectrum dominated by jet emission to a spectrum dominated by QSO-like emission. The Hα and Hβ emission lines affect the K and H band fluxes, respectively. Modelling the near-IR spectrum with a log-parabola plus the SWIRE TQSO1 template would overproduce the mid-infrared flux detected by *WISE* because of the prominent infrared contribution from the dust torus. This implies that the IR/optical flux ratio of the QSO-like contribution in this source must be smaller. We thus combined the disc+BLR component of the TQSO1 template at $\lambda < 11000$ Å (rest frame) with the torus component of the

BQSO1 template at $\lambda \geq 11000$ Å. The result is shown in Fig. 3.13 as a grey solid line. However, this composite template cannot explain the curvature of the near-IR spectrum at intermediate flux levels, which requires a brighter disc. We thus added a black-body component (grey dashed line in Fig. 3.13) to the composite template to obtain a final QSO-like contribution (blue solid line) that, once added to the jet emission (dot-dashed blue line), can produce a reasonable fit (black solid line) to the observing data. This implies a softening of the optical spectrum with increasing flux, confirming the guess by Palma et al. (2011).

0827+243

As in the 0528+134 case, the signature of a QSO-like emission contribution is already evident in the near-IR spectrum. In particular, the J-band excess is due to the contribution of the broad Hα emission line, while the Hβ line enters the SDSS z band, and the Mg II and Fe lines, giving rise to the little blue bump, contribute to the flux between the r and g bands. The composite QSO1 template explains the spectral slope of the faintest NIR data points. The model presented in Fig. 3.13 reproduces a brightness state traced by the 2MASS and SDSS data; it requires, besides the non-thermal contribution, an enhanced disc contribution, which was obtained, as in the case of 0528+134, by adding a black-body component to the QSO1 composite template.

0836+710

This is the farthest FSRQs in the GASP sample. The Hα line contributes to the K band, and the Hβ line enters the H band. Also in this case the near-infrared data suggest that the accretion disc may be brighter than predicted by the QSO1 template.

1156+295

Emission from the QSO-like component is not prominent: it appears in the SDSS spectrum, which shows the clear contribution of the Mg II line in the g band. Figure 3.13 displays a possible fit to the source SED at the SDSS and *IRAS* brightness level.

1226+023

The SED of 3C 273 in the infrared–optical band is known to be complex, and various authors have proposed interpretations in terms of synchrotron plus various dust components (see e.g. Türler et al., 2006) or dust plus various synchrotron contributions (see e.g. Soldi et al., 2008). The model fit we show in Fig. 3.13 includes a log-parabola synchrotron component (dot-dashed blue line) superimposed to a QSO-like emission (solid blue line) obtained from the composite QSO1 template (solid grey line), with enhanced disc (obtained by adding the dashed grey black body to the template) and enhanced dust around the W1 *WISE* band (obtained by adding the dotted grey black body). This latter component is responsible for the spectral break that causes the anticorrelation between $J - H$ and $H - K$ noticed in the previous section. The brightest

state traced by the *IRAS* data can be reproduced by increasing the jet flux. Notice that the 2MASS J band flux is underproduced by the model, but the spectral shape of the GASP data applied to the 2MASS points would suggest a lower value. We plotted the optical spectrum (red continuous line) from Buttiglione et al. (2009) to help us model the disc emission.

1253−055

The near-IR spectrum of 3C 279 remains steep even in faint states, so that the presence of a QSO-like emission contribution cannot be inferred. However, evidence for thermal emission was found by Pian et al. (1999) when analysing UV data of the source at a minimum brightness level.

1510−089

This source is know to present noticeable spectral variations in the near-IR–optical band (e.g. D'Ammando et al., 2011). Spectral variability is also suggested from the data points in Fig. 3.13, including observations from *Spitzer* (plus and cross symbols, Malmrose et al., 2011). To help SED modelling, in the figure we reported the faintest SED by D'Ammando et al. (2011), built with near-IR and optical data from the GASP (red dots), and optical–UV data from *Swift* (red empty circles) acquired in March 2008. Two model fits are then presented in the figure: one passing through the March 2008 spectrum, requiring a synchrotron peak at about $\log \nu = 13$, while the other one reproduces a higher state involving 2MASS data, with the synchrotron peak shifted at a higher energy, in agreement with D'Ammando et al. (2011).

1611+343

The shape of the near-IR spectrum is explained by the contributions from the Hα and Hβ lines to the H and J fluxes, respectively. The model fit displayed in Fig. 3.13 reproduces reasonably well the shape of the SDSS optical spectrum. The peak of the disc emission falls in the u band, which receives a contribution from the C IV] line. Mg II and Fe lines affect the r flux.

1633+382

A big observing effort on this source has recently been carried out by the GASP-WEBT; the results have been published by Raiteri et al. (2012). In Fig. 3.13 we display their faintest near-IR–UV SED, which was obtained in 2010 April (JD = 2455296). Red dots represent ground-based data, red empty circles are from the UVOT instrument onboard *Swift*[15]. The optical spectrum shows a brightness level similar to that of the SDSS. The observed flux in u, b, and i bands is enhanced by the contribution from the Lyα, C IV], and Mg II lines, respectively. The very hard near-IR spectrum traced by the 2MASS data points is not confirmed by the GASP data (neither those presented in this paper, nor those published in Raiteri et al. 2012), which indicate a higher flux in the K band. The model fit shown in Fig. 3.13 satisfactorily

[15]We enhanced the UVOT v-band flux by 10% to account for calibration problems (see Raiteri et al., 2012).

reproduces the *WISE* spectrum as well as the near-IR–optical spectrum traced by the SDSS and 2010 April data, with a QSO-like component in agreement with the $R = 17.85$ estimate given in Raiteri et al. (2012).

1641+399

The near-IR spectrum always maintains a steep slope, showing no hints of QSO-like emission. The SDSS data points suggest a spectral flattening with increasing optical flux, which is not easy to explain.

1739+522

The GASP observations were done during a low brightness state and draw a near-IR spectrum that reveals flux contributions from the Hα and Hβ lines in the H and J bands, respectively. The lack of a flux excess in the H band in the 2MASS data implies that the QSO-like component becomes negligible at that flux level.

2230+114

Marginal evidence for thermal emission was found by Impey & Neugebauer (1988) in *IRAS* data and tentative detection of dust was reported by Malmrose et al. (2011) analysing *Spitzer* data. *Spitzer* observed the source in two epochs: 2007 June–July (crosses in Fig. 3.13), and 2007 December – 2008 January (plus signs). Some of these data are affected by large errors. The model fit presented in Fig. 3.13 aims at reproducing a high brightness state as traced by *IRAS*, *Spitzer*, and SDSS data points. The excess flux in J band can be accounted for by the Hα line flux contribution.

2251+158

For this very famous blazar, many infrared data are available, as shown in Fig. 3.13. In particular, *ISO* observed the source in two epochs: 1996 December 6 (red circles) and 1997 December 18 (grey circles). According to Haas et al. (2004), these data may reveal a thermal dust bump, which however is not confirmed by the *IRAS* data. *Spitzer* spectra are from Ogle et al. (2011); the bright state was observed in 2005 July, while the low state was observed in 2006 December. Data from the IRAC detector are plotted as plus signs, those from IRS as crosses; the two instruments were not pointing at the source at the same time. Observations by *Herschel* on 2010 November 30 – December 1 and 2011 January 8 (Wehrle et al., 2012) are shown as red stars. To better characterise the interplay between the jet and QSO-like emission, we also plotted three infrared-to-UV SEDs (small filled and empty red circles) taken from Raiteri et al. (2011). The highest and intermediate SEDs were built with GASP-WEBT and *Swift* data acquired during a multifrequency campaign on this source; the lowest SED is originally from Neugebauer et al. (1979). The QSO-like emission signature is best visible in this faint state,

where the flux excess in the J/UV$m2$ bands is the signature of the Hα/Lyα broad emission line (see also Raiteri et al., 2008), and the spectral curvature in the optical band is due to the little blue bump. The models displayed in Fig. 3.13 show possible fits to the SEDs, where a jet emission component is superimposed to a QSO-like contribution with enhanced disc emission.

Conclusions

In this chapter we have investigated the near-IR properties of blazars. The *WISE* and 2MASS catalogues allow us to study the statistical properties of the whole class and in particular to investigate the differences between the two blazar subtypes of FSRQs and BL Lac objects. The addition of the SDSS database makes it possible to complete the information on blazar SEDs around the peak of the synchrotron emission component.

However, blazars are characterised by strong variability at all wavelengths and a deeper understanding of the blazar phenomenon can be achieved only through long-term monitoring, which is possible only for a limited number of sources.

We have thus considered the 28 blazars (14 FSRQs and 14 BL Lac objects) that belong to the target list of the GASP project of the WEBT, and for which continuous monitoring was performed since the project birth in 2007. Data in the near-IR come from the Campo Imperatore and Teide observatories.

Among the blazars in the *WISE*, 2MASS, and SDSS catalogues, the GASP sources are well distributed in infrared colours and redshifts, but generally have high infrared–optical fluxes, so they represent a mini-sample of bright blazars.

We have shown JHK light curves of these objects, revealing noticeable variability for most of them. In average, the mean fractional flux variation is greater for FSRQs than for BL Lac objects, with the notable exception of AO 0235+164, which was found to be the most variable object in the considered period. Indeed, this blazar has often shown a behaviour more similar to FSRQs than to BL Lacs. We have compared variability in the three near-IR bands: while in general the BL Lacs show more variability at higher frequency, the reverse is true for FSRQs. This is the consequence of the different emission components overlapping in this band. Colour variability is very small in BL Lac objects, not exceeding a few percent. The nearly achromaticity of the near-IR emission of BL Lacs is a characteristic of the dominant synchrotron jet emission. In contrast, the larger spectral changes exhibited by FSRQs are due to the overlapping between synchrotron and quasar-like emission components.

We have built infrared SEDs of these sources, including the results of the GASP-WEBT near-IR monitoring plus archive and literature data from *WISE*, 2MASS, *IRAS*, *ISO*, *Spitzer*, and *Herschel*, as well as optical information from the SDSS and literature. Although these SEDs do not contain simultaneous data, as would be desirable for these variable objects, they can nevertheless help us understand the interplay among the various emission contributions: synchrotron radiation from the jet, QSO-like emission including torus, disc, and BLR radiation, and radiation from the host galaxy. We have modelled the synchrotron emission with a

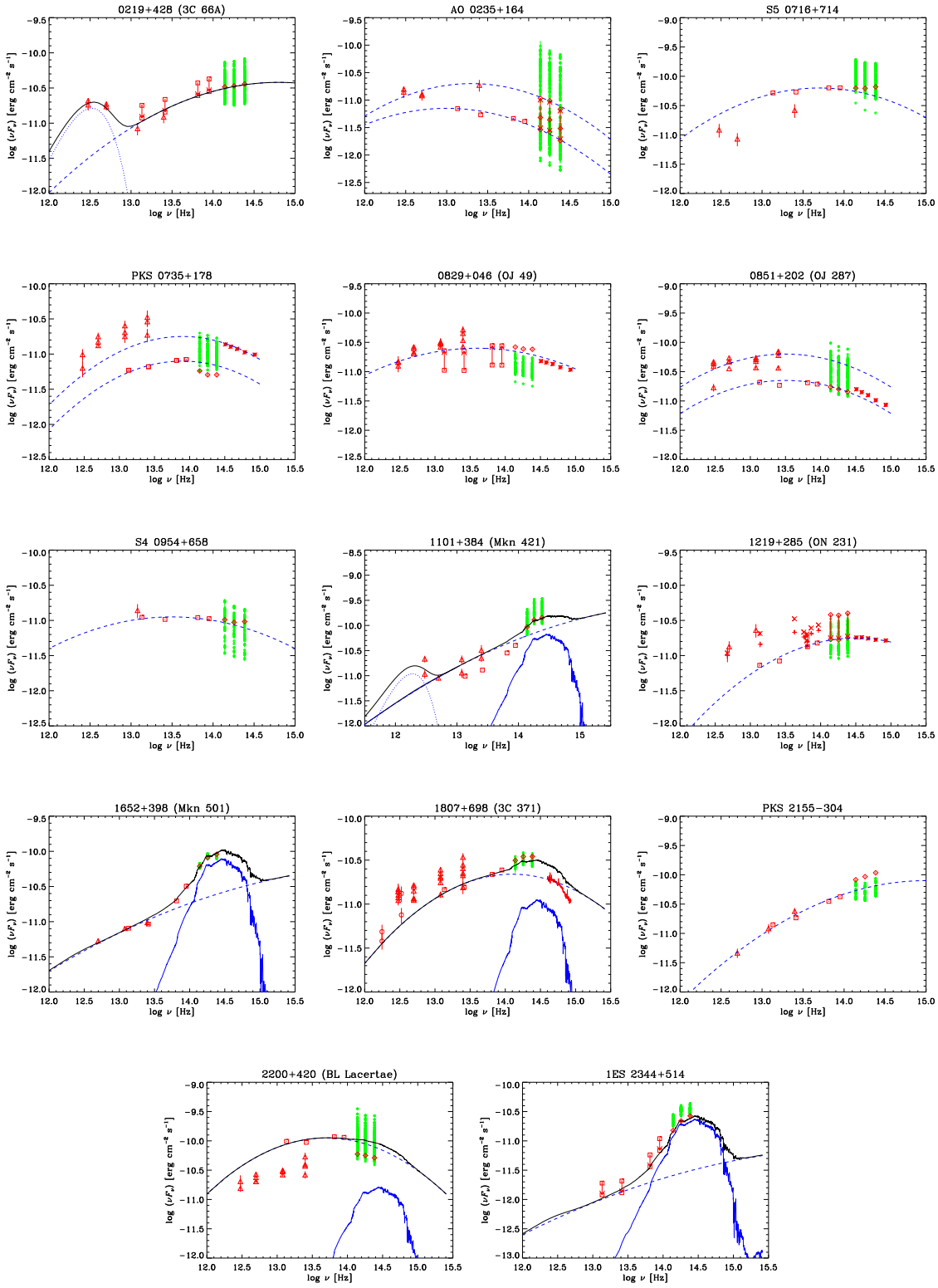

FIGURE 3.12— Spectral energy distribution of the GASP-WEBT BL Lac objects. Data from *ISO* (red circles), *IRAS* (triangles), *Spitzer* (plus signs and crosses), *WISE* (squares), 2MASS (diamonds), and SDSS (asterisks) are shown. The green circles represent the results of the GASP near-IR monitoring at the Campo Imperatore and Teide observatories. The optical spectrum of 1807+698 by Buttiglione et al. (2009) is also plotted. Contributions from the synchrotron (dashed line) and host galaxy (solid line) emission are displayed in blue. In the cases of 3C 66A and Mkn 421, thermal dust emission is added, which is modelled as a black-body (blue dot-dashed line). The black line represents the sum of all components.

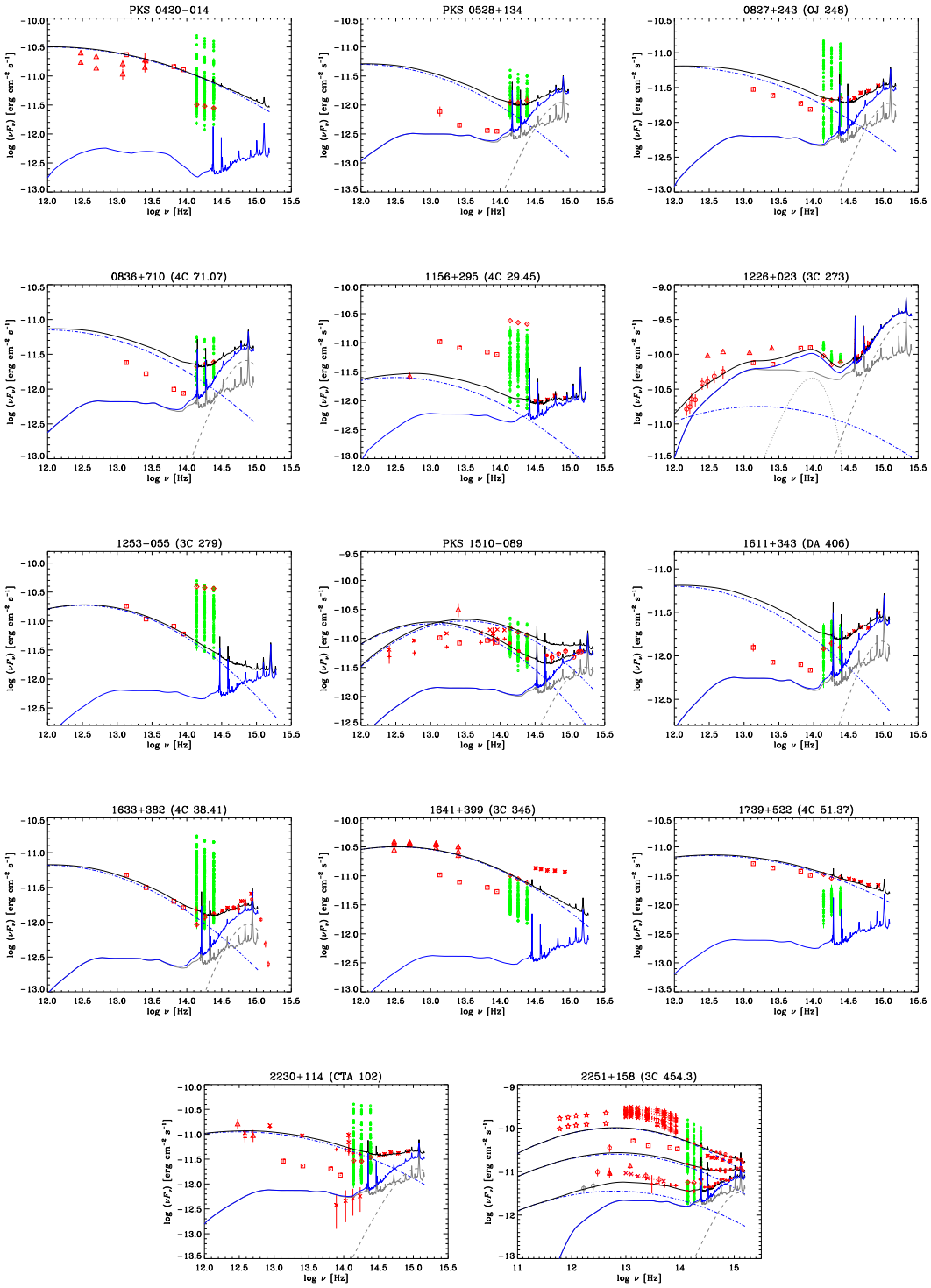

FIGURE 3.13— Spectral energy distribution of the GASP-WEBT FSRQs. Data from *ISO* (red circles), *IRAS* (triangles), *Herschel* (stars), *Spitzer* (plus signs and crosses), *WISE* (squares), 2MASS (diamonds), and SDSS (asterisks) are shown. The green circles represent the results of the GASP near-IR monitoring at the Campo Imperatore and Teide observatories. The optical spectrum of 1226+023 by Buttiglione et al. (2009) as well as near−IR−to−UV SEDs of 1510−089, 1633+382, and 2251+158 already published in papers by the GASP-WEBT collaboration are also plotted. Contributions from the synchrotron (dot-dashed line) and QSO-like (solid line) emission are displayed in blue. The latter is derived from the SWIRE QSO1 templates, but when a brighter disc is required, a black-body component is added. In these cases we show in grey both the QSO1 template (solid line) and the black body (dashed line). The model fit to the 3C 273 SED requires further dust emission, obtained by adding another black-body component (grey dotted line). The black line represents the sum of all components.

log-parabola, while for the host galaxy and QSO-like contributions we have adopted SWIRE templates, with the possible inclusion of black-body components to simulate additional dust emission or enhanced disc emission. We have used single temperature black-bodies for these additional components instead of multi-temperature black-bodies or dusty galaxy templates to keep the interpretation as simple as possible.

A strong host galaxy signature has been found in the SED of Mkn 421, and especially in those of Mkn 501 and 1ES 2344+514, the three closest and high-energy peaked BL Lacs, which were the first ones to be detected at TeV energies. At nearly the same redshift of 1ES 2344+514 lies 3C 371, which shows an important host galaxy contribution too. A bit farther, BL Lacertae does not show evidence of host galaxy in its SED, even if we know that the host affects the source photometry in faint states (e.g. Raiteri et al., 2013). Apart from the above cases, all other BL Lac SEDs are well fitted by a synchrotron component; the only indications for the presence of dust thermal emission are found for 3C 66A and Mkn 421, as previously reported (Impey & Neugebauer, 1988).

For many FSRQs, the near-IR band signs the transition from a non-thermal, synchrotron-dominated emission to a thermal, QSO-like dominated emission. The cases of PKS 0528+134 and 4C 71.07, whose *WISE* data were acquired in very faint states, suggest that torus emission is relatively weak in FSRQs. A particularly bright disc is required to explain the SEDs of 9 out of the 14 GASP FSRQs. From the SED fits we can derive disc luminosities at the peak of $\log(\nu L_\nu) \sim 44.8$–$46.6$ [erg s^{-1}], the highest values characterising 4C 71.07, PKS 0528+134, and 4C 38.41, which are the most distant objects. For comparison, various authors analysing different QSO samples obtained mean values ranging from ~ 44.9 to ~ 45.8, with large dispersion (see Elvis et al., 2012, and references therein). Hence, our FSRQs have accretion discs with luminosities in the same range as QSO, up to the highest values. In the case of 3C 273, an extra dust contribution peaking at $\log \nu \sim 14$ [Hz] is needed to explain the near-to-medium infrared SED.

4

Multiwavelength behaviour the FSRQ object OJ 248.

We present an analysis of the multiwavelength behaviour of the blazar OJ 248 at $z = 0.939$ in the period 2006–2013. We use low-energy data (optical, near-infrared, and radio) obtained by 21 observatories participating in the GLAST-AGILE Support Program (GASP) of the Whole Earth Blazar Telescope (WEBT), as well as data from the *Swift* (optical–UV and X-rays) and *Fermi* (γ-rays) satellites, to study flux and spectral variability and correlations among emissions in different bands. We take into account the effect of absorption by the damped Lyman α intervening system at $z = 0.525$. Two major outbursts were observed in 2006–2007 and in 2012–2013 at optical and near-IR wavelengths, while in the high-frequency radio light curves prominent radio outbursts are visible peaking at the end of 2010 and beginning of 2013, revealing a complex radio-optical correlation. Cross-correlation analysis suggests a delay of the optical variations after the γ-ray ones of about a month, which is a peculiar behaviour in blazars. We also analyse optical polarimetric and spectroscopic data. The average polarization percentage P is less than 3%, but it reaches $\sim 19\%$ during the early stage of the 2012–2013 outburst. A vague correlation of P with brightness is observed. There is no preferred electric vector polarisation angle and during the outburst the linear polarization vector shows wide rotations in both directions, suggesting a complex behaviour/structure of the jet and possible turbulence. The analysis of 140 optical spectra acquired at the Steward Observatory reveals a strong Mg II broad emission line with an essentially stable flux of $6.2 \times 10^{-15}\,\mathrm{erg\,cm^{-2}\,s^{-1}}$ and a full width at half-maximum of $2053\,\mathrm{km\,s^{-1}}$.

Introduction

The emission of active galactic nuclei (AGNs) is explained by the existence of a supermassive black hole (SMBH) at the centre of the host galaxy, which converts gravitational energy of material located in the surroundings into electromagnetic energy. This material forms a disk and loses angular momentum due to the viscosity in the disk, finally falling onto the black hole. In general, the AGN spectra may show broad and narrow emission lines produced in regions close to the nucleus. Sometimes they can also show lines from the host galaxy. In radio-loud

AGNs two plasma jets are ejected in direction perpendicular to the disc.

Among the different types of radio-loud AGNs, the objects called "blazars" (BL Lacs and flat spectrum radio quasars, FSRQs) are powerful emitters from radio wavelengths up to γ-ray energies. They present strong flux variability and high and variable polarization (e.g. Smith, 1996). The most accepted scenario to explain these features suggests that we are observing the emission from a jet of material accelerated to relativistic velocities in the vicinity of the SMBH, and oriented very close to our line of sight. Thus the jet radiation is Doppler boosted and dominates over the other emission components from the nucleus (disc, broad line region - BLR, narrow line region) or host galaxy. The origin of the low-frequency radiation (radio to UV or X-ray band) from the jet is attributed to synchrotron emission and the high-energy radiation (X- to γ-rays) to an inverse-Compton process by the same relativistic electrons producing the synchrotron photons. After the launch of satellites for high-energy observations such as the *Astrorivelatore Gamma ad Immagini Leggero* (AGILE; Tavani et al., 2009) and *Fermi* (Abdo et al., 2009; Atwood et al., 2009), the number of sources detected at γ-rays has increased significantly, allowing a more detailed investigation of the high-energy processes occurring in blazars.

In this paper, we present multifrequency observations of the FSRQ OJ 248 (0827+243) in 2006–2013 performed in the framework of a campaign led by the Whole Earth Blazar Telescope[1] (WEBT). The WEBT radio–optical observations are complemented by high-energy data from the *Swift* and *Fermi* satellites.

In the Roma BZCAT multi-frequency catalog of blazars[2] (Massaro et al., 2009) OJ 248 appears with a redshift $z = 0.939$ flagged as uncertain. Mg II and Fe II absorption lines at $z = 0.525$ were detected by Ulrich & Owen (1977) in the source optical spectrum. This intervening Damped Lyman α (DLA) system was subsequently studied by Rao & Turnshek (2000), who estimated a hydrogen column density $N_{\rm H} = (2.0 \pm 0.2) \times 10^{20}\,{\rm cm}^{-2}$. The DLA system is likely a disc galaxy with ongoing star formation (Steidel et al., 2002; Rao et al., 2003). Although it does not affect the blazar photometry because of its faintness (Rao et al., 2003), its absorption of the source radiation must be taken into account.

OJ 248 was detected by the Energetic Gamma Ray Experiment Telescope (EGRET) instrument on board the *Compton Gamma Ray Observatory* (CGRO) with a variable flux. In the third EGRET catalog of high-energy γ-ray sources (Hartman et al., 1999) it appears with a flux $F(E > 100\,{\rm MeV}) = (24.9 \pm 3.9) \times 10^{-8}\,{\rm ph\,cm^{-2}\,s^{-1}}$, single measurements ranging from 15.6 to $111.0 \times 10^{-8}\,{\rm ph\,cm^{-2}\,s^{-1}}$. It has $F(E > 100\,{\rm MeV}) = (5.3 \pm 0.5) \times 10^{-8}\,{\rm ph\,cm^{-2}\,s^{-1}}$ and a spectral index 2.67 ± 0.07 in the Second Fermi-LAT catalog (2FGL; Nolan et al., 2012). In the 1990s the source was very active also in the optical band (e.g. Villata et al., 1997; Raiteri et al., 1998).

[1] http://www.oato.inaf.it/blazars/webt

[2] Edition 4.1.1, August 2012; http://www.asdc.asi.it/bzcat

4.1 Optical and near-IR photometry

Optical photometric observations were provided in the R band by several observatories participating in this WEBT project, including the GASP-WEBT collaboration and the Steward Observatory program in support of the *Fermi* γ-ray telescope (Smith et al., 2009). They are: Abastumani (Georgia, FSU), Calar Alto[3] (Spain), Crimean (Ukraine), Lowell (Perkins telescope, USA), Lulin (Taiwan), Mt. Maidanak (Uzbekistan), Roque de los Muchachos (Liverpool telescope, Spain), Rozhen (Bulgaria), San Pedro Martir (Mexico), St. Petersburg (Russia), Steward (USA), Teide (IAC80 telescope, Spain), Tijarafe (Spain), Torino (Italy), Vidojevica (Serbia).

The period of interest goes from 2006 March up to 2013 July. We collected a total of 1356 data points, 1211 of which survived the light curve cleaning process, through which we discarded data with large errors as well as clear outliers.

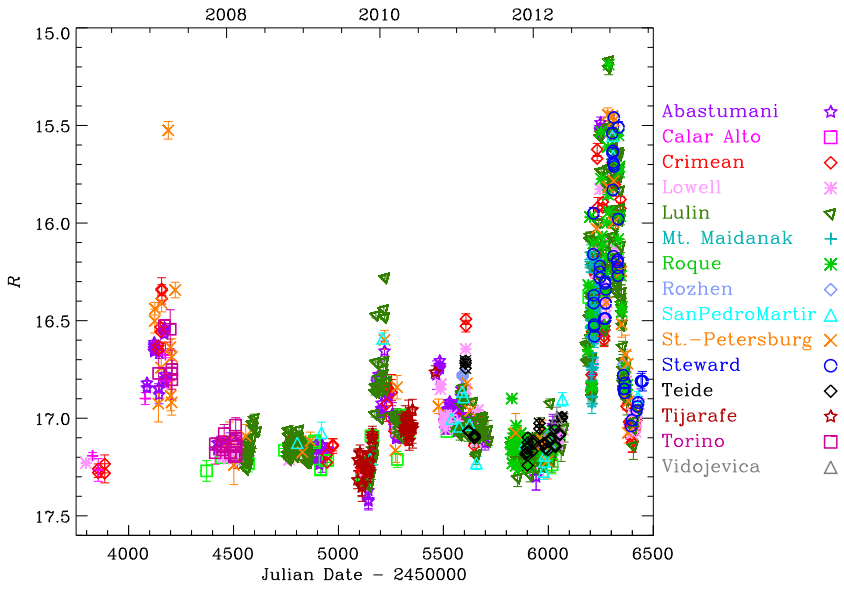

FIGURE 4.1— Light curve of OJ 248 in R band. It includes 1211 points from 15 observatories, distinguished by different colours and symbols.

In the light curve of Fig. 4.1 we can see two major flaring periods, in 2006–2007 and 2012–2013. The first flare is of similar brightness ($R = 15.6$) as the one observed in November 1995 by Raiteri et al. (1998), which was a historical maximum. The second outburst appears more prominent and shows a stronger variability. Two minor events are visible in 2009–2010 and in early 2011.

The 2007 peak was very sharp and was characterized by a brightening of $\sim$ 1.3 mag in 11 days and about 1.0 mag fading in 9 days. A noticeable variability also characterises the

[3]Calar Alto data was acquired as part of the MAPCAT project: http://www.iaa.es/∼iagudo/research/MAPCAT

2012–2013 outburst, with variations of about 1 mag in less than 6 days. This can be compared with variations of 1.43 mag in 16 days observed by Raiteri et al. (1998), of 1.16 mag in 63 days observed by Villata et al. (1997), and of 1.05 mag in 58 days reported by Fan et al. (2004). But the source also exhibits short-term variability. In particular, we found a couple of changes of ~ 0.3 mag in about 7.5 hours in late 2012. Intraday variability was previously reported by Raiteri et al. (1998), who observed a brightness decrease of 0.73 mag in 20 hours.

The GASP-WEBT near-IR data are collected in the J, H, K bands at the Campo Imperatore (Italy) and Teide (TCS, Spain) observatories. Details on the data acquisition and reduction are given in Raiteri et al. (2014). A comparison between the R-band and near-IR source behaviour is shown in Fig. 4.2. Although the near-IR light curves are less sampled than the optical one, we can recognize the same main features, in particular the two outbursts of 2006–2007 and 2012–2013. The variation amplitude increases with wavelength, as it is usually observed in FSRQs (e.g. Raiteri et al., 2012), suggesting the presence of a "stable" blue emission component, likely thermal radiation from the accretion disc.

Among blazars, in general BL Lacs are objects of lower luminosity with featureless spectra or very weak emission lines. In contrast, FSRQs have higher luminosities and stronger emission lines.

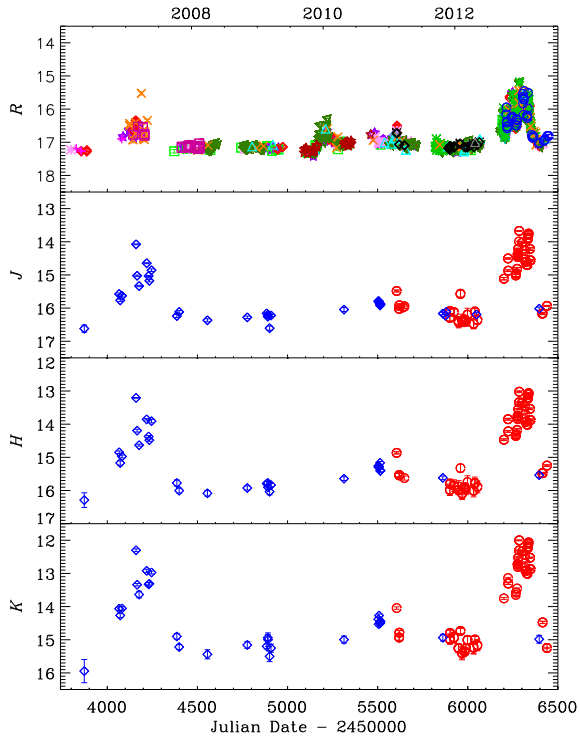

FIGURE 4.2— Light curves of OJ 248 in optical (R band) and near-IR (J, H, K bands) in 2006–2013 built with GASP-WEBT data. In the near-IR light curves the blue diamonds are from the Campo Imperatore Observatory and the red points from the Teide Observatory.

4.2 Optical polarimetry

Blazars are known to show variable polarization in both polarized flux percentage (P) and electric vector polarization angle (EVPA) (e.g. Smith, 1996). In particular, wide rotations of the linear polarisation vector have been detected in a number of cases (Marscher et al., 2008; Marscher & Jorstad, 2010; Larionov et al., 2013; Sorcia et al., 2014), which have been interpreted as the effect of motion along spiral trajectories.

Optical polarization data for this paper were provided by the Calar Alto, Crimean, Lowell, San Pedro Martir, St. Petersburg, and Steward observatories. In Fig. 4.3 we show the time evolution of the polarization percentage P compared with the R-band light curve. For most of the time, the source showed low P (average value of $\sim 3\%$), but during the brightening phase of the 2012–2013 outburst P reached $\sim 19\%$, suggesting a correlation between P and brightness typical of FSRQs (e.g. Smith, 1996; Raiteri et al., 2013). Figure 4.4 shows P versus the de-absorbed flux density in the R band (see Sect. 8). For any value of F_R there is a large dispersion of P, but the highest values of P ($> 13\%$) are reached when the source is bright ($F_R > 1.3$ mJy). The linear Pearson's correlation coefficient is 0.60, indicating a marginal correlation.

In order to investigate whether possible rotations of the linear polarisation vector occurred, we first examine the behaviour of the Q and U Stokes' parameters. Figure 4.5 shows that OJ 248 spent most of the time with Q and U being close to zero. With this being the case, even small variations in Q and U necessarily lead to large EVPA rotations that are difficult to accurately follow unless the observations are very dense. The problem is mitigated during the 2012–2013 outburst, when Q and U exhibit large variations. This appears clearer in the Q versus U plot in Fig. 4.6, where subsequent data belonging to short time periods with good sampling have been connected to show the time evolution during the 2012–2013 outburst. With this in mind, in Fig. 4.7 we finally plot the EVPA as a function of time during the outburst. The $\pm n\pi$ ambiguity was fixed by assuming that the most likely value is that minimizing the angle variation, i.e. we added/subtracted 180 when needed to minimize the difference between subsequent points separated by less than 5 days. It seems that there is not a preferable EVPA value and that the linear polarisation vector underwent wide rotations in both directions and with different ranges of angles. All this suggests a complex behaviour/structure of the magnetic field in the jet as is expected e.g. from a turbulent plasma flowing at a relativistic speed down the jet (Marscher, 2014).

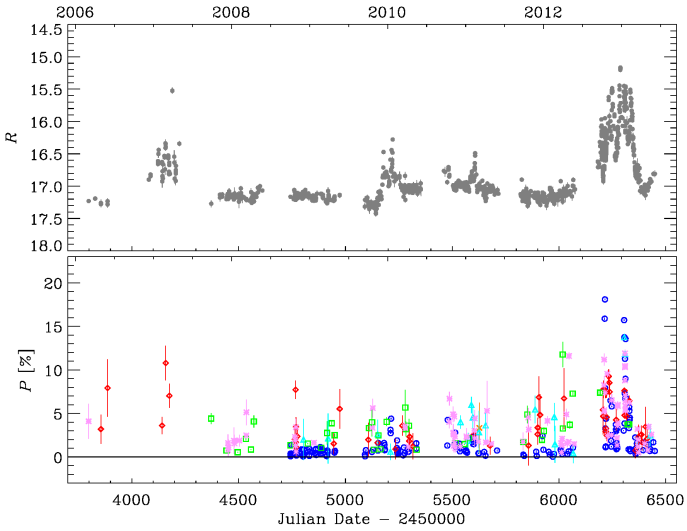

FIGURE 4.3— Time evolution of the optical magnitude in R band (top panel) and of the percentage of polarized flux (bottom panel). The data are from different observatories: Calar Alto (green squares), Crimean (red diamonds), Lowell (pink asterisks), San Pedro Martir (cyan triangles), Steward (blue circles), and St. Petersburg (orange crosses).

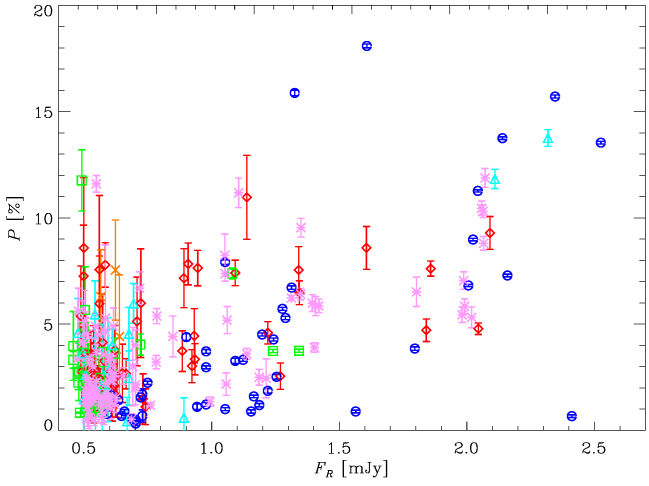

FIGURE 4.4— Optical polarization percentage P plotted against the de-absorbed flux density in the R band. The data are from different observatories: Calar Alto (green), Crimean (red), Lowell (pink), San Pedro Martir (cyan), Steward (blue), and St. Petersburg (orange).

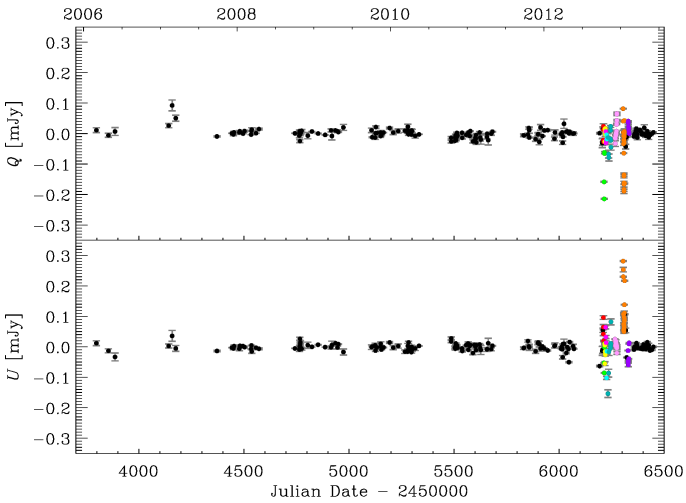

FIGURE 4.5— The evolution of the Q and U Stokes'parameters as a function of time. Different colours during the 2012–2013 outburst highlight the data of the selected periods indicated in Fig. 4.6.

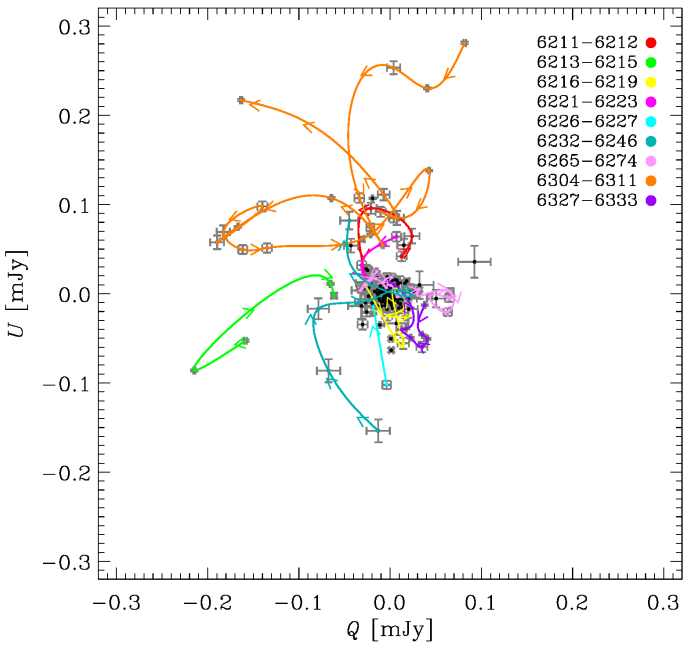

FIGURE 4.6— Q versus U for all the data shown in Fig. 4.5. Coloured lines connect subsequent data belonging to the periods listed in the legend (JD-2450000). The direction is indicated by the arrows.

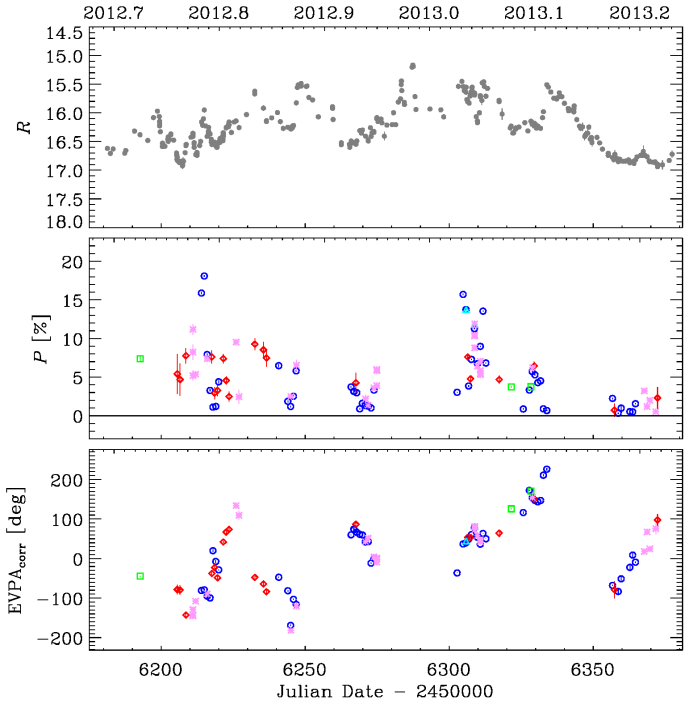

FIGURE 4.7— Time evolution of the optical magnitude in R band (top panel), of the percentage of polarized flux (middle panel) and of the EVPA "corrected" for the $\pm n\pi$ ambiguity (bottom panel, see text for explanation) during the 2012–2013 outburst. Data are from different observatories: Calar Alto (green squares), Crimean (red diamonds), Lowell (pink asterisks), San Pedro Martir (cyan triangles), Steward (blue circles), and St. Petersburg (orange crosses).

4.3 Optical spectroscopy

Several previous studies found that there is no correlation between the jet activity and the behaviour of the broad emission lines in blazars (see e.g. Corbett et al., 2000; Raiteri et al., 2007). Indeed, the BLR gas is likely ionized by the accretion disc radiation, whose variability is weaker and occurs on longer time scales than the variability of the beamed jet emission (see e.g. Kaspi et al., 2000). However, León-Tavares et al. (2013) detected a flare-like variability of the Mg II emission line in the blazar 3C 454.3 during an outburst and claimed that the broad emission line fluctuations are linked to the non-thermal continuum emission from the jet. With this in mind, we analyse the spectroscopic behaviour of OJ 248 during our monitoring period.

Optical spectra were taken at the Steward Observatory of the University of Arizona for the "Ground-based Observational Support of the *Fermi* Gamma-ray Space Telescope" program[4]. Data for this program are taken at the 2.3 m Bok telescope and 1.54 m Kuiper telescope (Smith et al., 2009); 140 spectra of OJ 248 were acquired during the first five cycles of the *Fermi* mission, from October 2008 to June 2013.

All spectra show a prominent Mg II $\lambda\lambda 2796, 2803$ broad emission line, which was measured

[4]http://james.as.arizona.edu/~psmith/Fermi/

by fitting a Gaussian model with a single component, after subtracting a linear fit to the continuum. We used ad-hoc routines developed in IDL and based on the MPFIT[5] libraries (Markwardt, 2009). The continuum region was selected from adjacent regions to the emission line, which are free of features. The uncertainty of the measured flux was estimated from the average of the residuals obtained after the continuum fitting and was then used to determine the parameter confidence limits applying the routines in the MPFIT library.

In Fig. 4.8 we show two of the spectra corresponding to different brightness states and in Fig. 4.9 the line and continuum fits as well as the residuals. The results of the Mg II analysis are shown in Fig. 4.10. The line flux presents some dispersion around a mean value of $6.2 \times 10^{-15}\,\mathrm{erg\,cm^{-2}\,s^{-1}}$ with standard deviation of $0.5 \times 10^{-15}\,\mathrm{erg\,cm^{-2}\,s^{-1}}$. The possible presence of line variability can be checked e.g. by calculating the mean fractional variation $f = \sqrt{\sigma^2 - \delta^2}/< F >$, where σ is the standard deviation, δ the mean square uncertainty of the fluxes, and $< F >$ the average flux (Peterson, 2001). The result is $f = 0.08$, which means that the line flux is basically stable, and this is true also during the 2012–2013 outburst period, when the continuum flux increased by a factor ~ 6. Moreover, no delayed line flux increase was detected also after the outburst. Hence, the enhanced jet activity responsible for the outburst does not affect the BLR.

We measured the line full width at half-maximum[6]. The corresponding de-projected gas velocity, of course, depends on the geometry and orientation of the BLR (see e.g. Decarli et al., 2011). In the blazar model, the BLR should be nearly face on, so measurements of FWHM are likely to be underestimated, since the measurement of the radial velocity will likely miss most of the orbital component.

In the bottom panel of Fig. 4.10 we finally plot the equivalent width (EW) versus the continuum flux density. The EW decreases when the source brightens, which confirms that the jet is not the ionizing source of the BLR. We notice that, according to the classical definition (Stickel et al., 1991), blazars with rest-frame EW less than 5 Å are classified as BL Lacs; in the case of OJ 248, this happens when the observed EW goes below $5\,\text{Å} \times (1+z) \sim 9.7$ Å, which occurs when the source continuum flux density around the Mg II line[7] exceeds $\sim 0.6 \times 10^{-15}\,\mathrm{erg\,cm^{-2}\,s^{-1}\,Å^{-1}}$. This underlines the limit of the classical distinction between BL Lacs and FSRQs based on the EW, which depends on the source brightness.

Fig. 4.8 shows a strong absorption line at $\lambda = 4270$ Å due to Mg II absorption in the intervening DLA system at $z = 0.525$ mentioned in the Introduction. We cannot perform a more detailed analysis of this line because the resolution of our spectra is about 20 Å, implying a velocity resolution of $\sim 1400\,\mathrm{km\,s^{-1}}$, while the FWHM of the Mg II absorption line is $\simeq 270\,\mathrm{km\,s^{-1}}$ (Steidel et al., 2002).

[5] http://www.physics.wisc.edu/∼craigm/idl/fitting.html

[6] Corrected for the instrumental broadening of the line. (FWHM), from which one can derive the velocity of the gas clouds in the BLR. The average value is $v_{\mathrm{FWHM}} = 2053\,\mathrm{km\,s^{-1}}$ with a standard deviation of $\sim 310\,\mathrm{km\,s^{-1}}$

[7] We estimated the continuum flux density in the spectral regions 5320–5360 Å and 5500–5530 Å and then took the mean value.

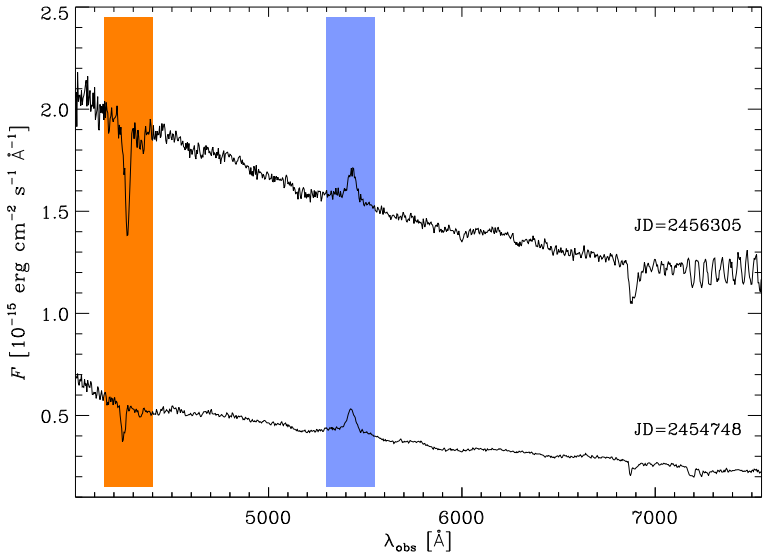

FIGURE 4.8— Optical spectra of OJ 248 during different brightness states obtained at the Steward Observatory, showing the Mg II emission line at $z = 0.939$ (blue) and the Mg II absorption line at $z = 0.525$ (orange).

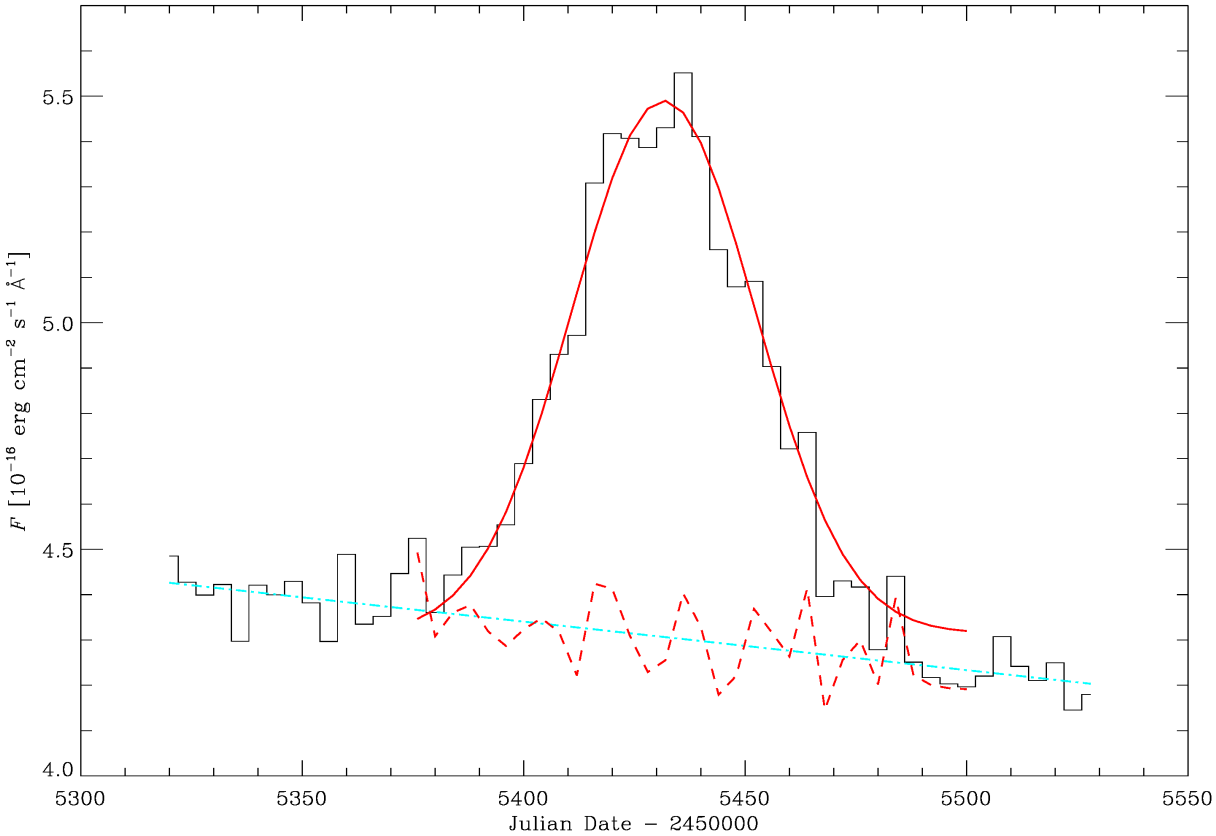

FIGURE 4.9— Gaussian fit (red solid line) to the Mg II emission line of the spectrum taken on 2008 October 30 and shown in Fig. 4.8. The cyan line indicates the linear fit to the continuum; the red dashed line represents the residuals.

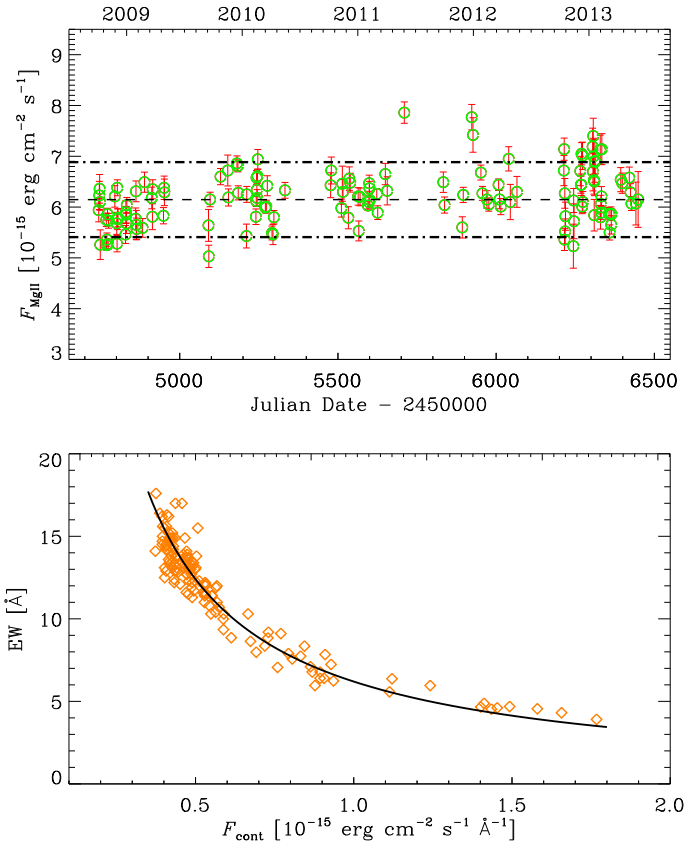

FIGURE 4.10— Top: time evolution of the Mg II broad emission line flux; the dashed line represents the average value and the dotted-dashed line the standard deviation around the mean. Bottom: EW of Mg II versus the continuum flux density; the solid line displays the behaviour of the EW assuming a constant line flux equal to its average value.

4.4 Observations at radio and millimetre wavelengths

Radio and mm observations were performed with the Medicina (5, 8, and 22 GHz), Metsähovi (37 GHz), Noto (43 GHz), IRAM (86 and 230 GHz), and Submillimeter Array (SMA, 230 and 345 GHz) telescopes.

A detailed description of the 43 GHz measurements performed with the Noto Radiotelescope can be found in Leto et al. (2009). For the Medicina observations, see e.g. Bach et al. (2007).

The 37 GHz observations were made with the 13.7 m diameter Metsähovi radio telescope. The flux density scale is set by observations of DR 21. Sources NGC 7027, 3C 274 and 3C 84 are used as secondary calibrators. The error estimate in the flux density includes the contribution from the measurement root mean square and the uncertainty of the absolute calibration. A detailed description of the data reduction and analysis is given in Teraesranta et al. (1998).

IRAM 30 m Telescope data were acquired as part of the POLAMI (Polarimetric AGN Monitoring with the IRAM 30 m Telescope) and MAPI (Monitoring AGN with Polarimetry at the

IRAM 30 m Telescope) programs. Data reduction was performed following the procedures described in Agudo et al. (2006, 2010).

Millimetre and submillimetre data were also obtained at the Submillimeter Array (SMA) near the summit of Mauna Kea (Hawaii). OJ 248 is included in an ongoing monitoring program at the SMA to determine the fluxes of compact extragalactic radio sources that can be used as calibrators at mm wavelengths (Gurwell et al., 2007). OJ 248 was also observed as part of a dedicated program to follow sources on the *Fermi* LAT Monitored Source List (PI: A. Wehrle) in 2009 and 2010. In the ongoing monitoring sessions, available potential calibrators are observed for 3 to 5 minutes, and the measured source signal strength calibrated against known standards, typically solar system objects (Titan, Uranus, Neptune, or Callisto). In addition, from time to time calibrator data obtained during regular science observations are also used to obtain flux density measurements. Data from this program are updated regularly and are available at the SMA website[8].

As one can see in Fig. 4.11, the mm data (230 and 86 GHz) show two prominent outbursts of the same strength peaking in late 2010 and early 2013. Going to lower frequency (37 GHz), the second outburst becomes fainter than the first, and it completely disappears at 8 GHz. A comparison with the optical light curve suggests that the 2013 mm–radio outburst is the time delayed counterpart of the 2012–2013 optical event, while a possible correlation between the optical and radio variations in correspondence of the 2010–2011 mm–radio outburst is more difficult to establish. Indeed, there are no visible optical flares either contemporaneous or slightly preceding the lower-frequency outburst, but just one event about one year before, which however is more likely connected with the pre-outburst bumps visible at 230 and 37 GHz. In fact, there is a definite rise in the 230 GHz light curve that starts at essentially the same time as the late 2009–early 2010 optical event. Most likely the more or less prominent optical counterpart of the main mm–radio outburst remained unobserved due to the 2010 seasonal gap: indeed, some residual activity can be seen at the start of the subsequent observing season. The 2006–2007 optical outburst might be correlated with a minor radio event observed a few months later at 86 (and 230) GHz. We used the discrete correlation function (DCF; Edelson & Krolik, 1988; Hufnagel & Bregman, 1992) to analyse cross-correlations among light curves. Figure 4.12 shows the DCF between the optical de-absorbed (see Sect. 4.7) and 230 GHz flux densities. The peak value is 0.8, which implies good correlation, and the time delay corresponding to the peak is 28 days, which would be the time lag of the mm variations after the optical ones. However, this result is dominated by the last outburst and the DCF run on the pre-outburst period gives no significant signal.

Flares can be produced by shocks propagating downstream the jet and/or by variations of the Doppler factor δ, which depends on both the bulk Lorentz factor of the relativistic plasma, $\Gamma_{\rm b}$, and the viewing angle θ, $\delta = [\Gamma_{\rm b}\,(1-\beta\,\cos\theta)]^{-1}$, where β is the velocity in units of the light speed. The different behaviour of OJ 248 in various epochs, i.e. different correlation between optical and radio variations, can be explained in terms of a misalignment of the region emitting the bulk of the optical radiation with respect to the zone emitting the bulk of radio photons (see

[8]http://sma1.sma.hawaii.edu/callist/callist.html

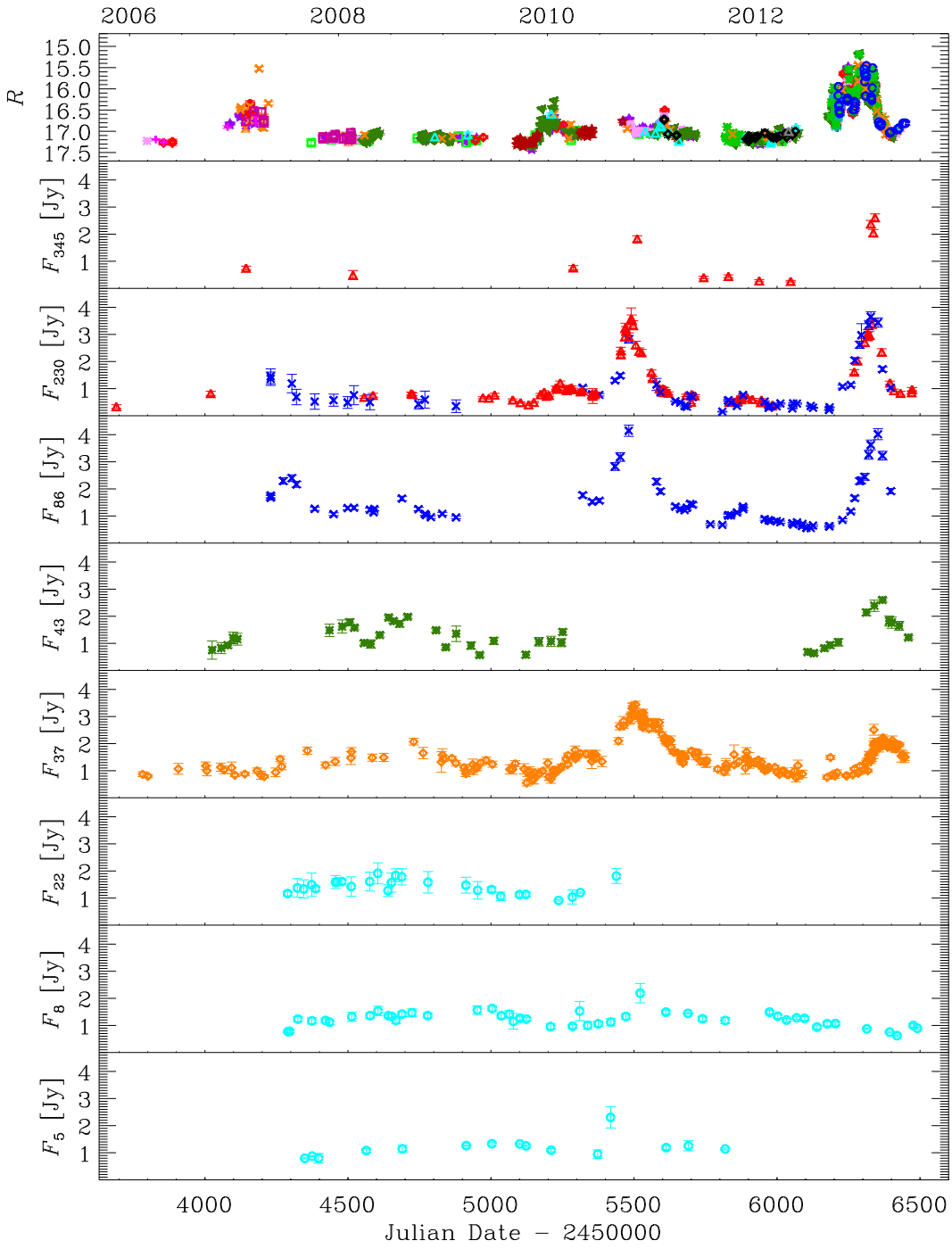

FIGURE 4.11— Light curves of OJ 248 at different frequencies in 2006–2013. From top to bottom: R-band optical magnitudes (see also Fig. 4.1), 345 GHz data from SMA, 230 GHz data from SMA (red triangles) and IRAM (blue crosses), 86 GHz data from IRAM, 43 GHz data from Noto, 37 GHz data from Metsähovi, 22, 8, and 5 GHz data from Medicina.

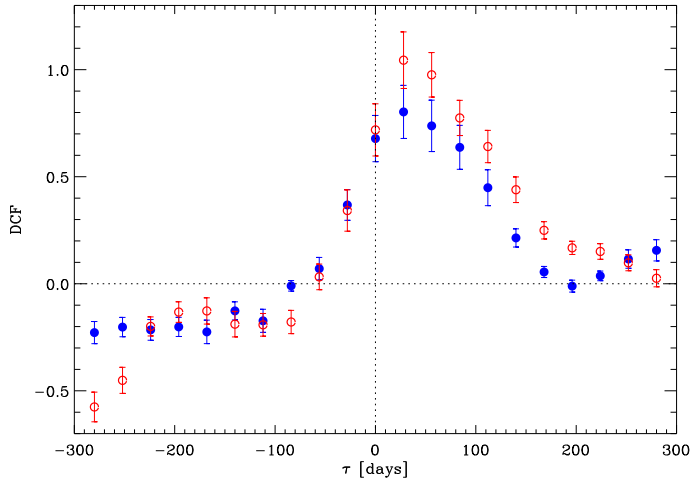

FIGURE 4.12— Discrete correlation functions between the R-band de-absorbed and 230 GHz flux densities (blue filled circles) and between the 230 and 37 light curves (red empty circles).

e.g. Villata et al., 2007, 2009,?; Raiteri et al., 2011). The radiation coming from the jet region with a smaller viewing angle will in fact be more Doppler boosted. According to this interpretation, in 2010–2011 the radio emitting region was more aligned with the line of sight than the optical zone, while in 2012–2013 the most external jet regions, emitting the low-frequency radio photons, had a larger viewing angle, and the strong optical outburst was the effect of a viewing angle smaller than ever.

We finally notice that there is a time delay of the radio flux variations going toward longer wavelengths; in particular, by means of the DCF we could estimate the time lag between the 230 and 37 GHz flux changes (see Fig. 4.12). The peak of the DCF is strongly asymmetric, so that a better estimate of the delay in this case is given by the centroid of the distribution (Peterson et al., 1998), which indicates a value of 40–50 days. Moreover, the amplitude of the flux variations decreases at lower frequencies (the ratio between the maximum and minimum flux density is ~ 24 at 230 GHz, 7.4 at 86 GHz, and 6.3 at 37 GHz), and the light curves become smoother with longer-lasting events. This is what we expect if the radio emission at longer wavelengths comes from more external (because of synchrotron self-absorption) and more extended regions of the jet.

An alternative picture to explain the radio–optical variability is in terms of a disturbance, e.g. shock wave, propagating downstream the jet where the delay from high radio frequencies towards low radio frequencies is naturally caused by opacity effects. In case the optical and mm emitting regions are co-spatial, the reason why the mm peak is time delayed may be due to a rather high lower-energy cutoff to the electron energy distribution in the early stages of the outburst.

4.5 *Swift* observations

The *Swift* satellite (Gehrels et al., 2004) carries three instruments that work simultaneously in different frequency ranges: the X-Ray Telescope (XRT), observing between 0.3 and 10 keV (Burrows et al., 2005), the Ultraviolet-Optical Telescope (UVOT), between 170 and 600 nm (Roming et al., 2005), and the Burst Alert Telescope (BAT), between 14 and 195 keV (Barthelmy et al., 2005). OJ 248 was observed by *Swift* 86 times between 2008 January and 2013 May.

4.5.1 UVOT observations

The UVOT telescope can acquire data in optical (v, b, u) and UV $(w1, m2, w2)$ bands (Poole et al., 2008). The data reduction was performed with the **HEASoft** package version 6.13 and the Calibration Database (CALDB) 20130118 of the NASA's High Energy Astrophysics Science Archive Research Center[9] (HEASARC). We extracted the source counts within a 5 arcsec radius aperture and the background counts from a nearby circular region with 15 arcsec radius. We summed multiple observations in the same filter with the `uvotimsum` task and then processed them with `uvotsource`.

The resulting light curves are shown in Fig. 4.13. No observations were available in the b band. After 2010.0 the difference between the maximum and minimum magnitudes in the different bands is 1.12 in $w2$, 1.05 in $m2$, 1.15 in $w1$, 1.25 in u. It is 0.67 in v, but in this case we have only four points. We can see that the variability in general decreases when the frequency increases, extending the trend we noticed in Sect. 4.1 for the optical and near-IR light curves.

4.5.2 XRT observations

Reduction of the XRT data was performed with the **HEASoft package** version 6.13 with the calibration file 20130313. There are 83 observations in photon-counting (PC) mode. We ran the task `xrtpipeline` with standard screening criteria. For further analysis we only kept the 64 observations with more than 50 counts. Source counts were extracted with the `xselect` task from a circular region of 30 pixel radius centred on the source and the background counts were derived from a surrounding annular region of 50 and 70 pixel radii. No correction for pile-up was needed since the count rate is always lower than 0.5 counts/s. We performed spectral fits with the **Xspec** package in the 0.3–10 keV energy range, using the Cash statistics because of the low count number. We modelled the spectra with a power law with photoelectric absorption, adopting a hydrogen atomic column density $N_{\rm H} = 4.6 \times 10^{20}\,{\rm cm}^{-2}$ obtained by summing the Galactic value $2.6 \times 10^{20}\,{\rm cm}^{-2}$ (Kalberla et al., 2005) to that of the intervening DLA system at $z = 0.525$ (Rao & Turnshek, 2000).

The X-ray spectrum acquired on 2012 October 2 is shown in Fig. 4.14 as an example. It was best-fitted with a power law with photon index $\Gamma = 1.49 \pm 0.10$.

In Fig. 4.15 we plotted Γ as a function of the flux density at 1 keV for the 58 observations with error less than 30% of the flux. The values of Γ range between 1.06 and 2.07, with an

[9] http://heasarc.gsfc.nasa.gov

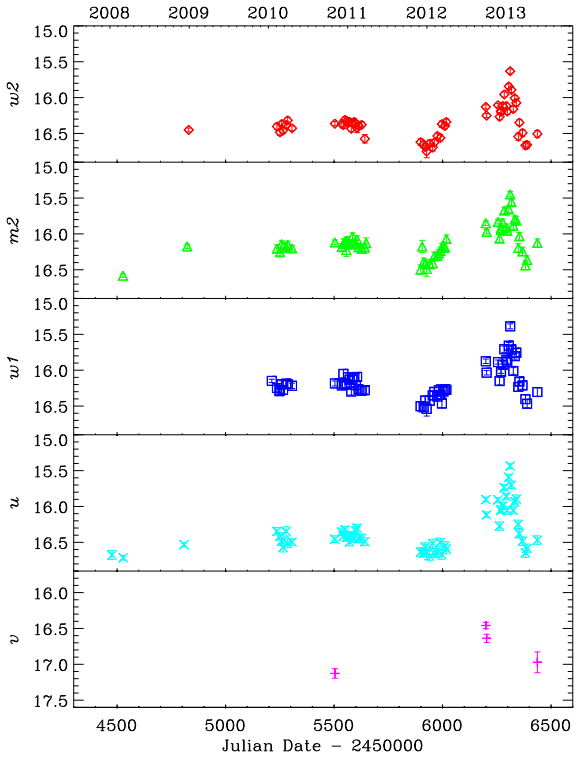

FIGURE 4.13— Light curves of OJ 248 built with *Swift*-UVOT data in optical and UV.

average value of 1.65 and no significant trend of Γ with flux, in contrast to the harder-when-brighter trend sometimes found in FSRQs (e.g. Vercellone et al., 2010). The smaller dispersion of the data points corresponding to the 2012–2013 outburst (standard deviation $\sigma = 0.09$) with respect to the pre-outburst data ($\sigma = 0.24$) is likely due to their higher precision because of the larger count number. In both cases the standard deviation is less than the average error (0.16 and 0.29, respectively), indicating that the data are consistent with a constant value.

Notice that Jorstad & Marscher (2004) analysed Chandra data using $N_{\rm H} = 3.62 \times 10^{20}\,{\rm cm}^{-2}$, i.e. the Galactic value according to Dickey & Lockman (1990), and that **?** found a value of $N_{\rm H} = (7 \pm 2) \times 10^{20}\,{\rm cm}^{-2}$ when analysing XRT data with an absorbed power law with freely varying $N_{\rm H}$.

The resulting X-ray light curve (flux densities at 1 keV) is shown in Fig. 4.16, where it is compared to the source behaviour at other frequencies.

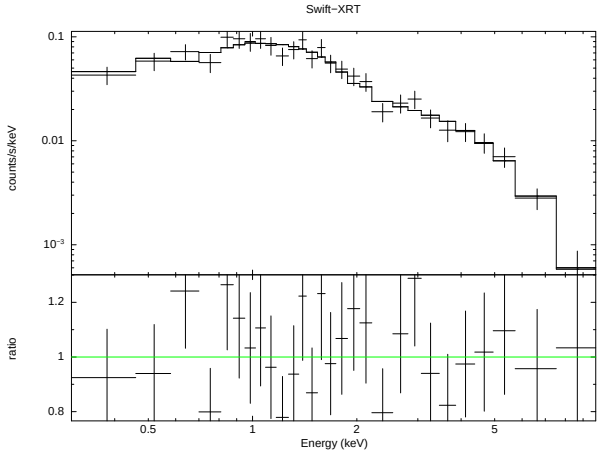

FIGURE 4.14— The XRT spectrum of OJ 248 on 2012 October 2. The best fit was obtained with a power law with fixed absorption given by the sum of the Galactic and intervening DLA $N_{\rm H}$ values. The bottom panel shows the ratio of the data to the folded model.

4.6 *Fermi* observations

The *Fermi* satellite was launched on 2008 June 11. Its aim is to perform a daily mapping of the γ-ray sources in the Universe. The primary instrument of *Fermi* is the Large Area Telescope (LAT; Atwood et al., 2009). The energy range covered is approximately from 20 MeV to more than 300 GeV. The field of view of the LAT covers about 20% of the sky, and maps all the sky every three hours.

The data in this paper were collected from 2008 August 4 (JD = 2454683) to 2013 November 8 (JD = 2456605). We performed the analysis with the **SCIENCETOOLS** software package version v9r32p5. The data were extracted within a Region of Interest (ROI) of 10 radius and a maximum zenith angle of 100 to reduce contamination from the Earth limb γ-rays, which are produced by cosmic rays interacting with the upper atmosphere. Only events belonging to the 'Source' class were used. The time intervals when the rocking angle of the LAT was greater than 52 were rejected. For the spectral analysis we used the science tool `gtlike` with the response function `P7REP_SOURCE_V15`. Isotropic (iso_source_v05.txt) and Galactic diffuse emission (gll_iem_v05.fit) components were used to model the background[10].

We evaluated the significance of the γ-ray signal from the sources within the ROI by means of the Test Statistics TS $= 2\,(\log \mathrm{L}_1 - \log \mathrm{L}_0)$, where L_1 and L_0 are the likelihood of the data given the model with or without the source, respectively (Mattox et al., 1996). As was done in the 2FGL catalog (Nolan et al., 2012), for the spectral modelling of OJ 248 we adopted a power law, $N(E) = N_0\,(E/E_0)^{-\Gamma}$, where $E_0 = 392.1$ MeV is the reference energy between 0.1 and 100 GeV. We first ran `gtlike` with the `DRMNFB` optimizer, including all point sources of the catalog within 15 from our target, and using power-law fits to model the spectra of these sources. We then ran `gtlike` a second time with `NEWMINUIT` as optimizer, after selecting the sources with

[10]http://fermi.gsfc.nasa.gov/ssc/data/access/lat/BackgroundModels.html

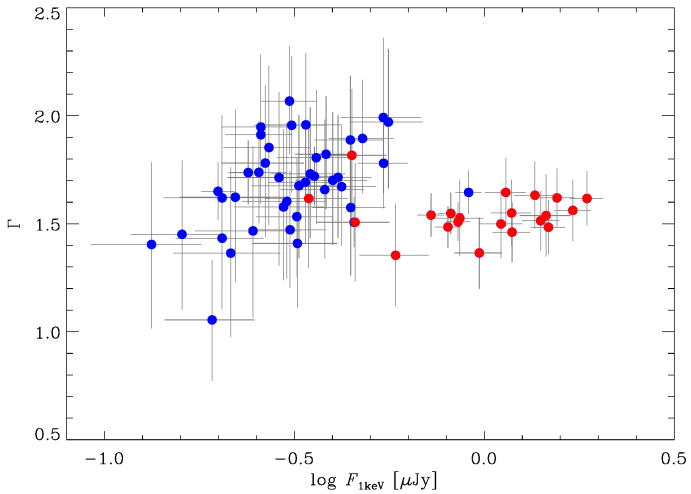

FIGURE 4.15— The X-ray photon index Γ as a function of the unabsorbed flux density at 1 keV. Only data with error less than 30% of the flux are shown. Red points correspond to data acquired after JD = 2456100, i.e. during the 2012–2013 outburst.

TS > 10 and the predicted number of counts $N_{\mathrm{pred}} > 3$.

The results of the analysis are reported in Table 4.1 for time bins of about six months. The average photon index is 2.68, and its standard deviation is 0.22. This value is essentially the same as that reported in the 2FGL catalog (2.67 ± 0.07), while an analysis over the whole period considered in this paper yields $\Gamma = 2.56 \pm 0.03$ and a flux of $(8.6 \pm 0.3) \times 10^{-8}$ ph cm^{-2} s^{-1}. The photon index variability is dominated by errors, since the variance σ^2 is smaller than the mean square uncertainty δ^2 (see Sect. 4). In Fig. 4.16 we can see the corresponding γ-ray light curve (red points). We also plotted a monthly-binned light curve (blue points) that includes many upper limits (cyan points) because of the source faintness. Finally, during the 2013 outburst we performed weekly bins when there was a good count number to detail the flux variations (green points).

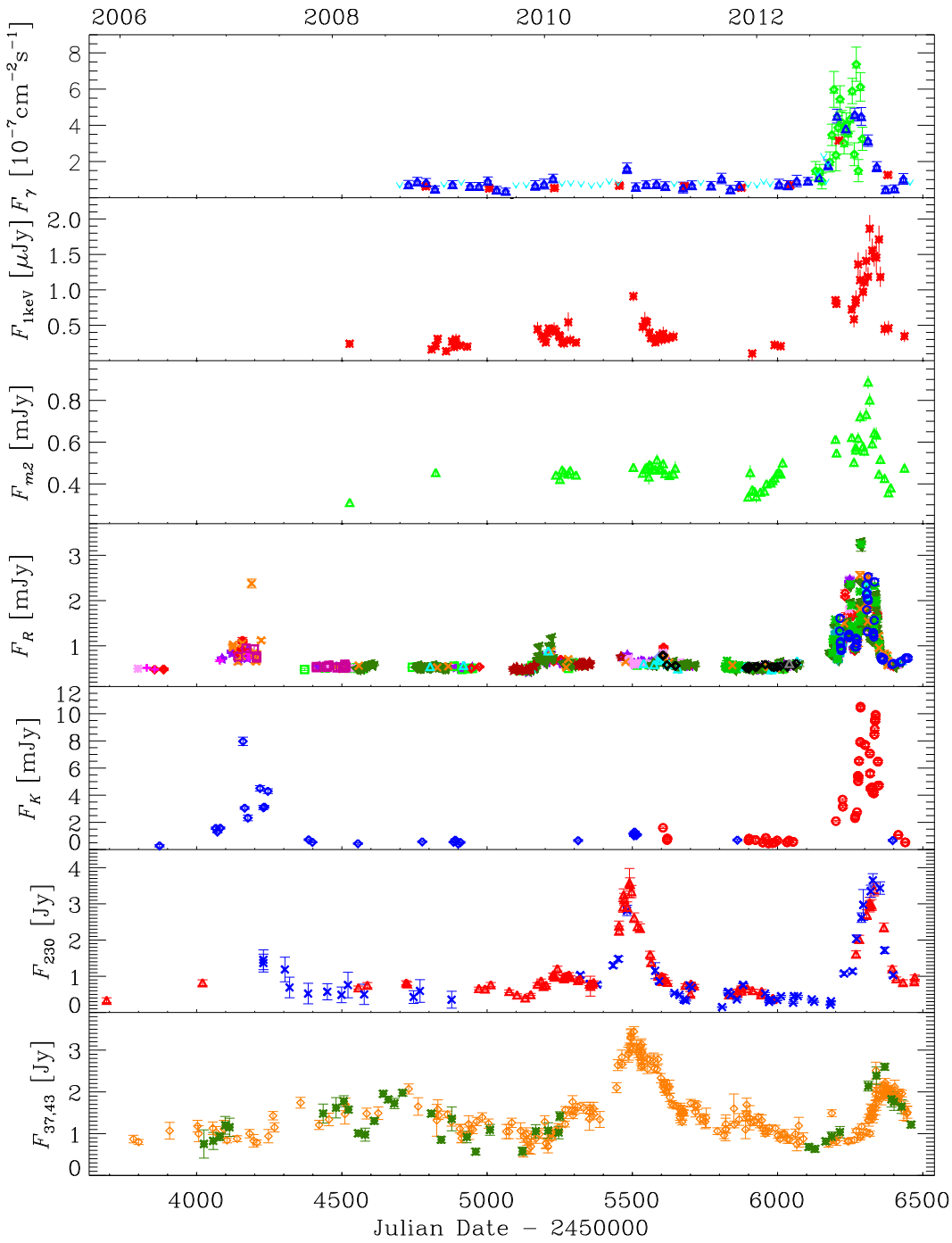

FIGURE 4.16— Light curves of OJ 248 at different frequencies in 2006–2013. From top to bottom: the *Fermi*-LAT 0.1–100 GeV fluxes (10^{-8} ph cm^{-2} s^{-1}) derived with different time bins (red symbols refer to data binned over roughly six-month time intervals, blue ones to monthly binned data, and green symbols to weekly-binned data in the outburst period; cyan arrows indicate upper limits); the 1-keV *Swift*-XRT flux densities (μJy); the *Swift*-UVOT $m2$ flux densities (mJy); the GASP-WEBT R-band flux densities (mJy); the GASP-WEBT K-band flux densities (mJy); the 230 GHz flux densities (Jy); the 37 GHz (orange points) and 43 GHz (green points) flux densities (Jy). The X-ray, UV, optical and near-IR light curves were corrected by both Galactic and DLA absorption.

TABLE 4.1— Results of the spectral analysis of the *Fermi*-LAT data of OJ 248 in the 0.1–100 GeV energy range. The reference energy E_0 was fixed to 392.1 MeV. The fitted model was a power law with photon index Γ.

Date	$N_{\rm pred}$	TS	Γ	$F_{0.1-100\rm GeV}$ $[10^{-8}\,\rm ph\,cm^{-2}\,s^{-1}]$
2008 Aug 04 - 2009 Mar 05	539	125	2.77 ± 0.12	6.2 ± 0.8
2009 Mar 05 - 2009 Oct 15	465	131	2.55 ± 0.11	5.2 ± 0.8
2009 Oct 15 - 2010 May 27	406	104	2.60 ± 0.12	5.3 ± 0.8
2010 May 27 - 2011 Jan 05	466	100	2.83 ± 0.12	6.6 ± 0.9
2011 Jan 06 - 2011 Aug 18	439	97	2.81 ± 0.13	6.4 ± 1.0
2011 Aug 18 - 2012 Feb 02	283	43	3.13 ± 0.23	5.5 ± 1.0
2012 Feb 02 - 2012 Jul 19	392	107	2.66 ± 0.13	6.9 ± 1.0
2012 Jul 19 - 2013 Jan 03	1975	2106	2.38 ± 0.03	31.5 ± 1.3
2013 Jan 03 - 2013 Jun 20	730	401	2.48 ± 0.07	12.6 ± 1.1
2013 Jun 20 - 2013 Nov 08	313	103	2.56 ± 0.13	6.5 ± 1.1

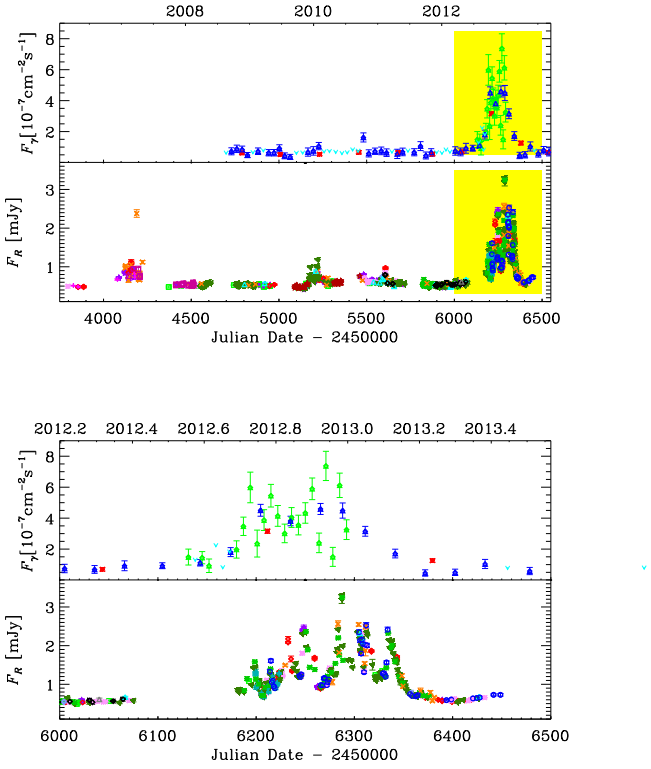

FIGURE 4.17— Light curves in the γ-ray and optical (R) bands over the whole period (top), and during the 2012–2013 outburst period indicated by the yellow stripe (bottom).

4.7 Correction for Galactic and DLA extinction

In the previous sections we presented light curves of OJ 248 as observed magnitudes. But the near-IR, optical, and UV radiation from the source suffers absorption by both the Galaxy dust and the dust contained in the intervening DLA system at $z = 0.525$ mentioned in the Introduction. This is a problem similar to that met when analyzing data from another well-known blazar, AO 0235+16 (Raiteri et al., 2005).

We estimated the Galactic reddening in the $UBVRIJHK$ optical and near-IR bands by using the Cardelli et al. (1989) extinction law, with $R_V = A_V/E(B-V) = 3.1$, which is the standard value for the diffuse interstellar medium. The results are reported in Table 4.2 (Column 2). An estimate of the extinction due to the DLA system can be calculated starting from the hydrogen column density $N_H = (2.0 \pm 0.2) \times 10^{20}\,\mathrm{cm}^{-2}$ obtained by Rao & Turnshek (2000) and adopting a gas-to-dust ratio equal to the average value in the Milky Way: $N_H = 4.93 \times 10^{21}\,\mathrm{cm}^{-2}\,\mathrm{mag}^{-1} \times E(B-V)$ (Diplas & Savage, 1994). This yields $E(B-V) = 0.04$, and assuming again $R_V = 3.1$, we obtain $A_V = 0.124$ at $z = 0.525$. Then, by applying the same Cardelli et al. (1989) law properly blueshifted, we get the values reported in Table 4.2 (Column 3). We note that the DLA system is a more important absorber than the Galaxy. The assumption that the DLA system has the same absorbing characteristics of the Milky Way is justified by its being a spiral galaxy (Rao et al., 2003). The values of the total extinction that we must apply to correct our data for absorption in both the Galaxy and the DLA system are given in Column 4.

In the case of the *Swift*-UVOT bands, because of the asymmetric shape of the filter responses and of the bumped shape of the extinction law in the UV, we calculated the absorption in the various bands by integrating the Cardelli et al. (1989) law with the filter effective areas (see e.g. Raiteri et al., 2010). The results are shown in Table 4.2.

TABLE 4.2— Extinction [mag] in the various Bessel (Bessell et al., 1998) and *Swift*-UVOT bands toward OJ 248. Both the Galactic absorption and that by the DLA system at $z = 0.525$ are given. The value of the total extinction suffered by the source radiation is the sum of the two.

Band	A_λ(Gal)	A_λ(DLA)	Total
Swift-UVOT bands			
$w2$	0.249	0.397	0.646
$m2$	0.261	0.343	0.604
$w1$	0.211	0.331	0.542
u	0.150	0.349	0.499
b	0.125	0.240	0.365
v	0.095	0.196	0.291
Bessel bands			
U	0.142	0.316	0.458
B	0.122	0.235	0.357
V	0.093	0.195	0.288
R	0.077	0.173	0.250
I	0.055	0.131	0.186
J	0.027	0.074	0.101
H	0.017	0.045	0.062
K	0.011	0.028	0.039

4.8 Cross-correlation between variability at high and low energies

In order to better investigate the relationship between the source behaviour in γ-rays and that in the optical band, we show in Fig. 4.17 the corresponding whole light curves as well as an enlargement of the 2012–2013 outburst period, where the correlation is easier to study. The start of the γ-ray outburst is not covered in the optical band because of the solar conjunction, but the first point after the seasonal gap is about 0.3 mag brighter than before, suggesting that the outburst has already begun. In contrast, the optical light curve is very well sampled in the outburst decline phase, where the γ-ray curve has a worst time resolution because of the low flux. It seems that the γ and optical fluxes may well have risen and declined together, but that the period of major γ activity preceded the phase of strongest optical activity.

To get a quantitative estimate of this time shift, we calculate the DCF (see Sect. 4.4) between the γ-ray fluxes and the R-band flux densities corrected for the total absorption reported in Table 4.2[11]. The DCF is displayed in Fig. 4.18. It shows a peak at a lag of $\tau_{\rm p} = 28$ days with $\mathrm{DCF_p} = 1.3$ that indicates strong correlation with the optical variations following the γ-ray ones after four weeks. The delay is 29 days if we take the centroid instead of the peak. The figure inset displays the result of 2000 Monte Carlo simulations according to the "flux randomization-random subset selection" method (Peterson et al., 1998; Raiteri et al., 2003). From these simulations it is possible to estimate the uncertainty on the delay. We obtained that 88% of the realizations led to a centroid value between 22 and 36 days. Hence, we infer that the optical flux variations follow the γ flux changes with a delay of 29 ± 7 days.

[11] We considered the weekly γ fluxes during the outburst period, and the monthly fluxes before and after that (see Fig. 4.17), while we binned the optical data in seven-day bins.

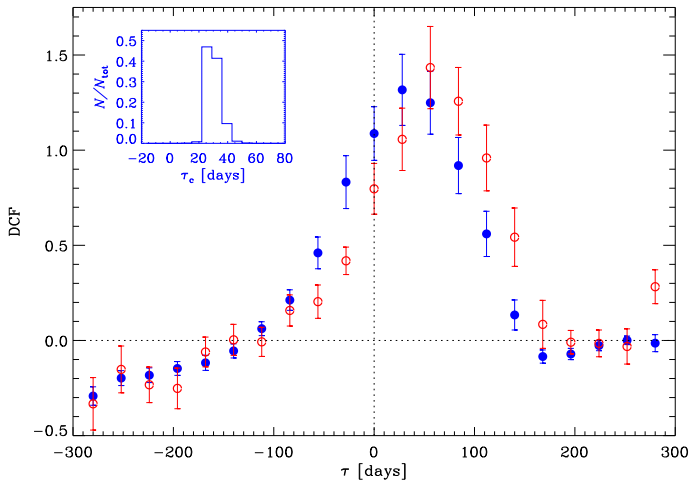

FIGURE 4.18— Discrete correlation functions between the γ-ray fluxes and the R-band de-absorbed flux densities (blue filled circles) and between the γ-ray fluxes and the X-ray flux densities at 1 keV (red empty circles). The inset shows the results of Monte Carlo simulations of the γ-optical correlation (see text for details).

However, if the γ emission is due to inverse-Compton scattering of soft photons off the same electrons producing the optical radiation, then its variations are expected to be simultaneous or delayed with respect to those characterising the optical radiation, as resulting from modelling non-thermal flares with shocks in a jet (e.g. Sikora et al., 2001; Sokolov et al., 2004; Sokolov & Marscher, 2005). This was observed in several blazars, in particular in the FSRQs 4C 38.41 (Raiteri et al., 2012), 3C 345 (Schinzel et al., 2012), and 3C 454.3 (Bonning et al., 2009; Vercellone et al., 2010; Raiteri et al., 2011). In contrast, γ variations leading the optical ones were observed e.g. in the FSRQs PKS 1510-09 by Abdo et al. (2010) and D'Ammando et al. (2011), and 3C 279 by Hayashida et al. (2012). The latter authors found a lag of about 10 days and explained it by assuming that the energy density of the external seed photons for the inverse-Compton process decreases faster along the jet than the energy density of the magnetic field causing the synchrotron optical emission (see also Janiak et al., 2012). Analogous interpretations may also hold for OJ 248.

Alternatively, the complex optical/γ-ray correlation may be explained by considering the effects of turbulence in the jet (Marscher, 2014). The fluctuating magnitude and direction of a turbulent magnetic field affects mostly the synchrotron radiation, and therefore adds a component to the optical variability that is not present in the gamma-ray light curve.

Figure 4.18 also displays the DCF between the γ-ray fluxes and the X-ray flux densities at 1 keV, suggesting a delay of the X-ray variations of about 2 months. We finally investigated the γ-mm correlation, finding a strong signal and a $\sim$ 70 days delay of the mm variations.

Another interesting correlation holds between the X-ray and mm flux densities. Indeed, beside the 2012–2013 outburst, the X-ray light curve also shows a peak during the maximum of the mm light curve at the end of 2010 (see Fig. 4.16). The DCF in Fig. 4.19 displays a strong

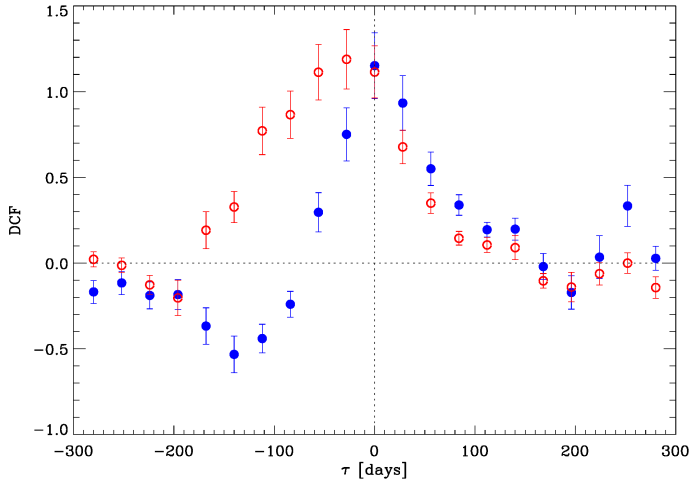

FIGURE 4.19— Discrete correlation functions between the X-ray and 230 GHz flux densities (blue filled circles) and between the X-ray and R-band de-absorbed flux densities (red empty circles).

correlation with no time lag, which suggests that the X-ray and mm radiation are produced in the same region, with the mm emission likely due to inverse-Compton on the mm photons. A correlation between the X-ray and mm variability has already been found, e.g. in BL Lacertae (Raiteri et al., 2013).

In Fig. 4.19 we also show the DCF between the X-ray and optical flux densities, indicating that the optical variations precede those in the X-rays by about one month.

Cross-correlations of the γ-ray, X-ray, and R-band data with the 37 GHz data only led to weak and somewhat confused signals. This is due to the different behaviour of the corresponding light curves, in particular to the dominance of the 2010–2011 outburst with respect to the 2013 one at 37 GHz.

4.9 Broad-band SED

Three broad-band SEDs of OJ 248 are plotted in Fig. 4.20. They correspond to the peak of the γ-ray emission (JD = 2456284), to the peak of the X-ray emission (JD = 2456317), and to a faint post-outburst epoch (JD = 2456368). The SEDs are built with simultaneous near-IR, optical, UV, X-ray, and γ-ray data. Because of the smoother radio variability, we gave a tolerance of a few days to the radio data.

Emission in the optical–UV receives an important contribution from the accretion disc radiation, whose signature is more evident in the faint, post-outburst SED. The concave shape of the near-IR spectrum is due to the intersection between the disc contribution and the non-thermal jet emission. These two components have been modelled by Raiteri et al. (2014), who found that the OJ 248 disc is more luminous than a typical type 1 QSO disc.

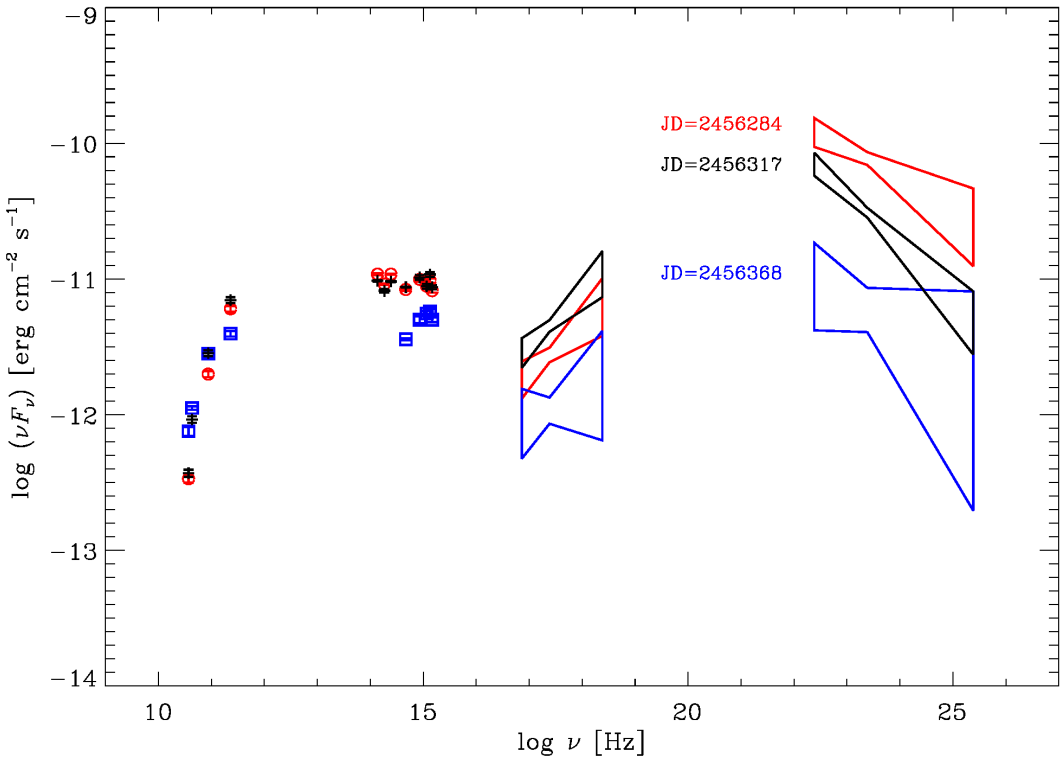

FIGURE 4.20— Spectral energy distributions of OJ 248 from the radio to the γ-ray frequencies during three epochs characterised by different brightness states.

Notice that the faintest SED at high energies has also the lowest radio flux at 230 GHz, but it exceeds the fluxes of the other SEDs at longer radio wavelengths.

Summary and Conclusions

In this chapter we have presented the results of a huge multiwavelength observing effort led by the GASP-WEBT Collaboration on the blazar OJ 248. Data were collected starting from 2006 and up to 2013, including two optical-NIR outbursts in 2006–2007 and 2012–2013 and two major radio outbursts in 2010–2011 and 2012–2013. The 2012–2013 outburst was also detected at high energies by the *Swift* and *Fermi* satellites. The correlation between the optical and radio outbursts is clear in 2012–2013, while the optical counterpart of the 2010–2011 radio outburst is difficult to identify. Something likely changed in the source in the period between the two outbursts, one possibility being a slightly better alignment of the optical emitting region with the line of sight with the consequent increase of the Doppler beaming. A strong correlation between the flux variations at γ-rays and those in the optical band is found, but with the optical variations delayed by about one month, which is a peculiar behaviour already found in other blazars. Strong correlation with no time delay has also been found between the X-ray and millimetre flux changes, supporting a common emission region in the jet.

We have analysed the polarimetric behaviour of the source. The fraction of polarised flux

remained low for most of time but during the 2012–2013 outburst, when P reached $\sim 19\%$. Wide rotations of the linear polarisation vector can reliably be detected only during the outburst and they occur in both directions, suggesting a complex behaviour of the magnetic field in the jet possibly due to turbulence, and/or a complex jet structure involving spiral paths.

Optical spectra show Mg II lines both in absorption and emission. The absorption line is due to an intervening system at z=0.525 whose reddening effects on the NIR, optical, and UV source emission have been estimated and taken into account. The presence of the intervening system must be considered also when analysing the X-ray radiation. As for the Mg II emission line from the source BLR, we estimated a mean velocity of $(2053 \pm 310)\,\mathrm{km\,s^{-1}}$. The line flux is essentially stable around a mean value of $(6.2 \pm 0.5) \times 10^{-15}\,\mathrm{erg\,cm^{-2}\,s^{-1}}$ also during the 2012–2013 outburst and after, confirming that the jet emission did not affect the BLR, even when considering up to a few months of possible time delay.

5

Multiwavelength behaviour of the BL Lac object Mrk 421.

We report on long-term multi-wavelength monitoring of blazar Mrk 421 in photometry, spectroscopy and polarimetry by the GASP-WEBT collaboration and Steward Observatory. We study the source behaviour in the period 2007-2015, characterized by several extreme X-ray and optical flares. The ratio between the optical and X-ray fluxes is very variable.

We analyse spectropolarimetric data and find wavelength dependence of the polarization degree (P) which is compatible with the presence of the host galaxy and no wavelength dependence of the electric vector polarisation angle (EVPA). Optical polarimetry shows a lack of simple correlation between P and flux and wide rotations of the EVPA.

We build broad-band spectral energy distributions (SEDs) with simultaneous near-infrared and optical data from the GASP-WEBT and UV and X-ray data from the *Swift* satellite. They show strong variability in both flux and X-ray spectral shape and suggest that the synchrotron peak can shift in frequency by a factor ~ 30. This shift does not depend in a simple way on the brightness state.

The interpretation of the flux and spectral variability seems to require jet models including more than one emission components or, alternatively, an inhomogeneous jet where the emitting regions can change their orientation with respect to the line of sight.

Introduction

As already mentioned the typical blazar emission consists of two spectral components: the low energy one contributes to the radio through optical regime and is attributed to synchrotron radiation from relativistic electrons; the high energy one is likely inverse Compton scattering radiation, peaking in the γ-ray regime.

Polarized radiation from blazars, conforming the synchrotron nature of the low-energy emis-

sion, can vary sharply. Thus, the polarization of blazars is of interest for understanding the origin, confinement, and propagation of jets, due to the dependence of the polarization on the jet's magnetic field structure (e.g. Visvanathan & Wills, 1998).

Mrk 421 at z=0.031 (Ulrich et al., 1975) was the first blazar to be detected at γ-ray energy E >500 GeV (Punch et al., 1992). It is classified as a high-energy-peaked BL Lac (HBL), a relatively low-luminosity source with both synchrotron and inverse Compton peaks located at relatively high energies.

In this chapter we present the optical and near-infrared data obtained by the GASP-WEBT collaboration[1]. We compare the optical flux variations with the X-ray light curves obtained by *Swift*, by performing a cross-correlation analysis on the full dataset available from 2007 to 2015. Moreover, we analyse the spectropolarimetric data acquired at the Steward Observatory in the framework of the monitoring program in support to the *Fermi* mission[2]. Finally, broad-band SEDs are built from the near-infrared to the X-ray energies to investigate the source spectral variability.

5.1 Optical photometry

Optical observations in R band for the GASP-WEBT were performed with 33 telescopes in 26 observatories around the World. These observatories are: Abastumani (Georgia), AstroCamp (Spain), Belogradchik (Bulgaria), Calar Alto (Spain), Castelgrande (Italy), Crimean (Russia), Lowell (USA), L'Ampolla (Spain), Lulin (Taiwan), New Mexico Skies (USA), Pulkovo (Russia), ROVOR (USA), Roque de los Muchachos (Spain), Rozhen (Bulgaria), Sabadell (Spain), Sirio (Italy), Skinakas (Greece), St. Petersburg (Russia), Talmassons (Italy), Teide (Spain), Tijarafe (Spain), Torino (Italy), Tuorla (Finland), Videojevica (Serbia) and West Mountain (USA).

[1] http://www.oato.inaf.it/blazars/webt/
[2] http://james.as.arizona.edu/ psmith/Fermi/

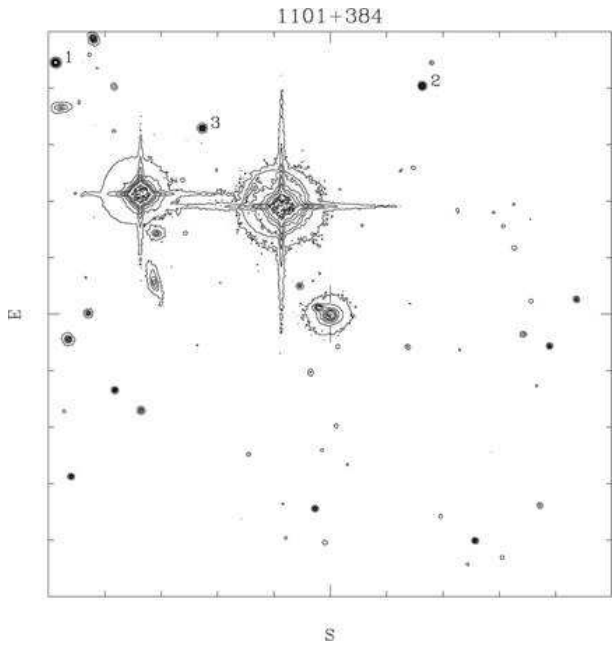

FIGURE 5.1— Finding chart for Mrk 421 with the stars of the optical photometric sequence labelled from 1 to 3. The field of view is ∼10'×10'.

Calibration of the source magnitude was obtained with respect to the reference stars 1, 2 and 3 shown in Fig. 5.1 (Villata et al., 1998). The presence of two extremely bright stars in the field between the source and the reference stars makes photometry of Mrk 421 a delicate task, especially in the near-infrared.

We collected 5230 optical data points in the period 2007 November 08 (JD=2454412.7) to 2015 July 23 (JD=2457227.4). Light curves in R band were built by carefully assembling the datasets coming from the different telescopes. Moreover, binning was used to reduce the noise of data acquired close in time by the same telescope. Offsets caused by partial inclusion of the host galaxy were minimized by adopting the same prescriptions for the photometry: an aperture radius of 7.5 arcsec for the source and reference stars, and an annulus of 10 and 16 arcsec radii centred on them for the background. The final light curves are shown in Fig. 5.2 where different symbols and colours highlight data from the various telescopes. The data points represent observed magnitudes, with no correction for the Galactic extinction and host-galaxy contribution.

Strong variability characterises the entire period on a large variety of time-scales. In particular, in different epochs we observed a variation amplitude (mag_{max} - mag_{min}) of ∼0.5 mag in ∼25 day, in a couple of cases we found ∼1.3 mag in ∼230 days and in the last tree seasons we saw variation amplitudes of ∼0.6 mag in ∼13 days.

We analysed the light curve to search for the most noticeable intraday variability (IDV) episodes, and found changes of 0.15 - 0.2 mag within the night.

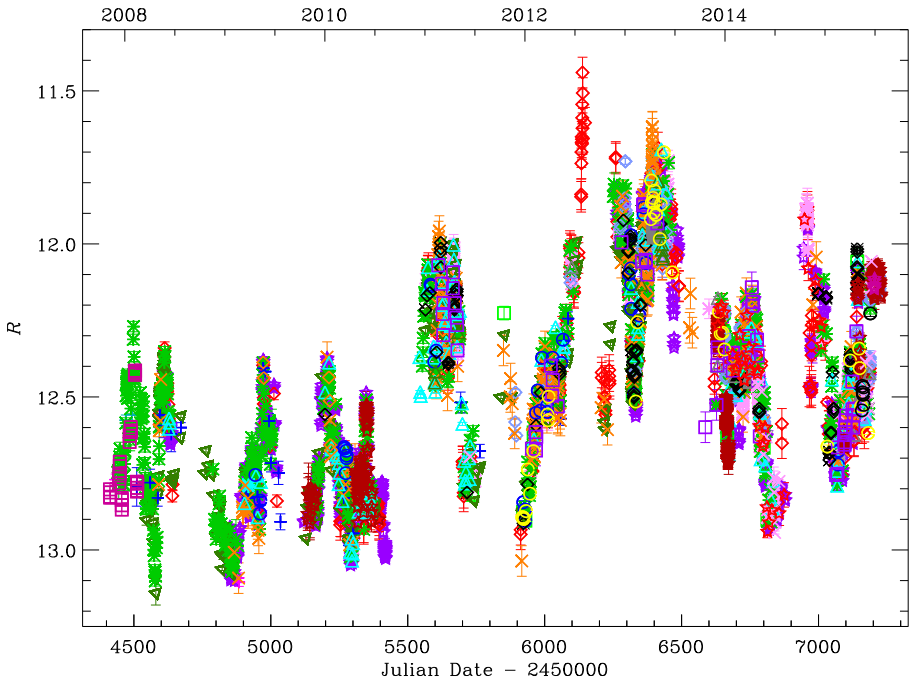

FIGURE 5.2— Optical light curve of Mrk 421 built with data from the GASP-WEBT collaboration in R band. Different colours and symbols highlight data from different telescopes.

5.2 Near-infrared photometry

The near-infrared light curves of Mrk 421 in the period 2011-2015 are shown in Fig. 5.3 in JHK bands. The GASP-WEBT observations were performed by the TCS telescope in the Teide observatory. The light curves were carefully checked and cleaned by reducing the data scattering through binning data close in time. These light curves are generally under-sampled to allow a detailed statement about a correspondence with the optical data, but where sufficient sampling has been achieved, they indicate that a close correspondence exists, as expected. We note that the variability is nearly the same in the three bands. This is due to the important flux contribution by the host galaxy to the near-infrared emission (see the next Section), which hides colour effects (see Section 5.5).

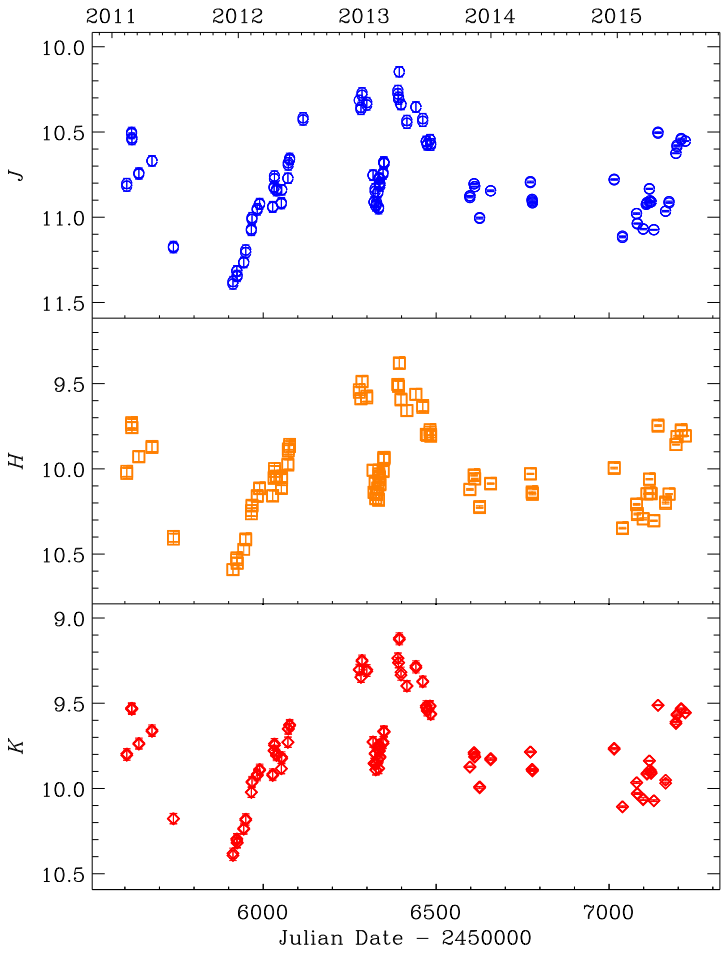

FIGURE 5.3— Near-infrared light curves of Mrk 421 built with data from the GASP-WEBT collaboration in J, H and K bands.

5.3 Removal of the host galaxy contribution

The Mrk 421 host galaxy is relatively bright in optical bands, very strong in the near-infrared, and its flux is small in UV bands.

We used the de Vaucouleurs profile for removing the host galaxy contribution as done by Raiteri et al. (2010) for BL Lacertae. Surface brightness of elliptical galaxies falls off smoothly with radius. Measured along the major axis of the galaxy, the profile is usually well represented by the $r^{1/4}$ de Vaucouleurs law:

$$I(r) = I(0)e^{-kr^{1/4}}$$

where k is a constant. This can be rewritten as:

$$I(r) = I_e e^{\{-7.67[(r/r_e)^{0.25}-1]\}}$$

where r_e is the effective radius, i.e. the radius of the isophote containing half of the total luminosity. I_e is the surface brightness at the effective radius. Typically, the effective radius of an elliptical galaxy is a few kpc.

For Mrk 421 we used r_e=8.2±0.2 arcsec and R_{host}=13.18 mag (Nilsson et al., 2007) to estimate that the host galaxy contribution to the observed fluxes is p = 48% of the whole galaxy flux with a aperture radius of 7.5 arcsec, as used by the WEBTers. We also estimated a p = 25% contribution for a 3.0 arcsec aperture, as adopted for the Steward data in V band and p = 37% for 5.0 arcsec for UV case (see Table. 5.1). We found that the R band observed flux densities must be corrected by 7.862 mJy to clean them from the host galaxy pollution.

We then calculated the host galaxy contribution in the other bands adopting the colour indices determined for elliptical galaxies by Mannucci et al. (2001), applied to the de-reddened R band mag. We adopted a Galactic extinction value of A_R = 0.041 from Schlegel, Finkbeiner & Davis (1998). We note that the colour indices found by Manucci et al (2001) are compatible with those derived from the elliptical galaxy template from the SWIRE database used below.

The optical and near-infrared host magnitudes were converted into flux densities using the zero-mag fluxes given by Bessell et al. (1998). The whole galaxy flux densities were multiplied for the p(r) values to derive the contributions to the source photometry. The results are shown in Table. 5.1.

In the UV case, we used the template of a 13 Gyr elliptical galaxy, available from the SWIRE project[3] (Polletta et al., 2007). We scaled the template in order to have the host galaxy flux expected in the U filter. Galactic extinction in each UVOT band was estimated by convolving the Cardelli et al. (1989) laws with the filter effective areas and source spectrum, adopting R_V=A_V/E(B-V)=3.1, the mean value for the interstellar medium. The results are in Table. 5.1. As can be seen that the host galaxy contribution is relevant in near-infrared and whereas in the UV is negligible.

We checked that using the SWIRE Template method at lower frequencies gives the same results obtained by the colour indices method within a few mJy.

[3]http://www.iasf-milano.inaf.it/ polletta/templates/swiretemplates.html

TABLE 5.1— UV, optical and near-infrared observing bands with the corresponding Galactic extinction values, photometry aperture radius, fractions of the host galaxy contribution included in the given aperture, host galaxy flux density contribution to the source photometry and median observed flux.

Filters	A_λ[mag]	Ap. Rad.[arcsec]	p(r)[%]	F_{gal}[mJy]	$< F_\nu^{obs} >$(total)[mJy]
w2	0.112	5.0	37	0.039	12.011
m2	0.118	5.0	37	0.067	14.305
w1	0.095	5.0	37	0.122	13.922
U	0.083	5.0	37	0.497	
V	0.051	3.0	25	2.794	26.584
R	0.041	7.5	48	7.862	31.412
J	0.014	7.5	48	22.613	74.873
H	0.009	7.5	48	26.786	96.256
K	0.006	7.5	48	20.409	77.443

5.4 Colour analysis

Analysis of colour variations is an important tool to investigate the spectral behaviour of the source and, in turn, the nature of its emission.

In Fig 5.4 we show the J-band light curve in the 2011-2015 period (top panel) together with the corresponding J-K colour indices as a function of time (middle panel) and of brightness level (bottom panel). The colour indices were calculated by selecting J and K data points with small errors and taken by the same telescope within at most 15 min. We obtained that the average J - K value is 1.08, with a standard deviation of 0.03. The data were corrected by the host galaxy contribution as explained in the previous Section.

It can be seen that most of the time, the values of J-K decrease with increasing flux, which is more evident in the bottom panel, where the behaviour of the colour index with brightness is displayed. We observe a loose bluer-when-brighter trend, as expected for a BL Lac object (e.g. Ikejiri et al., 2011). We obtained a linear Pearson's correlation coefficient of 0.56 and Spearman's rank correlation coefficient of 0.55.

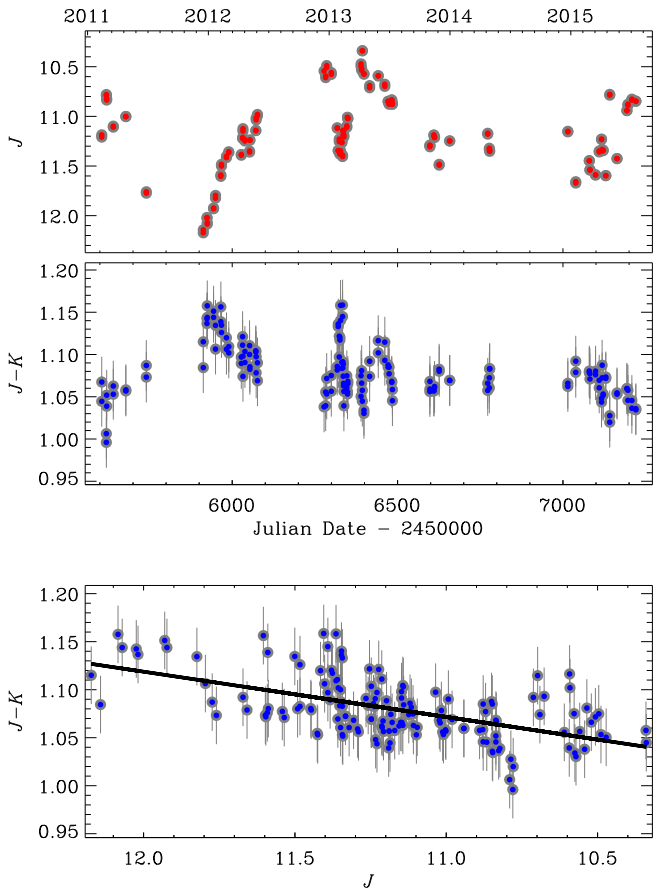

FIGURE 5.4— The J-band light curve in the 2011-2015 period (top panel); the corresponding J-K colour as a function of time (middle panel) and of brightness level (bottom panel). In the bottom panel the solid line represents a linear fit to the data.

5.5 Observations by *Swift*

Here we will present the photometry obtained by the instruments UVOT and XRT. During the 2007-2015 period, the source was observed by the *Swift* satellite during 727 epochs.

5.5.1 UVOT

The photometry obtained in the optical bands v, b, u and UV bands w1, m2 and w2 by the UVOT experiment on board the satellite *Swift* from the NASA's High Energy Astrophysics Science Archive Research Center (HEASARC)[4] archive is presented in this section. We reduced the Mrk 421 observations with the HEASOFT package version 6.17 and the calibration release

[4]http://heasarc.nasa.gov

20150717 of the CALDB data base available at HEASARC. For each epoch, multiple images in the same filter were first summed with the task *uvotimsum* and then aperture photometry was performed with *uvotsource*.

We extracted source counts from a circular region with 5 arcsec radius centred on the source and background counts from a circle with 15 arcsec radius in a source free field region.

The UVOT light curves are shown in Fig. 5.5. They confirm the trend shown by the ground-based optical and near-infrared curves in Fig. 5.2 and Fig. 5.3.

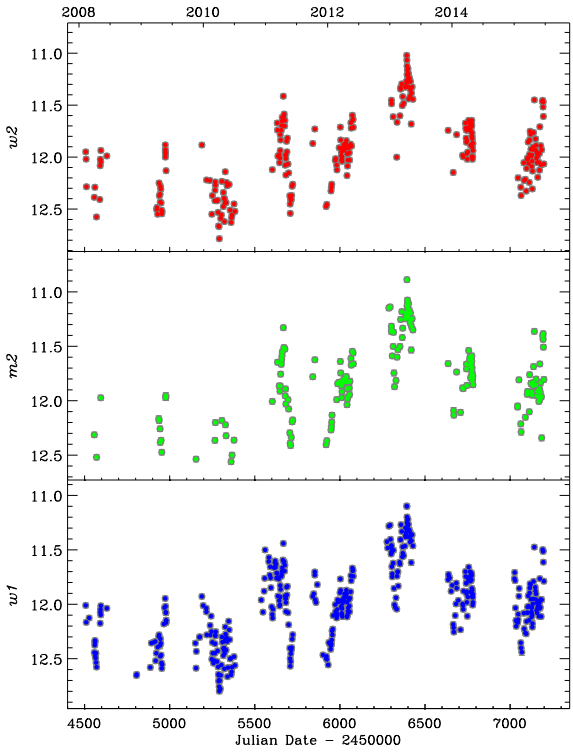

FIGURE 5.5— UV light curves of Mrk 421 built with *Swift*-UVOT data.

5.5.2 XRT

We processed the X-ray Telescope (XRT; Burrows et al., 2005) data with the HEASOFT package version 6.17 and the CALDB calibration files updated 20150721. The task *xrtpipeline* was executed with standard screening criteria. Only observations performed in pointing mode and with more than 50 counts were selected for further analysis. In the 2007-2015 period, we were left with 710 observations in Windowed timing (WT) mode and 16 in photon counting (PC) mode.

We checked the observations and find that all PC observations have a mean rate greater than 0.5 cts s^{-1}, which is the pile up value implies that pile-up correction is needed. In the epochs when we have long exposures in WT mode we did not use the PC observations. In the case of WT mode we found that only three observations have a mean rate greater than 100 cts s^{-1}, implying pile-up.

For the data acquired in WT mode, we selected event grades 0-2 (see Fig. 2.19). We used the same circular region of 70 arcsec radius centred on the source to extract the source counts, and a similar region shifted away from the source along the window to extract the background counts. We thus verified that the background is negligible. We punctured the source-extraction region, discarding the inner 3-pixel radius circle, to correct for pile-up.

The *xrtmkarf* task was used to generate ancillary response files (ARF), which account for different extraction regions, vignetting, and PSF corrections. The X-ray light curve is shown in Fig. 5.6 and is discussed in the next section.

The task *grppha* was used to group the source spectra with the ARF and CALDB redistribution matrix function (RMF) files and bin them in order to have a minimum of 20 counts in each bin for the χ^2 statistics. These spectra were then analysed with the *xspec* package, using the energy channels greater than 0.35 keV to improve the goodness of the fit.

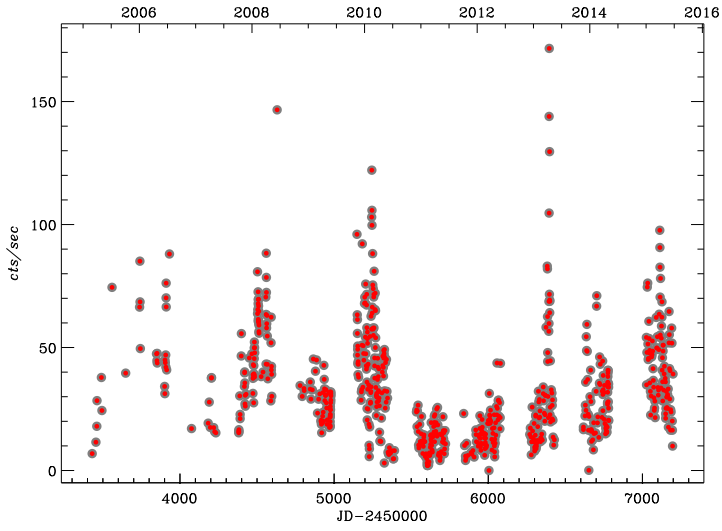

FIGURE 5.6— X-ray light curve of Mrk 421 obtained from data by the XRT instrument onboard the *Swift* telescope in the period 2007-2015.

We applied three different models for the spectral fitting. 1) An absorbed power-law model, where absorption is modelled according to Wilms et al. (2000) and the hydrogen column is fixed to the $N_{\rm H} = 1.61 \times 10^{20} {\rm cm}^{-2}$ as derived from the 21 cm measure by Lockman & Savage (1995); 2) an absorbed power law model but with the $N_{\rm H}$ free; 3) an absorbed log parabola model with $N_{\rm H}$ fixed to the Galactic value. We favoured the third model, whose χ^2 is usually smaller than

the other models, and that produces results with smaller errors. In Fig. 5.7 we show the χ^2 versus the number of degrees of freedom (ndof). The χ^2 is more stable when the log parabola model is applied but it increases with ndof. This is possibly due to a pronounced curvature. Fig. 5.8 shows an example of XRT spectrum. It was best-fitted with a log parabola.

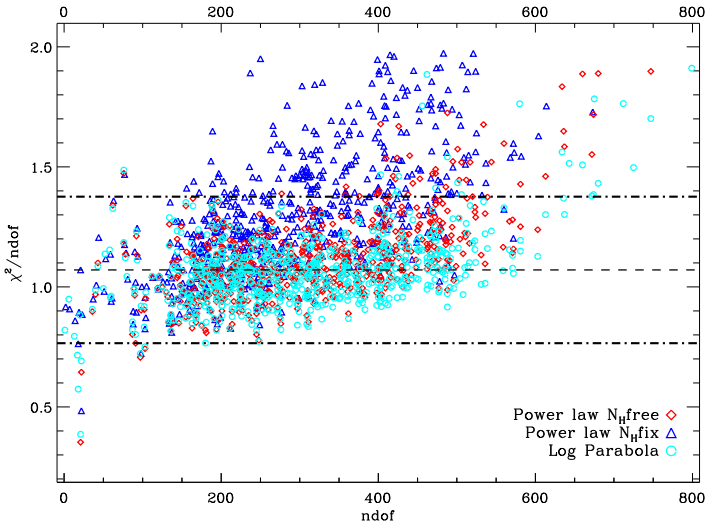

FIGURE 5.7— Reduced χ^2 versus the number of degrees of freedom for the different models applied to the XRT spectra. Blue triangles represent the results of the power law model with fixed $N_{\rm H}$, red diamonds those of the power law model with $N_{\rm H}$ free and the cyan circles those of the log parabola model.

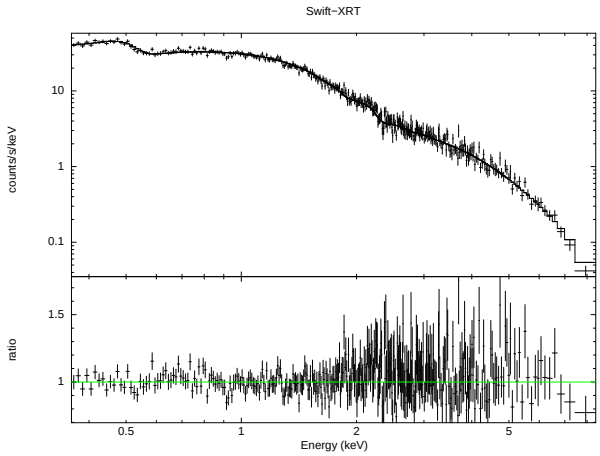

FIGURE 5.8— The XRT spectrum of Mkr 421 on 2008 February 13. The best fit was obtained with a log parabola model. The bottom panel shows the ratio of the data to the folded model.

In the following we will not consider the case of power law model with $N_{\rm H}$ free because it implies a large spread of $N_{\rm H}$ values, which very unlikely correspond to a physical scenario (see Fig. 5.9). In the case of power law model with fixed $N_{\rm H}$ the photon index Γ ranges from 1.66 to 2.99, indicating a spectrum that oscillates from hard to soft. The average value is 2.34, with standard

deviation of 0.26. To understand whether these spectral changes correspond to real variations or are due to noise, we recall the definition of the mean fractional variation $F_{var}=\sqrt{\sigma^2-\delta^2}/\langle f\rangle$ (Peterson, 2001), which is commonly used to characterise variability. Here $\langle f\rangle$ is the mean value of the variable we are analysing, σ^2 its variance and δ^2 the mean square uncertainly. In our case, F_{var}=0.11, so we conclude that the variations reflect genuine source variability rather than noise. Fig. 5.10 displays the photon index Γ as a function of the flux density at 1 keV. We note that the lowest Γ values correspond to the highest fluxes, in agreement with the harder-when-brighter trend often observed in blazars.

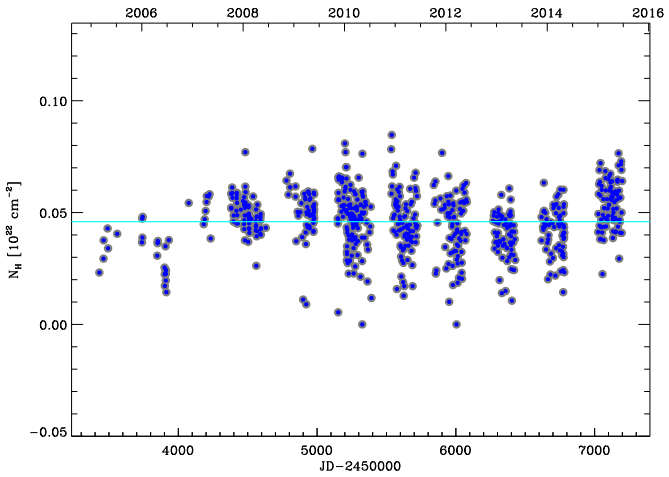

FIGURE 5.9— Time evolution of the Galactic hydrogen column $N_{\rm H}$ when a power law model with free absorption is applied to the XRT spectra. The cyan line marks the average value.

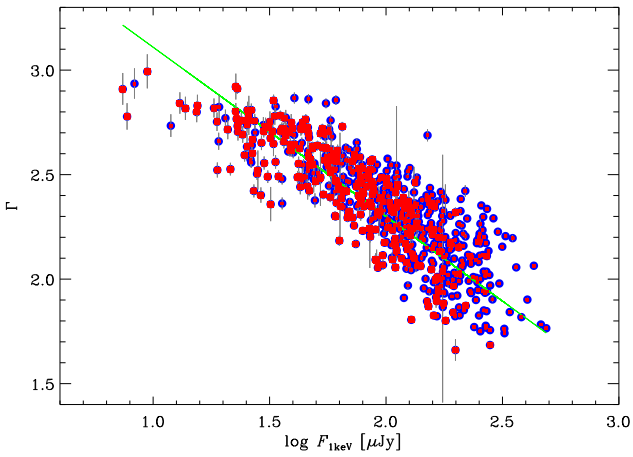

FIGURE 5.10— The X-ray photon index Γ as a function of the unabsorbed flux density at 1 keV. Data with error less than 30% of the flux are shown. Red squares refer to the best-fitted cases, where χ^2 is in the range 0.8-1.2 and the number of degrees of freedom is > 10. The solid line represents a linear fit to the data.

The log parabola model has largely been used to fit the X-ray spectrum of this source. It offers a statistically better fit to the data in the case of curved spectrum. In this model the photon index Γ is replaced by the two parameters: α, the photon index, and β, the spectral curvature. We obtained α values in the range from 1.58 to 2.99, similar to that found for Γ in the power-law case. The average value is 2.27, with standard deviation of 0.28. The mean fractional variation is F_{var}=0.12. The β parameter goes from -0.09 to 0.66, with an average value of 0.24 and standard deviation of 0.10. The mean fractional variation is F_{var}=0.29. The large range of β values indicates strong curvature changes. However, large uncertainties affect the most extreme β values, demanding caution.

In Fig. 5.11 we show the trend of the α and β parameters of the log-parabola model applied to the X-ray spectra of Mrk 421 as a function of the source flux. While α behaves similarly to Γ (Fig. 5.10), confirming the harder-when-brighter spectral property, no clear correlation between β and flux is recognizable. We obtained a linear Pearson's correlation coefficient of 0.86/0.20 and Spearman's rank correlation coefficient of 0.88/0.16 for the α/β cases.

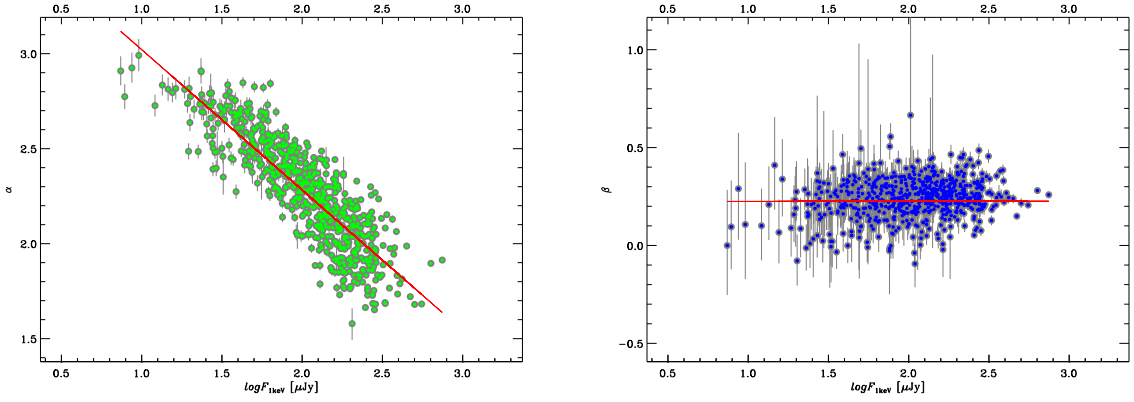

FIGURE 5.11— The behaviour of the α (left) and β (right) parameters of the log parabola model applied to the XRT spectra of Mrk 421. The solid line represents a linear fit to the data.

5.6 Multiwavelength light curves of Mrk 421

Fig. 5.12 shows the multi-wavelength light curves of Mrk 421 from near-infrared to X-ray bands between 2007–2015.

A clear correlation between the X-ray, UV, optical and NIR is visible during the outbursts in 2013, while the X-ray outbursts in 2008 and 2010 lack a major optical counterpart and are difficult to identify in UV because of poor sample. In contrast, in 2011 we see an outburst in UV, optical and NIR, but not in X-rays.

In Fig. 5.13 we compare the light curves in X-ray and R bands. Interpolations with a cubic spline through the 15-day binned light curves are drawn to highlight the longterm behaviour.

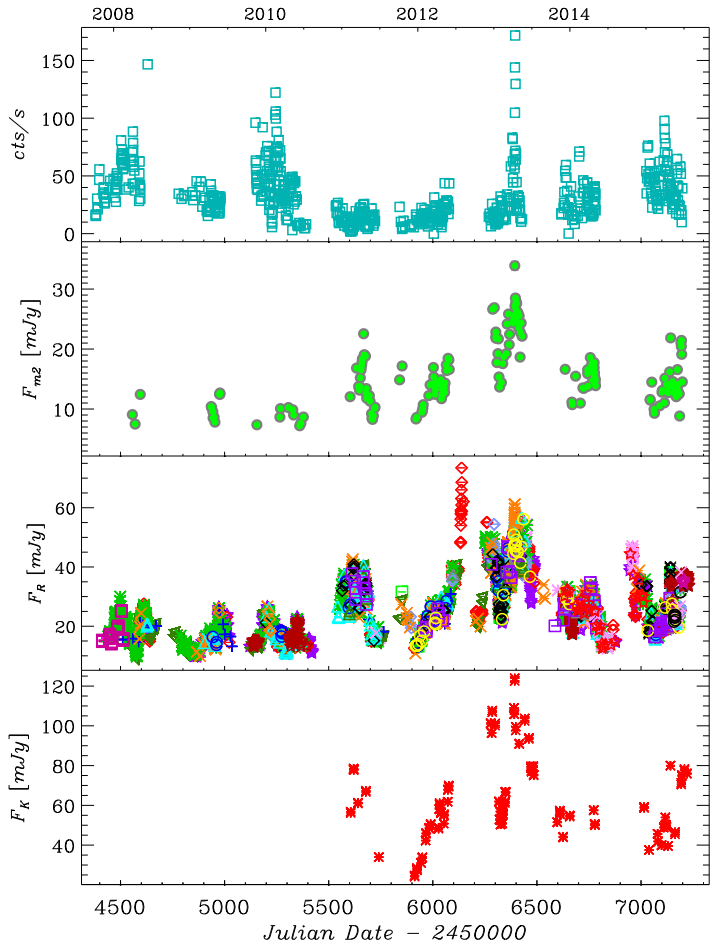

FIGURE 5.12— Light curves of Mrk 421 at different frequencies in 2007-2015. From top to bottom: 1) the X-ray light curve from *Swift*-XRT (counts s^{-1}); 2) the *Swift*-UVOT light curve in the uvm2 band (mJy); 3) the GASP-WEBT R-band flux density light curve (mJy); 4) the near-infrared K band flux density light curve (mJy). The light curves in the m2, R and K bands were corrected for the host galaxy contribution.

The bottom panel shows the ratio between the spline fits to the X-ray and R band. The X-ray emission appears to be strongly dominant in the first two observing periods (OPs) June 2007 to June 2009. Then it decreases in the third OP (June 2009 – July 2010) and reaches a minimum value in the fourth and fifth OPs (October 2010 – June 2012), when the optical emission shows strong activity. Since the year 2013, the X-ray/optical ratio seems to be slowly increasing again.

If both the X-ray and optical radiations in Mrk 421 are produced by synchrotron process, the change in the X-ray/optical ratio then suggests that they do not come from the same jet emission region. This change may indicate a different (and varying) viewing angle of the corresponding emitting zones, with consequent difference in the relativistic Doppler beaming. According to this interpretation, the jet region responsible for the X-ray emission would be more closely aligned

with the line of sight in the first OPs, and more misaligned in the fourth and fifth OPs, while the optical emission would be more Doppler-enhanced during the optical outbursts.

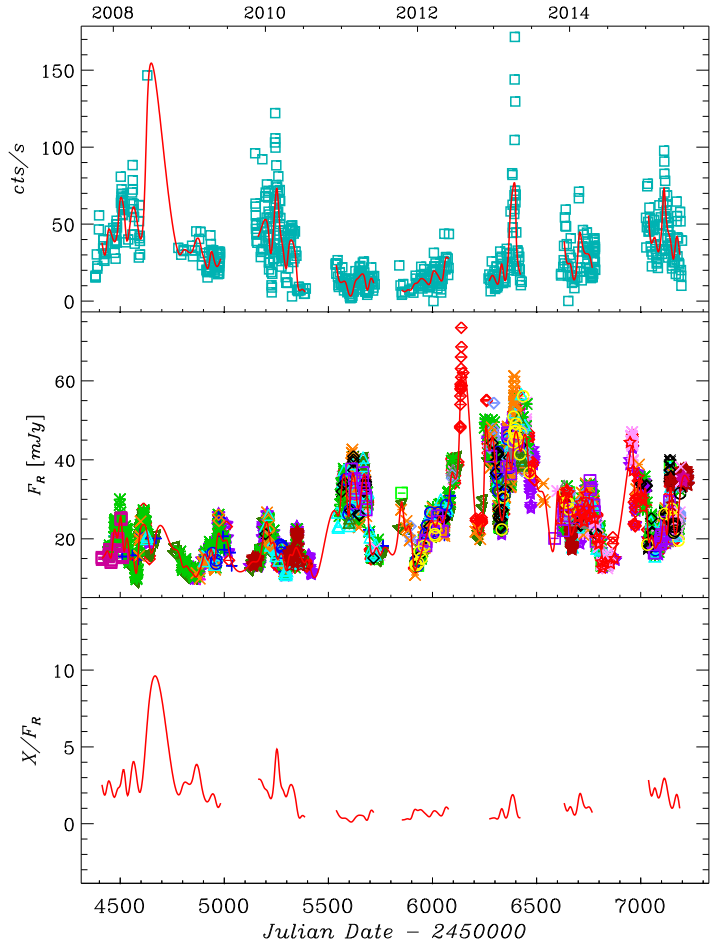

FIGURE 5.13— From top to bottom: 1)the X-ray light curve from *Swift*-XRT (counts s^{-1}) with the cubic spline interpolation through the 15-day binned data; 2) the GASP-WEBT R-band flux density light curve (mJy) with the cubic spline interpolation through the 15-day binned data; 3) the ratio between the spline fits to the X-ray and R band.

5.7 Long term optical polarization variability

Blazar emission is characterised by variable degree of linear polarisation P and electric vector polarisation angle (EVPA; Smith, 1996). We collected 1430 polarisation data in the R-band from the Lowell (Perkins), Crimean, Calar Alto and Steward observatories. While the data of the first three come from photometry, the measurements from the Steward Observatory are derived from 4000-7550 $\mathring{A}$ spectropolarimetry with resolution of $\sim 15\mathring{A}$. The reported P and EVPA values are constructed from the median Q/I and U/I in the 5000-7000 $\mathring{A}$ band. The effective wavelength

of this bandpass is not too different from the Cousin's R-band and the wavelength dependence of the polarization seen in the spectropolarimetry during this period is not strong enough to significantly affect the analysis. Details on the data acquisition and reduction procedures can be found in Jorstad et al. (2010), Larionov et al. (2008) and Smith et al. (2003).

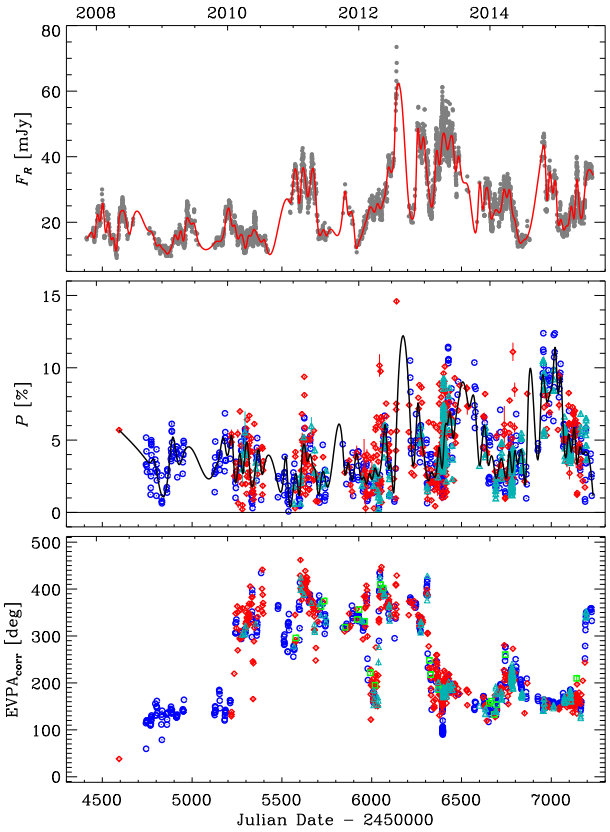

FIGURE 5.14— From top to bottom: a) R-band flux density light curve with cubic spline interpolation through the 15 day binned data (red line); b) polarisation percentage with cubic spline interpolation through the 15 day binned data (black line); different symbols and colours refer to different observatories: Calar Alto (green squares), Crimean (red diamonds), Lowell (cyan triangles) and Steward (blue circles); c) EVPA after correction for the $\pm 180^{\circ} n$ ambiguity.

Fig. 5.14 shows the behaviour of the observed P and EVPA as a function of time for the period 2007-2015. These are compared to the R-band light curve. To solve the $\pm 180°n$ ambiguity in EVPA, we minimized the angle difference between subsequent points, taking the errors on the EVPAs into account. Cubic spline interpolations though the 15-day binned light and polarisation curves are drawn to highlight the long-term behaviour. Visual inspection of the figure reveals that in some cases periods of high flux correspond to periods of high polarisation degree while in other cases the opposite is true. The mean value of P is about 4%, but with variations between 0.07% and 14.6%. We notice that the EVPA values cluster around a mean value of $\sim 4°$ (see Fig. 5.15) but when the $\pm 180°n$ ambiguity is solved, wide rotations appear.

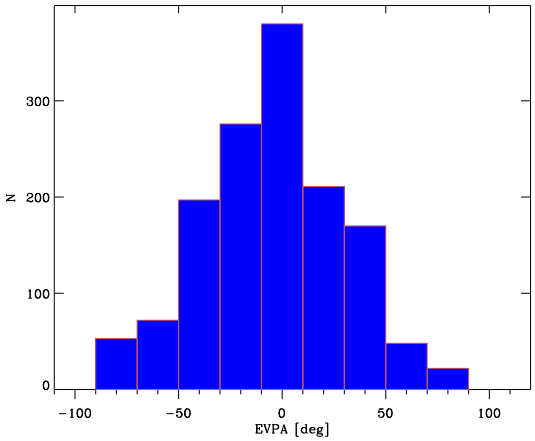

FIGURE 5.15— Histograms of electric vector polarisation angle (EVPA).

In Fig. 5.16 we plot an enlargement of Fig. 5.14 in different periods to better distinguish the variability properties. We warn that in some cases wide rotations derive from EVPA shifts performed when the angle difference between subsequent points was around 90°. Even if we have considered the angle uncertainties, it is clear that an underestimate of the error in these cases could lead to a rotation. This happens on the following dates: JD=2455234, 2455340, and 2455974. In contrast, there are cases where the rotation appears quite robust. In particular, around JD=2456040 we observe a counter-clockwise rotation of $\sim 250°$ in about 10 days. This happens when P reaches a local maximum of $\sim 10\%$ and the flux is rising toward the peak of July–August 2012. Another noticeable episode accurred in the last campaign. The EVPA remained stable for several months, and then rotated by $\sim 200°$ in a counter-clockwise direction in about one month around JD=2457180. In that period P and the flux were in a state of moderate variability. We note that at about half way of the rotation, P experienced a local minimum and the flux showed a small peak. These features are compatible with a geometric scenario where the EVPA rotation is due to a bent trajectory of an emitting blob (e.g. Nalewajko (2010)), where however the blob gives only a limited contribution to the total observed flux. This is a further indication that a multizone scenario is necessary to understand the emission properties of Mrk 421.

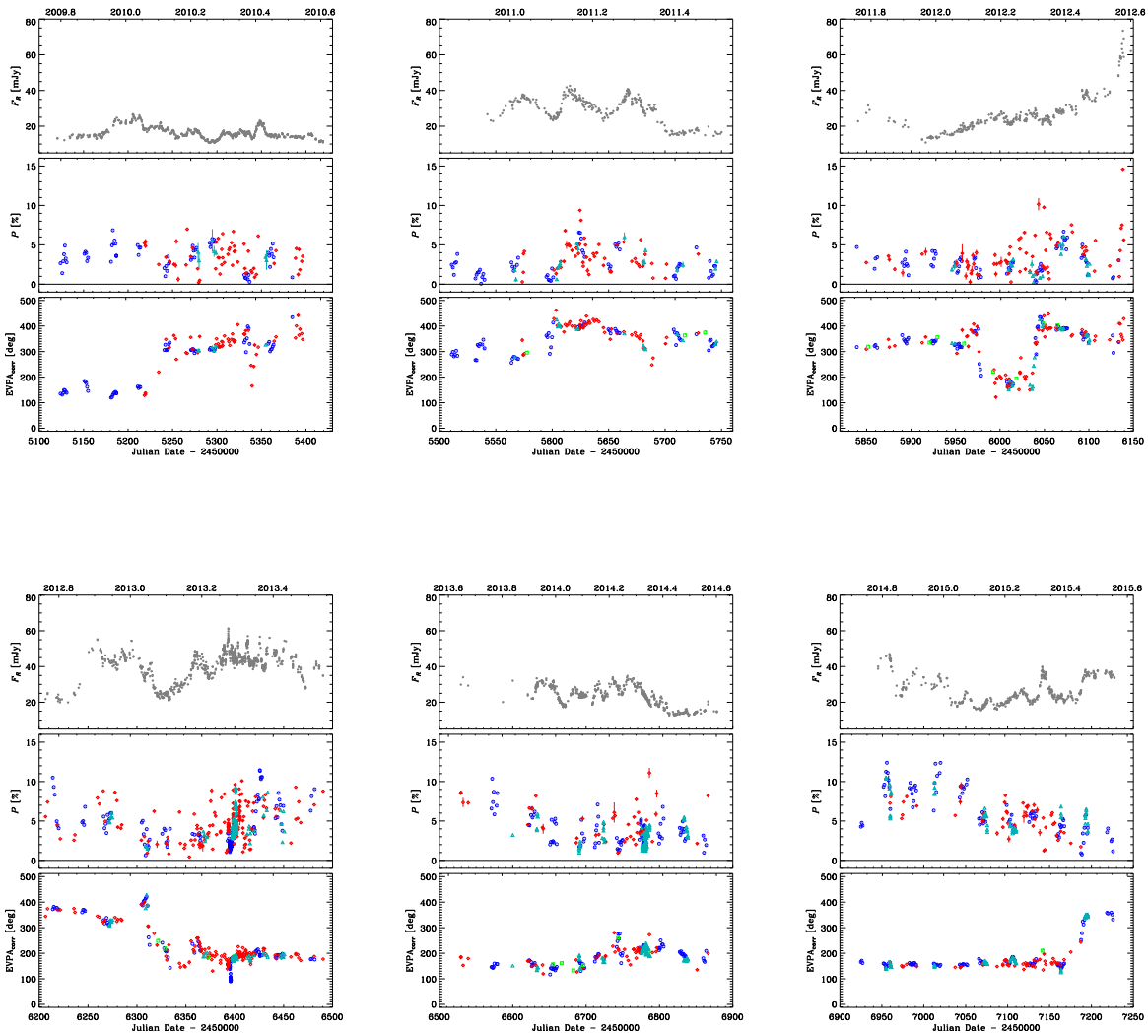

FIGURE 5.16— An enlargement of Fig. 5.14 for different periods where activity is noteworthy.

Up to now we have been dealing with the polarization degree corresponding to the total observed flux. In order to determine the degree of polarization intrinsic to the jet, the unpolarized contribution of the galaxy must be subtracted. In Table 5.1 we have provided the galaxy contribution for a given filter/aperture. The intrinsic polarization is computed using the following expression:

$$P_{jet} = \frac{F_{pol}}{F_{jet}} = \frac{P_{obs} \times F_{obs}}{F_{obs} - F_{gal}}$$

In Fig. 5.17 we show P_{obs} / P_{jet} as a function of the R-band flux density observed/jet. It can be noticed that no apparent correlation exists between the two quantities.

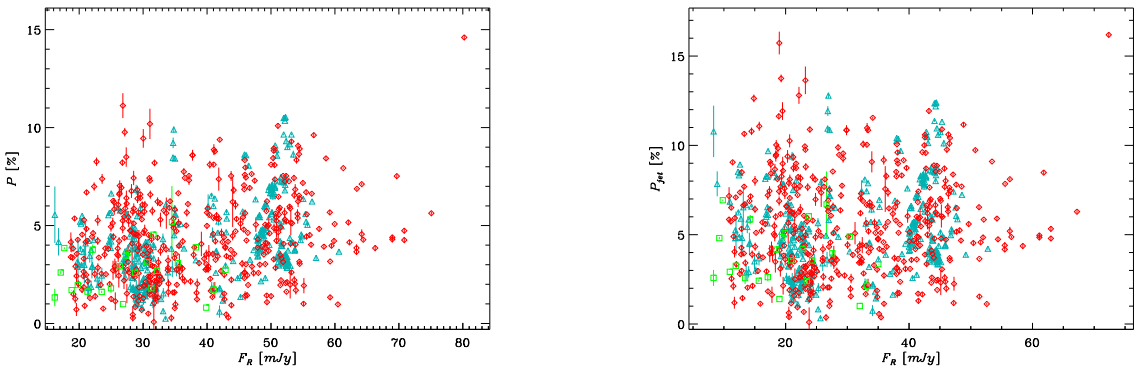

FIGURE 5.17— Degree of polarisation as a function of the R-band flux density. Right: after correction for the host galaxy contribution, left: observed. Different symbols and colours refer to different observatories.

Fig. 5.18 shows the distribution of the Stokes parameters of Mrk 421 in the u versus q plot, highlighting the EVPA rotation occurred during the period of May-June 2015. Subsequent points have been connected with a cubic spline interpolation. The arrows indicate the orientation. The distance of the spline from the origin confirms the genuine nature of the rotation.

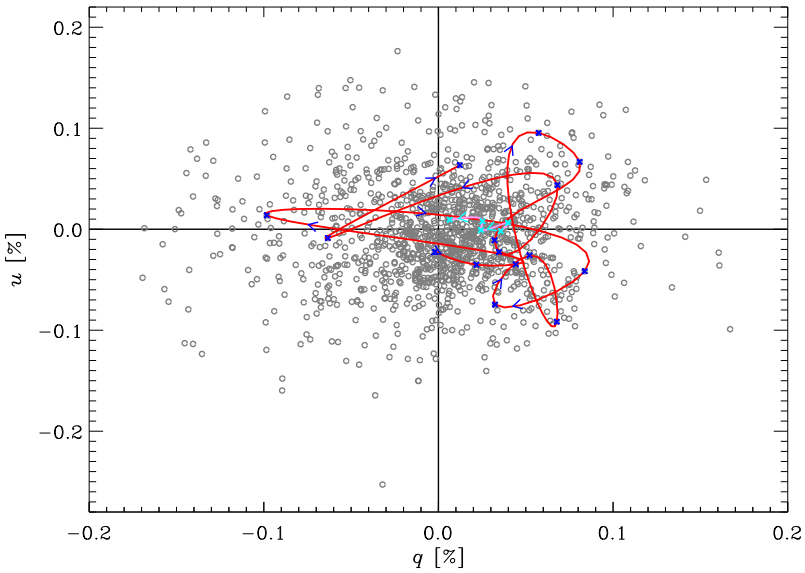

FIGURE 5.18— Stokes parameters q an u of the optical polarization of Mrk 421. Subsequent points have been connected with a cubic spline interpolation. The arrows indicate the orientation.

5.8 Spectral variability of optical polarization

The Steward spectropolarimetry database can be used to examine in detail the optical spectral variability of Mrk 421. We used 603 spectropolarimetric data.

In Figs. 5.19 we display the source spectra corresponding to the maximum and minimum brightness states. They are featureless and show a clear bluer-when-brighter trend.

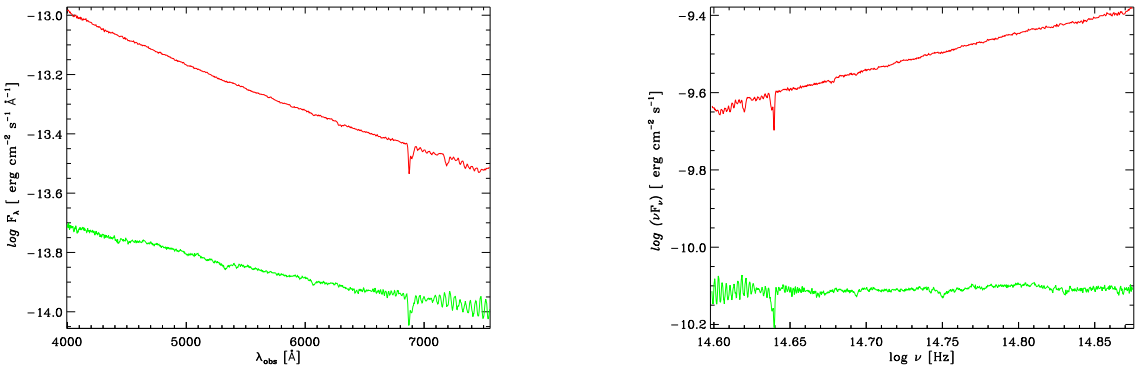

FIGURE 5.19— Left panel: Two of the Mrk 421 spectra obtained at the Steward Observatory. They correspond to the maximum and minimum brightness states, differing by a factor ~ 5 in flux density. Right panel: the same spectra in the $log(\nu F_\nu)$ versus $log(\nu)$ representation.

Fig. 5.20 shows the colour of Mrk 421 as a function of brightness in the V band. The colour is determined as the ratio between the median flux in the range 4000-5000 $\mathring{A}$ ("blue") and that in the 5800-6800 $\mathring{A}$ range ("red"). Although the spectra extend to 7550 $\mathring{A}$, using a redder measurement would include uncorrected terrestrial oxygen and water absorption features and would corrupt the determination of the continuum flux ratio. The bluer-when brighter trend in Figs. 5.19 and 5.20 confirms the broad-band filter results shown in Fig. 5.4.

We then considered the optical polarization, which is derived from the spectropolarimetric data of the Steward Observatory as the median value in the 5000-7000 $\mathring{A}$ range.

We did not find correlation between the degree of optical linear polarisation P and the ratio between the blue and the red fluxes (see Fig. 5.21).

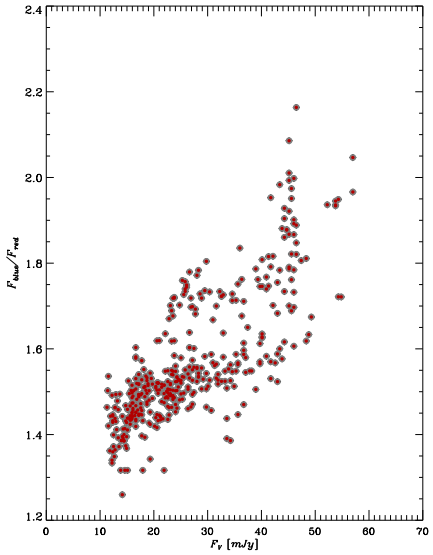

FIGURE 5.20— The continuum colour ("blue" to "red" flux ratio) of Mrk 421 as a function of the source brightness (V-band flux densitiy 5510$\mathring{A}$ in mJy).

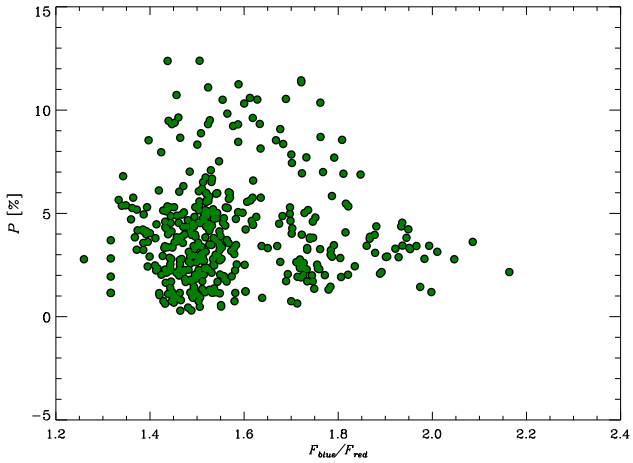

FIGURE 5.21— The observed degree of polarisation plotted against the optical continuum colour of Mrk 421. The polarisation and flux ratio measurements are simultaneous. The polarisation is derived from the Steward Observatory spectropolarimetry as the median value within the 5000-7000 $\mathring{A}$ range.

In Fig. 5.22 we represent the flux densities and polarization percentages from the spectra for the two different ranges of wavelengths. The flux is more variable and polarized in the blue than in the red. This is consistent with the greater contribution from the host galaxy in the red.

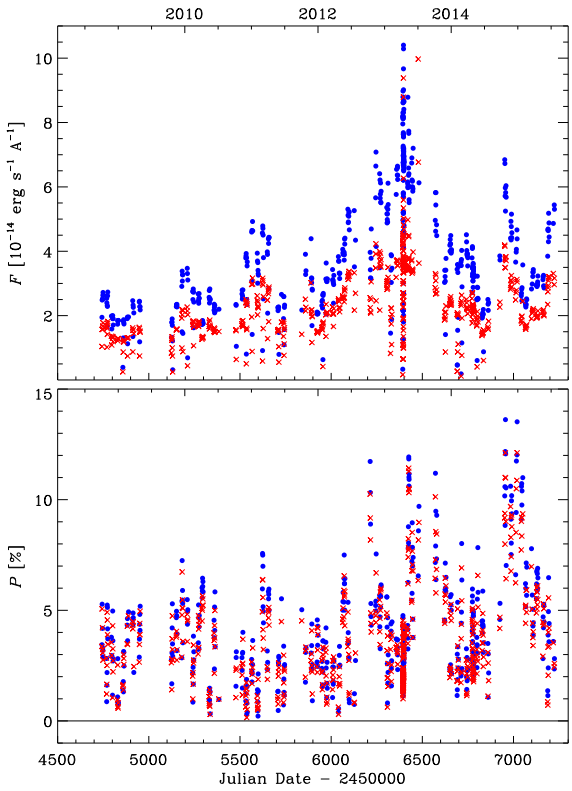

FIGURE 5.22— Time evolution of the observed flux density (top) and degree of polarization (bottom) in two different wavelength ranges (blue and red).

Fig. 5.23 shows the flux ratio between the blue and the red bins plotted against the ratio of the observed polarisation in the same bins. As the blazar becomes redder (fainter), the polarisation in the blue tends to be higher than in the red because of the increasing contribution from the red and unpolarized host galaxy light. However, in the faint states the low levels of polarisation result in relatively large uncertainties in P_{blue}/P_{red}. Fig. 5.23 also shows the difference between the polarisation position angles determined in the two continuum bins. Most observations are consistent with no wavelength dependence in electric vector polarization angle (EVPA). This suggests that there is likely only a single source of polarised flux from the jet. If a second non-thermal source of polarised flux that has a significantly different spectral index and polarisation position angle becomes bright enough to compete with the original source, then a strong wavelength dependence in EVPA would occur although this does not seem to happen frequently (Raiteri et al., 2013).

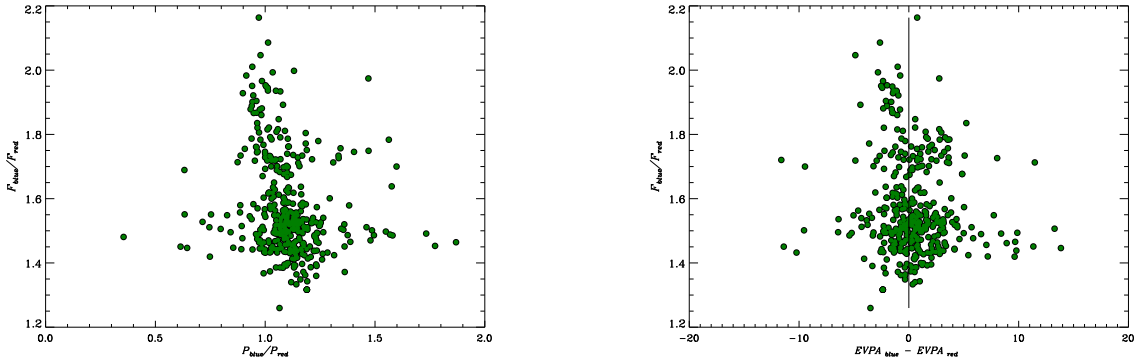

FIGURE 5.23— Left panel: relationship between the ratio of observed polarisation in the blue to red bins and colour, defined as in Fig. 5.20. Right panel: colour versus the difference between the polarisation position angles in the blue and red bins.

5.9 Discrete Correlation Function (DCF)

We apply the Discrete Correlation Function analysis to the data shown in Fig. 5.12 in order to investigate the existence of characteristic time scales of variability and the correlation between the X-ray and optical fluxes. This is a method specifically designed for unevenly sampled datasets (Edelson & Krolik, 1988; Hufnagel & Bregman, 1992), which also allows us to estimate the accuracy of its results.

Given two datasets a_i and b_j, one has first to combine all pairs, calculating the unbinned discrete correlations:

$$UDCF_{ij} = \frac{(a_i - \bar{a})(b_j - \bar{b})}{\sigma_a \sigma_b}$$

where $\bar{a}$,$\bar{b}$ are the average values of the two datasets, and σ_a,σ_b their standard deviations. The DCF is obtained by binning the UDCF_{ij} in time for each time lag τ:

$$DCF(\tau) = \frac{1}{M} \sum UDCF_{ij}(\tau)$$

where M is the number of pairs a_i, b_j whose time lag $\triangle_{ij}$=t_j-t_i is inside the τ bin. Spurious correlations can be found, of the order of $\pm M^{-1/2}$. The standard error for each bin is:

$$\sigma_{DCF(\tau)} = \frac{1}{M-1} \{ \sum [UDCF_{ij} - DCF(\tau)]^2 \}^{1/2}$$

A positive peak of the DCF means correlation, which is stronger as the value of the peak approaches and exceeds one. A negative peak implies anticorrelation. Moreover, the width of the peak must be comparable to those of the autocorrelation functions, obtained by applying the DCF to each dataset coupled with itself.

A preliminary binning of data in time before calculating the DCF usually leads to better results, smoothing out flickering. The size of this binning is crucial especially at the high frequencies, where short-term variations are frequent, since it can remove important information. Furthermore, an increase of the data binning interval implies an increase of the spurious correlations, while an increase of the DCF bin size has opposite effect. The choice of the DCF binning is a delicate point, determining the balance between resolution and noise. In general, a similar value of M for each DCF bin and a limit of 10% to the appearance of spurious correlations must be assured in order to get reliable results.

The discrete correlation function between the X-ray and the R-band light curves over the whole 2007-2015 period is shown in the Fig. 5.24. The lack of a strong signal indicates that the X-ray and optical emissions are in general not correlated. The two peaks with DCF 0.20-0.25 indicate optical events preceding X-ray ones and likely refer to the major flares in 2012 and 2013.

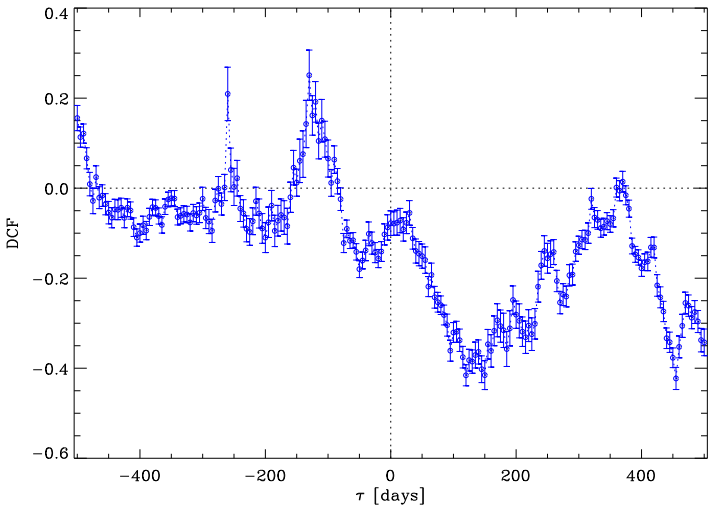

FIGURE 5.24— Discrete correlation function between the X-ray and the R-band light curves over the whole 2007-2015 period.

The optical and X-ray ACF (Auto-Correlation Function) are plotted in Fig. 5.25. The data have previously been binned over 4 days, while the ACF was obtained with a bin size of 20 days. We observed in the optical ACF an important double-peaked signal at $\tau \sim$ 500-575 days, and another one at $\tau \sim$ 860 days. A visual inspection of the optical light curve in Fig. 5.2 confirms these features. In the X-ray ACF we observe a double-peaked signal at $\tau \sim$ 560-635 days, and at $\tau \sim$ 920 days.

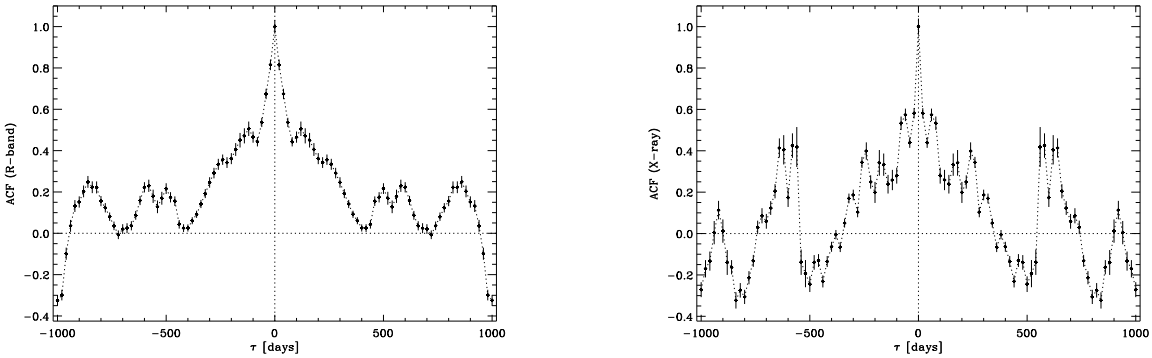

FIGURE 5.25— Auto-correlation function for the galaxy subtracted for the optical fluxes (left) and X-ray rates (right). The data have been binned over 4 days, while the ACF was obtained with a bin size of 20 days.

In Fig. 5.26 we compare in the same plot the optical and X-ray ACFs together with the optical ACF shifted by 60 days. With this shift the optical and X-ray signals overlap. Although these signals are weak, it is interesting to notice that (Sandrinelli et al., 2014, 2016) found periodicities in the optical band that are about half those detected at γ-rays in the blazars PKS $2155-304$ and PKS $0537-441$. This suggests the possible existence of frequency-dependent characteristic time scales of variability in the same objects, with shorter scales corresponding to lower frequencies.

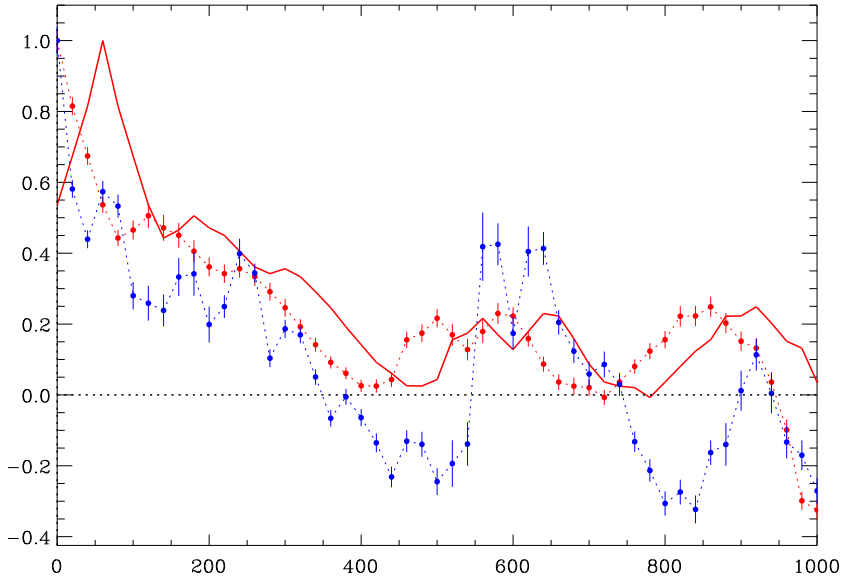

FIGURE 5.26— Optical (red points) and X-ray (blue points) ACFs. The red line represents the optical ACF shifted by 60 days.

5.10 Broad-band spectral variability

We built broad-band SEDs to investigate the spectral variability of Mrk 421 around the synchrotron peak. We searched for observing epochs where simultaneous data in the K, H, J, R bands from the WEBT Collaboration and at UV and X-ray frequencies from the *Swift* satellites were available. Eight of these SEDs are shown in Fig. 5.27, covering a wide range of fluxes. In three cases we also found UVOT data in the v band. The errors in the near-IR and optical flux densities are typically around 3% and are included in the symbol size, while we conservatively assumed a 10% error on the UVOT data. The X-ray spectra are the result of a log-parabola model fitting, including the uncertainties on the flux normalization and α and β parameters.

We note several interesting features. The shape of the low-energy part (near-IR to UV) of all SEDs is very similar, following a wavy path. This starts with a sharp jump from the K to the H filter, remains more or less stable up to the R band, and then rises abruptly toward the UV. We were expecting a kind of power-law shape in the near-IR to optical energy range, so we tend to ascribe the large gap from K to H to a systematically too high flux in the H band. We cannot exclude that it can be due to the uncertainties affecting the subtraction of the host galaxy contribution, which is very important in the near-IR.

The only exception to the above general trend is shown by the SED corresponding to JD=2455678, where the UV spectrum is steep. Interestingly, this corresponds to the faintest and softest X-ray spectrum. We also note that its near-IR and optical part is fairly matching that observed at JD=2457193, but the latter has much brighter UV and X-ray states. If the UV spectrum steepness were real and not due to data uncertainties, its extrapolation to the higher energies would not meet the X-ray spectrum, rising the question whether more than one components are contributing to the source flux or, alternatively, whether the emission comes from an inhomogeneous jet region. Similar mismatches have sometimes been observed in other high-energy peaked BL Lacs, as PG 1553+113 (Raiteri et al., 2015) and H1722+119 (Ahnen et al., 2016). In these two cases, they have been interpreted in terms of orientation effects in an inhomogeneous helical jet model.

An agreement in the near-IR and optical band together with a mismatch in the UV also characterizes the Mrk 421 SEDs at JD=2456038 and 2456335. Here a higher UV state corresponds to a softer and less curved X-ray spectrum.

The X-ray spectral variability is quite strong and suggests that the frequency of the synchrotron peak can shift over a large range. Unexpectedly, the highest peak frequency (JD=2457129) does not correspond to the highest X-ray flux (JD=2456393).

At this point and given the complexity of the observed features, we have not tried modelling the SED with any physical model, which in turn will be the subject of a future work. Mrk 421 has often been modelled with a one-zone synchrotron self-Compton (SSC) model (e.g. Aleksić et al., 2012) or with lepto-hadronic models involving proton synchrotron radiation and/or photopion interactions (e.g. Böttcher et al., 2013).

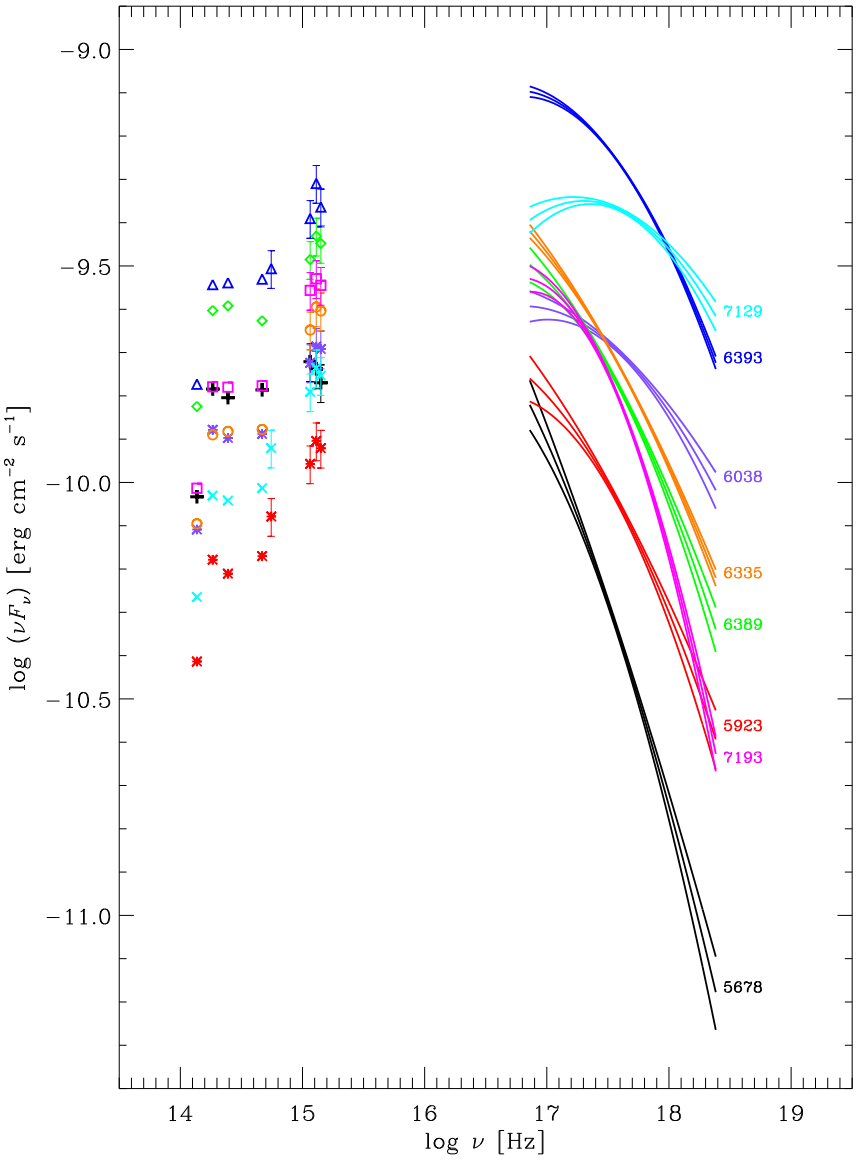

FIGURE 5.27— Broad-band SEDs of Mrk 421 at eight different epochs where simultaneous near-IR, optical, UV and X-ray data are available. They correspond to different brightness states of the source and different spectral shapes in the X-ray energy range. The number correspond with the different JD-2450000.

Summary and Conclusions

We presented an analysis of the long-term multiwavelength emission behaviour of Mrk 421. Near-infrared and optical data were provided by the GASP-WEBT Collaboration, while UV and X-ray data come from observations by the *Swift* satellite. Moreover, spectropolarimetric information acquired at the Steward Observatory was used to study a possible dependency of polarization degree P and angle EVPA on frequency. We calculated the host galaxy contribution

to the source photometry in the near-IR, optical, and UV bands and subtract it to analyse the jet emission.

We found unceasing activity at all wavelenghts over all the 2007–2015 period considered. The near-IR and UV fluxes are well correlated with the optical ones, while the X-ray flux appears to behave in a different way. Prominent X-ray flares occurred in 2008, 2010 and 2013, while major optical flares were observed in 2012–2013. The spectral variability increases with frequency: broad-band SEDs show that the near-IR to optical spectral shape is rather stable for different brightness states, while the upturn toward the UV can be more or less pronounced, and this corresponds to a different X-ray spectral form. Indeed, X-ray spectra exhibit a large range of slopes and curvatures and suggest that the synchrotron peak may cover a large range of frequencies, from $\log \nu \sim 16$ to ~ 17.5.

While in commonly proposed models to interpret blazar variability the SED changes have usually been ascribed to variations in the energy distribution of the synchrotron emitting relativistic electrons, we propose different scenarios. One possibility is the existence of more than one emitting region contributing to the low energy (near-IR to UV) flux, with only one producing also the X-ray radiation. The latter would likely be more internal (i.e. closer to the jet apex) and thus smaller, so that faster variability can arise. Another picture is that of an inhomogeneous jet, where synchrotron radiation of increasing wavelength is coming from zones of increasing distance from the black hole, and where the orientation of these regions can change in time. In this view, periods of high X-ray activity would be observed when the part of the jet producing such radiation are more closely aligned with the line of sight. Similarly, when the viewing angle of the optical emitting region decreases, the optical flux would be more Doppler enhanced.

Polarimetry can in principle help to understand whether geometrical effects play a role. We thus examined the polarimetric information on the source to find episodes where the behaviour of P and EVPA can suggest a curved motion in the source, as expected in case of e.g. a helical jet. We may have found one case in which this scenario is plausible. Indeed, in general P and EVPA variations are not correlated with flux. This again may support the existence of multiple emission regions with different polarization characteristics. Alternatively, the source polarimetric properties are mostly determined by stochastic variations due to turbulence (Marscher, 2014).

6

Blazar polarimetry on a sample of blazars

Introduction

Polarization measurements provide the only direct way of obtaining information on the magnetic field within the synchrotron emission region. The level of linear polarization of a blazar gives a measure of the degree of ordering of the magnetic field within the emitting zone. The polarization position angle yields the orientation of the field responsible for the polarized flux projected on the sky.

In a multiwavelength study of the blazar 4C 38.41 carried out by the WEBT, Raiteri et al. (2012) found that the intrinsic polarization of the optical synchrotron emission increases with the jet flux. The authors showed that this may be explained by variations of the viewing angle of the optical emission region in a jet crossed by shock waves of different strength. A similar interpretation was found to successfully explain the polarimetric behavior of another blazar, BL Lacertae (Raiteri et al., 2013), although in this case the degree of polarization decreases with flux. The difference in polarimetric behaviour between 4C 38.41 and BL Lacertae turned out to depend on the value of the Lorentz factor of the plasma bulk motion.

Ikejiri et al. (2011) searched for correlations between flux and optical polarization variations in a sample of about 30 blazars. They found weak correlation between optical flares and polarization changes, although a third of their sample exhibits significant correlation, both positive and negative. This seems to support the fact that observed polarization may come from different components. Indeed, multiple synchrotron contributions, likely originating from different locations in the jet, were sometimes proposed to explain the multifrequency behavior of blazars.

We now know that rotations of the optical polarization angle are common during optical and γ-ray outbursts (Abdo et al., 2010) and support the concept of magnetic acceleration and collimation. Modelling these rotations is a difficult task, since they also may be produced by plasma turbulence (Marscher & Jorstad, 2010). The complexity of γ-ray flares with different properties, i.e. some accompanied by optical polarization angle rotations and others not, or some with contemporaneous optical flares and others not, indicates that there are multiple scenarios on which

a general paradigm for the innermost regions of blazar jets can be based. Before starting to test general models, we still need to understand the mentioned differences in behavior. Important information can be provided by near-infrared polarimetry. These wavelengths are essential to understand the observed non different behavior of the optical and mm polarization variability.

In 2011 we obtained near-infrared polarimetric data for 26 blazars at the William Herschel Telescope in the Roque de los Muchachos Observatory. Preliminary results are presented in section 6.3. Moreover, we have also analysed the huge spectropolarimetric database made available by Paul Smith at Steward Observatory. In this chapter, we report on preliminary results obtained about this topic.

6.1 A long-term analysis of the optical polarimetry in a sample of bright γ-ray blazars

We selected the sample of bright γ-ray blazars monitored by the Steward Observatory Support Program of the *Fermi* mission. This program is designed to study the connections between the γ-ray flux variability and the optical behavior. Correlations detected between these two spectral regions will provide important information and constraints on models for the high energy γ-ray emission from the relativistic jets of these AGNs. The program aims at monitoring the optical linear polarization of the *Fermi* blazar sample. Moreover, the spectropolarimetry of the objects yields measurements of the brightness and spectral index of the optical synchrotron light.

The observations are performed with two telescopes of the Steward Observatory: the 2.3 m Bok Telescope and the 1.54 m Kuiper Telescope[1]. The instrument used for the observations is the SPOL CCD. This combines polarizing optics and a transmission-optics spectrograph into a self contained, portable, and high throughput instrument. Spectral resolutions of $4 - 15\mathring{A}$ are available over a range in useful spectral response of 3800–9000 $\mathring{A}$. The detection of polarization at a level P$< 0.05\%$ is possible. Different slits with apertures in the range $2" - 12.7"$ are used.

Polarization is derived from spectropolarimetry, as the median value of the Stokes parameters q and u in the wavelength range from 5000 to 7000 $\mathring{A}$. The degree of polarization $P = 100 * \sqrt{q^2 + u^2}$ is corrected for the statistical bias associated with the parameter being a positive defined quantity (Wardle & Kronberg, 1974). Usually, this value is very small given the high S/N of most of the data presented. The EVPA is calculated as EVPA$= 1/2 * \arctan(u/q)$, with 0°, and equivalently 180°, indicating that the polarization is aligned north-south.

Here we present a preliminary variability analysis of the multifrequency photometric and optical polarimetric behaviour of a sample of blazars included in the Steward Observatory Program. We study the relationship between the degree of polarization and the flux in different bands for the various objects. The occurrence of wide rotations of the position angle is also

[1]For both telescopes, the southern declination limit is about -40°, however for Kuiper Telescope the declinations higher than 61° are not accessible.

investigated, as they may reveal helical or in general curved magnetic fields.

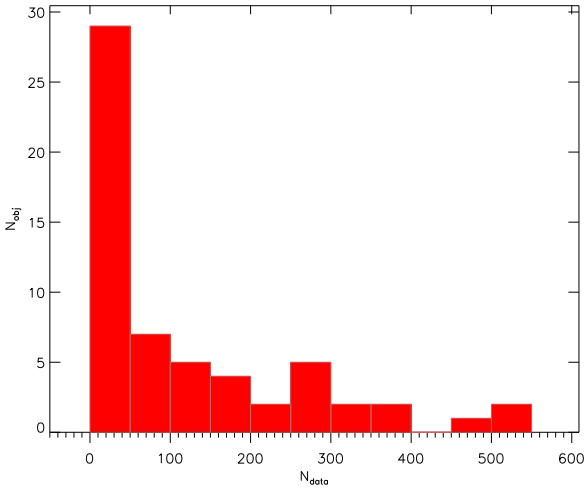

FIGURE 6.1— Histogram showing the number of objects N_{obj} with N_{data} polarization measurements in the Steward Observatory blazar program database.

We considered the whole sample, including 67 blazars, but for this work we concentrated only on the objects with more than 200 polarimetric points (see. Fig. 6.1). In particular, we here analyse 6 BL Lacs and 6 FSRQs, as the remaining two well sampled objects are OJ 248 and Mrk 421, for which we have already presented specific studies in previous chapters.

The optical photometric and spectropolarimetric information will be compared to the γ-ray data from the *Fermi* space mission and, when available, also to the millimetre data at 230 and 345 GHz from the SubMillimeter Array (SMA) on Mauna Kea in Hawaii[2].

6.1.1 Polarization behaviour in BL Lac type

In Fig. 6.2 we show the flux in the γ-ray band, flux densities in the optical V band and in the mm band, polarization degree (P) and angle (EVPA) behaviour for the six selected BL Lacs as a function of time. The data cover the period 2008-2015, which allows us to analyse the long-term variability properties of the sources. Different observing epochs are highlighted by different colours. The same choice is adopted in Fig. 6.3, showing P versus V.

In general, all BL Lacs show noticeable variability of both flux and P. We calculated the fractional variability (F_{var}) for the γ-ray flux resulting after binning into one day and one week, the same procedure is applied to the V band, the 230GHz fluxes and P. The results are shown in Table 6.1.

[2]https://www.cfa.harrard.edu/sma

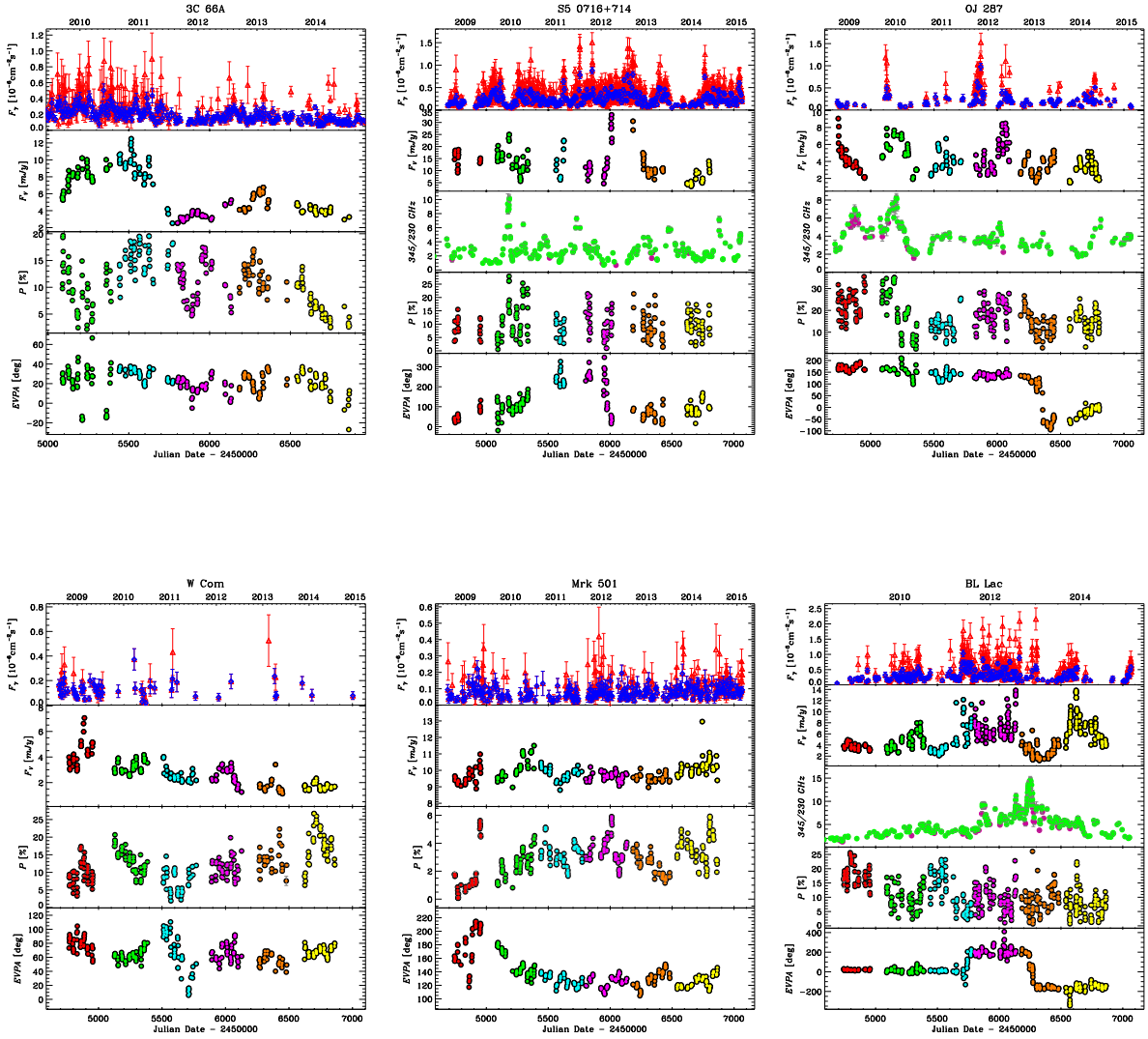

FIGURE 6.2— The BL Lacs sample. From top to bottom: a) the *Fermi*-LAT 0.1–100 GeV fluxes (10^{-6} ph cm^{-2} s^{-1}) derived with different time bins (red symbols refer to daily binned data, blue ones to weekly binned data, b) V-band magnitude light curve with different colours distinguishing the various observing cycles; c) 230 and 345 GHz data from the SMA (only for S5 0716+714, OJ 287 and BL Lac); d) Polarisation percentage; e) EVPA after correction for the $\pm 180°$ ambiguity.

TABLE 6.1— Fractional variability of the flux at different frequencies and the polarization degree P for the six selected BL Lacs.

	F_{var}				
	F_γ day	F_γ week	F_V	F_{230GHz}	P
3C 66A	0.44	0.37	0.42		0.39
S5 0716+714	0.44	0.51	0.48	0.61	0.54
OJ 287	0.69	0.57	0.38	0.41	0.41
W Com	0.36	0.32	0.40		0.41
Mrk 501	0.31	0.20	0.05		0.43
BL Lac	0.55	0.51	0.50	0.57	0.55

3C 66A: The fractional variability is around 40% for all quantities, but they do no show obvious correlations.

S5 0716+714: The largest variability is found in the millimetre flux.

OJ 287: The one day binned γ-ray light curve shows a much more pronounced variability. An EVPA rotation of about 200° occurs in a period characterised by no flares.

W Com: A continuous decrease of the optical flux corresponds to a general increase of P.

Mrk 501: The presence of a bright host galaxy prevents the detection of important optical flux variability.

BL Lacertae: We note a strong correlation between the γ-ray and optical fluxes: a major outbursts in 2011–2012 and noticeable flares in 2009–2010 and 2013–2014. In contrast the mm light curve shows a maximum at the end of 2012 when the source was in a optical faint state and just before a short γ-ray flare. The EVPA is quite stable at $0° = +180° = -180°$. Two wide EVPA rotation occurred in 2011 just at the beginning of the big γ and optical outbursts and the end of 2012, at the time of the mm maximum.

Figure 6.3 shows large dispersion of P versus V, indicating the lack of clear correlations between the two quantities.

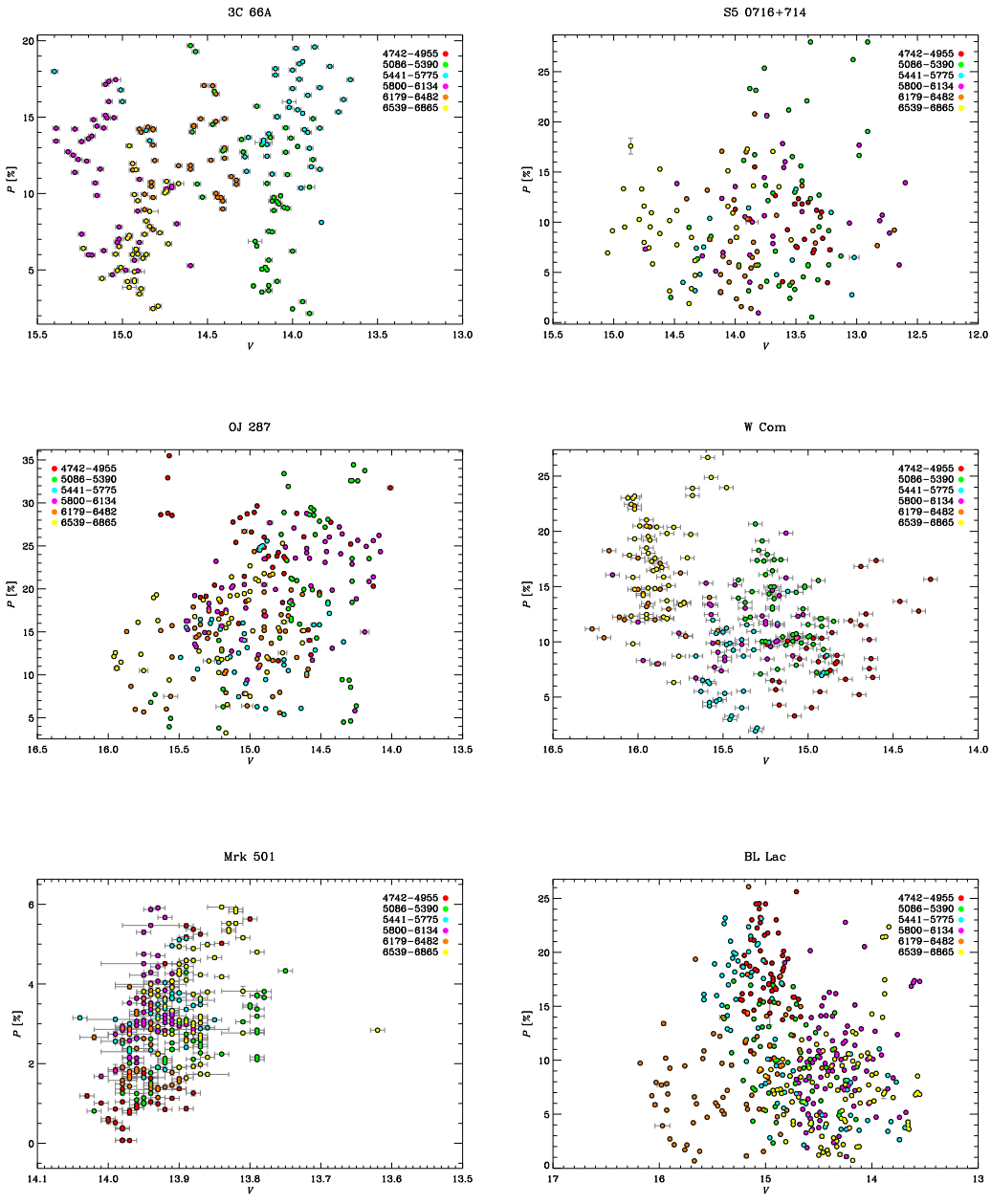

FIGURE 6.3— The BL Lacs sample. Optical polarization percentage P plotted against the V band magnitude. The different colours highlight the different observation cycles.

6.1.2 Polarization behaviour observed in FSRQ types

Figures 6.4, 6.5 display the same information as Figures 6.2 6.3 but for the selected FSRQs. Table 6.2 shows the fractional variability values.

TABLE 6.2— Fractional variability of the flux at different frequencies and the polarization degree P for the six selected FSRQs.

	F_{var}				
	F_γ day	F_γ week	F_V	F_{230GHz}	P
PKS 1222+216	0.98	1.05	0.44	0.55	0.68
3C 273	0.89	0.95	0.04	0.41	0.81
3C 279	0.77	0.78	0.55	0.28	0.61
PKS 1510-089	0.88	0.97	0.39	0.37	1.07
4C 38.41	0.52	0.71	0.59	0.46	0.78
3C 454.3	1.37	1.37	0.93	0.61	0.78

PKS 1222+216: We observed strong γ-ray activity in the period 2009–2011, whereas in the period 2013–2015 variability was found to be moderate. The opposite is true in the optical band, while the mm light curve shows a continuous increase with a major peak at the beginning of 2011. A general rising trend is also recognizable in the P behaviour. Moreover, we notice two wide EVPA rotations.

3C 273: The optical variability is attenuated by the strong emission contribution of the big-blue-bump likely due to radiation from the accretion disk. Its dilution effect is the reason why P is so small.

3C 279: This source is well known for its complex relationship between γ and optical emission (Hayashida et al., 2015). The polarization data show very high values of P and very wide rotations of EVPA.

PKS 1510-089: In 2009 the source showed correlated variability of the γ, optical, mm fluxes and P. At the end of 2010 a maximum in P was observed during a mm flare and a small optical, but no γ, flux increase. EVPA rotations seem to be very frequent.

3C 38.41: In this source the fluxes in γ, optical and mm bands and the polarization percentage show a similar trend. Wide rotations of the EVPA are observed.

3C 454.3: We note a strong activity period lasting until the beginning of 2011. Then the source remains in a sort of quiescent state for a couple of observing seasons. A remarkable, fast, and strongly polarized optical flare occurred in 2014, accompanied by minor activity at γ-rays and some flux increase in the mm bands.

In contrast to the BL Lacs cases the plots of P versus V for the FSRQs indicate that some correlation between the optical polarization degree and optical flux does exists.

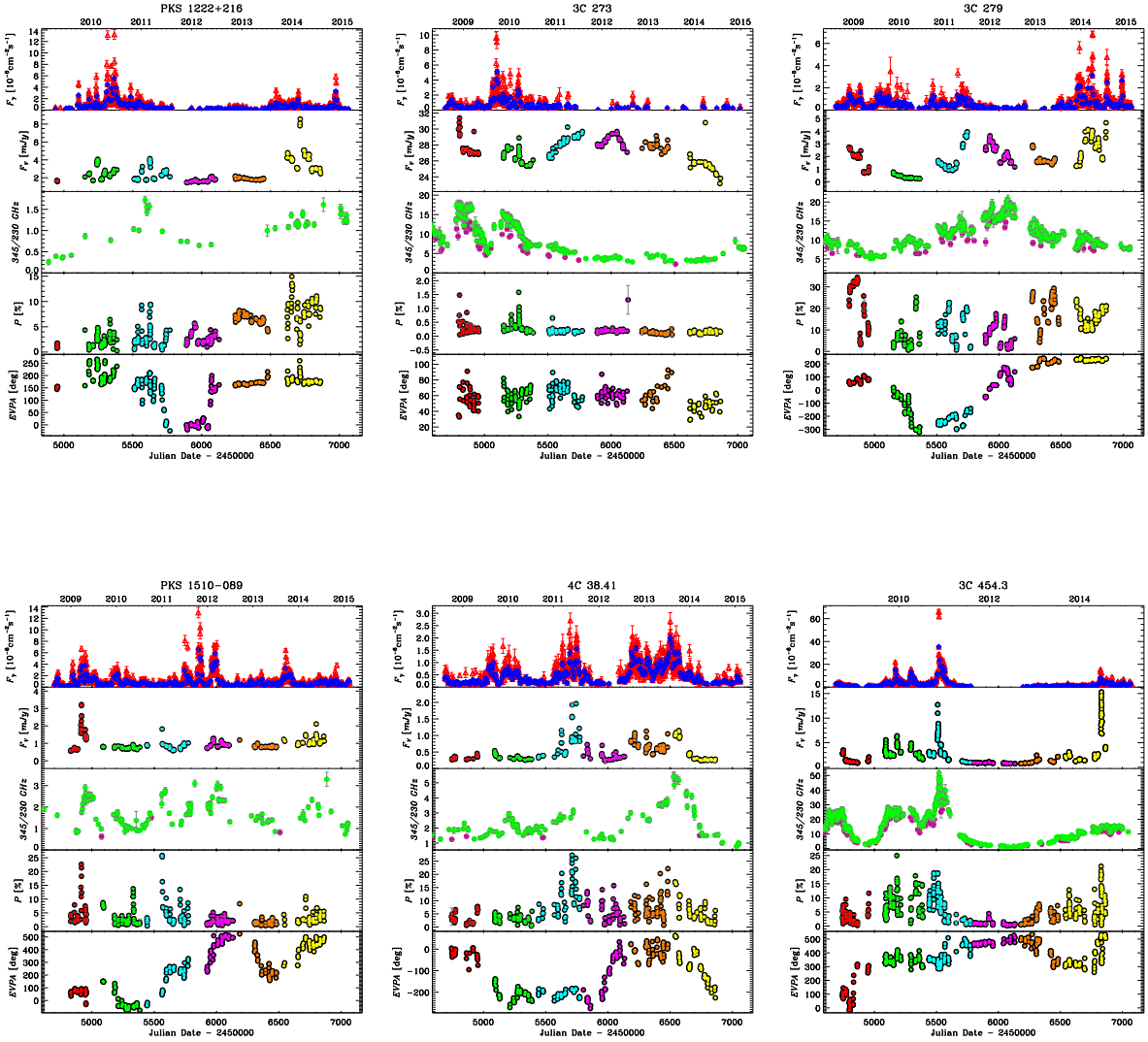

FIGURE 6.4— The FSRQs sample. From top to bottom: a) the *Fermi*-LAT 0.1–100 GeV fluxes (10^{-6} ph cm^{-2} s^{-1}) derived with different time bins (red symbols refer to daily binned data, blue ones to weekly binned data, b) V-band magnitude light curve with different colours distinguishing the various observing cycles; c) 230 and 345 GHz data from the SMA; d) Polarisation percentage; e) EVPA after correction for the $\pm 180^{\circ}$ ambiguity.

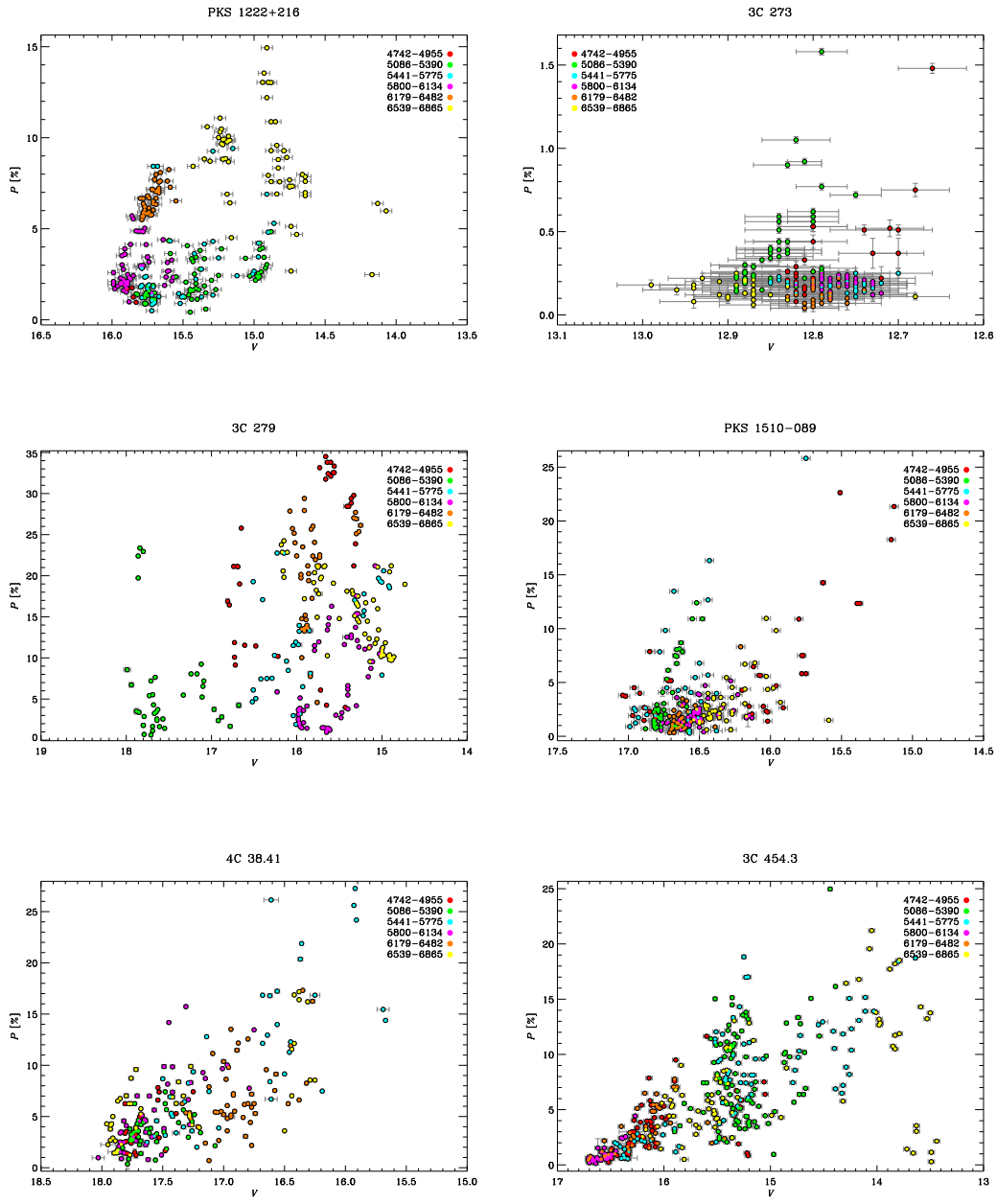

FIGURE 6.5— The FSRQs sample. Optical polarization percentage P plotted against the V band magnitude. The different colours highlight the different observation cycles.

A more detailed investigation of this database is under way to understand which variability mechanisms are more likely at work in these objects.

6.2 Multi band polarimetry behaviour

While optical polarimetric studies are becoming more and more frequent, very little has been done in the field of near-infrared polarimetry. In the following, we report on NIR polarimetry measurements for ten blazars selected from a sample of 26 objects that were observed with LIRIS at the 4.2m WHT (La Palma) in two observing runs during 2011. These data have been complemented with NIR photometry obtained at the Carlos Sanchez Telescope (Teide Observatory) and compared with different optical and radio observations. The optical photo-polarimetric data were collected from the Steward, Calar Alto and Lowell observatories with the addition of photometric data from the telescope IAC80 (Teide Observatory). The majority of the blazars were observed more than one epoch using two filters (J and K_s). Photometry was also derived directly from the polarimetric images. For a more detailed analysis, we expand our data-set with the VLBA radio data from the Boston group[3] (43 GHz) and the MOJAVE Project[4] (15 GHz).

The aim is twofold: on one side we want to investigate the relation between flux and polarization variability. Another aspect we want to analyse is whether the polarization degree and angle depend on wavelength, which is an important diagnostic for the identification of multiple polarized non-thermal and unpolarized thermal emission regions.

6.2.1 Near-infrared polarimetry observations and data reduction

Our observations were performed using the Long-slit Intermediate Resolution Infrared Spectrograph (LIRIS) mounted at the Cassegrain focus of the William Herschel Telescope (WHT) at the Observatorio Roque de Los Muchachos, La Palma, Spain, during two runs in 2011 March and October. LIRIS is equipped with a 1024×1024 pixel Hawaii detector covering the wavelength range 0.8-2.5μm. The pixel projection onto the sky is 0.25" yielding a field of view of 4.27'×4.27'. Polarimetric observations can be performed using a wedged double Wollaston (WeDo) device, consisting of a combination of two Wollaston prisms that deliver four simultaneous images of the polarized flux at angles 0°, 90°, 45°, and 135°. An aperture mask 4'×1' in size is used to prevent overlapping effects between the different polarization vector images. The observations were gathered using the J and Ks band filters. Each object was observed in single- shot mode with the imaging WeDoWo. In general, a five dithered pattern was used along the long side of the mask to a proper subtraction of the sky background contribution. The dither pattern cycle was repeated a few times for each target to increase the signal-to-noise ratio of the final

[3]http://www.bu.edu/blazars/VLBAproject.html
[4]http://www.physics.purdue.edu/astro/MOJAVE/allsources.html

measurements. Observations of unpolarized an polarized standard stars were used in each run to check the instrumental polarization and set the relative transmission factor.

The data were reduced using a dedicated package developed within IRAF (*lirisdr*). Each frame is trimmed into four strips. Each strip is processed following standard near infrared data reduction steps: flat-fielding, sky subtraction, geometric distortion and lately combined by the "shift-and-add" technique. The Stokes parameters were derived using the expressions found in Alves et al. (2011). The flux calibration was based on differential photometry using a reference star close by to the blazars.

6.2.2 Results

In the Fig. 6.6 we assembled the light curves of the BL Lac objects in the sample. The plot shows the photometric light curves, the time evolution of the polarization percentage P, and the EVPA at different frequencies. The $\pm n\pi$ ambiguity was fixed by assuming that the most likely value is that minimizing the angle variation, i.e. we added/subtracted 180° when needed to minimize the difference between subsequent points taking the error into account.

Figure 6.7 displays the same information for the FSRQs of the sample. In the following notes on the individual sources, we indicate the polarization degrees in the optical, near-IR, and radio bands at 43 and 15 GHz as $P_{\rm opt}$, $P_{\rm nir}$, $P_{\rm 43GHz}$, $P_{\rm 15GHz}$, respectively. Similarly, we define $\rm EVPA_{opt}$, $\rm EVPA_{nir}$, $\rm EVPA_{43GHz}$, and $\rm EVPA_{15GHz}$.

3C 66A: At the beginning of the considered period, the source was experiencing an optical outburst phase and a peak $P_{\rm opt} \sim 20\%$ is observed when the optical flux reached a maximum. After solar conjunction, the object remains more or less stable on a much fainter flux level, while $P_{\rm opt}$ falls under 10% only after JD=2455840. The radio $P_{\rm 43GHz}$ and $P_{\rm 15GHz}$ seem to fairly agree and always stay below 5%. Interestingly, between JD=2455840 and 2455850 $P_{\rm opt}$ decreases down to $P_{\rm 43GHz}$, and $P_{\rm nir}$ follows this trend. We note a different behaviour of the EVPA at the two radio wavelengths: while $\rm EVPA_{15GHz}$ remains nearly constant at -25––$20°$, $\rm EVPA_{43GHz}$ shows oscillations between 0 and 40°, in some epochs overlapping with $\rm EVPA_{opt}$ and $\rm EVPA_{nir}$.

0235+164: This source was observed in a quite faint state. The radio polarization is always below 4%, while the $P_{\rm opt}$ values are very sparse and $P_{\rm nir}$ shows systematic higher values in the K rather than in the J band. The EVPA at all frequencies seem to fairly match. The better sampled $\rm EVPA_{opt}$ suggests a rotation of about 220°.

OJ 287: In contrast to the previously presented BL Lacs, this object shows values of $P_{\rm 43GHz}$ comparable to those of $P_{\rm opt}$, while $P_{\rm 15GHz}$ remains lower. Even if the source was not in an outburst state, $P_{\rm opt}$ reaches $\sim 30\%$, and $P_{\rm nir} \sim 20\%$. Both the optical and radio EVPAs show oscillation around an angle of 140–150°.

BL Lacertae: This source is characterized by a $P_{15\mathrm{GHz}}$ greater than $P_{43\mathrm{GHz}}$, and a very variable P_{opt}. Both optical and radio polarization angles are preferentially set at $0 = 180°$. $\mathrm{EVPA_{opt}}$ suggests a rotation of almost $2 \times \pi$ in about 20 days. Near-infrared data seem to agree with the optical ones.

PKS 0420-014: The radio emitting zone is only weakly polarized, while P_{opt} and P_{nir} even exceed 20%.

3C 279: The flux shows an increasing trend and the same is true for both P_{opt} and $P_{43\mathrm{GHz}}$, confirming a general correlation between flux and polarization degree. Some variability characterizes both the optical and radio EVPAs, with the magnetic field orientation of the optical and radio emitting regions possibly crossing each other at some times.

4C 38.41: We observed the source around the peak of the 2011 outburst. P_{opt} shows a strong correlation with the optical flux, with two maxima exceeding 25%. In contrast, the radio polarization degree is always very low. The radio and optical EVPAs show oscillating paths, with $\mathrm{EVPA_{nir}}$ possibly matching $\mathrm{EVPA_{43GHz}}$ more than $\mathrm{EVPA_{opt}}$.

3C 345: P_{opt} and $P_{43\mathrm{GHz}}$ present similar values up to JD=2455780; afterwards they diverge, with P_{opt} (and P_{nir}) rising above 10%, and $P_{43\mathrm{GHz}}$ decreasing below 4%. $\mathrm{EVPA_{43GHz}}$ shows a larger variability than P_{opt} that, together with $\mathrm{EVPA_{nir}}$, remains fixed at $\sim 60°$.

CTA 102: The source was in a quiescent phase characterized by low values of P_{opt} and $P_{43\mathrm{GHz}}$. The magnetic fields of the corresponding emitting regions may be slightly misaligned.

3C 454.3: This very active blazar was observed in a dimming phase, with low and constant P_{opt}. In contrast, $P_{43\mathrm{GHz}}$ shows an increasing trend, up to $\sim 17\%$ and $P_{15\mathrm{GHz}}$ exhibits intermediate values. Apart from the very beginning, the EVPAs are in substantial agreement, with $\mathrm{EVPA_{opt}}$ displaying some spread.

We have noticed that in some sources there are episodes of both flux-polarization correlation and anti-correlation. In particular, in the BL Lac objects we observed a general agreement between the optical and infrared polarization. The radio polarization is often lower than the optical and infrared ones and shows less variability. The same is true for FSRQs, with the notable exception of 3C 454.3, which displays higher and more variable polarization in the radio than in the optical band. Our findings and other evidences suggest that the observed polarization may come from different components. Indeed, multiple synchrotron contributions, likely originating from different locations in the jet, have been proposed to explain the multifrequency behaviour of blazars by several authors (e.g. Marscher & Gear, 1985; Villata & Raiteri, 1999; Donnarumma et al., 2009; Raiteri et al., 2010).

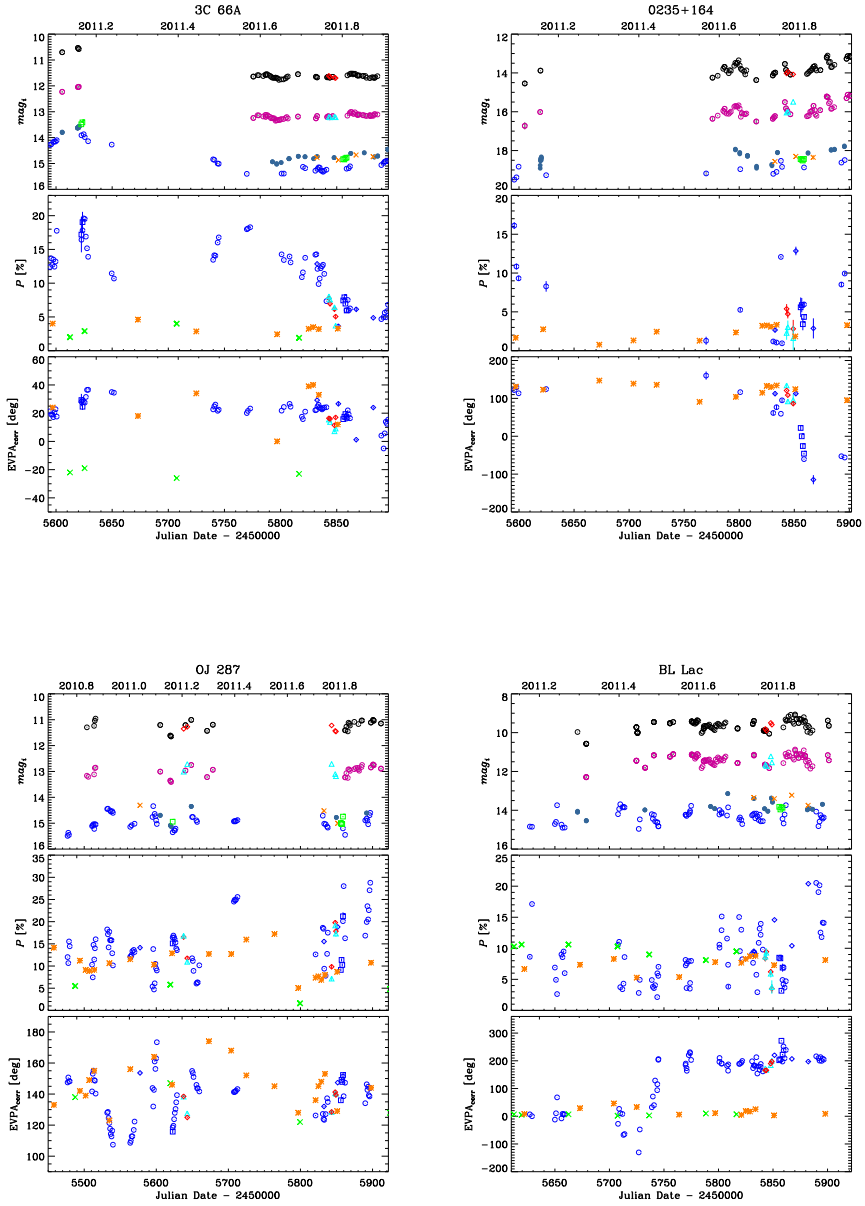

FIGURE 6.6— The BL Lacs sample. From top to bottom: a) light curves at different frequencies; black/red symbols represent data from Teide/WHT in the K-band, pink/cyan symbols those in the J-band, while the R-band optical flux densities come from the Teide (filled blue circles), Lowell (green squares), and Calar Alto (orange crosses) observatories, and those in the V-band (blue empty circles) are from the Steward Observatory b) Polarization percentage; blue symbols refer to the optical R band, red and cyan symbols to the K and J bands, respectively, and the green crosses and orange asterisks represent radio data from the Mojave project (15 GHz) and Boston group (43 GHz), respectively; d) EVPA after correction for the $\pm 180^{\circ} n$ ambiguity.

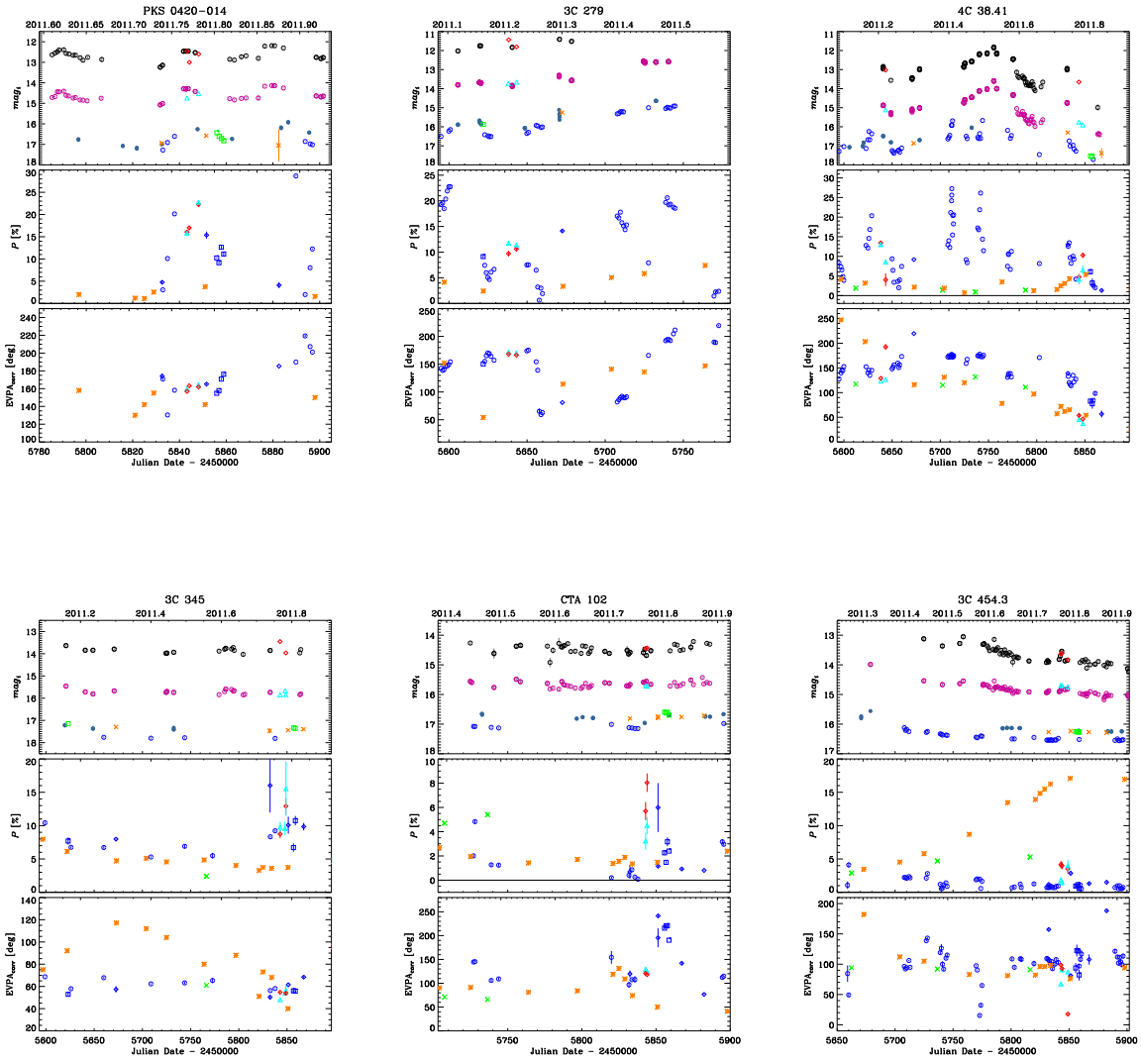

FIGURE 6.7— The FSRQs sample. From top to bottom: a) light curves at different frequencies; black/red symbols represent data from Teide/WHT in the K-band, pink/cyan symbols those in the J-band, while the R-band optical flux densities come from the Teide (filled blue circles), Lowell (green squares), and Calar Alto (orange crosses) observatories, and those in the V-band (blue empty circles) are from the Steward Observatory b) Polarization percentage; blue symbols refer to the optical R band, red and cyan symbols to the K and J bands, respectively, and the green crosses and orange asterisks represent radio data from the Mojave project (15 GHz) and Boston group (43 GHz), respectively; d) EVPA after correction for the $\pm 180^{\circ} n$ ambiguity.

7

Conclusions.

This work is focused on the multifrequency study of Blazars. Blazars are characterised by strong variability at all wavelengths and a deeper understanding of the blazar phenomenon can be achieved only through long-term monitoring which is possible only for a limited number of sources. The work presented here is based on the data collected within the GASP-WEBT Collaboration in the optical, near-infrared and radio frequencies, and on the publicly available spectropolarimetric data taken at the Steward Observatory. Moreover, data acquired by the space observatories *Swift* at UV and X-ray frequencies and *Fermi* at γ-ray energies were also used.

For this thesis, 28 sources from the GASP-WEBT Collaboration, and 7 sources from the MAGIC Collaboration have been monitored, as list of targets with near-infrared and optical observations. Optical observations were performed with the IAC80 and STELLA telescopes and near-infrared observations with the Carlos Sanchez Telescope, all of them located at the Teide Observatory.

In the first part of the thesis a study on the infrared properties of blazars is presented. We investigated the differences between the two blazar subtypes: FSRQs and BL Lac objects. We selected 14 FSRQs and 14 BL Lacs objects to be used as samples for our research. We built light curves, which reveal noticeable variability for most of them. In average, the mean fractional flux variation is greater for FSRQs than for BL Lacs objects, with the notable exception of AO 0235+164. We compared variability in the three near-infrared bands: while the BL Lacs show more variability at higher frequency, the opposite is true for FSRQs. This is the consequence of the different emission components overlapping in this band. Colour variability is very small in BL Lac objects, not exceeding a few percent. The nearly achromaticity of the near-IR emission of BL Lacs is a characteristic of the dominant synchrotron jet emission. In contrast, the large spectral changes exhibited by FSRQs are due to the overlapping between synchrotron and quasar-like emission components. With the data of the GASP-WEBT, WISE, 2MASS, IRAS, ISO, Spitzer and Herschel for the near-infrared and SDSS for the optical band we built Spectral Energy Distributions (SEDs). These allowed us to reveal the interplay among the various emission contributions: synchrotron radiation from the jet, QSO-like emission including torus, disc, and

BLR radiation, and radiation from the host galaxy. We modelled the synchrotron emission with a log-parabola, while for the host galaxy and QSO-like contributions we adopted galaxy templates from the SWIRE database, with the possible inclusion of black-body components to simulate additional dust emission or enhanced disc emission. We used single temperature black-bodies for these additional components instead of multitemperature black-bodies or dusty galaxy templates to keep the interpretation as simple as possible. We found the following results:

- For the BL Lac objects we notice that in same cases the host galaxy is strong, like in Mrk 421, Mrk 501 and 1ES 2344+514, the three closest and high-energy peaked BL Lacs. The BL Lac SEDs are well fitted by a synchrotron component; the only indications for the presence of dust thermal emission are found for 3C 66A and Mrk 421.

- For the FSRQs, the near-infrared band marks the transition from a non-thermal, synchrotron-dominated emission to a thermal, QSO-like dominated emission. The cases of PKS 0528+134 and 4C 71.07 suggest that torus emission is relatively weak in FSRQs. A bright disc component is required to explain the SEDs of 9 out of 14 GASP FSRQs.

We performed two long-term multifrequency studies, on the FSRQ OJ 248 and the BL Lac Mrk 421.

FSRQ OJ 248 behaviour was studied from radio to γ-ray frequencies in the period 2006–2013. We observed two optical-NIR flares, the first one in 2006–2007 and the following one in 2012–2013. The second flare was also detected at high energies by the *Swift* and *Fermi* satellites. A strong correlation between the flux variations at γ-rays and those in the optical band is found, but with the optical variations delayed by about one month, which is a peculiar behaviour in blazars. We noticed another strong correlation between X-ray and millimetre flux changes but in this period no time delay was appreciated, supporting a common emission region in the jet. We also studied the evolution of the polarization for FSRQ OJ 248, finding that the fraction of polarised flux remained low for most of the time, but raised to $\sim 19\%$ during the flare of 2012–2013. The rotation of the EVPA can be detected only during the flare and it goes in both directions, suggesting a complex behaviour of the magnetic field in the jet possibly due to turbulence, and/or a complex jet structure involving spiral paths.

The BL Lac Mrk 421 variability was studied from the near-infrared to X-ray energies in the period 2007–2015. This source has a strong host galaxy contribution, which must be subtracted in order to analyse the blazar/jet emission. We observed that the near-infrared and UV flux variations are well correlated with the optical ones, while the X-ray flux appears to behave in a different way. The SEDs show that the near-infrared to optical spectral shape is rather stable for different brightness states while the upturn toward the UV can be more or less pronounced, and this corresponds to a different X-ray spectral form. Indeed X-ray spectra exhibit a large range of slopes and curvatures and suggest that the synchrotron peak may cover a large range of frequencies, from $\log \nu \sim 16$ to ~ 17.5. To interpret the variations of the SED we propose different scenarios. One possibility is the existence of more than one emitting region: one contributing to the low energy and another one producing the X-ray radiation. Another possibility is that

of an inhomogeneous jet, where synchrotron radiation of increasing wavelength is coming from zones of increasing distance from the black hole, and where the orientation of these regions can change in time. Moreover, spectropolarimetric information acquired at the Steward Observatory was used to study a possible dependency of polarization degree P and EVPA on frequency. We examined the polarimetric information to find episodes where the behaviour of P and EVPA can suggest a curved motion in the source, as expected in case of e.g. helical jet, but in general P and EVPA variations are not correlated with flux. This again suggests the existence of multiple emission regions with different polarization characteristics.

The multifrequency studies allowed us to obtain a better understanding of the correlation between emissions at different spectral ranges, which in turn gives information on the location of the jet regions that emit at high energies and the mechanism responsible for such emission.

We have studied the polarization at optical and near-infrared wavelengths in a wide context, including multifrequency photometry. A preliminary analysis on two different databases are reported. We observed that in the BL Lac objects the variations in the degree of polarization are not always correlated with flux variations. Although the correlation between P and flux is weak, it is shown by a significative fraction of the objects in the samples. This seems to indicate that polarization variability is not so random as it appears. On the other hand, for the FSRQs objects, we observed a significant correlation between P and flux which suggests some determinist process. We plan to carry out further studies especially in the near-infrared in order to have a more comprehensive view of blazar jet physics.

A development of the here presented effort in understanding blazars properties and their emission mechanism in a multifrequency context, is represented by a massive project on the FSRQ 4C 71.07, whose optical emission is characterized by a strong thermal contribution from the disk and BLR. Being a high-declination source (0836+710), it is visible all year long. Moreover, its X-ray flux is high enough for a detailed X-ray spectral analysis. We obtained monthly observations by *Swift* for two years (October 2014–September 2016) and simultaneous optical spectroscopic monitoring with the WHT and NOT (and one TNG spectrum in the near-infrared). The WEBT collaboration is also following the source with continuous observations in the optical, radio, and near-IR bands complemented by optical polarimetry. We aim at separating the jet from the nuclear emission component and be able to characterize both of them. In particular, we will study the emission line properties in the context of the AGN unification scheme.

A

Other multiwavelength studies.

During the period of my PhD thesis I participated in other multifrequency studies on blazars that led to publications on refereed main journals. In the following I present the list of these works, including the title, bibliographic reference and abstract,

A.1 Variability of the blazar 4C 38.41 (B3 1633+382) from GHz frequencies to GeV energies

Reference: Raiteri, C. M., Villata, M....,Carnerero, M. I. et al. (2012) A&A , 545, A48

Context. After years of modest optical activity, the quasar-type blazar 4C 38.41 (B3 1633+382) experienced a large outburst in 2011, which was detected throughout the entire electromagnetic spectrum, renewing interest in this source.

Aims. We present the results of low-energy multifrequency monitoring by the GLAST-AGILE Support Program (GASP) of the Whole Earth Blazar Telescope (WEBT) consortium and collaborators, as well as those of spectropolarimetric/spectrophotometric monitoring at the Steward Observatory. We also analyse high-energy observations of the Swift and Fermi satellites. This combined study aims to provide insights into the source broad-band emission and variability properties.

Methods. We assemble optical, near-infrared, millimetre, and radio light curves and investigate their features and correlations. In the optical, we also analyse the spectroscopic and polarimetric properties of the source. We then compare the low-energy emission behaviour with that at high energies.

Results. In the optical-UV band, several results indicate that there is a contribution from a quasi-stellar-object (QSO) like emission component, in addition to both variable and polarised jet emission. In the optical, the source is redder-when-brighter, at least for R $> \sim$ 16. The optical spectra display broad emission lines, whose flux is constant in time. The observed degree of polarisation increases with flux and is higher in the red than the blue. The spectral energy distribution reveals a bump peaking around the U band. The unpolarised emission component

is likely thermal radiation from the accretion disc that dilutes the jet polarisation. We estimate its brightness to be RQSO ∼17.8518 and derive the intrinsic jet polarisation degree. We find no clear correlation between the optical and radio light curves, while the correlation between the optical and γ-ray flux apparently fades in time, likely because of an increasing optical to γ-ray flux ratio. Conclusions. As suggested for other blazars, the long-term variability of 4C 38.41 can be interpreted in terms of an inhomogeneous bent jet, where different emitting regions can change their alignment with respect to the line of sight, leading to variations in the Doppler factor δ. Under the hypothesis that in the period 20082011 all the γ-ray and optical variability on a one-week timescale were due to changes in δ, this would range between ∼7 and ∼21. If the variability were caused by changes in the viewing angle θ only, then θ would go from ∼2.6∘ to ∼5∘. Variations in the viewing angle would also account for the dependence of the polarisation degree on the source brightness in the framework of a shock-in-jet model.

A.2 The awakening of BL Lacertae: observations by Fermi, Swift and the GASP-WEBT

Reference: Raiteri, C. M., Villata, M....,Carnerero, M. I. et al. (2013) MNRAS, 436, 1530.

Since the launch of the Fermi satellite, BL Lacertae has been moderately active at γ-rays and optical frequencies until 2011 May, when the source started a series of strong flares. The exceptional optical sampling achieved by the GLASTAGILE Support Program of the Whole Earth Blazar Telescope in collaboration with the Steward Observatory allows us to perform a detailed comparison with the daily γ-ray observations by Fermi. Discrete correlation analysis between the optical and γ-ray emission reveals correlation with a time lag of 0 ± 1 d, which suggests cospatiality of the corresponding jet emitting regions. A better definition of the time lag is hindered by the daily gaps in the sampling of the extremely fast flux variations. In general, optical flares present more structure and develop on longer time-scales than corresponding γ-ray flares. Observations at X-rays and at millimetre wavelengths reveal a common trend, which suggests that the region producing the mm and X-ray radiation is located downstream from the optical and γ-ray-emitting zone in the jet. The mean optical degree of polarization slightly decreases over the considered period and in general it is higher when the flux is lower. The optical electric vector polarization angle (EVPA) shows a preferred orientation of about 15°, nearly aligned with the radio core EVPA and mean jet direction. Oscillations around it increase during the 20112012 outburst. We investigate the effects of a geometrical interpretation of the long-term flux variability on the polarization. A helical magnetic field model predicts an evolution of the mean polarization that is in reasonable agreement with the observations. These can be fully explained by introducing slight variations in the compression factor in a transverse shock waves model.

A.3 MAGIC gamma-ray and multi-frequency observations of flat spectrum radio quasar PKS 1510-089 in early 2012

Reference: Aleksić, J., Ansoldi, S.....,Carnerero, M. I. et al. (2014) MNRAS, A&A, 46A.

Aims. Amongst more than fifty blazars detected in very high energy (VHE,E > 100 GeV) γ-rays, only three belong to the subclass of flat spectrum radio quasars (FSRQs). The detection of FSRQs in the VHE range is challenging, mainly because of their soft spectra in the GeV-TeV regime. MAGIC observed PKS 1510089 (z=0.36) starting 2012 February 3 until April 3 during a high activity state in the high energy (HE,E > 100 MeV) γ-ray band observed by AGILE and Fermi. MAGIC observations result in the detection of a source with significance of 6.0 standard deviations (σ). We study the multi-frequency behaviour of the source at the epoch of MAGIC observation, collecting quasi -simultaneous data at radio and optical (GASP-WEBT and F-Gamma collaborations, REM, Steward, Perkins, Liverpool, OVRO, and VLBA telescopes), X-ray (Swift satellite), and HE γ-ray frequencies.

Methods. We study the VHE γ-ray emission, together with the multi-frequency light curves, 43 GHz radio maps, and spectral energy distribution (SED) of the source. The quasi-simultaneous multi-frequency SED from the millimetre radio band to VHE γ-rays is modelled with a one-zone inverse Compton model. We study two different origins of the seed photons for the inverse Compton scattering, namely the infrared torus and a slow sheath surrounding the jet around the Very Long Baseline Array (VLBA) core.

Results. We find that the VHE γ-ray emission detected from PKS 1510089 in 2012 February-April agrees with the previous VHE observations of the source from 2009 March -April. We find no statistically significant variability during the MAGIC observations on daily, weekly, or monthly time scales, while the other two known VHE FSRQs (3C 279 and PKS 1222+216) have shown daily scale to sub-hour variability. The γ-ray SED combining AGILE, Fermi and MAGIC data joins smoothly and shows no hint of a break. The multi-frequency light curves suggest a common origin for the millimetre radio and HE γ-ray emission, and the HE γ-ray flaring starts when the new component is ejected from the 43 GHz VLBA core and the studied SED models fit the data well. However, the fast HE γ-ray variability requires that within the modelled large emitting region, more compact regions must exist. We suggest that these observed signatures would be most naturally explained by a turbulent plasma flowing at a relativistic speed down the jet and crossing a standing conical shock.

A.4 The WEBT campaign on the BL Lac object PG 1553+113 in 2013. An analysis of the enigmatic synchrotron emission

Reference: Raiteri, C. M., Stamerra, A....,Carnerero, M. I. et al. (2015) MNRAS, 454, 353R.

A multifrequency campaign on the BL Lac object PG 1553+113 was organized by the Whole Earth Blazar Telescope (WEBT) in 2013 AprilAugust, involving 19 optical, two near-IR, and

three radio telescopes. The aim was to study the source behaviour at low energies during and around the high-energy observations by the Major Atmospheric Gamma-ray Imaging Cherenkov telescopes in AprilJuly. We also analyse the UV and X-ray data acquired by the Swift and XMM-Newton satellites in the same period. The WEBT and satellite observations allow us to detail the synchrotron emission bump in the source spectral energy distribution (SED). In the optical, we found a general bluer-when-brighter trend. The X-ray spectrum remained stable during 2013, but a comparison with previous observations suggests that it be-comes harder when the X-ray flux increases. The long XMMNewton exposure reveals a curved X-ray spectrum. In the SED, the XMMNewton data show a hard near-UV spectrum, while Swift data display a softer shape that is confirmed by previous Hubble Space Telescope/Cosmic Origins Spectrograph and International Ultraviolet Explorer observations. Polynomial fits to the opticalX-ray SED show that the synchrotron peak likely lies in the 430 eV energy range, with a general shift towards higher frequencies for increasing X-ray brightness. However, the UV and X-ray spectra do not connect smoothly. Possible interpretations include: (i) orientation effects, (ii) additional absorption, (iii) multiple emission components, and (iv) a peculiar energy distribution of relativistic electrons. We discuss the first possibility in terms of an inhomogeneous helical jet model.

A.5 Multiwavelength Study of Quiescent States of Mrk 421 with Unprecedented Hard X-ray Coverage Provided by NuSTAR in 2013

Reference: Baloković, M., Paneque, D.,...,Carnerero, M. I. et al. (2016) ApJ, 819, 156B.

We present coordinated multiwavelength observations of the bright, nearby BL Lacertae object Mrk 421 taken in 2013 JanuaryMarch, involving GASP-WEBT, Swift, NuSTAR, Fermi-LAT, MAGIC, VERITAS, and other collaborations and instruments, providing data from radio to very high energy (VHE) γ-ray bands. NuSTAR yielded previously unattainable sensitivity in the 3 79 keV range, revealing that the spectrum softens when the source is dimmer until the X-ray spectral shape saturates into a steep $\Gamma \approx 3$ power law, with no evidence for an exponential cutoff or additional hard components up to $\sim$ 80 keV. For the first time, we observed both the synchrotron and the inverse-Compton peaks of the spectral energy distribution (SED) simultaneously shifted to frequencies below the typical quiescent state by an order of magnitude. The fractional variability as a function of photon energy shows a double-bump structure that relates to the two bumps of the broadband SED. In each bump, the variability increases with energy, which, in the framework of the synchrotron self-Compton model, implies that the electrons with higher energies are more variable. The measured multi band variability, the significant X-ray-to-VHE correlation down to some of the lowest fluxes ever observed in both bands, the lack of correlation between optical/UV and X-ray flux, the low degree of polarization and its significant (random) variations, the short estimated electron cooling time, and the significantly longer variability timescale observed in the NuSTAR light curves point toward in situ electron acceleration and suggest that there are multiple compact regions contributing to the broadband emission of Mrk 421 during low-activity states.

A.6 Exceptional outburst of the blazar CTA 102 in 2012: The GASP-WEBT campaign and its extension

Reference: Larionov, V. M., Villata, M.,...,Carnerero, M. I. et al. (2016) in press for MNRAS (arXiv:1606.07836).

After several years of quiescence, the blazar CTA 102 underwent an exceptional outburst in 2012 SeptemberOctober. The flare was tracked from γ-ray to near-infrared frequencies, including Fermi and Swift data as well as photometric and polarimetric data from several observatories. An intensive GASP-WEBT collaboration campaign in optical and NIR bands, with an addition of previously unpublished archival data and extension through fall 2015, allows comparison of this outburst with the previous activity period of this blazar in 20042005. We find remarkable similarity between the optical and γ-ray behaviour of CTA 102 during the outburst, with a time lag between the two light curves of ≈ 1 hour, indicative of co-spatiality of the optical and γ-ray emission regions. The relation between the γ-ray and optical fluxes is consistent with the SSC mechanism, with a quadratic dependence of the SSC γ-ray flux on the synchrotron optical flux evident in the post-outburst stage. However, the γ-ray/optical relationship is linear during the outburst; we attribute this to changes in the Doppler factor. A strong harder-when-brighter spectral dependence is seen both the in γ-ray and optical non-thermal emission. This hardening can be explained by convexity of the UVNIR spectrum that moves to higher frequencies owing to an increased Doppler shift as the viewing angle decreases during the outburst stage. The overall pattern of Stokes parameter variations agrees with a model of a radiating blob or shock wave that moves along a helical path down the jet.

Bibliography

Abdo A. A., Ackermann M., Ajello M., et al., 2009, Astroparticle Physics, 32, 193

Abdo, A. A., Ackermann, M., Agudo, I., et al. 2010, ApJ, 721, 1425

Abdo, A. A., Ackermann, M., Ajello, M., et al. 2010, ApJ, 715, 429

Acero, F., Ackermann, M., Ajello, M., et al. 2015, ApJS, 218, 23

Ackermann, M., Ajello, M., Allafort, A., et al. 2011, ApJ, 743, 171

Ackermann, M., Ajello, M., Atwood, W. B., et al. 2015, ApJ, 810, 14

Agudo, I., Krichbaum, T. P., Ungerechts, H., et al. 2006, A&A, 456, 117

Agudo, I., Thum, C., Wiesemeyer, H., & Krichbaum, T. P. 2010, ApJS, 189, 1

Ahnen, M. L., Ansoldi, S., Antonelli, L. A., et al. 2016, MNRAS, 459, 3271

Aleksić, J., Alvarez, E. A., Antonelli, L. A., et al. 2012, A&A, 542, A100

Alves, F. O., Acosta-Pulido, J. A., Girart, J. M., Franco, G. A. P., & López, R. 2011, AJ, 142, 33

Atwood, W. B., Abdo, A. A., Ackermann, M., et al. 2009, ApJ, 697, 1071

Baade, W., & Minkowski, R. 1954, ApJ, 119, 206

Bach, U., Raiteri, C. M., Villata, M., et al. 2007, A&A, 464, 175

Barthelmy, S. D., Barbier, L. M., Cummings, J. R., et al. 2005, Space Science Reviews, 120, 143

Bertin, E., & Arnouts, S. 1996, A&AS, 117, 393

Bessell, M. S., Castelli, F., & Plez, B. 1998, A&A, 333, 231

Blandford, R. D., & McKee, C. F. 1977, MNRAS, 180, 343

Blandford, R. D., Koumlnigl, A. 1979, ApJ, 232, 34

Blandford, R. D., & Payne, D. G. 1982, MNRAS, 199, 883

Bolton, J. G., Stanley, G. J., & Slee, O. B. 1949, Nature, 164, 101

Bonning, E. W., Bailyn, C., Urry, C. M., et al. 2009, ApJL, 697, L81

Böttcher, M., Reimer, A., Sweeney, K., & Prakash, A. 2013, ApJ, 768, 54

Bregman, J. N., Glassgold, A. E., Huggins, P. J., et al. 1990, ApJ, 352, 574

Burrows, D. N., Hill, J. E., Nousek, J. A., et al. 2005, Space Science Reviews, 120, 165

Buttiglione S., Capetti A., Celotti A., Axon D. J., Chiaberge M., Macchetto F. D., Sparks W. B., 2009, A&A, 495, 1033

Capetti A., Raiteri C. M., Buttiglione S., 2010, A&A, 516, A59

Cardelli, J. A., Clayton, G. C., & Mathis, J. S. 1989, ApJ, 345, 245

Carroll, B. W., & Ostlie, D. A. 1996, Institute for Mathematics and Its Applications,

Chen P. S., Fu H. W., Gao Y. F., 2005, New Astron, 11, 27

Corbett E. A., Robinson A., Axon D. J., Hough J. H., 2000, MNRAS, 311, 485

Cutri R. M. et al., 2003, 2MASS All Sky Catalog of point sources.

D'Abrusco R., Massaro F., Ajello M., Grindlay J. E., Smith H. A., Tosti G., 2012, ApJ, 748, 68

D'Abrusco R., Massaro F., Paggi A., Masetti N., Tosti G., Giroletti M., Smith H. A., 2013, ApJS, 206, 12

D'Alessio F. et al., 2000, in Presented at the Society of Photo-Optical Instrumentation Engineers (SPIE) Conference, Vol. 4008, Proc. SPIE Vol. 4008, p. 748-758, Optical and IR Telescope Instrumentation and Detectors, Masanori Iye; Alan F. Moorwood; Eds., Iye M., Moorwood A. F., eds., pp. 748–758

D'Ammando F. et al., 2011, A&A, 529, A145

Decarli, R., Dotti, M., & Treves, A. 2011, MNRAS, 413, 39

Dickey, J. M., & Lockman, F. J. 1990, ARA&A, 28, 215

Diplas, A., & Savage, B. D. 1994, ApJ, 427, 274

Donnarumma, I., Vittorini, V., Vercellone, S., et al. 2009, ApJL, 691, L13

Edelson, R. A., & Krolik, J. H. 1988, ApJ, 333, 646

Elvis M. et al., 2012, ApJ, 759, 6

Fan, J.-H., Kurtanidze, O. M., Nikolashvili, M. G., et al. 2004, Chinese J. Astron. Astrophys, 4, 133

Fanaroff, B. L., & Riley, J. M. 1974, MNRAS, 167, 31P

Francis, P. J., Hewett, P. C., Foltz, C. B., et al. 1991, ApJ, 373, 465

Frank, J., King, A., & Raine, D. J. 2002, Accretion Power in Astrophysics, by Juhan Frank and Andrew King and Derek Raine, pp. 398. ISBN 0521620538. Cambridge, UK: Cambridge University Press, February 2002., 398

Gabuzda D. C., Cawthorne T. V., Roberts D. H., Wardle J. F. C., 1992, ApJ, 388, 40

Gehrels, N., Chincarini, G., Giommi, P., et al. 2004, ApJ, 611, 1005

Ghisellini G., Tavecchio F., Foschini L., Ghirlanda G., 2011, MNRAS, 414, 2674

Giommi P., Padovani P., Polenta G., Turriziani S., D'Elia V., Piranomonte S., 2012, MNRAS, 420, 2899

González-Pérez, J. N., Kidger, M. R., & Martín-Luis, F. 2001, AJ, 122, 2055

Gurwell, M. A., Peck, A. B., Hostler, S. R., Darrah, M. R., & Katz, C. A. 2007, From Z-Machines to ALMA: (Sub)Millimeter Spectroscopy of Galaxies, 375, 234

Haas M. et al., 2004, A&A, 424, 531

Hartman, R. C., Bertsch, D. L., Bloom, S. D., et al. 1999, ApJS, 123, 79

Hayashida, M., Madejski, G. M., Nalewajko, K., et al. 2012, ApJ, 754, 114

Hayashida, M., Nalewajko, K., Madejski, G. M., et al. 2015, ApJ, 807, 79

Heckman, T. M. 1980, A&A, 87, 152

Hine, A. C., Hobbs, C. H., Jones, J. R., & Cameron, C. 1979, Journal of Sedimentary Research, 49, 323

Ho, L. C., Filippenko, A. V., & Sargent, W. L. W. 1993, Bulletin of the American Astronomical Society, 25, 17.05

Hufnagel, B. R., & Bregman, J. N. 1992, ApJ, 386, 473

Ikejiri, Y., Uemura, M., Sasada, M., et al. 2011, , 63, 639

Impey C. D., Neugebauer G., 1988, AJ, 95, 307

Janiak, M., Sikora, M., Nalewajko, K., Moderski, R., & Madejski, G. M. 2012, ApJ, 760, 129

Jorstad, S. G., & Marscher, A. P. 2004, ApJ, 614, 615

Jorstad, S. G., Marscher, A. P., Larionov, V. M., et al. 2010, ApJ, 715, 362

Kalberla, P. M. W., Burton, W. B., Hartmann, D., et al. 2005, A&A, 440, 775

Karouzos M., Britzen S., Witzel A., Zensus J. A., Eckart A., 2012, A&A, 537, A112

Kaspi, S., Smith, P. S., Netzer, H., et al. 2000, ApJ, 533, 631

Khachikian, E. Y., & Weedman, D. W. 1974, ApJ, 192, 581

Laing, R. A., Jenkins, C. R., Wall, J. V., & Unger, S. W. 1994, The Physics of Active Galaxies, 54, 201

Landoni M., Falomo R., Treves A., Sbarufatti B., Barattini M., Decarli R., Kotilainen J., 2013, AJ, 145, 114

Landoni M., Falomo R., Treves A., Sbarufatti B., Decarli R., Tavecchio F., Kotilainen J., 2012, A&A, 543, A116

Larionov, V. M., Jorstad, S. G., Marscher, A. P., et al. 2008, A&A, 492, 389

Larionov, V. M., Jorstad, S. G., Marscher, A. P., et al. 2013, ApJ, 768, 40

Laurent-Muehleisen S. A., Kollgaard R. I., Feigelson E. D., Brinkmann W., Siebert J., 1999, ApJ, 525, 127

León-Tavares, J., Chavushyan, V., Patiño-Álvarez, V., et al. 2013, ApJL, 763, L36

Leto, P., Umana, G., Trigilio, C., et al. 2009, A&A, 507, 1467

Lister M. L. et al., 2013, AJ, 146, 120

Lockman, F. J., & Savage, B. D. 1995, ApJS, 97, 1

Malmrose M. P., Marscher A. P., Jorstad S. G., Nikutta R., Elitzur M., 2011, ApJ, 732, 116

Mannucci, F., Basile, F., Poggianti, B. M., et al. 2001, MNRAS, 326, 745

Marcha, M. J. M., & Browne, I. W. A. 1996, MNRAS, 279, 72

Markwardt, C. B. 2009, Astronomical Data Analysis Software and Systems XVIII, 411, 251

Marscher, A. P., & Gear, W. K. 1985, ApJ, 298, 114

Marscher, A. P., Jorstad, S. G., D'Arcangelo, F. D., et al. 2008, Nature, 452, 966

Marscher, A. P., & Jorstad, S. G. 2010, ArXiv e-prints, 1005.5551

Marscher, A. P. 2014, ApJ, 780, 87

Massaro, E., Perri, M., Giommi, P., & Nesci, R. 2004, A&A, 413, 489

Massaro E., Giommi P., Leto C., Marchegiani P., Maselli A., Perri M., Piranomonte S., Sclavi S., 2009, A&A, 495, 691

Massaro F., D'Abrusco R., Ajello M., Grindlay J. E., Smith H. A., 2011, ApJL, 740, L48

Massaro F., D'Abrusco R., Paggi A., Masetti N., Giroletti M., Tosti G., Smith H. A., Funk S., 2013a, ApJS, 206, 13

Massaro F., D'Abrusco R., Tosti G., Ajello M., Gasparrini D., Grindlay J. E., Smith H. A., 2012, ApJ, 750, 138

Massaro F., Paggi A., Errando M., D'Abrusco R., Masetti N., Tosti G., Funk S., 2013b, ApJS, 207, 16

Mattox, J. R., Bertsch, D. L., Chiang, J., et al. 1996, ApJ, 461, 396

Miller, H. R., Carini, M. T., & Goodrich, B. D. 1989, Nature, 337, 627

Moretti, A., Campana, S., Mineo, T., et al. 2005, SPIE, 5898, 360

Nalewajko, K. 2010, International Journal of Modern Physics D, 19, 701

Neugebauer G., Oke J. B., Becklin E. E., Matthews K., 1979, ApJ, 230, 79

Nenkova, M., Sirocky, M. M., Nikutta, R., Ivezić, Ž., & Elitzur, M. 2008, ApJ, 685, 160-180

Nilsson K., Pasanen M., Takalo L. O., Lindfors E., Berdyugin A., Ciprini S., Pforr J., 2007, A&A, 475, 199

Nilsson K., Pursimo T., Sillanpää A., Takalo L. O., Lindfors E., 2008, A&A, 487, L29

Nilsson K., Pursimo T., Villforth C., Lindfors E., Takalo L. O., Sillanpää A., 2012, A&A, 547, A1

Nolan P. L. et al., 2012, ApJS, 199, 31

Ogle P. M., Wehrle A. E., Balonek T., Gurwell M. A., 2011, ApJS, 195, 19

Osterbrock, D. E. 1998, Revista Mexicana de Astronomia y Astrofisica Conference Series, 7, 180

Pacholczyk, A. G. 1970, Series of Books in Astronomy and Astrophysics, San Francisco: Freeman, 1970,

Palma N. I. et al., 2011, ApJ, 735, 60

Peterson, B. M., Wanders, I., Horne, K., et al. 1998, PASP, 110, 660

Peterson B. M., 2001, in Advanced Lectures on the Starburst-AGN Connection, Aretxaga I., Kunth D., Mújica R., eds., Singapore: World Scientific, p. 3

Pian E. et al., 1999, ApJ, 521, 112

Pian E. et al., 1998, ApJL, 492, L17

Pita S. et al., 2013, ArXiv e-prints

Plotkin R. M., Anderson S. F., Brandt W. N., Markoff S., Shemmer O., Wu J., 2012, ApJL, 745, L27

Polletta M. et al., 2007, ApJ, 663, 81

Poole, T. S., Breeveld, A. A., Page, M. J., et al. 2008, MNRAS, 383, 627

Punch, M., Akerlof, C. W., Cawley, M. F., et al. 1992, Nature, 358, 477

Raiteri, C. M., Ghisellini, G., Villata, M., et al. 1998, A&AS, 127, 445

Raiteri, C. M., Villata, M., Tosti, G., et al. 2003, A&A, 402, 151

Raiteri, C. M., Villata, M., Ibrahimov, M. A., et al. 2005, A&A, 438, 39

Raiteri C. M., Villata M., Capetti A., Heidt J., Arnaboldi M., Magazzù A., 2007, A&A, 464, 871

Raiteri C. M. et al., 2008, A&A, 491, 755

Raiteri, C. M., Villata, M., Bruschini, L., et al. 2010, A&A, 524, A43

Raiteri C. M. et al., 2011, A&A, 534, A87

Raiteri C. M. et al., 2012, A&A, 545, A48

Raiteri C. M. et al., 2013, MNRAS, 436, 1530

Raiteri, C. M., Villata, M., Carnerero, M. I., et al. 2014, MNRAS, 442, 629

Raiteri, C. M., Stamerra, A., Villata, M., et al. 2015, MNRAS, 454, 353

Rao, S. M., & Turnshek, D. A. 2000, ApJS, 130, 1

Rao, S. M., Nestor, D. B., Turnshek, D. A., et al. 2003, ApJ, 595, 94

Roming, P. W. A., Kennedy, T. E., Mason, K. O., et al. 2005, Space Science Reviews, 120, 95

Rybicki, G. B., & Lightman, A. P. 1979, Astronomy Quarterly, 3, 199

Sandrinelli A., Treves A., Falomo R., Farina E. P., Foschini L., Landoni M., Sbarufatti B., 2013, AJ, 146, 163

Sandrinelli, A., Covino, S., & Treves, A. 2014, ApJL, 793, L1

Sandrinelli, A., Covino, S., & Treves, A. 2016, ApJ, 820, 20

Scarpa R., Urry C. M., Falomo R., Pesce J. E., Treves A., 2000, ApJ, 532, 740

Schinzel, F. K., Lobanov, A. P., Taylor, G. B., et al. 2012, A&A, 537, A70

Schlegel D. J., Finkbeiner D. P., Davis M., 1998, ApJ, 500, 525

Sikora, M., Błażejowski, M., Begelman, M. C., & Moderski, R. 2001, ApJ, 554, 1

Smith A. G., 1996, in Astronomical Society of the Pacific Conference Series, Vol. 110, Blazar Continuum Variability, Miller H. R., Webb J. R., Noble J. C., eds., p. 3

Smith, P. S., Schmidt, G. D., Hines, D. C., & Foltz, C. B. 2003, ApJ, 593, 676

Smith, P. S., Montiel, E., Rightley, S., et al. 2009, ArXiv e-prints, 0912.3621

Sokolov, A., Marscher, A. P., & McHardy, I. M. 2004, ApJ, 613, 725

Sokolov, A., & Marscher, A. P. 2005, ApJ, 629, 52

Soldi S. et al., 2008, A&A, 486, 411

Sorcia, M., Benítez, E., Hiriart, D., et al. 2014, ApJ, 794, 54

Steidel, C. C., Kollmeier, J. A., Shapley, A. E., et al. 2002, ApJ, 570, 526

Stickel M., Fried J. W., Kuehr H., Padovani P., Urry C. M., 1991, ApJ, 374, 431

Stocke J. T., Morris S. L., Gioia I. M., Maccacaro T., Schild R., Wolter A., Fleming T. A., Henry J. P., 1991, ApJS, 76, 813

Tadhunter, C. N., Morganti, R., Robinson, A., et al. 1998, MNRAS, 298, 1035

Tadhunter, C. 2008, New Astronomy Reviews, 52, 227

Tavani M., Barbiellini G., Argan A., Boffelli F., Bulgarelli A., Caraveo P., Cattaneo P. W., Chen A. W., Cocco V., Costa E., D'Ammando F., 2009, A&A, 502, 995

Teraesranta, H., Tornikoski, M., Mujunen, A., et al. 1998, A&AS, 132, 305

Türler M. et al., 2006, A&A, 451, L1

Ulrich, M.-H., Kinman, T. D., Lynds, C. R., Rieke, G. H., & Ekers, R. D. 1975, ApJ, 198, 261

Ulrich, M.-H., & Owen, F. N. 1977, Nature, 269, 673

Urry, C. M., & Padovani, P. 1995, PASP, 107, 803

Vercellone, S., D'Ammando, F., Vittorini, V., et al. 2010, ApJ, 712, 405

Vermeulen R. C., Ogle P. M., Tran H. D., Browne I. W. A., Cohen M. H., Readhead A. C. S., Taylor G. B., Goodrich R. W., 1995, ApJL, 452, L5

Véron-Cetty M.-P., Véron P., 2003, A&A, 412, 399

Villata, M., Raiteri, C. M., Ghisellini, G., et al. 1997, A&AS, 121,

Villata, M., Raiteri, C. M., Lanteri, L., Sobrito, G., & Cavallone, M. 1998, A&AS, 130, 305

Villata, M., & Raiteri, C. M. 1999, A&A, 347, 30

Villata M. et al., 2002, A&A, 390, 407

Villata M. et al., 2006, A&A, 453, 817

Villata, M., Raiteri, C. M., Aller, M. F., et al. 2007, A&A, 464, L5

Villata M. et al., 2008, A&A, 481, L79

Villata, M., Raiteri, C. M., Larionov, V. M., et al. 2009, A&A, 501, 455

Villata, M., Raiteri, C. M., Gurwell, M. A., et al. 2009, A&A, 504, L9

Visvanathan, N., & Wills, B. J. 1998, AJ, 116, 2119

Wardle, J. F. C., & Kronberg, P. P. 1974, ApJ, 194, 249

Wehrle A. E., Grupe D., Gurwell M., Jorstad S., Marscher A., 2012, The Astronomer's Telegram, 4557, 1

Wilms, J., Allen, A., & McCray, R. 2000, ApJ, 542, 914

Wright E. L. et al., 2010, AJ, 140, 1868

List of Figures

1.1 Tridimensional classification of AGNs (Tadhunter, 2008). 5
1.2 In panel (a) the image of the Seyfert galaxy NGC 1275 (multi-wavelength composite) and in Panel (b) the spectrum of NGC 1667 (Seyfert 2). (Ho et al., 1993) 6
1.3 In panel (a) an image of NGC 1052 galaxy taken by Sloan Digital Sky Survey (SDSS) and in panel (b) its spectrum (Ho et al., 1993) 7
1.4 Artistic view of a quasar (a) and its spectrum (b) (Francis et al., 1991). 7
1.5 Image (a) and spectrum (b) of the radio galaxy Cygnus A.(Osterbrock, 1998) . . 8
1.6 Artistic view of a blazar. Image courtesy of NASA/Goddard Space Flight Center Conceptual Image Lab. 10
1.7 Unified Model of AGNs (Urry & Padovani, 1995). 11
1.8 AGN model. Image credit: Brooks/Cole Thomson Learning. 12
1.9 Structure of an accretion disk (Carroll & Ostlie, 1996). 13
1.10 Relationship between the magnetic field and the accretion disk (Carroll & Ostlie, 1996). 14
1.11 Geometry assumed to explain apparent superluminal expansion of radio sources. 16
1.12 The apparent transverse velocity of a source moving at an angle θ to the observer's line of sight. 17
1.13 Single electron spectrum due to synchrotron radiation. Hughes(1991). 20
1.14 FSRQ SED of 1633+382. 24
1.15 LBL SED of 0716+71. 25
1.16 IBL SED of 0219+428. 25
1.17 HBL SED of 1101+384. 26

2.1 The WEBT collaboration logo. 27
2.2 IAC80 telescope. 29
2.3 STELLA-I telescope. 30
2.4 TCS telescope. 32
2.5 Figure showing the correction of the scrambled central columns. Left panel shows the image before correction and right panel the image corrected after readjusting the affected columns. 33
2.6 Flatfield image of Kshort filter. 34
2.7 Mask to correct bad pixels. 35
2.8 Sky subtraction. 36
2.9 Combination of different images of the "dither" cycle. 37

2.10 A typical image after setting astrometric information. The reference target is marked with two concentric rings, the identified 2MASS sources are marked by red circumferences and the blue cross indicates possible saturation. 38
2.11 Instrumental magnitude versus calibrated magnitude. Different panels correspond to different aperture radii. The red circle represents the target. 38
2.12 Selection of reference sources based on the magnitude limits. The red square represents the target to be calibrated. 39
2.13 Election of the limit distance. 39
2.14 Aperture growth curves for the different sources to be used as references. The red curve is our target of interest. 40
2.15 Setting for calculating the calibrated magnitude. 40
2.16 The *Swift* Telescope. 41
2.17 Instrument on board of the *Swift* satellite. 42
2.18 All-sky map showing classification of the BAT 70 month survey sources. 43
2.19 The definition of the XRT grades for PC (left) and WT (right) modes. 44
2.20 XRT image 45
2.21 XRT light curves over (a) one orbit or (b) several orbits. 46
2.22 UVOT image in uvw2 band. The green/cyan circle is the source/background extraction region. 48
2.23 *Fermi* Telescope. 49
2.24 Sky observed by *Fermi*. 49

3.1 Colour-colour diagrams built with *WISE* data for FSRQs (left) and BL Lacs (right). Only objects with $S/N > 3$ in all *WISE* bands were considered. The points corresponding to the 28 sources monitored by the GASP-WEBT are highlighted with coloured diamonds. The black squares in the bottom left represent the SWIRE templates of 5 and 13 Gyr old elliptical galaxies at different values of redshift. The locations of Type 1 QSO spectra (TQSO1 SWIRE template) of various redshift, and power-law (PL) spectra with different spectral index are also plotted. 53
3.2 The redshift versus *WISE* W1-W2 colour for FSRQs (left) and BL Lacs (right). Only objects with $S/N > 3$ in all *WISE* bands were considered. Black crosses indicate sources with uncertain redshift; black plus signs those with undetermined z. The points corresponding to the 28 sources monitored by the GASP-WEBT are highlighted with coloured diamonds. The black squares in the bottom left represent the SWIRE templates of 5 and 13 Gyr old elliptical galaxies at different values of redshift. The location of Type 1 QSO spectra (TQSO1 SWIRE template) of various redshift is also plotted. 56
3.3 Colour-colour diagram built with 2MASS data for FSRQs (left) and BL Lac objects (right). The 2MASS magnitudes have been corrected for Galactic reddening according to Schlegel, Finkbeiner & Davis (1998). GASP sources are overplotted with coloured diamonds. 57

3.4 Colour-colour diagram built with *WISE* and 2MASS data for FSRQs (left) and BL Lac objects (right). The 2MASS magnitudes have been corrected for Galactic reddening according to Schlegel, Finkbeiner & Davis (1998). GASP sources are overplotted with coloured diamonds. 58

3.5 Spectral energy distributions of the BZCAT FSRQs (left) and BL Lac objects (right) built with infrared and optical data from *WISE*, 2MASS and SDSS. *WISE* and SDSS data are plotted only for objects with $S/N > 3$ and magnitudes brighter than the survey limits, respectively, in all bands. The 2MASS and SDSS data are corrected for the Galactic extinction according to Schlegel, Finkbeiner & Davis (1998). Mean SEDs are highlighted with black plus signs; GASP sources are overplotted with coloured diamonds. 60

3.6 Near-IR light curves of the GASP-WEBT BL Lac objects. Blue squares indicate data from Campo Imperatore, red diamonds those from Teide. 64

3.7 Near-IR light curves of the GASP-WEBT BL Lac objects. Blue squares indicate data from Campo Imperatore, red diamonds those from Teide. 65

3.8 Near-IR light curves of the GASP-WEBT FSRQs. Blue squares indicate data from Campo Imperatore, red diamonds those from Teide. 66

3.9 Near-IR light curves of the GASP-WEBT FSRQs. Blue squares indicate data from Campo Imperatore, red diamonds those from Teide. 67

3.10 Near-IR colour-colour plots for the GASP-WEBT BL Lac objects. Data have been corrected for Galactic extinction. Blue squares indicate data from Campo Imperatore, red diamonds those from Teide. The black cross indicates the point obtained from the 2MASS catalogue. 68

3.11 As in Fig. 3.10 but for the GASP-WEBT FSRQs. 69

3.12 Spectral energy distribution of the GASP-WEBT BL Lac objects. Data from *ISO* (red circles), *IRAS* (triangles), *Spitzer* (plus signs and crosses), *WISE* (squares), 2MASS (diamonds), and SDSS (asterisks) are shown. The green circles represent the results of the GASP near-IR monitoring at the Campo Imperatore and Teide observatories. The optical spectrum of 1807+698 by Buttiglione et al. (2009) is also plotted. Contributions from the synchrotron (dashed line) and host galaxy (solid line) emission are displayed in blue. In the cases of 3C 66A and Mkn 421, thermal dust emission is added, which is modelled as a black-body (blue dot-dashed line). The black line represents the sum of all components. 78

3.13 Spectral energy distribution of the GASP-WEBT FSRQs. Data from *ISO* (red circles), *IRAS* (triangles), *Herschel* (stars), *Spitzer* (plus signs and crosses), *WISE* (squares), 2MASS (diamonds), and SDSS (asterisks) are shown. The green circles represent the results of the GASP near-IR monitoring at the Campo Imperatore and Teide observatories. The optical spectrum of 1226+023 by Buttiglione et al. (2009) as well as near−IR−to−UV SEDs of 1510−089, 1633+382, and 2251+158 already published in papers by the GASP-WEBT collaboration are also plotted. Contributions from the synchrotron (dot-dashed line) and QSO-like (solid line) emission are displayed in blue. The latter is derived from the SWIRE QSO1 templates, but when a brighter disc is required, a black-body component is added. In these cases we show in grey both the QSO1 template (solid line) and the black body (dashed line). The model fit to the 3C 273 SED requires further dust emission, obtained by adding another black-body component (grey dotted line). The black line represents the sum of all components. 79

4.1 Light curve of OJ 248 in R band. It includes 1211 points from 15 observatories, distinguished by different colours and symbols. 83

4.2 Light curves of OJ 248 in optical (R band) and near-IR (J, H, K bands) in 2006–2013 built with GASP-WEBT data. In the near-IR light curves the blue diamonds are from the Campo Imperatore Observatory and the red points from the Teide Observatory. 84

4.3 Time evolution of the optical magnitude in R band (top panel) and of the percentage of polarized flux (bottom panel). The data are from different observatories: Calar Alto (green squares), Crimean (red diamonds), Lowell (pink asterisks), San Pedro Martir (cyan triangles), Steward (blue circles), and St. Petersburg (orange crosses). 86

4.4 Optical polarization percentage P plotted against the de-absorbed flux density in the R band. The data are from different observatories: Calar Alto (green), Crimean (red), Lowell (pink), San Pedro Martir (cyan), Steward (blue), and St. Petersburg (orange). 86

4.5 The evolution of the Q and U Stokes'parameters as a function of time. Different colours during the 2012–2013 outburst highlight the data of the selected periods indicated in Fig. 4.6. 87

4.6 Q versus U for all the data shown in Fig. 4.5. Coloured lines connect subsequent data belonging to the periods listed in the legend (JD-2450000). The direction is indicated by the arrows. 87

4.7 Time evolution of the optical magnitude in R band (top panel), of the percentage of polarized flux (middle panel) and of the EVPA "corrected" for the $\pm n\pi$ ambiguity (bottom panel, see text for explanation) during the 2012–2013 outburst. Data are from different observatories: Calar Alto (green squares), Crimean (red diamonds), Lowell (pink asterisks), San Pedro Martir (cyan triangles), Steward (blue circles), and St. Petersburg (orange crosses). 88

4.8 Optical spectra of OJ 248 during different brightness states obtained at the Steward Observatory, showing the Mg II emission line at $z = 0.939$ (blue) and the Mg II absorption line at $z = 0.525$ (orange). 90

4.9 Gaussian fit (red solid line) to the Mg II emission line of the spectrum taken on 2008 October 30 and shown in Fig. 4.8. The cyan line indicates the linear fit to the continuum; the red dashed line represents the residuals. 90
4.10 Top: time evolution of the Mg II broad emission line flux; the dashed line represents the average value and the dotted-dashed line the standard deviation around the mean. Bottom: EW of Mg II versus the continuum flux density; the solid line displays the behaviour of the EW assuming a constant line flux equal to its average value. 91
4.11 Light curves of OJ 248 at different frequencies in 2006–2013. From top to bottom: R-band optical magnitudes (see also Fig. 4.1), 345 GHz data from SMA, 230 GHz data from SMA (red triangles) and IRAM (blue crosses), 86 GHz data from IRAM, 43 GHz data from Noto, 37 GHz data from Metsähovi, 22, 8, and 5 GHz data from Medicina. 93
4.12 Discrete correlation functions between the R-band de-absorbed and 230 GHz flux densities (blue filled circles) and between the 230 and 37 light curves (red empty circles). 94
4.13 Light curves of OJ 248 built with *Swift*-UVOT data in optical and UV. 96
4.14 The XRT spectrum of OJ 248 on 2012 October 2. The best fit was obtained with a power law with fixed absorption given by the sum of the Galactic and intervening DLA $N_{\rm H}$ values. The bottom panel shows the ratio of the data to the folded model. 97
4.15 The X-ray photon index Γ as a function of the unabsorbed flux density at 1 keV. Only data with error less than 30% of the flux are shown. Red points correspond to data acquired after JD = 2456100, i.e. during the 2012–2013 outburst. 98
4.16 Light curves of OJ 248 at different frequencies in 2006–2013. From top to bottom: the *Fermi*-LAT 0.1–100 GeV fluxes (10^{-8} ph cm^{-2} s^{-1}) derived with different time bins (red symbols refer to data binned over roughly six-month time intervals, blue ones to monthly binned data, and green symbols to weekly-binned data in the outburst period; cyan arrows indicate upper limits); the 1-keV *Swift*-XRT flux densities (μJy); the *Swift*-UVOT $m2$ flux densities (mJy); the GASP-WEBT R-band flux densities (mJy); the GASP-WEBT K-band flux densities (mJy); the 230 GHz flux densities (Jy); the 37 GHz (orange points) and 43 GHz (green points) flux densities (Jy). The X-ray, UV, optical and near-IR light curves were corrected by both Galactic and DLA absorption. 99
4.17 Light curves in the γ-ray and optical (R) bands over the whole period (top), and during the 2012–2013 outburst period indicated by the yellow stripe (bottom). . 100
4.18 Discrete correlation functions between the γ-ray fluxes and the R-band de-absorbed flux densities (blue filled circles) and between the γ-ray fluxes and the X-ray flux densities at 1 keV (red empty circles). The inset shows the results of Monte Carlo simulations of the γ-optical correlation (see text for details). 103
4.19 Discrete correlation functions between the X-ray and 230 GHz flux densities (blue filled circles) and between the X-ray and R-band de-absorbed flux densities (red empty circles). 104
4.20 Spectral energy distributions of OJ 248 from the radio to the γ-ray frequencies during three epochs characterised by different brightness states. 105

5.1 Finding chart for Mrk 421 with the stars of the optical photometric sequence labelled from 1 to 3. The field of view is ∼10'×10'. 109

5.2 Optical light curve of Mrk 421 built with data from the GASP-WEBT collaboration in R band. Different colours and symbols highlight data from different telescopes. 110

5.3 Near-infrared light curves of Mrk 421 built with data from the GASP-WEBT collaboration in J, H and K bands. 111

5.4 The J-band light curve in the 2011-2015 period (top panel); the corresponding J-K colour as a function of time (middle panel) and of brightness level (bottom panel). In the bottom panel the solid line represents a linear fit to the data. . . . 114

5.5 UV light curves of Mrk 421 built with *Swift*-UVOT data. 115

5.6 X-ray light curve of Mrk 421 obtained from data by the XRT instrument onboard the *Swift* telescope in the period 2007-2015. 116

5.7 Reduced χ^2 versus the number of degrees of freedom for the different models applied to the XRT spectra. Blue triangles represent the results of the power law model with fixed $N_{\rm H}$, red diamonds those of the power law model with $N_{\rm H}$ free and the cyan circles those of the log parabola model. 117

5.8 The XRT spectrum of Mkr 421 on 2008 February 13. The best fit was obtained with a log parabola model. The bottom panel shows the ratio of the data to the folded model. 117

5.9 Time evolution of the Galactic hydrogen column $N_{\rm H}$ when a power law model with free absorption is applied to the XRT spectra. The cyan line marks the average value. 118

5.10 The X-ray photon index Γ as a function of the unabsorbed flux density at 1 keV. Data with error less than 30% of the flux are shown. Red squares refer to the best-fitted cases, where χ^2 is in the range 0.8-1.2 and the number of degrees of freedom is > 10. The solid line represents a linear fit to the data. 118

5.11 The behaviour of the α (left) and β (right) parameters of the log parabola model applied to the XRT spectra of Mrk 421. The solid line represents a linear fit to the data. 119

5.12 Light curves of Mrk 421 at different frequencies in 2007-2015. From top to bottom: 1) the X-ray light curve from *Swift*-XRT (counts s^{-1}); 2) the *Swift*-UVOT light curve in the uvm2 band (mJy); 3) the GASP-WEBT R-band flux density light curve (mJy); 4) the near-infrared K band flux density light curve (mJy). The light curves in the m2, R and K bands were corrected for the host galaxy contribution. 120

5.13 From top to bottom: 1)the X-ray light curve from *Swift*-XRT (counts s^{-1}) with the cubic spline interpolation through the 15-day binned data; 2) the GASP-WEBT R-band flux density light curve (mJy) with the cubic spline interpolation through the 15-day binned data; 3) the ratio between the spline fits to the X-ray and R band. 121

5.14 From top to bottom: a) R-band flux density light curve with cubic spline interpolation through the 15 day binned data (red line); b) polarisation percentage with cubic spline interpolation through the 15 day binned data (black line); different symbols and colours refer to different observatories: Calar Alto (green squares), Crimean (red diamonds), Lowell (cyan triangles) and Steward (blue circles); c) EVPA after correction for the $\pm 180^{\circ} n$ ambiguity. 122

5.15 Histograms of electric vector polarisation angle (EVPA). 123

5.16 An enlargement of Fig. 5.14 for different periods where activity is noteworthy. . 124

5.17 Degree of polarisation as a function of the R-band flux density. Right: after correction for the host galaxy contribution, left: observed. Different symbols and colours refer to different observatories. 125

5.18 Stokes parameters q an u of the optical polarization of Mrk 421. Subsequent points have been connected with a cubic spline interpolation. The arrows indicate the orientation. 125

5.19 Left panel: Two of the Mrk 421 spectra obtained at the Steward Observatory. They correspond to the maximum and minimum brightness states, differing by a factor ~ 5 in flux density. Right panel: the same spectra in the $log(\nu F_{\nu})$ versus $log(\nu)$ representation. 126

5.20 The continuum colour ("blue" to "red" flux ratio) of Mrk 421 as a function of the source brightness (V-band flux densitiy 5510$\mathring{A}$ in mJy). 127

5.21 The observed degree of polarisation plotted against the optical continuum colour of Mrk 421. The polarisation and flux ratio measurements are simultaneous. The polarisation is derived from the Steward Observatory spectropolarimetry as the median value within the 5000-7000 $\mathring{A}$ range. 127

5.22 Time evolution of the observed flux density (top) and degree of polarization (bottom) in two different wavelength ranges (blue and red). 128

5.23 Left panel: relationship between the ratio of observed polarisation in the blue to red bins and colour, defined as in Fig. 5.20. Right panel: colour versus the difference between the polarisation position angles in the blue and red bins. . . . 129

5.24 Discrete correlation function between the X-ray and the R-band light curves over the whole 2007-2015 period. 130

5.25 Auto-correlation function for the galaxy subtracted for the optical fluxes (left) and X-ray rates (right). The data have been binned over 4 days, while the ACF was obtained with a bin size of 20 days. 131

5.26 Optical (red points) and X-ray (blue points) ACFs. The red line represents the optical ACF shifted by 60 days. 131

5.27 Broad-band SEDs of Mrk 421 at eight different epochs where simultaneous near-IR, optical, UV and X-ray data are available. They correspond to different brightness states of the source and different spectral shapes in the X-ray energy range. The number correspond with the different JD-2450000. 133

6.1 Histogram showing the number of objects N_{obj} with N_{data} polarization measurements in the Steward Observatory blazar program database. 137

6.2 The BL Lacs sample. From top to bottom: a) the *Fermi*-LAT 0.1–100 GeV fluxes (10^{-6} ph cm^{-2} s^{-1}) derived with different time bins (red symbols refer to daily binned data, blue ones to weekly binned data, b) V-band magnitude light curve with different colours distinguishing the various observing cycles; c) 230 and 345 GHz data from the SMA (only for S5 0716+714, OJ 287 and BL Lac); d) Polarisation percentage; e) EVPA after correction for the ±180° ambiguity. . . 138
6.3 The BL Lacs sample. Optical polarization percentage P plotted against the V band magnitude. The different colours highlight the different observation cycles. 140
6.4 The FSRQs sample. From top to bottom: a) the *Fermi*-LAT 0.1–100 GeV fluxes (10^{-6} ph cm^{-2} s^{-1}) derived with different time bins (red symbols refer to daily binned data, blue ones to weekly binned data, b) V-band magnitude light curve with different colours distinguishing the various observing cycles; c) 230 and 345 GHz data from the SMA; d) Polarisation percentage; e) EVPA after correction for the ±180° ambiguity. 142
6.5 The FSRQs sample. Optical polarization percentage P plotted against the V band magnitude. The different colours highlight the different observation cycles. 143
6.6 The BL Lacs sample. From top to bottom: a) light curves at different frequencies; black/red symbols represent data from Teide/WHT in the K-band, pink/cyan symbols those in the J-band, while the R-band optical flux densities come from the Teide (filled blue circles), Lowell (green squares), and Calar Alto (orange crosses) observatories, and those in the V-band (blue empty circles) are from the Steward Observatory b) Polarization percentage; blue symbols refer to the optical R band, red and cyan symbols to the K and J bands, respectively, and the green crosses and orange asterisks represent radio data from the Mojave project (15 GHz) and Boston group (43 GHz), respectively; d) EVPA after correction for the $\pm 180°n$ ambiguity. 147
6.7 The FSRQs sample. From top to bottom: a) light curves at different frequencies; black/red symbols represent data from Teide/WHT in the K-band, pink/cyan symbols those in the J-band, while the R-band optical flux densities come from the Teide (filled blue circles), Lowell (green squares), and Calar Alto (orange crosses) observatories, and those in the V-band (blue empty circles) are from the Steward Observatory b) Polarization percentage; blue symbols refer to the optical R band, red and cyan symbols to the K and J bands, respectively, and the green crosses and orange asterisks represent radio data from the Mojave project (15 GHz) and Boston group (43 GHz), respectively; d) EVPA after correction for the $\pm 180°n$ ambiguity. 148

List of Tables

2.1 List of the sources monitored by the GASP 28
2.2 Instrument characteristics of BAT. 43
2.3 Instrument characteristics of XRT. 43
2.4 Instrument characteristics of UVOT. 48

3.1 The BL Lac objects in the GASP target list. 54
3.2 The FSRQs in the GASP target list. 55
3.3 Mean fractional variation of the near-IR flux densities, f_i, average de-reddened colour indices $< J-H >$ and $< H-K >$ with their standard deviations (σ) and their mean fractional variations f_{J-H} and f_{H-K} for the BL Lac objects in the GASP target list. 61
3.4 Mean fractional variation of the near-IR flux densities, f_i, average de-reddened colour indices $< J-H >$ and $< H-K >$ with their standard deviations (σ) and their mean fractional variations f_{J-H} and f_{H-K} for the FSRQs in the GASP target list. 62

4.1 Results of the spectral analysis of the *Fermi*-LAT data of OJ 248 in the 0.1–100 GeV energy range. The reference energy E_0 was fixed to 392.1 MeV. The fitted model was a power law with photon index Γ. 100
4.2 Extinction [mag] in the various Bessel (Bessell et al., 1998) and *Swift*-UVOT bands toward OJ 248. Both the Galactic absorption and that by the DLA system at $z = 0.525$ are given. The value of the total extinction suffered by the source radiation is the sum of the two. 102

5.1 UV, optical and near-infrared observing bands with the corresponding Galactic extinction values, photometry aperture radius, fractions of the host galaxy contribution included in the given aperture, host galaxy flux density contribution to the source photometry and median observed flux. 113

6.1 Fractional variability of the flux at different frequencies and the polarization degree P for the six selected BL Lacs. 139
6.2 Fractional variability of the flux at different frequencies and the polarization degree P for the six selected FSRQs. 141